Multi-scale modelling of Gibraltar Straits and its regulating role of the Mediterranean climate

Nicolas M. Gonzalez

To cite this version:

Nicolas M. Gonzalez. Multi-scale modelling of Gibraltar Straits and its regulating role of the Mediterranean climate. Ocean, Atmosphere. Université Paul Sabatier - Toulouse III, 2023. English. NNT : 2023TOU30090 . tel-04257734

HAL Id: tel-04257734
https://theses.hal.science/tel-04257734v1

Submitted on 25 Oct 2023

Université Fédérale
Toulouse Midi-Pyrénées

THÈSE

En vue de l'obtention du

DOCTORAT DE L'UNIVERSITÉ DE TOULOUSE

Délivré par l'Université Toulouse 3 - Paul Sabatier

Présentée et soutenue par

Nicolas M. GONZALEZ

Le 24 mars 2023

Modélisation multi-échelle du détroit de Gibraltar et de son rôle de régulateur du climat méditerranéen

---

Ecole doctorale : **SDU2E - Sciences de l'Univers, de l'Environnement et de l'Espace**

Spécialité : **Océan, Atmosphère, Climat**

Unité de recherche :
CNRM - Centre National de Recherches Météorologiques

Thèse dirigée par
Hervé GIORDANI et Robin WALDMAN

Jury
Mme Nadia PINARDI, Rapporteure
M. Achim WIRTH, Rapporteur
M. Casimir DE LAVERGNE, Examinateur
M. JOSE C. SáNCHEZ GARRIDO, Examinateur
M. Hervé GIORDANI, Directeur de thèse
M. Robin WALDMAN, Co-directeur de thèse
Mme Claude ESTOURNEL, Présidente

Abstract

The Strait of Gibraltar (SoG) is a narrow and shallow channel that forms the primary connection between the Mediterranean Sea and the global Ocean. This oceanic pathway is home to tremendous exchanges of water masses, closing the Mediterranean thermohaline and biogeochemical balances. Despite the broad impacts of these exchanges on the Mediterranean Sea, various mechanisms at play within the SoG and their influence on the Mediterranean climate remain, so far, unclear. This PhD investigates tidal and fine-scale processes at the SoG, their relevance to the Mediterranean climate, and their representation in numerical models. To do so, we rely on two numerical models of the Mediterranean region, providing different perspectives on the SoG and its large-scale influence. The first one is an ocean model, used in stand alone mode and characterized by high-resolution at the SoG, allowing us to investigate fine-scale and non-linear mechanisms within the strait. The second one, developed in the scope of this PhD, is a fully-coupled regional model of the Mediterranean region, with refinement capacity at the SoG and explicit or parameterized tides. It allows us to build a hierarchy of numerical simulations that aims at isolating the respective and combined influences of tidal and fine-scale processes at the strait on the Mediterranean Sea and overlying atmosphere. We first focus on understanding the mechanisms driving tide-induced water mass transformations across the SoG, so-called tidal mixing. We show that tidal mixing relies on fine-scale dynamics, forced by the interaction of tidal currents with the abrupt topography of the strait. More specifically, the mixing is driven by a periodic enhancement of vertical shear near the seafloor and a weakening vertical stratification in the vicinity of topographic obstacles, where tidal convergence and divergence patterns feed recirculation cells. Then, we show that tidal and fine-scale processes within the strait significantly influence Mediterranean hydrography, particularly for salinity, ultimately modulating the Mediterranean deep convection. In this way, local processes at the SoG indirectly affect the hydrography of intermediate and deep water masses as well as long-term hydrographic trends over deep layers. For the first time to our knowledge, we reveal that these processes also impact on the atmosphere. Specifically, in the summertime, tidal mixing at the SoG moderately cools and dries the near-surface atmosphere. Ultimately, this drives a moderate decrease in cloudiness over the Sea and coastal areas and a decrease in precipitation over the western Mediterranean region. Finally, we investigate a tidal mixing parameterization for coarse-resolution non-tidal models of the Mediterranean Sea. We show that the parameterization reproduces remarkably well the main characteristics of the water mass transformations across the strait, but further developments are needed to parameterize tidal advection mechanisms. Overall, these results highlight that both explicit tides and kilometric resolution at the SoG should be included in numerical models of the Mediterranean Sea for use over decadal time-scales. When

this is not possible, parameterizations should be used. This works provides a first step in this direction.

Résumé en Français

Le détroit de Gibraltar (DdG) est un chenal étroit et peu profond constituant la principale connexion entre la mer Méditerranée et l'océan global. Cette "passerelle" maritime est le siège de considérables échanges de masses d'eau, fermant les équilibres thermohalins et biogéochimiques de la Méditerranée. Malgré les larges impacts de ces échanges sur la mer Méditerranée, les différents mécanismes en jeu dans le DdG et leur influence sur le climat méditerranéen restent, jusqu'à présent, peu clairs. Cette thèse étudie les mécanismes de marée et de fine-échelle en jeu dans le DdG, leur pertinence pour le climat méditerranéen et leur représentation dans les modèles numériques. Pour ce faire, on s'appuie sur deux modèles numériques de la région méditerranéenne, offrant différentes perspectives sur le DdG et son influence à grande échelle. Le premier est un modèle océanique, utilisé en mode forcé et caractérisé par une haute résolution au DdG. Il nous permet d'étudier les mécanismes de fine échelle dans le détroit. Le second modèle, développé dans le cadre de cette thèse, est un modèle régional de la Méditerranée entièrement couplé, avec une capacité de raffinement au DdG et des marées explicites ou paramétrisées. Il nous permet de construire une hiérarchie de simulations numériques visant à isoler les influences respectives et combinées des processus de marée et de fine échelle au détroit sur la mer Méditerranée et l'atmosphère environnante. Nous nous concentrons d'abord sur la compréhension des mécanismes contrôlant la transformation des masses d'eau traversant le détroit (appelé mélange de marée ci-après). Nous montrons que le mélange de marée repose sur de fines structures dynamiques, forcées par l'interaction des courants de marée avec la topographie abrupte du détroit. Plus précisément, le mélange est causé par une intensification périodique du cisaillement vertical près du plancher océanique et un affaiblissement de la stratification verticale à proximité des obstacles topographiques, où des zones de convergence et de divergence induites par la marée alimentent des cellules de recirculation. Ensuite, nous montrons que les processus de marée et de fine échelle à l'intérieur du détroit influencent significativement l'hydrographie de la Méditerranée, en particulier sa salinité, modulant à terme la convection profonde en mer Méditerranée. Ainsi, les processus locaux au DdG affectent indirectement l'hydrographie des masses d'eau Méditerranéennes intermédiaires et profondes ainsi que les tendances hydrographiques à long terme sur les couches profondes. Pour la première fois à notre connaissance, nous révélons que ces processus ont également un impact sur l'atmosphère. Plus précisément, en été, le mélange des marées au niveau du SoG refroidit et assèche modérément l'atmosphère proche de la surface. A terme, cela entraîne une diminution modérée de la nébulosité sur la mer et les zones côtières et une diminution des précipitations sur la région de la Méditerranée occidentale. Enfin, nous étudions une paramétrisation du mélange de marée pour les modèles de la mer Méditerranée à basse résolution et sans marée. Nous montrons que la paramétrisation reproduit remarquablement bien les princi-

pales caractéristiques des transformations de la masse d'eau au travers du détroit. Cependant, des développements supplémentaires sont nécessaires pour paramétrer les mécanismes advectifs de marée. Dans l'ensemble, ces résultats soulignent que les modèles numériques de la mer Méditerranée utilisés sur des périodes décennales devraient inclure à la fois des marées explicites et une résolution kilométrique au DdG. Lorsque cela n'est pas possible, des paramétrisations devraient être utilisées. Ce travail fait un premier pas dans cette direction.

Acknowledgements

Quelle aventure ! Si ce texte apparaitra en début de manuscrit aux curieux qui le liront, il marque pour moi la fin de ma thèse. Il vient donc naturellement avec quelques remerciements pour toutes les personnes qui m'ont accompagné ces trois dernières années.

Pour commencer, je voudrais remercier mes encadrants, Robin Waldman, Hervé Giordani, et Samuel Somot. J'estime avoir eu beaucoup de chance de réaliser ma thèse à leurs côtés, car ils possèdent tous les trois des qualités humaines et scientifiques remarquables. En particulier, j'aimerais remercier Robin pour sa pédagogie et son impressionnante culture scientifique. Il m'a beaucoup appris sur la physique de l'océan, mais aussi plus généralement sur la démarche scientifique et la vulgarisation, qui sont essentielles à tout chercheur. Merci aussi pour les agréables moments que l'on a pu passer en dehors du travail. J'espère que de nombreux autres les suivront. Merci à Hervé de m'avoir partagé son expertise physique difficile à égaler, en particulier sur les mécanismes en lien avec la turbulence, mais aussi sa fine connaissance des rouages de la modélisation numérique. J'ai beaucoup apprécié les discussions scientifiques que j'ai pu avoir avec lui, et j'espère en avoir encore dans les années à venir. Merci à Samuel pour ses conseils et remarques toujours avisés. Je suis très admiratif de son recul sur les nombreuses thématiques scientifiques qui touchent à la physique du bassin Méditerranéen et sa grande implication dans la communauté scientifique. J'espère un jour pouvoir approcher sa perspicacité.

Je voudrais ensuite remercier les personnes, qui, bien qu'elles ne soient pas directement responsables de mon encadrement, on prit de leur temps pour m'accompagner. Merci à Gianmaria Sannino, que je considère comme mon quatrième encadrant. Il m'a permis de passer un séjour à Rome tout autant riche scientifiquement que culturellement. Côté numérique, un grand merci à Florence Sevault pour tout le temps qu'elle a consacré à m'apprendre le fonctionnement du modèle d'océan du CNRM, et pour m'avoir aidé à résoudre les problèmes variés qui viennent avec son utilisation. Un grand merci également à Jérôme Chanut, d'avoir pris de son temps pour me partager sa grande expertise du code NEMO. Enfin merci à Jonathan Beuvier, pour m'avoir partagé ses larges connaissances sur la configuration NEMOMED12 utilisée au CNRM.

Je voudrais aussi remercier mes proches, qui m'ont soutenu au quotidien en dehors de mon cadre de travail. En premier, merci à mes parents, Catherine et Jean, de m'avoir soutenu dans mes études et mes activités musicales. Merci aussi pour les moments de détente que l'on a pu passer ensemble. Pour rester à Antibes, merci à mes grands-parents, Anne-Marie et Pierre Millot, pour leur bonne humeur, leur bienveillance, et leur accueil toujours chaleureux. A Toulouse maintenant, gracias abuela, por los domingos que pasamos en familia comiendo paella. Merci à mes frères Adrien et Matthias, qui me font prendre du recul sur moi-même et m'inspirent au quotidien. Merci Adri, de montrer à tout le monde qu'avec de la motivation et du courage on peut poursuivre ses passions. Merci Matthias, de me permettre de me sentir encore un peu étudiant avec toi. Merci aussi à ma famille toulousaine, tantes, oncles, cousines et cousins. Plus particulièrement, merci Patricia, Serge, Louis et Guilhem, pour les repas et les après-midis de construction de meubles. Sans eux je travaillerais encore peut-être sur des cartons... Merci Anna, Paloma et Marina, pour les après-midis de détente chez Mémé.

Bien sûr, merci à Eléna Dupuy, qui a eu la patience de m'accompagner pendant ces trois années intenses. Merci pour son aide précieuse au quotidien, et surtout, de me donner une seconde perspective sur les petites et grandes choses de la vie, j'ai beaucoup appris durant ces dernières années. Merci aussi à toute sa famille, en particulier à Corinne, Claude, et Pauline pour les bons moments que l'on a pu partager. Merci à mes amis proches, d'Antibes comme de Toulouse, je sais qu'ils sauront se reconnaître.

Enfin, merci à tous mes collègues du CNRM pour tous les échanges intéressants que l'on a pu avoir. Plus spécifiquement, merci à l'équipe IOGA pour leur accueil et leur bienveillance. Merci de m'avoir fait découvrir vos travaux et de vous être intéressés aux miens. Merci aux doctorants du CNRM pour la bonne ambiance et la convivialité au labo : Isaline, Lucas, Maya, Raphaël, Romain, Thomas, Tony, William. Mention spéciale à mon co-bureau Antoine Doury, qui a toujours été là pour m'aider à prendre du recul sur mon travail et m'inciter à conserver un bon équilibre avec ma vie personnelle.

Contents

Chapter 1

Introduction

1.1 A brief introduction to straits

1.1.1 Straits and the global Ocean

Straits, sometimes referred to as channels, passes, or passages, are narrow oceanic pathways connecting two larger bodies of water (see Figure 1.1). By definition, a strait is bounded by two landmasses, which may be continents (Strait of Bering, Strait of Gibraltar), islands (strait of Bonifacio, North Channel), or a combination of both (Fram strait, Strait of Magellan). From the ocean surface, straits display a large variety of shapes, ranging from relatively large pathways (Fram Strait, Davis strait) to narrow and elongated channels (Dardanelles, Strait of Malacca). This geometric diversity is even more remarkable beneath the ocean surface, which reveals complex topographic structures. In fact, straits are often characterized by deep cavities, down to 1500m depth for the Lombok Strait, abrupt seamounts stretching over several hundred meters, as the Majuan Bank at the Strait of Gibraltar, or conversely, a relatively flat seafloor, which may be as shallow as that of the Torres Strait (7 to 20m depth; GEBCO Bathymetric Compilation Group, 2022).

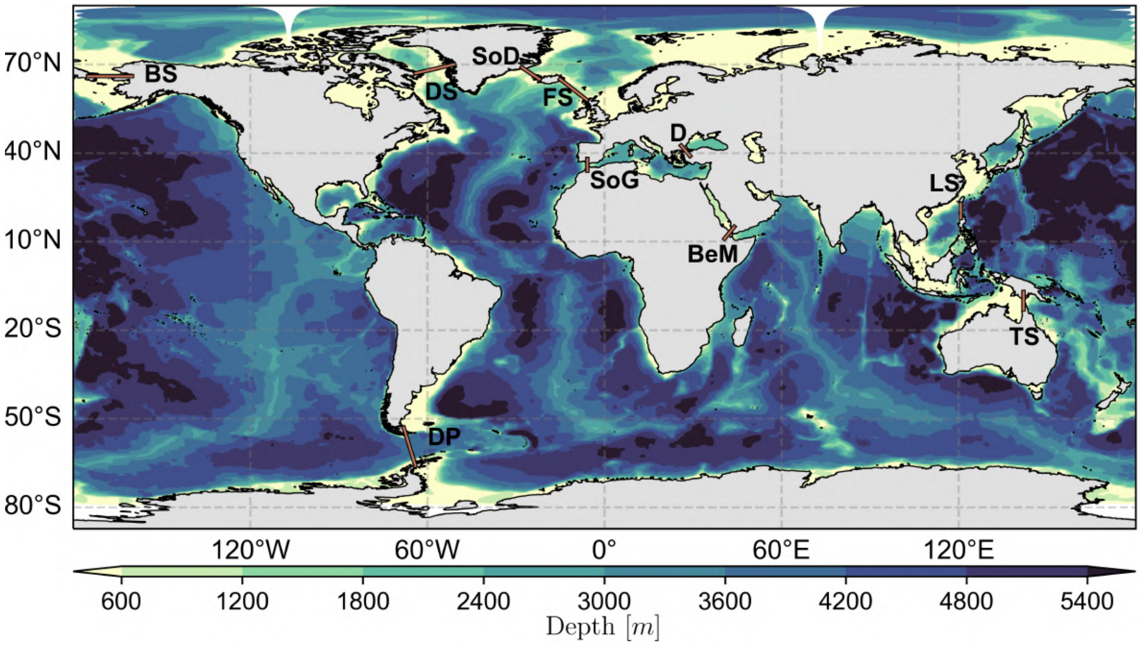

Figure 1.1: Global Ocean bathymetry with some major straits. From north to south, Devis Strait (DS), Strait of Denmark (SoD), Bering Strait (BS), Fram Strait (FS), Dardanelles (S), Strait of Gibraltar (SoG), Luzon Strait (LS), Bab-el-Mandab (BeM), Torres Strait (TS), Drakes Passage (DP)

From a physical perspective, straits are key components of the global ocean. Their large-scale influence is primarily related to the global ocean geometry. Indeed, unlike the atmosphere, the ocean water masses are enclosed in large basins bounded by solid Earth. By providing a narrow passage, straits exert a significant dynamical influence on the water masses crossing them. The Drake passage (DP in Figure 1.1), which shapes the Antarctic Circumpolar Current (ACC), is a vivid example of this influence. Indeed, the width, depth, and orientation of Drake passage are essential parameters for the expression of the ACC (de Boer et al, 2022; Toumoulin et al, 2020; Viebahn et al, 2016). Similarly, other major straits of the world ocean exert a substantial influence on large scale-circulation, such as the Bering, Fram, and Davis straits (BS, FS, and DS in Figure 1.1) for the Arctic ocean (Timmermans and Marshall, 2020) and the north Atlantic (Wadley and Bigg, 2002), or the Luzon strait (LS in Figure 1.1) for the South China Sea (Zhu et al, 2019). Smaller straits generally have a weaker dynamic influence. However, their number can result in structures of great influence, such as the network of straits that shapes the Indonesian Throughflow, substantially impacting the circulation of the Indian and Pacific oceans (Lee et al, 2002).

Because they provide a connection between large oceanic basin, straits are home to intense heat, salt, and biogeochemical exchanges. In fact, large straits such as the Bering or the Denmark straits (BS and SoD in Figure 1.1) have a significant influence on the global ocean heat and salt circulation (thermohaline circulation hereinafter) (Dickson and Brown, 1994; Weijer et al, 2001; Send et al, 2011; von Appen et al, 2014; Hu et al, 2015). More locally, many straits influence the hydrographic and biogeochemical properties of large oceanic basins. For example, the exchanges through the Kurils straits have an impact on the water mass properties of the North Pacific Ocean and the Okhotsk Sea (Nakamura et al, 2004; Ono et al, 2007), indirectly modulating the Pacific thermohaline circulation (Kawasaki and Hasumi, 2010). Finally, strait dynamics can sometimes impact atmospheric circulation by modulating large-scale surface stratification. This is the case in the Indian Ocean, where the surface cooling and freshening induced by the Indonesian Throughflow (Song, 2004) influences the regional atmospheric circulation (Koch-Larrouy et al, 2010).

1.1.2 Home to a variety of physical processes

Besides their large-scale influence, straits are home to a variety of non-linear mechanisms, making them a rich scientific benchmark for oceanographers. In particular, straits generally are highly turbulent areas, where in situ microstructure measurements reveal turbulence levels several orders of magnitude higher than in the open Ocean (Bryden and Nurser, 2003). Although the mechanism driving strait turbulence depends on their shape or dimension, a relatively common feature is dense water overflow, a gravitational current resulting from the advection of dense water in a lighter environment. This uncommon physical process encompasses both turbulent and advective mechanisms (see Figure 1.2). Upon cascading along the sloped seafloor, overflow currents drive significant diapycnal mixing through friction and entrainment of the overlying water masses (Legg et al, 2008). In addition, overflows have a dynamic influence on the overlaying water masses. In fact, variations of the velocity or the thickness of overflow water masses can influence the large-scale circulation patterns (Yang and Price, 2007; Kida et al, 2008; Peliz et al, 2009). Because of their significant role in the global thermohaline circulation, the overflows of major straits have been extensively studied. The most notable of them are perhaps that of the Denmark strait (Girton and Sanford, 2003) and the Strait of Gibraltar (SoG in Figure 1.1 Bower et al, 2002), but less influential overflows occur in various other locations, such as the Bab-el-Mandab (BeM in Figure 1.1 Peters et al, 2005) and the Brass strait (Middleton and Cirano, 2005).

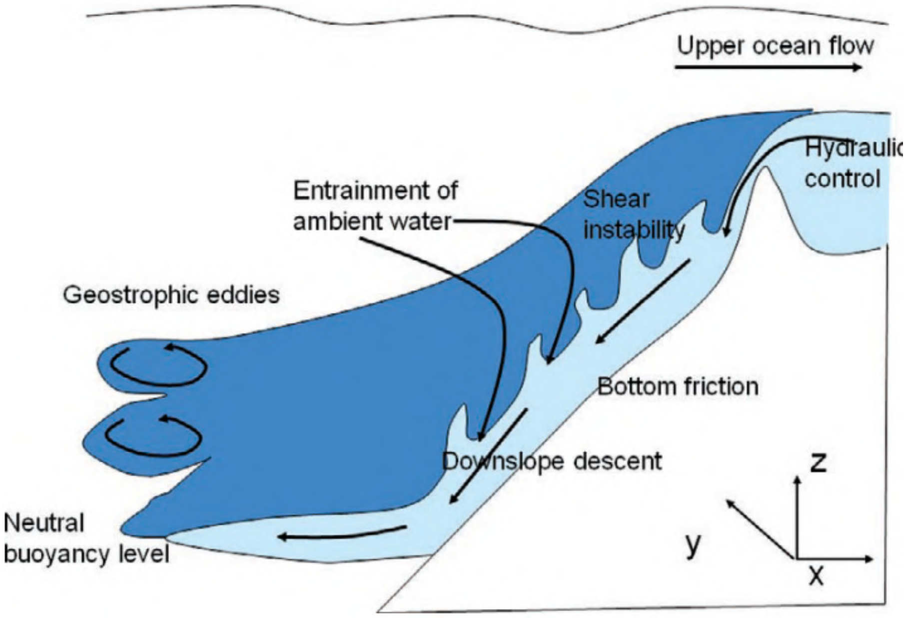

Figure 1.2: Physical processes acting in overflows. Figure and legend from Legg et al (2009)

Other non-linear mechanisms are specific to a particular type of straits, as they rely on specific geometric properties. In particular, narrow straits are commonly subject to intense turbulence. Generally, this enhanced turbulence is related to supercritical flows, forced by either or both significant channel shrinkage and tidal currents. By interacting with large topographic obstacles, these intense flows can generate internal waves of various shapes and behaviors (Vázquez et al, 2006; Buijsman et al, 2010; Petrusevich et al, 2018; Purwandana et al, 2020, 2021). For example, in the Luzon strait, the combination of asymmetric barotropic (depth-constant) tidal currents, internal tide resonances on topographic obstacles, and the baroclinic (depth-varying) mean flow results in the propagation of asymmetric internal waves on each side of the strait (Buijsman et al, 2010). Asymmetric internal waves are also generated at the Strait of Gibraltar due to interactions between the baroclinic flow, barotropic tidal currents, and abrupt topographic obstacles (Brandt et al, 1996). During their propagation, various non-linear mechanisms interfere with these waves (Vlasenko et al, 2009; Farmer et al, 2011), which progressively dissipate, driving turbulent mixing that may induce intense and large-scale hydrographic anomalies (Wesson and Gregg, 1994; Tian et al, 2009; Itoh et al, 2011; Yagi and Yasuda, 2012; Purwandana et al, 2021).

Finally, a less common feature, also related to straits geometry, is the generation of submesoscale eddies. These eddies, resulting from the interaction of intense currents through the strait and topographic slopes, can be generated at the surface, as in the Luzon Strait (Xu et al, 2015; Zhang et al, 2020, 2022), but also at mid-depths as for the Strait of Gibraltar ($\sim$ 1000m depth) (Bashmachnikov et al, 2015) or the Brass Strait ($\sim$ 600m depth) (Baird and Ridgway, 2012). Depending on their lifetime, these structures can drive significant heat and salt transports, as for the Mediterranean water eddies in the Atlantic Ocean (Ienna et al, 2022).

1.2 The Strait of Gibraltar: a narrow channel with large-scale influence

1.2.1 Main characteristics

The Strait of Gibraltar (SoG hereinafter, displayed in Figure 1.3) is a narrow and shallow channel, constituting the only connection between the Atlantic Ocean and the Mediterranean Sea. From the ocean surface, it is an approximately 60km-long pathway, 15km wide at its narrowest section of the Tarifa Narrows (TN in Figure 1.3). Beneath the surface, it displays a steep and irregular seafloor, marked by several prominent topographic obstacles. From the western edge of the strait, the approximately 1000m deep seafloor rapidly shoals above 300m depth at the shallowest sill of the Camarinal (CS hereinafter, see Figure 1.3), just west of the Tarifa Narrows. Further west, the strait locally deepens, forming the so-called Tangier Basin, bounded to the west by the 300m deep Espartel Sill (ES hereinafter, see Figure 1.3). Just north of the ES, the shallow seamount of the Majuan Bank, culminating at $\sim$ 60m depth, splits the main underwater channel into two sub-channels, that reconnect further west, where the seafloor progressively deepens toward the Atlantic Ocean.

In stark contrast with its modest dimensions, the SoG is home to a tremendous water mass exchange between the Atlantic Ocean and the Mediterranean Sea. On climatic scales, this exchange can be described as a simple two-layer exchange flow. Qualitatively, over the upper 150m depth, relatively warm and fresh surface Atlantic waters are advected into the Mediterranean Basin, whereas, underneath, colder and saltier deep Mediterranean waters are exported to the Atlantic Ocean (Lacombe and Richez, 1982). Quantitatively, this exchange flow is characterized by strong currents (1m.s^{-1} on average), which sustain an intense flow of 0.85 ± 0.1 Sverdrups ($10^6\text{m}^3.\text{s}^{-1}$, Sv hereinafter) toward the Mediterranean and 0.80 ± 0.08Sv toward the Atlantic (Jordà et al, 2017b). At high-frequency the picture is more complex. Indeed, intense tidal currents propagating from the Atlantic Ocean interfere with the two-layer exchange flow. Due to their predominant barotropic structure and their great intensity (Candela et al, 1990; Candela, 1991), these tidal currents periodically reverse the exchange flow (Bryden et al, 1994; Lafuente et al, 2000; García-Lafuente et al, 2018) and generate large internal waves, mainly toward the Mediterranean Sea (Vázquez et al, 2009).

1.2.2 Influence on the global Ocean

For the Atlantic Ocean, the SoG is a heat sink and salinity source. After crossing the strait, the relatively warm and fresh Atlantic water masses are mainly advected eastward in the Mediterranean sea, where they are progressively saltened and cooled by the atmospheric forcing. Over time, the densified Atlantic water masses sink to mid and bottom depths of the Mediterranean. Those dense waters are in part advected back to the Atlantic Ocean as Mediterranean Outflow Waters (MOW) (Millot

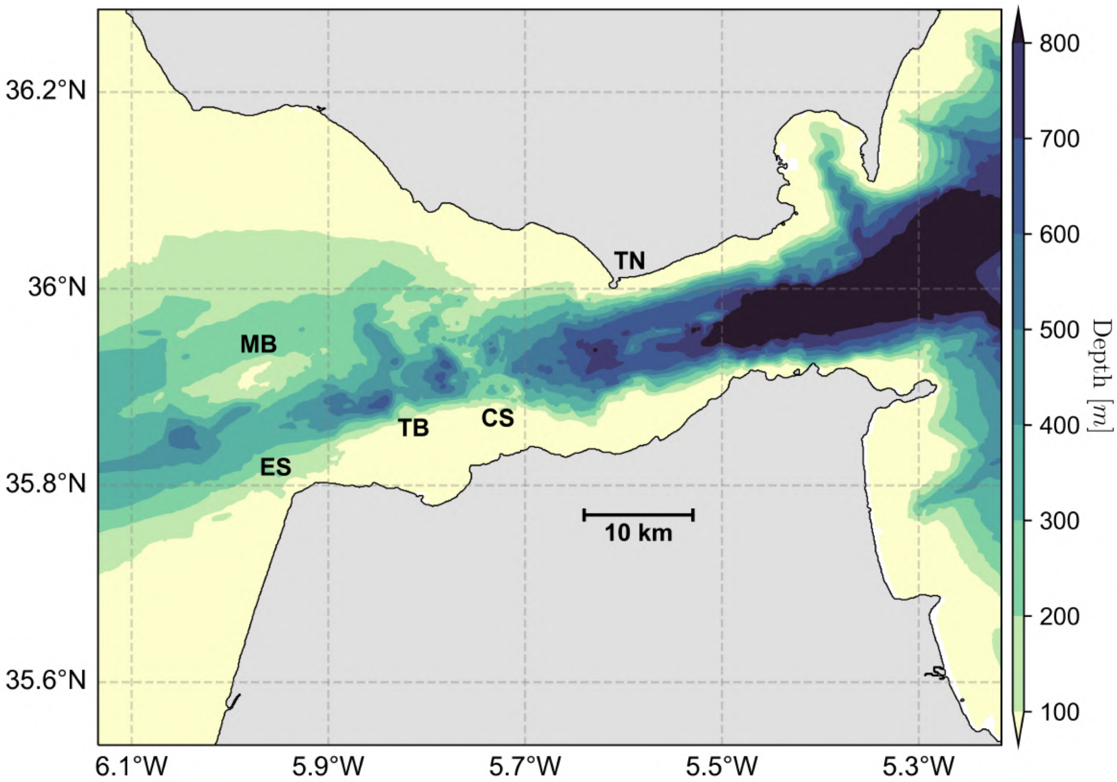

Figure 1.3: Strait of Gibraltar bathymetry from EMODnet Digital Bathymetry (DTM 2020) (EMODnet Bathymetry Consortium https://doi.org/10.12770/bb6a87dd-e579-4036-abe1-e649cea9881a). The acronyms “TN”, “CS”, “TB”,“ES”, and“MB”, displayed in black, stand for Tarifa Narrows, Camarinal Sill, Tangier Basin, Espartel Sill, And Majuan Bank, respectively.

and Taupier-Letage, 2005; Pinardi et al, 2015; Estournel et al, 2021). In the Gulf of Cádiz, west of the SoG, these dense water masses cascade along the Iberian continental slope. They mainly flow westward, entraining along their path the overlying water masses (Iorga and Lozier, 1999a; Baringer and Price, 1999) until they reach the western edge of the Gulf of Cádiz. The MOWs then enter the Tagus Basin at a buoyant depth of $\sim$ 1000m, where they form an anticyclonic gyre (Daniault et al, 1994; De Pascual-Collar et al, 2019). From this retention area, a fraction of the MOWs recirculates toward the Gulf of Cádiz, but most of them spread northward, either along an indirect westward anticyclonic pathway or directly, following the western European continental slope (Iorga and Lozier, 1999a,b; Bower et al, 2002; Lozier and Stewart, 2008; Carracedo et al, 2014).

The northward flow of MOW described above is believed to influence the Nordic seas convective activity and, thus, the Atlantic Meridional Overturning Circulation (AMOC hereinafter). This large-scale influence of the SoG was originally proposed by Reid (1979), who argued that upon reaching the northern seas, the MOW could act as a salt source for the North Atlantic deep water formation. However, this hypothesis is criticized due to the lack of direct observational evidence of MOW in the Northern Seas and the significant amount of energy needed for the MOW to cross the shallow sills enclosing them, such as the Wyville-Thomson Ridge (Hill and Mitchelson-Jacob, 1993; McCartney and Mauritzen, 2001). A more likely scenario

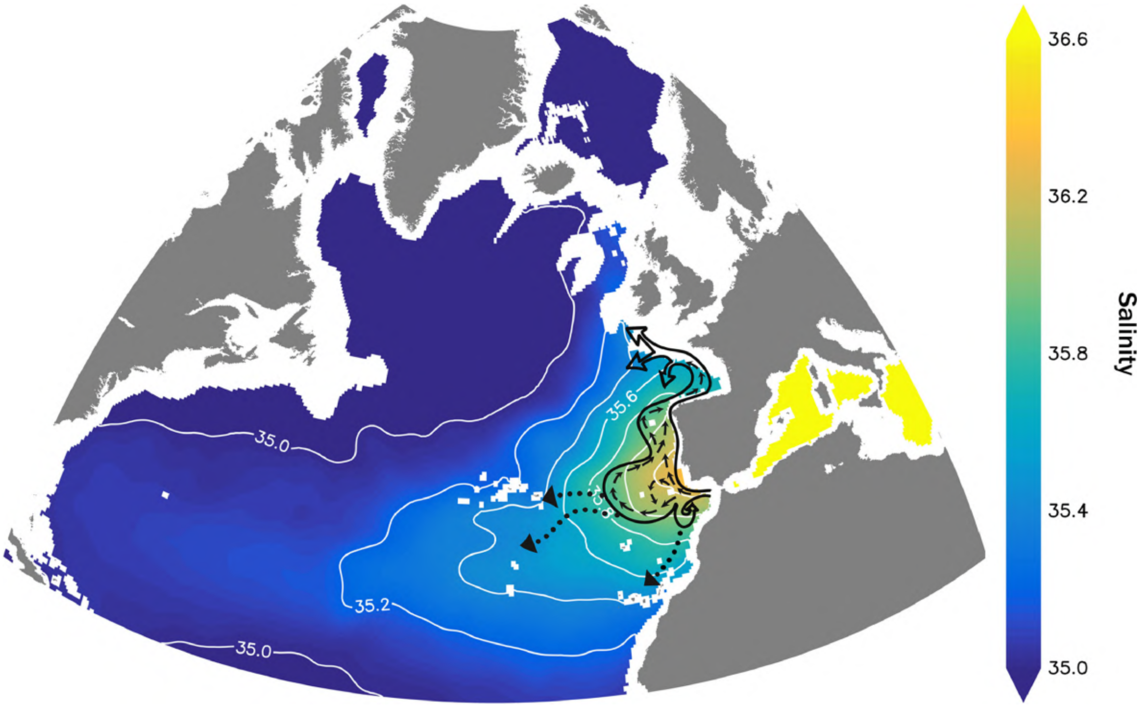

Figure 1.4: Mediterranean Salt Tongue representation on the World Ocean Atlas 2013 salinity field at 1200m depth (Zweng Mm Reagan Jr, 2019). The overlaid scheme (modified after Lozier et al (2019)) indicates the permanent MOW pathways (continuous arrows) and the preferred paths of meddies (dotted arrows). Figure and legend from Izquierdo and Mikolajewicz (2019)

is thus that the MOW indirectly enhances deep convection in the Northern Seas by acting as a salt source for the north Atlantic (McCartney and Mauritzen, 2001). Despite the lack of observational evidences, connections between the MOWs and the AMOC have been highlighted in several modeling studies. Based on coupled atmosphere-ocean general circulation model simulations, Chan and Motoi (2003) and Ivanovic et al (2014) argue that the MOW contributes 1–2Sv of flow to the AMOC. Furthermore, paleoclimatic studies have suggested that during the last glacial periods (Voelker et al, 2006) and past sapropel events (Swingedouw et al, 2019), modulations of the MOW intensity and characteristics had a substantial impact on the AMOC.

In addition to the northward flow, MOWs also spread in the Atlantic as isolated and coherent eddies, so-called meddies, which mainly form along the Iberian coast (Chérubin et al, 1997; Richardson et al, 2000; Serra et al, 2002; Bashmachnikov et al, 2015) due to the interaction between the MOW flow and the seafloor (D'Asaro, 1988; Pichevin and Nof, 1996; Aiki and Yamagata, 2004; Chérubin et al, 2007). These structures, typically 300-1000m thick and 20-60km large (Bashmachnikov et al, 2015), propagate over long distances in the Atlantic Ocean (Bashmachnikov et al, 2015), influencing the ocean stratification from the surface to great depth. In particular, meddies have been estimated to contribute to more than half of the formation of the Mediterranean water Tongue (Arhan et al, 1994; Sparrow et al, 2002), a prominent core of warm and saline water masses in the North Atlantic Ocean, centered at $\sim$ 1000m depth.

Finally, in the context of climate change, the MOW represents a fast-changing water mass for the Atlantic ocean (Potter and Lozier, 2004; Millot et al, 2006; Millot, 2007; Naranjo et al, 2017; García-Lafuente et al, 2021). Indeed, following the latest estimate of García-Lafuente et al (2021), MOWs have been warming at a substantial rate of 0.34°C over the 2013–2022 decade, raising the question of the possible impact of these modifications on the Atlantic ocean.

1.2.3 Influence on the Mediterranean Sea

The exchange flow through the SoG is essential to the Mediterranean basin-scale volume, heat, and salt budgets. On average, the Atlantic inflow exceeds by 0.04 ± 0.02Sv the Mediterranean outflow (Jordà et al, 2017b), compensating for the net volume loss at the surface of the Mediterranean, where evaporation exceeds precipitations and river runoffs. The SoG can also be considered as a net heat source for the Mediterranean Sea, compensating the $4.5 \pm 4.1\text{W.m}^{-2}$ lost to the atmosphere (Jordà et al, 2017b). Regarding the salt budget, the higher salinity of the Mediterranean outflow is compensated by its weaker intensity with respect to the Atlantic inflow, resulting in almost zero net salt transport. Finally, the SoG is also one of the primary nutrient sources for the Mediterranean Sea (Huertas et al, 2012a; Ramírez-Romero et al, 2014). A good illustration of the influence of SoG on the Mediterranean Sea is the Messinian Salinity crisis, which occurred approximately 6 million years ago during the Miocene epoch. At that time, the Mediterranean Sea was disconnected from the global ocean and almost completely dried (Rouchy and Caruso, 2006). To a lesser extent, numerical simulations have shown that the depth of the SoG has by itself a significant impact on the western Mediterranean overturning circulation (Topper and Meijer, 2015; Alhammoud et al, 2010).

Besides basin-scale budgets, the Atlantic inflow and Mediterranean outflow modulate various dynamical and thermodynamical processes within the Mediterranean Sea. Regarding the Atlantic inflow, it has an evident influence on the Mediterranean circulation. Just east of the SoG, it organizes as a relatively narrow current, the Atlantic Jet, which acts as the main dynamical forcing for the Alboran Sea gyre circulation (Tintoré et al, 1991; Viúdez et al, 1996, 1998; Renault et al, 2012). In particular, Sánchez-Garrido et al (2013) highlighted that the tidal modulations of the Atlantic Jet act as a destabilizing force for the Alboran Sea circulation, which occasionally collapses under its influence. Further east, at the exit of the Alboran sea, the Atlantic Jet reorganizes along the African coast (mainly due to the Coriolis effect), shaping the Algerian Current, an essential brick of the Mediterranean circulation (Millot and Taupier-Letage, 2005). Other than the horizontal circulation, the Atlantic inflow indirectly influences the Mediterranean overturning circulation. Indeed, several numerical simulations have highlighted that modifications of inflowing Atlantic water masses result in modulations of the Western (Naranjo et al, 2014; Sannino et al, 2015) and Eastern (Beuvier et al, 2010a) Mediterranean convective activity.

On the other hand, the Mediterranean outflow is key to the renewal of Mediterranean deep water masses. In particular, three characteristic Mediterranean deep water masses are advected through the SoG: the Levantine Intermediate Waters, formed in the eastern Basin; the Tyrrhenian Deep Water, formed in the Tyrrhenian Sea; and the Western Mediterranean Deep water (WMDW), formed in the Gulf of Lions (Millot, 2009; Naranjo et al, 2015). Despite their large density, these water masses are drained out of the Mediterranean through the Bernoulli suction mechanism (Stommel) et al, 1973), which can be enhanced by the kinetic energy provided by the Western Alboran Gyre (Naranjo et al, 2012), tidal currents (Naranjo et al, 2014), and the atmospheric pressure (García-Lafuente et al, 2009). The proportion of the water masses outflowing from the Mediterranean varies seasonally, depending on the volume of WMDW formed during winter, which results in a more or less intense uplifting of old WMDW nearby the strait (García Lafuente et al, 2007; Naranjo et al, 2017). Other than deep ocean circulation, heat, and salt contents, this mechanism indirectly impacts on Mediterranean biogeochemical properties as it participates in both the renewal of organic matter at great depth (Tamburini et al, 2013) and the loss of nutrient-enriched water masses to the Atlantic Ocean (Huertas et al, 2012a; Durrieu de Madron et al, 2011).

With that in mind, various aspects of the role played by SoG in the Mediterranean Sea are not well understood. In particular, the influence of the local processes at the SoG on the Eastern Mediterranean basin, intermediate and deep Mediterranean water masses, and their interannual variability remain unclear. Finally, the possible influence of Atlantic water masses transformations across the SoG on air-sea fluxes and the impacts on the overlying atmosphere are yet to be investigated.

1.3 The exchange flow through the Strait of Gibraltar: a long-standing scientific matter

1.3.1 Overview of the exchange flow

The SoG has been a region of interest for physical oceanographers since the early 20th century (Schmidt, 1922; Jacobsen and Thomsen, 1934). However, technical difficulties, mainly related to the intense dynamics within the strait and the heavy marine traffic, prevented the acquisition of reliable observations until the late 1960s (Ziegenbein, 1969). Over the following years, various studies and observational campaigns progressively allowed scientists to bring light on the complex mechanisms at play within the strait. In the literature, these mechanisms are often distinguished by the time scales upon which they manifest. Three main regimes are often referred to (Lacombe and Richez, 1982; García Lafuente et al, 2002; Vargas et al, 2006; Sánchez-Román et al, 2012; García-Lafuente et al, 2021): sub-seasonal (seasonal and interannual periods), subinertial (from days to few months), and tidal (from tens of hours to hourly).

Sub-seasonal frequencies retain a small fraction of the exchange flow variability through the SoG (Candela et al, 1990; Boutov et al, 2014). However, they are essential to investigate basin-scale variations of the Mediterranean Sea volume, heat, and salt contents. Climatologically, the net volume flow through the SoG mainly balances the freshwater loss at the surface of the Mediterranean Sea. In this way, it is primarily driven by the basin-scale budget of evaporation and precipitation, although river runoff and exchanges with the black sea can have a secondary modulating effect (Fenoglio-Marc et al, 2013). Basin-scale volume variations also drive a seasonal modulation of the net flow, which peaks in late summer (August-September) (Lafuente et al, 2002; Soto-Navarro et al, 2010). Finally, the net flow follows a less intense semiannual cycle, characterized by a maximal peak in April (Soto-Navarro et al, 2010). However, this variability mode is challenging to interpret. So far, it has mainly been associated with wind stress and atmospheric pressure variations, which display similar patterns (Lafuente et al, 2002). Regarding the inflow and outflow, Boutov et al (2014) argue that the zonal wind stress mainly drives their interannual variability. The underlying mechanism consists of a wind-induced drag of the surface Atlantic layer, which indirectly affects the Mediterranean layer through mass continuity. On sub-annual scales, the inflow displays both seasonal (peak in August) and semiannual (maximal peak in April) variations. The seasonal cycle results from both basin-scale volume variations and the increased density gradient between Atlantic and Mediterranean water masses in summer (Soto-Navarro et al, 2010). The semiannual cycle is associated, as for the net flow, with the enhanced atmospheric forcing in winter. The outflow mainly displays a seasonal cycle, driven by the variation of the WMDW reservoir, refilled in spring (March-April), facilitating the suction of deep water through the SoG (García Lafuente et al, 2007; Sánchez-Román et al, 2009; Soto-Navarro et al, 2010; Sammartino et al, 2015). Unlike for the inflow, the enhancing effect of the stratification intensification in summer is cancelled by the basin-scale continuity condition.

On monthly scales, the net flow through the SoG is mainly modulated by atmospheric pressure variations (Candela et al, 1989; Candela, 1991) and, to a lesser extent, wind stress over the Atlantic Ocean (García Lafuente et al, 2002). Fortnightly oscillations, driven by the monthly (spring-neap) tidal cycle, have also been repeatedly observed (Candela et al, 1989; Bryden et al, 1994; Tsimplis and Bryden, 2000; García Lafuente et al, 2002; Vargas et al, 2006). However, the extent of their intensity is debated (see Table 1 of Vargas et al, 2006). The inflow and outflow are also subject to significant monthly and fortnightly oscillations. As for the net flow, the atmospheric forcing drives their monthly variability, whereas tidal currents drive their fortnightly variability. The monthly variability is more marked on the inflow, which responds primarily to the atmospheric forcing. Conversely, the outflow is rather related to the tidal forcing, reaching a maximum during neap tide (Lafuente et al, 2000; Vargas et al, 2006).

From hourly to daily frequency, the variability of the exchanged flows reaches its maximal amplitude (Figure 8, panel b of Sammartino et al, 2015). The volume transport through the strait is driven by the semidiurnal barotropic tidal currents (Candela, 1991), which periodically reverse the exchanged flows and produce internal waves, forcing substantial volume transports (Pettigrew and Hyde, 1990). However, these high-frequency variations mostly cancel out over the tidal cycle. Thus, they do not necessarily impact on the low-frequency transports through the strait. The residual effect of the tidal advection is often referred to as the "eddy flux" (Bryden et al, 1994). Its diagnosed intensity depends on the method used to compute the tidal and subinertial transports through the strait. However, previous studies generally agree on a significant eddy flux at the CS, where it contributes to the mean exchange by up to 45% (Bryden et al, 1994; Tsimplis and Bryden, 2000; Vargas et al, 2006), and much less intense at the eastern entrance of the strait (Lafuente et al, 2000; Baschek et al, 2001) and over the ES (Vargas et al, 2006; Sánchez-Román et al, 2009). Regarding the ES, Sammartino et al (2015) specify that although it is weak on average, the eddy flux has a notable influence during spring tides.

1.3.2 Non-linear processes and diapycnal mixing

Apart from Atlantic and Mediterranean exchanges, the SoG is characterized by the frequent occurrence of various non-linear processes. In fact, the SoG has long been recognized as a highly turbulent area (Bryden and Kinder, 1991). To some extent, these turbulent processes can be related to the energetic flows crossing the strait, which are periodically submitted to hydraulic control due to the interactions of tidal currents with steep topographic obstacles and channel shrinkage (Sannino et al, 2007). In addition to diapycnal mixing, directly induced by these intense dynamical structures, the relaxation of transient hydraulic control points during the tidal cycle produces large internal waves (illustrated in Figure 1.5), mainly toward the Mediterranean Sea (Lacombe and Richez, 1982; La Violette and Lacombe, 1988; Wesson and Gregg, 1988; Pettigrew and Hyde, 1990; Morozov et al, 2002; Alpers et al, 2008; Sánchez Garrido et al, 2008; Vázquez et al, 2009), but also toward the Atlantic Ocean (Farmer et al, 1988; Vázquez et al, 2006), and across the strait (Watson and Robinson, 1990; Richez, 1994). At the CS, internal waves are also produced under subcritical conditions, however, their intensity is substantially reduced (Vázquez et al, 2008). In turn these internal waves dissipate, powering turbulent mixing.

Thus, turbulent mixing encapsulates the influence of various non-linear processes occurring within the SoG. Furthermore it is by itself a determining feature of the Atlantic and Mediterranean exchanges, as it substantially influences the hydrographic properties of water masses crossing the strait. Indeed, intense temperature and salinity anomalies associated to diapycnal mixing have been repeatedly observed throughout the strait (Pettigrew and Hyde, 1990; Send and Baschek, 2001; Bruno et al, 2002; Macias et al, 2006; García-Lafuente et al, 2011). At the ES, long-term in situ observations show that the outflowing Mediterranean water is warmed by 0.1°C and saltened by 0.1‰ between the CS and ES (García-Lafuente et al, 2011). Besides in situ observations, diapycnal mixing at the SoG has also been highlighted in several numerical simulations (Macías et al, 2007; Sannino et al, 2009a; García Lafuente et al, 2013; Sanchez-Roman et al, 2018). More precisely, the tide-induced diapycnal mixing at the SoG was shown to significantly impact on the net heat and salt budgets through the SoG (Harzallah et al, 2014; Sanchez-Roman et al, 2018). Similarly, in the Alborán Sea, Naranjo et al (2014) show that the tide-induced diapycnal mixing cools the Atlantic jet by 0.37°C and saltens it by 0.47psu.

Unfortunately, the field investigation of diapycnal mixing at the SoG is chal-

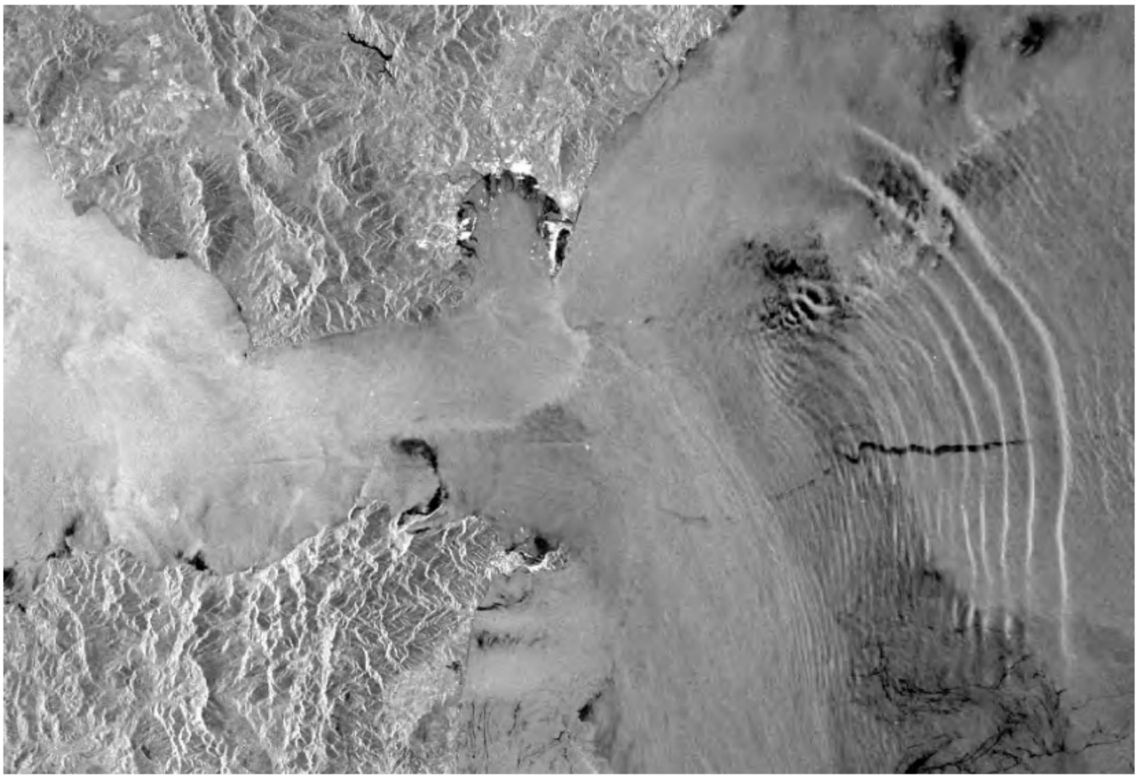

Figure 1.5: ERS-1 SAR image acquired on 1 January 1993 at 22:39 UTC (orbit: 7661) showing sea surface manifestations of a packet of internal solitary waves generated in the Strait of Gibraltar and propagating eastward into the Mediterranean Sea. The dark line intersecting the packet results from an oil spill, probably released from a ship. Imaged area: 100 km × 50 km. ©ESA. Figure and legend from Alpers et al (2008)

lenging and the underlying processes are still unclear at the present time. A few direct observations have been made so far, mainly during the Gibraltar Experiment (Kinder and Parilla, 1987). At that time several cruises equipped with Advanced Microstructure Profiler (Gregg et al, 1982) highlighted the presence of intense turbulent structures throughout the strait, orders of magnitude higher than in the open ocean (Wesson and Gregg, 1988, 1994). Those surveys allowed characterizing the high-frequency variability of these structures, mainly driven by semidiurnal tidal currents. In particular, during the westward tidal phase, high dissipation rates were measured at the CS, extending up to the Atlantic layer and to 1-2km west of the sill. In addition, compact unstable gravitational structures of 30-75m amplitude were evidenced at both spring and neap tides above the the crest of the CS and at its western flank. After the reversal of the westward tide, less intense but significant dissipation rates were measured east of the CS, at the interface between Atlantic and Mediterranean waters.

Regarding the underlying physical mechanism, Wesson and Gregg (1994) attribute the mixing and static instabilities near the CS to the shearing and thinning of the Mediterranean outflow, which is submitted to hydraulic control at the top of the CS. During the eastward tidal phase, the mixing is mainly related to an intensification of vertical shear at the interface between the exchanged water masses. Various observational studies have also highlighted the enhancement of diapycnal mixing along the trail of the eastward internal bore produced at the CS (Pettigrew and Hyde, 1990; Send and Baschek, 2001; Vázquez et al, 2006). In addition, Bruno et al (2013) related the diapycnal mixing to convergences and divergences patterns withing the strait. In the rest of the literature, diapycnal mixing at the SoG is often related to tidal intensification of the vertical shear (Bruno et al, 2002; Macías et al, 2007; Sanchez-Garrido et al, 2011; Sánchez-Garrido et al, 2013) and hydraulic transitions (Sannino et al, 2009a; García Lafuente et al, 2013; Naranjo et al, 2014). Overall, this relatively limited knowledge of the processes driving diapycnal mixing at the SoG represents a scientific barrier to understanding the heat and salt exchanges through the SoG. In addition, a better appreciation of these processes is needed in numerical modeling to better assess the capabilities and limitations of state-of-the-art numerical models.

1.4 Modeling the Strait of Gibraltar

1.4.1 Motivations and overview of available numerical models

The exchange flow through the SoG is key to the understanding of long-term thermohaline and dynamic modulations over Mediterranean Sea, and to a lesser extent, over the Atlantic and global oceans. However, it is complex to observe (Ziegenbein, 1969; Millot et al, 2006) and relies on non-linear mechanisms, displaying both significant temporal and spatial variability. In this way, the processes and tendencies investigated through observational campaigns are often limited by the locality and short-term coverage of the in situ dataset collected. In particular, seasonal and inter-annual variability of the mechanism at play within the SoG has long been a grey area (Lacombe and Richez, 1982; Wesson and Gregg, 1994; Bryden et al, 1994). Long time series at the ES are now available (Sammartino et al, 2015; García-Lafuente et al, 2021), allowing oceanographers to investigate the long-term variations of the exchange flow. However, the local character of these measurements remains problematic and requires interpolation methods, introducing additional uncertainties, in particular when investigating fine-scale processes (Soto-Navarro et al, 2010; García-Lafuente et al, 2011; Jordà et al, 2017b).

A possible solution for addressing these issues is that of numerical modeling, whereby the ocean dynamics and thermodynamics are simulated through a computer program based on mathematical equations. Although imperfect, these simulations benefit from a tunable and regular spatio-temporal coverage. At the present time, a large variety of numerical models exists, offering different representations of ocean physics. Because of its channel-like structure and the various processes at play within it, the SoG is eligible to many of these models. For example, tidal wave propagation within the strait can be studied based on models representing only depth-averaged (barotropic) ocean physics (Tejedor et al, 1998, 1999; Izquierdo et al, 2001). Conversely, to study the evolution of baroclinic structures through the strait, meridional variations can sometimes be neglected. In this way, two-dimensional "channel" models with a more or less sophisticated representation of the ocean water column can be adopted, ranging from a simple two-layer model

(Artale and Levi, 1987) to continuously stratified models (Morozov et al, 2002; Hilt et al, 2020). These two-dimensional models can also indirectly account for the channel width and its zonal variations, as for the two-layer models of Farmer and Armi (1986); Brandt et al (1996). Finally, the full spatial structure of the mechanisms at play within the strait can be studied based three-dimensional models, which are more commonly used in the ocean modeling community. This type of model was first adapted to the SoG by the pioneering work of Wang (1987, 1989, 1993) and more widely developed since the early 2000s (Sannino et al, 2004, 2007; Sanchez-Garrido et al, 2011; García Lafuente et al, 2013; Sannino et al, 2014; Sanchez-Roman et al, 2018; Álvarez et al, 2019).

Besides the number of dimensions represented, a determining criterion for numerical models is that of spatial resolution, which is often a limiting factor for the spatio-temporal coverage of numerical simulations. Indeed, numerical models with fine-scale resolution are computationally expensive and cannot be used to simulate large areas of the global ocean over long periods. In particular, due to the large extent of the Earth radius compared to the ocean depth, the limiting factor is mainly horizontal resolution. In the following, we thus distinguish numerical models depending on their horizontal resolution. We consider three main categories:

- Sub-regional Circulation Models (SRCM): SRCM are high-resolution models ($500 - 100$m), covering small regions of the world ocean. These models aim at investigating fine-scale mechanisms over short periods (typically, less than one year).
- Regional Circulation Models (RCMs): RCMs are intermediate resolution models ($10 - 1$km) covering large but finite areas of the global ocean. These models aim at representing regional dynamics over long periods (typically, from decadal to centennial scales), but at a finer spatial resolution than GCM, allowing modellers to simulate the largest eddy structures of the ocean circulation.
- General Circulation Models (GCMs): GCMs are coarse resolution model ($\sim$ 100km), representing the global ocean in its entirety. Most of the time, GCMs are used to investigate large-scale phenomena over long time scales (typically, from decadal to centennial scales). Although they are commonly used by the global ocean modeling community, we will not discuss OGCMs in the following as their horizontal resolution does not allow for a realistic representation of the SoG.

1.4.2 The strait of Gibraltar at high resolution: insight into fine-scale and non-linear mechanisms

When applied to the SoG, SRCMs resolve the strait and its direct surroundings. We can classify SRCMs into two main categories, depending on whether or not they rely on the hydrostatic assumption. Under this assumption, the gravity force is considered balanced by the vertical pressure gradient. Most low-resolution models rely on this assumption, which makes them significantly less computationally expensive.

However, relaxation of this hypothesis is sometimes necessary to investigate nonlinear mechanisms.

Hydrostatic SRCM are mainly used to investigate the hydraulic properties of the exchange flow through the SoG, which does not require the relaxation of the hydrostatic assumption (Sannino et al, 2014). In particular, those numerical simulations successfully represent the thickening of the inflowing Atlantic layer during the inflowing tidal phase and that of the outflowing Mediterranean layer during the outflowing phase (Sannino et al, 2007). In this way, SRCMs allow investigating the relations between hydraulic transition, water masses entrainment, and vertical displacements of the interface between Atlantic and Mediterranean layers (Sannino et al, 2002, 2007). These simulations also shed light on the relation between the hydraulic transition and the release of the main internal bore produced at the CS (Sannino et al, 2004; Álvarez et al, 2011). Finally, SRCMs have also been used to asses the local impact of tidal forcing in the Alborán sea, highlighting its influence on the gyres circulation (Sánchez-Garrido et al, 2013).

On the other hand, although computationally expensive, non-hydrostatic SRCMs allow investigating nonlinear and fine-scale mechanisms at play within the SoG. In particular, relaxation of the hydrostatic assumption is essential to simulate the generation of short-scale internal solitary waves (illustrated in Figure 1.6 Sammartino et al, 2014; Álvarez et al, 2019; Hilt et al, 2020). Such simulations have substantially improved the understanding of these non-linear processes. For example, they allowed oceanographers to relate the presence of quasi-stationary waves with depressions induced by the formation of the eastward internal bore (Morozov et al, 2002). These simulations also provided insights into the disintegration of internal waves at the strait. In particular, Brandt et al (1996) argue that it results from a non-hydrostatic and non-linear steepening of the bore, and Vlasenko et al (2009) explains that the bore can evolve into a non-rank-ordered wave train through energy transfer from low to high-order internal waves, resulting from reflections of the leading wave on the lateral boundaries of the strait, mainly due to the Coriolis force.

Non-hydrostatic SRCM are also used to highlight the occurrence of non-linear processes complex to observe due to their low intensity and short time-coverage. In this way, based on numerical simulations and in situ measurements, Vázquez et al (2006) highlight the occurrence of second order internal waves in addition to the main internal bore and document its intensity with respect to the main internal bore. This second type of internal waves is also reproduced in Hilt et al (2020).

Finally, non-hydrostatic SRCM are useful for assessing the capabilities and limitations of hydrostatic models. In this way, Álvarez et al (2019) suggest that hydrostatic simulations are able, to some extent, to replicate processes simulated by non-hydrostatic simulations. However, this requires the use of very high resolution. In the same way, based on a statistical analysis of the occurrence of hydraulic control throughout the strait, Sannino et al (2014) argue that a hydrostatic simulation of 500m horizontal resolution is sufficient to realistically simulate the hydraulic properties of the exchange flow through the SoG.

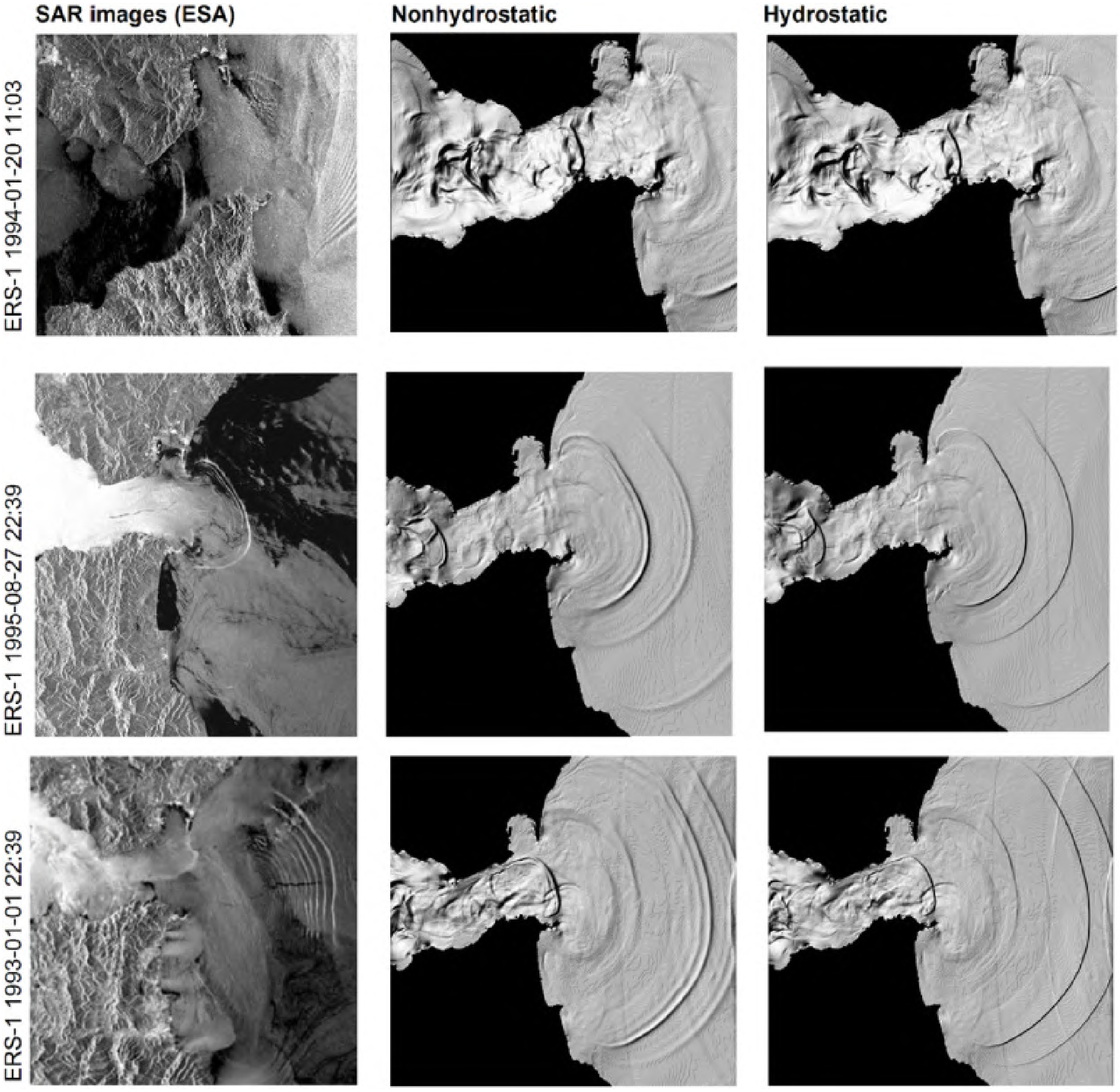

Figure 1.6: Satellite SAR images of surface manifestation of internal wavefronts (left), together with the modeled free-surface elevation (center: non-hydrostatic; right: hydrostatic) at the corresponding tidal phases. Figure and legend from Álvarez et al (2019)

1.4.3 The Strait of Gibraltar at intermediate resolution: A first glance at its influence on the Mediterranean Sea

Most RCMs simulating the SoG aim at representing the Mediterranean Sea and/or the Atlantic Ocean. In the following, we will mainly focus on regional models of the Mediterranean Sea. Models representing only the Atlantic ocean will not be discussed, as they are outside the scope of this PhD. Mediterranean RCMs are usually designed with a 10-5km horizontal resolution and vertical resolutions varying from a few meters at the ocean surface to hundreds of meters at its bottom (Pinardi and Masetti, 2000; Somot et al, 2006; Tonani et al, 2008; Sannino et al, 2009a; Naranjo et al, 2014; Harzallah et al, 2014; Soto-Navarro et al, 2015; Adloff et al, 2015). In the literature, Mediterranean RCMs have been shown to successfully represent the main circulation patterns of the Mediterranean Sea, with significant improvement over the past 20 years (Pinardi and Masetti, 2000; Demirov and Pinardi, 2002; Béranger et al, 2004; Tonani et al, 2008; Adloff et al, 2015; Pinardi et al, 2015; Nagy et al, 2019). They also offer a relatively accurate representation of the main mechanisms at play within the Mediterranean, such as the thermohaline circulation (Somot et al, 2006; Adloff et al, 2015; Waldman et al, 2018) and the deep convection in the Western Mediterranean Basin (Herrmann et al, 2010; Beuvier et al, 2012; Waldman et al, 2017b,a).

Although RCMs are able to reproduce the main dynamical and thermodynamical processes at play over the Mediterranean sea, they are also limited to some extent by their relatively coarse resolution and the physical simplifications they rely on. In fact, these limitations are particularly marked at the SoG, where non-linear fine-scale processes are at play. Regarding spatial resolution, Mediterranean RCMs offer a relatively rough representation of the strait geometry and topography, which are represented by few cells along the meridional direction (typically, two to three). The tuning of the model, in particular the lateral friction, bottom drag, and turbulent viscosity, allows simulating realistic volume exchanges through the strait (Tonani et al, 2008; Sannino et al, 2009b; Beuvier et al, 2012; Soto-Navarro et al, 2015). However, this type of ad-hoc correction does not ensure a realistic representation of the Atlantic inflow at the entrance of the Mediterranean Sea. More specifically, Sannino et al (2009b) highlighted that the model resolution at the SoG directly impacts on the properties of the simulated Atlantic inflow, which in turn affects the western Mediterranean basin stratification, and consequently, the associated convective activity.

Regarding physics simplifications, most RCMs do not include tidal forcing, although it is the main driver of diapycnal mixing between the exchanged water masses at the SoG (Wesson and Gregg, 1994). In some RCMs, omission of tidal currents at the SoG is parameterized through an artificial increase of the simulated vertical mixing (Oddo et al, 2009), or an enhancement of the bottom friction (Beuvier et al, 2012), however, these corrections are unlikely to fully compensate for the lack of tidal forcing, and their realism remains poorly documented so far. Several studies have investigated the differences between numerical simulations differing only by the inclusion or omission of tidal forcing, highlighting that tide-induced mixing at the SoG has a significant effect on the the heat and salt transports through the strait (Naranjo et al, 2014; Sannino et al, 2015; Harzallah et al, 2014; Sanchez-Roman et al, 2018). Over long periods, the omission of tidal forcing impacts the heat and salt contents of the Mediterranean Basin, mainly affecting the surface thermohaline characteristics, (see Figure 1.7), and thus, the stratification, regional circulation, and deep water formation. Overall, these inaccuracies can explain why state of the art RCMs display a large inter-model spread on the average exchanges through the SoG and their simulated trends over the historical and future climate (Harzallah et al, 2018; Llasses et al, 2018; Soto-Navarro et al, 2020).

Overall, these limitations represent a technical barrier to the investigation of the role played by the SoG on the Mediterranean Sea. In addition, they stand in the way of improving the state-of-the-art numerical models of the Mediterranean Sea and assessing their current limitations. Simply put, further work is needed to delineate the key elements of the SoG that are required to represent the Mediterranean Sea over long periods. In particular, although it is relatively clear that tides and

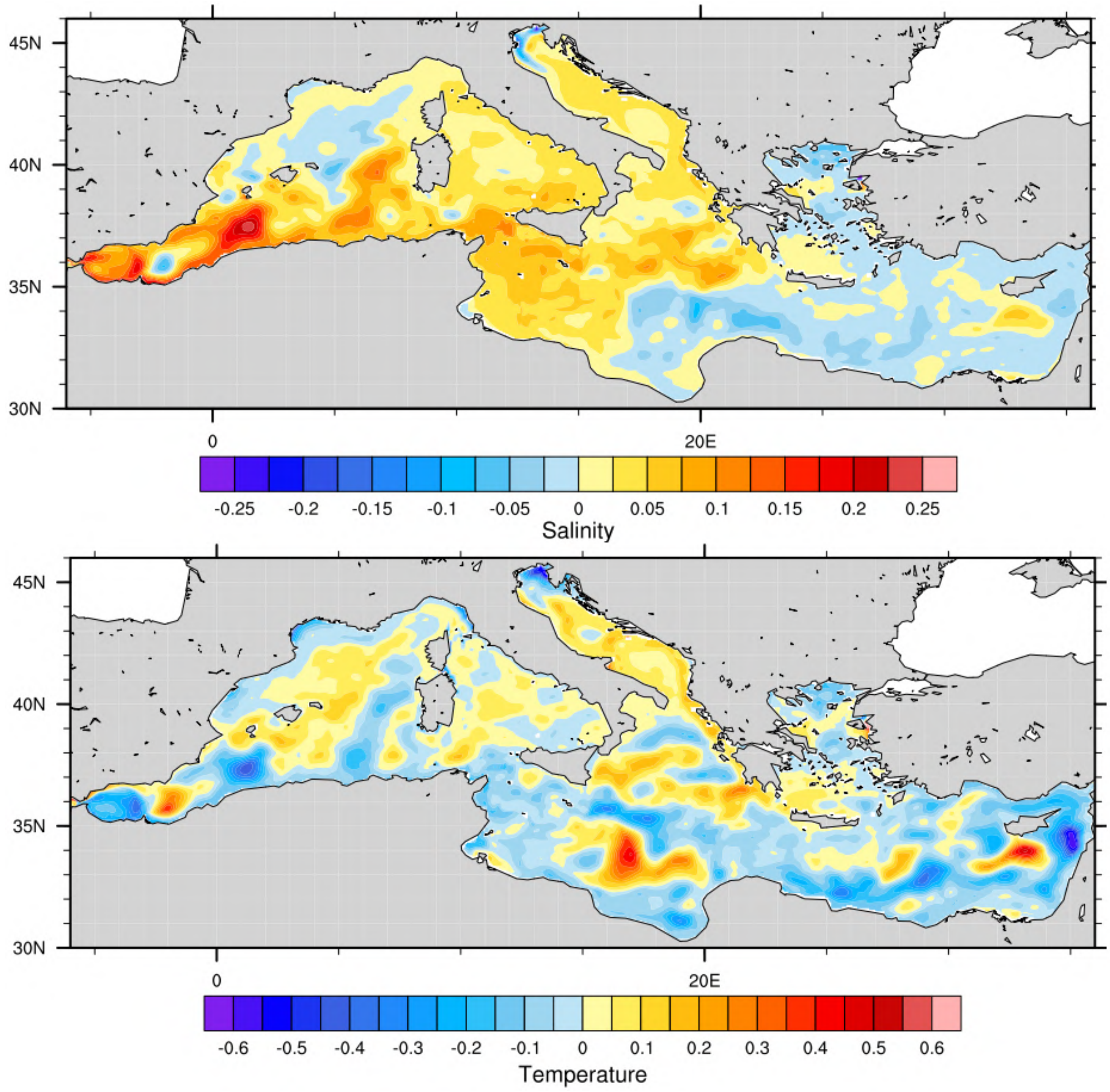

Figure 1.7: 0 – 150m average salinity (upper panel) and temperature (lower panel) anomalies induced by tidal forcing at the SoG. Anomalies are averaged over a temporal period of 10 years. Figure adapted from Figures 26 and 27 of Sannino et al (2015).

fine-scale resolution at the SoG are relevant to the Mediterranean surface hydrography, their respective importance need to be investigated in details.

1.5 PhD structure

To conclude on this introductory chapter, we have seen that the exchanges through the SoG involve various non-linear and fine-scale mechanisms, which have a large-scale influence on the Mediterranean Sea. Although many aspects of these mechanisms and their large-scale impacts are well understood, grey areas remain.

At the SoG, an intense diapycnal mixing is known to occur and fluctuate with tidal currents, significantly altering the water masses exchanged through the strait. This turbulent process is commonly associated with hydraulic transitions and vertical shear. However, the underlying mechanisms remain unclear. Besides deepening our understanding of the exchanges through the SoG, a better appreciation of this process is needed in numerical modeling. It would better assess the limitations of state-of-the-art numerical models and possibly offer alternatives to the rough representation of the SoG in coarse resolution models. In this PhD, we will address this problem by investigating the following question: **What physical processes drive tidal mixing at the Strait of Gibraltar?**

Besides diapycnal mixing, the exchanges through the SoG rely on various mechanisms that result from the interactions of barotropic tidal currents, fine-scale nonlinear dynamics, and topographic obstacles. In fact, different studies have highlighted that these elements significantly influence the western Mediterranean Basin through the hydrographic and dynamical properties of inflowing Atlantic water masses. However, the respective and combined effects of tidal currents, fine-scale dynamics, and geometry of the strait are unclear. In addition, a deeper understanding of these processes would provide valuable indications to ocean modelers questioning the added value of high resolution and tidal forcing at the SoG to represent the Mediterranean Sea over climatic scales. To address these scientific and technical matters, we will investigate the following question: **What are the key elements shaping the exchanges at the Strait of Gibraltar?**

Finally, several unknowns remain about the SoG influence on the Mediterranean Sea, particularly over decadal to centennial scales. Among these, the influence of the SoG on the Mediterranean convective activity and intermediate water masses must be better assessed, as previous studies were limited by the temporal coverage or coarse resolution of the simulations used (Sannino et al, 2009b; Naranjo et al, 2014; Harzallah et al, 2014; Sannino et al, 2015). In addition, although the SoG is known to primarily influence the Mediterranean Sea surface, possible feedbacks on the atmosphere have yet to be investigated. To lift these scientific barriers, we will investigate the following question: **What role does the Strait of Gibraltar play on the Mediterranean Climate?**

Besides the former introduction, this manuscript is organized into four chapters. The second chapter details the numerical developments carried out during this PhD. The scientific motivation underlying this technical work is to develop a numerical tool for assessing the respective and combined effects of tidal and fine-scale dynamics at the SoG and their influence on the Mediterranean Sea and climate. This numerical tool is used in the fourth and fifth chapters of this PhD. The third chapter investigates the mechanisms driving tidal mixing at the SoG in a kilometric resolution model of the Mediterranean Sea developed at the ENEA laboratory. The fourth chapter uses coupled ocean-atmosphere simulations to investigate the influence of tidal and fine-scale processes at the SoG on the Mediterranean Sea and its interactions with the atmosphere. Finally, the fifth chapter investigates an alternative to high-resolution and explicit tidal forcing at the SoG for coarse-resolution models. We draw our main conclusions and provide further prospects to this work in the last chapter.

Chapter 2

A Mediterranean Climate model with an enhanced representation of the SoG

This chapter details numerical developments I have carried out in the scope of this PhD, with the technical support of Jérôme Chanut, Florence Sevault, and Jonathan Beuvier. More specifically, it focuses on implementing a new Mediterranean configuration of the NEMO ocean model, based on that used at CNRM: NEMOMED12 (Beuvier et al, 2012; Hamon et al, 2016; Waldman et al, 2018). The main idea is to develop a configuration that simulates the Mediterranean Sea at climatic scales with an on-demand inclusion of tidal and fine-scale dynamics at the SoG. The underlying scientific motivation is to use this configuration to investigate the influence of improved exchanges at the SoG on the Mediterranean Sea climate, that is, its circulation, hydrographic properties, exchanges with the atmosphere, and their variations. From a more technical perspective, this numerical tool also aims at assessing the relative importance of the modeling choices made to represent the SoG.

2.1 The NEMOMED12 regional configuration

2.1.1 The basic brick: NEMO ocean model

The Nucleus for European Modelling of the Ocean, or NEMO model, is a state-of-the-art, freely available (http://www.nemo-ocean.eu, last access: November 6th, 2022) numerical software which allows representing and studying ocean physics. The version used in this PhD is NEMO3.6 (Madec, 2016), referred to as NEMO in the following. The NEMO ocean model comprises three prime components: NEMO-OPA for the ocean dynamics and thermodynamics, NEMO-LIM for the sea-ice dynamics and thermodynamics, and NEMO-TOP for the biogeochemistry. In the following, we focus on the OPA component, as the LIM and TOP components will not be used in the numerical experiments carried on.

The NEMO model relies on a mathematical description of ocean dynamics and thermodynamics. It is based on a set of primitive equations, coupling the Navier-Stokes equations and the seawater equation of state, ifself relying on the equations for temperature and salinity. Although very accurate, this system of equations is complex to handle, so the NEMO model makes use of several simplifying hypotheses on ocean physics:

- Spherical earth and thin shell approximations: The earth is considered a perfect sphere. Thus, gravity is parallel to the Earth radius. In addition, the ocean depth is considered negligible with respect to the earth radius.

- The Boussinesq hypothesis: Density variations are assumed to have no effect on the simulated flows except their contribution to the buoyancy force. This hypothesis builds on the hypothesis that relative density variations are weak, hence the velocity divergence is neglected.

- Hydrostatic assumption: The gravity force is supposed to balance the vertical pressure gradient; that is, the fluid is not undergoing significant vertical acceleration. Under this assumption, the pressure is simply expressed as a function of the gravitational acceleration, depth, and fluid density.

- Turbulence closure: The turbulent fluxes resulting from small-scale fluctuations are expressed in terms of the large-scale (resolved) flow.

The simplified equations built from these hypotheses represent the continuous evolution of the ocean temperature, salinity, density, pressure, currents, turbulent kinetic energy, and dynamic sea surface. However, there is no known analytical solution to this system yet. Instead, an approximate solution can be obtained through finite difference methods, which allow approximating temporal and spatial derivatives through a discrete representation of time and space. In the NEMO model, the spatial discretization is performed on the Arakawa C-grid, a cubic-shaped grid where scalar variables are defined at the center, fluxes on the faces, and their vorticity on the corners. Regarding temporal discretization, NEMO makes use of a thee-level time stepping. Non-diffusive terms are represented using a leapfrog scheme (Mesinger and Arakawa, 1976) and horizontal diffusive terms with a forward time difference scheme. Vertical diffusive terms can also be represented with a forward time difference scheme, but the latter must be combined with a time-splitting technique (see the following sections). Otherwise, a backward (implicit) time difference scheme is used.

2.1.2 The NEMOMED12 domain

NEMOMED12 is a Mediterranean configuration of the NEMO ocean model (see Figure 2.1). It has been mainly developed by CNRM (https://www.umr-cnrm.fr/) in collaboration with Mercator-Ocean (https://www.mercator-ocean.eu/), LOCEAN (https://www.locean.ipsl.fr/), LMD (https://ecoledesponts.fr/en/laboratories-research-dynamic-meteorology), and ENSTA (https://www.ensta-paris.fr/fr/les-laboratoires-d-ensta-paris) laboratories in the framework of the SiMED research program (https://publicwiki.met
The version of NEMOMED12 used in this PhD is the fruit of successive developments of NEMO Mediterranean configurations: OPAMED16 (Béranger et al, 2005), OPAMED8 (Somot et al, 2006), and NEMOMED8 (Sevault et al, 2009; Beuvier et al, 2010b; Sevault et al, 2014). The NEMOMED12 configuration is mainly used to investigate the Mediterranean Sea past variability and tendencies (Waldman et al, 2017b,a; Harzallah et al, 2018; Darmaraki et al, 2019; Dunić et al, 2019), its future evolution, and ocean-atmosphere interactions in coupled simulations (Voldoire et al, 2017; Darmaraki et al, 2019). NEMOMED12 was also used to produce the MEDRYS Mediterranean reanalysis (Hamon et al, 2016).

The NEMOMED12 domain extends over the Mediterranean Sea and a small part of the Atlantic Ocean, just west of the SoG. The horizontal grid is extracted from the tri-polar global ORCA12 grid. Its resolution varies from 7.5km at the south of the domain to 6km at the north (equivalent to 1/14° and 1/18°, respectively). This resolution is close to the first Rossby radius of deformation over the Mediterranean (Kurkin et al, 2020). Thus, the model is eddy-permitting but not fully eddy-resolving. The Strait of Gibraltar is approximately 10-points long and 3-points wide at its narrowest section. The vertical grid of NEMOMED12 comprises 75 z-levels, with partial steps. In simpler terms, it consists of fixed depth levels, which vary to some extent at the seafloor to provide a more realistic representation of the seafloor. The position and thickness of the vertical levels are determined

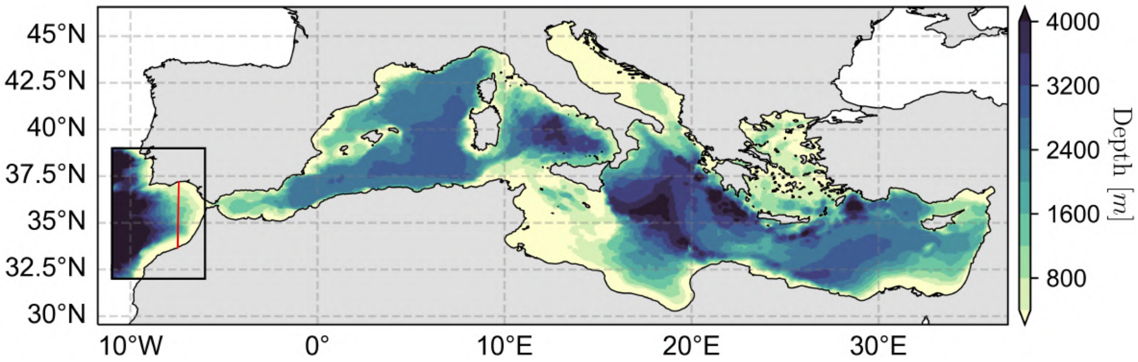

Figure 2.1: NEMOMED12 bathymetry. The black rectangle displays the location of the Atlantic buffer zone, and the red line delimits the area where the relaxation coefficient starts decreasing toward zero

from a reference bathymetry dataset based on logarithmic and hyperbolic tangent functions, respectively. Specifically, the NEMOMED12 reference bathymetry is the median of the MERCATOR-LEGOS 10th bathymetry (1/200°, ML10 hereinafter), with a hand-made check at the entrance of the SoG and the Aegean Sea. The ML10 dataset results itself from the merging of the MEDIMAP bathymetry (Group, 2005) and the Ifremer bathymetry of the Gulf of Lions (Berné et al, 2004). In the end, NEMOMED12 vertical cell thicknesses range from one meter at the surface to 130 meters at the bottom of the Mediterranean. The maximal depth is reached at the south of the Greek peninsula of Peloponnese and west of the Greek island of Rhodes, where the seafloor locally exceeds 4400m depth. At the SoG, a minimum depth of 270m (30 vertical levels) is reached near the Camarinal Sill. NEMOMED12 uses a time step of 720 seconds (i.e. 12 minutes).

2.1.3 Horizontal physics

The NEMO ocean model provides several options to simulate horizontal physics. We detail here the numerical choices made in the NEMOMED12 configuration. For the advective scheme, NEMOMED12 uses the vector invariant form of the momentum equations. In addition, the vorticity term is discretized with an Energy and ENstrophy conserving (EEN hereinafter) scheme, conserving both the potential enstrophy (vorticity variance) of horizontally non-divergent flow and the horizontal kinetic energy. In practice, the EEN scheme allows reducing the noise in the vertical velocity field (Le Sommer et al, 2009). In addition, when combined with a partial-step representation of the seafloor, it improves the simulated interaction between currents and topography (Barnier et al, 2006; Penduff et al, 2007). Regarding diffusion terms, NEMOMED12 uses a Laplacian operator for the tracers, which is oriented in the isoneutral direction, as suggested by observations (McDougall, 1987), and a bilaplacian operator for the momentum, oriented in the horizontal direction. The associated diffusion coefficients are constant, equal to $60\text{m}^2.\text{s}^{-1}$ for the tracers and $-1.25\ 10^{10}\text{m}^4.\text{s}^{-1}$ for the momentum.

At the solid boundaries, the normal velocity component is naturally zero. However, a choice must be made for the tangential velocity in order to set the vorticity

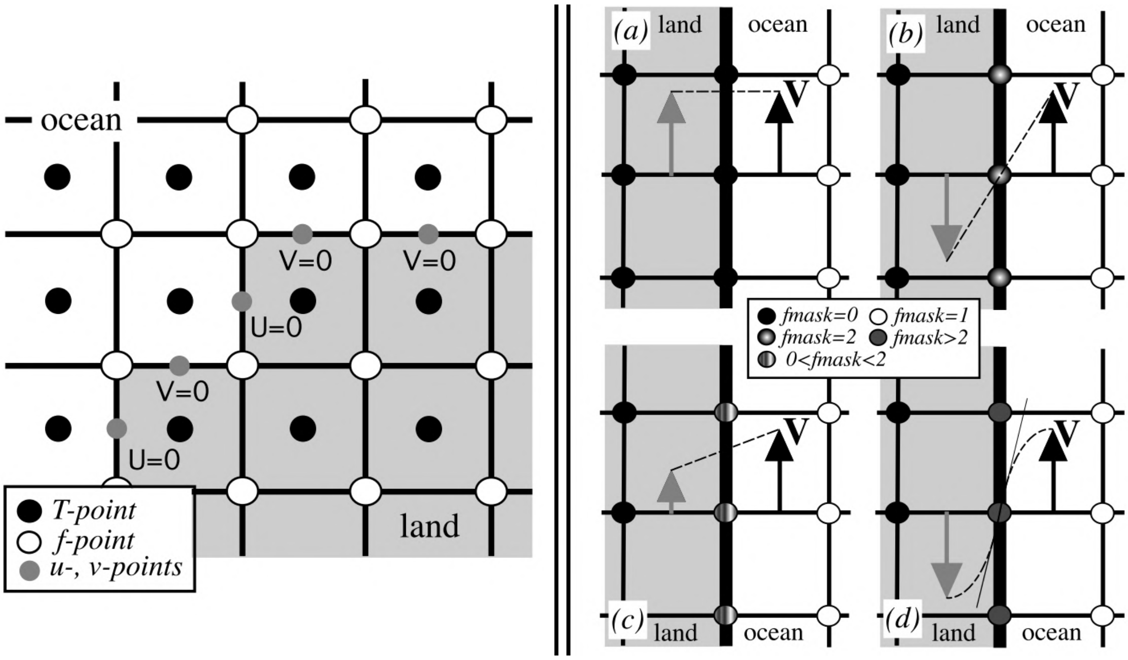

Figure 2.2: Lateral boundary conditions. The left panel shows that the velocity normal to the boundary is always zero. The right panel illustrates the evolution of tangential velocity with respect to the lateral boundary condition applied: (a) free-slip, (b) no-slip, (c) “partial” split, and (d) “strong” no-slip. “fmask” refers to the multiplicative factor applied on the vorticity at the coastline in order to set the boundary condition. Implied “ghost” velocity inside land area is displayed in grey. Figure extracted from Madec (2016)

induced by lateral boundaries. Physically, this choice is related to lateral friction, which can be considered negligible, or increasingly intense (see Figure 2.2). In the former case, the tangential velocity remains unchanged at the boundary (free-slip). Otherwise, the friction can be considered moderate, so the velocity at the boundary decreases to a non-zero value (“partial” free-slip); relatively intense, such that the velocity decreases to zero (no-slip); or very strong, so the velocity decreases more intensely close to the boundary (strong no-slip). In practice, this boundary condition is set by applying a multiplicative factor to the vorticity at the coastline, which is initially computed considering a zero velocity at the coast. This factor is 0 for a free-slip condition, between 0 and 2 for a “partial” free-slip, 2 for a no-slip, and higher than 2 for a strong no-slip. In NEMOMED12, this coefficient is set to 1.2, corresponding to a “partial” free-slip condition. This coefficient is used as a tuning parameter and set to simulate realistic transports through the SoG, which are substantially affected by lateral boundary conditions.

A final point of consideration for horizontal dynamics is the representation of the horizontal variations of surface pressure. In NEMO3.6, the surface pressure is defined from the sea surface elevation η, whose representation is variable among ocean models. Indeed, representing η through a dedicated prognostic equation introduces external gravity waves (EGWs hereinafter) as a class of solutions. Although these solutions are physically consistent, EGWs propagate fast, asking for fine temporal resolution, which is computationally expensive. Since EGWs are barotropic under the hydrostatic assumption, an alternative is to solve the equation of η and the associated barotropic dynamics with a small time-step, separately from the three-dimensional dynamics (Shchepetkin and McWilliams, 2005). This solution is referred to as a "split-explicit free surface". A second alternative is to keep a time step adapted to baroclinic dynamics and solve η implicitly, using an elliptic solver (Roullet and Madec, 2000). In that case, the high-frequency surface dynamics are filtered out. This solution is referred to as a "filtered free surface". Since there was no need to solve EGWs for the processes investigated with NEMOMED12 so far, it uses a filtered free surface. However, this choice makes the explicit representation of tides impossible. Thus, it will be reconsidered in the following sections.

2.1.4 Vertical physics

Under the hydrostatic assumption, the vertical velocity is a diagnostic variable, simply deduced from the convergence of horizontal currents through the continuity equation. However, the vertical advection simulated by NEMOMED12 is not sufficient to depict an accurate picture of ocean vertical physics. In fact, many processes are unresolved by NEMOMED12 as they manifest at fine scales, down to the Kolmogorov microscale ($\mathcal{O}(1mm)$). These processes mainly flux ocean properties down their gradient, driving substantial vertical transfers of tracers and momentum in the ocean (Philander and Pacanowski, 1980; Bryan, 1987). Thus, the unresolved fluxes (also called turbulent fluxes) are indirectly represented (i.e., parameterized) through diffusive (Kz_t) and viscous (Kz_m) vertical coefficients, determined by prognostic equations. The set of prognostic equations used to define Kz_t and Kz_m is commonly referred to as turbulence closure scheme, as it allows to complete (i.e. "close") the set of primitive equations resolved by the model.

NEMOMED12 uses the turbulent kinetic energy (TKE) closure scheme (Gaspar et al, 1990), with the same constant parameters as in Gaspar et al (1990). In this framework, based on a TKE budget, Kz_m is a function of the TKE, a mixing length, and a mixing efficiency coefficient. The mixing length can be interpreted as the characteristic size of the unresolved eddy structures and the mixing efficiency as a measure of turbulent mixing efficiency. Kz_t is proportional to the product of Kz_m and the Prandtl number, quantifying the ratio between momentum and tracer turbulent diffusivity. In this way, tracer and momentum diffusion increase with the TKE, which mainly relies on the balance between the destabilizing force of the vertical shear of horizontal currents and the stabilizing force of vertical stratification. It is important to note that under this framework, very low values of Kz_m and Kz_t can be computed under weak turbulence, even lower than their molecular values (minimal values encountered in the ocean) of $10^{-6}\mathrm{m}^2.\mathrm{s}^{-1}$ and $10^{-7}\mathrm{m}^2.\mathrm{s}^{-1}$, respectively. Thus, minimal values of Kz_m and Kz_t are prescribed to ensure a realistic background mixing. In addition, since NEMOMED12 does not resolve high-order internal waves, these thresholds are set to $10^{-4}\mathrm{m}^2.s^{-1}$ and $10^{-5}\mathrm{m}^2.s^{-1}$, respectively, to account for the turbulence generated by these unresolved processes. Finally, it is important to highlight that Kz_m and Kz_t represent a momentum and tracer gradient diffusion rate, respectively. Thus, they should always be interpreted in conjunction with the surrounding vertical stratification and vertical shear.

Besides vertical advection and turbulent diffusion, another process to account for is that of convection. Although it is an essential physical mechanism for the Mediterranean thermohaline circulation, NEMOMED12 does not explicitly represent convection due to the hydrostatic assumption it relies on. In compensation, convection is parameterized through an Enhanced Vertical Diffusion (EVD) scheme. In practice, the Kz_m and Kz_t coefficients are set to a very high value ($10\text{m}^2.\text{s}^{-1}$) upon occurrence of negative vertical stratification.

Finally, at the seafloor, NEMOMED12 uses a quadratic bottom drag. This parameterization influences momentum trends through an additional term, representing a downward momentum flux outside the logarithmic turbulent boundary layer. This flux is computed as the product of a non-dimentional drag coefficient (10^{-3} in NEMOMED12) with the square root of the TKE. In addition, a horizontally-variable turbulent kinetic energy background is imposed to represent the contribution of unresolved tidal currents to the TKE. This background coefficient corresponds to mean tidal energy, recovered from Lyard et al (2006). The tidal energy is maximal at the SoG ($1\text{m}^2.\text{s}^{-2}$) and significant in the Sicily Channel, the Gulf of Gabès, and the Adriatic Sea.

2.1.5 External forcing at the boundaries

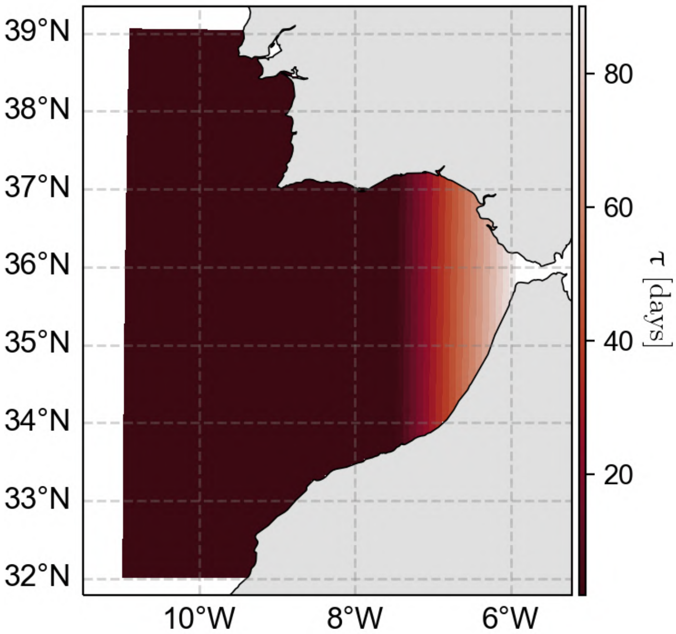

Figure 2.3: Characteristic relaxation time-scale of temperature and salinity in the NEMOMED12 Atlantic buffer. The relaxation time-scale varies from 2 days at the western edge of the buffer zone to 90 days at its eastern edge.

As previously mentioned, the NEMOMED12 domain extends from the eastern Mediterranean to the entrance of the Atlantic Ocean. At the western Atlantic boundary, the model is forced through a buffer zone (black box in Figure 2.1) covering most of the Atlantic domain, from 11°W to 6°W, just west of the SoG. Over this area, temperature, salinity, and sea surface elevation are relaxed toward the monthly global ocean reanalysis ORAS4 (Balmaseda et al, 2013), which sea surface elevation is corrected over the Atlantic buffer zone following Adloff et al (2018). The relaxation scheme used is three-dimensional and Newtonian, applied over the whole water column. For tracers, the characteristic time-scale is constant between 11°W to 7.5°W, set to 2 days, and increases linearly up to 90 days from 7.5°W to 6°W (see Figure 2.3). The characteristic time-scale associated with the sea surface elevation is ~ 20 minutes between 11-7.5°W and zero over the rest of the domain.

Besides the Atlantic boundary, the NEMOMED12 configuration is forced at the mouth of the main rivers listed in the global River Discharge dataset (RivDis, University of Wisconsin-Madison (2005)). Under the constant volume formulation, river discharge is simulated as a source for the sea level equation, plus a salinity sink, added over a variable fraction of the surface water column. More specifically, the vertical extent of the runoff is a fraction of a given maximal runoff depth. This fraction depends on the intensity of the runoff with respect to the maximal runoff allowed by the model. In NEMOMED12, the maximal runoff depth is set to 200m and the maximal runoff is $0.06\text{kg.m}^{-2}.\text{s}^{-1}$. In ocean-only mode (forced mode hereinafter), the forcing dataset is a monthly dataset from Ludwig et al (2009). The runoff from rivers not listed in the RivDis dataset is distributed over coastal grid points. In coupled mode, the runoff is provided by a land surface or river model (see next sections). Note that the Black Sea is represented as a river in NEMOMED12 due to its low salinity. Thus, a substantial freshwater runoff is imposed at the Dardanelles strait. It follows a monthly climatology deduced from the surface water budget of the Black Sea, except over 1993-1997 when it is set to monthly values deduced from Stanev and Peneva (2001).

In forced mode, the NEMOMED12 surface forcing is prescribed through a flux formulation. More specifically, the surface momentum, water, and heat fluxes are provided by a dynamical downscaling of the ERA-Interim reanalysis (Berrisford et al, 2009) using the regional climate model ALADIN-Climate (Colin et al, 2010; Herrmann et al, 2011). The resulting forcing, commonly referred to as ALDERA (Hamon et al, 2016; Waldman et al, 2017b,a; Dunić et al, 2019), has a spatial resolution of 12km and a three-hourly temporal resolution. In order to maintain consistency between the simulated ocean and the atmospheric forcing dataset, the sea surface temperature of NEMOMED12 is relaxed towards the ALDERA dataset (data from the ERA-Interim reanalysis in this case). This relaxation is performed through a Newtonian scheme with a constant relaxation coefficient of $-40\text{W.m}^{-2}.K^{-1}$. In practice, this corresponds to a characteristic relaxation time scale of 1.2 days for a one-meter-deep surface layer. The solar penetration over the upper ocean is prescribed using a monthly climatology of chlorophyll-a concentration (Ocean Colour Climate Change Initiative dataset, European Space Agency, available online at http://www.esa-oceancolour-cci.org/). In coupled mode, the ocean-atmosphere fluxes are directly computed by the coupling scheme.

2.1.6 Limitations of NEMOMED12

Although NEMOMED12 is a useful numerical tool for studying the Mediterranean Sea climate and its variability, it is also limited to some extent. One of these limitations is its rough representation of the SoG. Indeed, the few points attributed to the SoG (three at its narrowest section) do not allow for an accurate representation of its geometry and the fine-scale processes at play within it. Another limitation is the omission of tidal forcing and, thus, tidal mixing and recirculation at the SoG. The calibration of lateral friction and the tidal contribution to bottom friction allows us to overcome some of these limitations. However, it is unlikely to address them all. A final limitation discussed here is that of the Atlantic buffer zone. More specifically, the 3D relaxation performed over the area allows non-physical processes to occur in the vicinity of the SoG and provides only a coarse representation of the Gulf of Cadiz circulation (that of the forcing model).

Other than improving the model realism, a more realistic representation of the SoG in the NEMOMED12 configuration would permit the investigation of physical mechanisms currently out of reach. In the scope of this PhD, it would allow assessing the relative influence of tidal and fine-scale processes on the exchange flow through the strait and their impact on the Mediterranean Sea. In coupled mode, such configuration can also be used to assess the long-term influence of the SoG on the Mediterranean climate and its variability. Finally, such coupled configuration could be used to assess the role of the SoG in climate change scenario simulations.

Thus, in the following sections, we will address the aforementioned limitations of NEMOMED12 by developing a new NEMO configuration, referred to as NEMOMEDGIB. We aim for the NEMOMEDGIB configuration to include an explicit representation of tidal forcing and a computationally-affordable representation of the fine-scale dynamics of the SoG through an adaptive grid refinement. In addition, both of these functionalities must provide a straightforward on/off switch. Note that for the sake of conciseness, the effects of intermediate NEMOMED12 modifications, making it compatible with tidal forcing and with the adaptive grid refinement, will be shortly summarized in the following section. However, a detailed analysis of these modifications is available in Appendix A.

2.2 Explicit tidal forcing

This section details the modifications carried out on NEMOMED12 to simulate explicit tidal currents. These modifications can be divided into three steps addressing the main obstacles to the explicit representation of tides in NEMOMED12. First, we enable the model to resolve tidal waves. To do so, the filtered free surface is replaced by a split-explicit linear free surface, mentioned in the previous sections. Then, we modify the lateral boundary condition to allow for the prescription of the Atlantic tidal wave. To do so, the Atlantic buffer zone is replaced by open boundary conditions. Finally, we adapt the physics of the model to tidal dynamics and disable tidal parameterizations. Once these three steps are completed, we add the tidal forcing to the model.

2.2.1 Split-Explicit linear free surface

As previously mentioned, the time-splitting formulation of linear free-surface consists of specific handling of the barotropic dynamics, which are resolved separately from the baroclinic dynamics with a finer temporal resolution. In practice, this implies using different parts of the NEMO source code, which must be recompiled to include the procedures associated with time splitting. The compiled code is selected through C Pre-Processor keys (CPP keys hereinafter). In particular, the split-explicit free surface formulation is activated at compilation by the **key_dynspg_ts** key, which replaces **key_dynspg_flt**. Once the new NEMO executable is created, the time-splitting parameters are set in the namelist file (namsplit section, see Table 2.1), which inputs variables in the NEMO code (character, logical, real number, and integer number).

The most important parameter to set is the barotropic time step, *nn_baro*. To do so, we perform several experiments (including tidal forcing) in which the model diagnoses the needed number of barotropic iterations for one baroclinic iteration to ensure a maximal Courant number (measuring the numerical stability of the model) of 0.8 (*ln_bt_nn_auto*="True" and *rn_bt_cmax*=0.8). We select the average number of iterations returned by the model, which is 40. Since the NEMOMED12 baroclinic time step is 720 seconds, this yields a barotropic time step of 18. We choose a forward barotropic time-stepping for the barotropic dynamics, which provides us with sufficient numerical stability and a lesser computational expense with respect to a backward scheme. As suggested in the NEMO user book (Madec, 2016), we apply a time filtering to the barotropic variables in order to ensure viable numerical stability (*ln_bt_av*="True"). We choose a time window of one baroclinic time-step, which provides a good compromise between numerical stability and computational cost (*ln_bt_flt*=1).

Finally, it is important to note that the time-splitting formulation asks to compute most momentum trends before the tracer trends. This order of computation makes the time-splitting formulation incompatible with the semi-implicit time discretization scheme of the hydrostatic pressure gradient. Instead, we must use the only available alternative: the leapfrog scheme (*ln_dynhpg_imp* set to "False"), which provides less numerical stability. However, I did not encounter any major stability issues upon running the model. This is, thus, a reasonable constraint.

2.2.2 Open boundary conditions

A necessary step before adding open boundary conditions is to remove the Atlantic buffer zone, that is, the Newtonian relaxation applied over the Atlantic domain. This is done through the namelist booleans *ln_tsd_tradmp*, *ln_tradmp*, and *ln_ssh_sshdmp*. The *ln_tsd_tradmp* boolean informs the code of the relaxation in order to adequately handle the reference data at the model initialization. The two other booleans activate or disable tracers and sea surface elevation relaxations. All these booleans are set to the logical "False".

As for time-splitting, the activation of the open boundary functionality requires

Namelist parameter	Value	Description
nn_baro	40	Number of barotropic iterations performed for one baroclinic iteration.
ln_bt_nn_auto	False	Allows to set the barotropic time step automatically in order to ensure that the Courant number associated to internal barotropic waves remains lower than the value defined
rn_bt_cmax	0.8	Maximal Courent number associated to internal barotropic waves
ln_bt_fw	True	Defines the split-explicit time stepping scheme used. If set to “True”, the scheme is a forward scheme.
ln_bt_av	True	Defines whether or not a time filtering should be applied to the barotropic variables provided to the baroclinic solver.
ln_bt_flt	1	Set the size (in multiples of baroclinic time step) of the temporal window used for the filtering baroclinic values

Table 2.1: namsplit section of the NEMO namelist.

recompiling the NEMO source code with a specific CPP key: **key_bdy**. The open boundaries are then set through different namelist sections. The first one (nambdy, see Table 2.2) sets the number of boundaries and the lateral conditions. We define three boundaries (*nb_bdy*=3), matching the north, west, and south edges of the Atlantic domain. The width of the relaxation zone is set to 10 points, a typical value suggested in the NEMO user book (Madec, 2016). Note that the validation of the simulated tides, addressed in the following chapter, gives further confidence in this choice. Regarding the open boundaries schemes, we choose a Flather radiation scheme for the barotropic variables (*nb_dyn2d*=“Flather”) and the Flow Relaxation Scheme (FRS) for the baroclinic variables (*nb_dyn3d* = *cn_tra*=“Flather”). The Flather scheme (Flather, 1994) is the “True” open boundary condition, allowing gravity waves to both exit and enter the simulated domain. In practice, it mainly consists of a radiation condition on the normal depth-mean transport across the open boundary. The FRS scheme (Davies, 1976; ENGEDAHL, 1995) is a simple Newtonian relaxation scheme. The characteristic time scale used is a fraction of the model time-step defined from a hyperbolic tangent function of the distance to the boundary. The open boundary volume conservation option (*ln_vol*) is disabled as it handles only low-frequency volume variations and is, thus, incompatible with tidal forcing. However, the Flather scheme maintains sufficient volume conservation for the model to remain realistic.

For each open boundary, its shape and position are set through a dedicated namelist section (*nambdy_index*). The boundaries are defined as straight-line segments (see Table 2.3). It is important to specify that the boundary position (*nbdyind*) is that of the first velocity cell inside the computational domain (See Figure 2.4).

Finally, the datasets used at the boundaries are specified in a last set of namelist sections (*nambdy_dta*, see Table 2.4). The external data is extracted from the same files used for the NEMOMED12 Atlantic buffer zone. More specifically, it consists of the ORAS4 ocean reanalysis temperature, salinity, and velocity fields. As for NEMOMED12, the Sea surface elevation is corrected following Adloff et al (2018). The open boundary dataset was created with a Python script, following the indications provided in the NEMO documentation (Madec, 2016).

Namelist parameter	Value	Description
nn_bdy	3	Number of open boundaries
nn_rimwidth	10	Width of the relaxation zone
cn_dyn2d	"flather"	Boundary scheme to use for the barotropic dynamics
nn_dyn2d_dta	1	Data to be considered at the boundary. 0: boundaries set to the initial state; 1: barotropic velocities only 2: tidal harmonic constants only; 3: both velocity and tidal data
cn_dyn3d	"FRS"	Boundary scheme to use for the baroclinic dynamics
nn_dyn3d_dta	1	Data to be considered at the boundary. 0: boundaries set to the initial state; 1: baroclinic velocities only
cn_tra	"FRS"	Boundary scheme to use for the tracers
cn_tra_dta	1	Same as nn_dyn3d_dta for tracers
ln_vol	False	Forces total volume in the regional model to be constant

Table 2.2: nambdy section of the NEMO namelist, which sets the number of open boundaries and the forcing schemes used. For conciseness, parameters specific to the sea-ice NEMO model (unused in NEMOMED12 configuration) or alternative methods to define the boundaries position are not included.

Namelist parameter	Section	Value	Description
ctypebdy	North	"N"	Orientation of the boundary
	West	"W"	
	South	"S"	
nbdyind	North	128	Index of velocity cell at which the boundary is defined
	West	2	
	South	26	
nbdybeg	North	2	Index of the boundary start
	West	26	
	South	2	
nbdyend	North	21	Index of the boundary end
	West	129	
	South	22	

Table 2.3: Values used in the three nambdy_index sections of the NEMO namelist. These values set the position and orientation of the open boundaries.

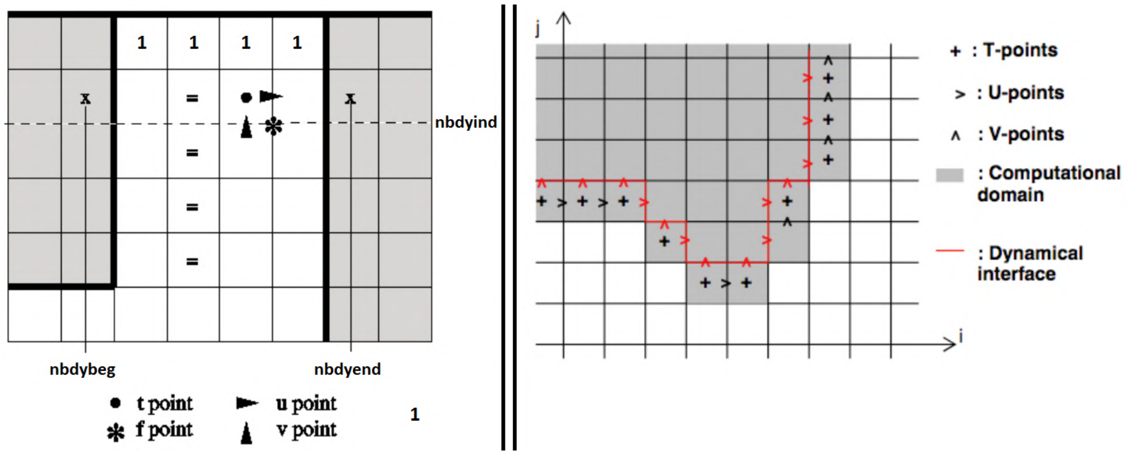

Figure 2.4: Open boundary geometry. The left panel shows the location of the North open boundary points, with the first row of model cells (considered as land points) marked with the digit 1. The right panel shows the boundary geometry at the edges of the domain. Figure extracted from Madec (2016)

Namelist parameters	Description
bn_ssh	Specify the needed information to access sea surface elevation data (file, data label, frequency) and if the data needs to be interpolated over time.
bn_u3d & bn_v3d	Same as bn_ssh for baroclinic zonal and meridional velocities, respectively
bn_tem & nb_sal	Same as bn_ssh for temperature and salinity, respectively
cn_dir	Location of the directory containing the external data
ln_full_vel	Specify if the baroclinic velocity dataset contains “full” velocities (i.e., the barotropic component was not removed), in this way, the barotropic velocities can be derived directly from the baroclinic ones

Table 2.4: nambdy_dta namelist section. It specifies the datasets to be prescribed at the open boundaries. For each open boundary defined, one nambdy_dta namelist section must be filled.

In practice, note that the activation of open boundary conditions must be done jointly with the activation of time-splitting. Indeed, the handling of barotropic waves at the boundaries requires a fine temporal resolution. In addition, the time splitting is incompatible with the sea surface relaxation scheme used in the Atlantic buffer zone, which has been implemented only under the specific framework used by the NEMOMED12 configuration. Concretely, this means that the effects of time-splitting and open boundaries on the NEMOMED12 solution can only be interpreted as a whole. We detail these effects in Appendix A. In a nutshell, the effects are significant and mainly attributable to the open boundary conditions. Indeed, with respect to the buffer zone, the greater freedom of the model in the Atlantic domain allows for a more realistic circulation to take place, modifying the source of the jet of Atlantic water entering the SoG. Ultimately, this results in an intense cooling (up to -1° C near 50m depth) and freshening (up to -0.2 ‰near 80m depth) of the inflowing Atlantic waters at the SoG.

2.2.3 Vertical physics adaptations

As previously discussed, the NEMOMED12 configuration includes several parameterizations to account for the effects of unresolved tidal currents. We will now disable these parameterizations, so the effects of tides are not accounted for twice. In addition, we will adapt aspects of the resolved physics to the tidal dynamics.

The first point to address is the high background vertical turbulent diffusion (Kz_t) and viscosity (Kz_m) coefficients used in NEMOMED12. These background values mainly represent the mixing induced by unresolved physics. Thus, they should be reduced upon inclusion of tidal waves. However, it is important to maintain minimum level of mixing to account for the remaining unresolved processes. To do so, we decrease the background values of Kz_t and Kz_m below their molecular values, but we keep a background TKE of 10^{-6}m^2.s^{-2}. These modification are performed by setting the namelist parameters *rn_avm0* to 1.4 10^{-7}m^2.s^{-2} for the viscosity (de Lavergne et al, 2016), and *rn_avt0* to 10^{-10}m^2.s^{-2} for diffusivity. Thus, the minimal values of Kz_t and Kz_m are set by the model consistently with a background level of turbulent kinetic energy. Note that we also change the formulation of the characteristic length scales used in the TKE closure scheme (*nn_mxl* set to 3 instead of 2). Under this formulation, the dissipative and mixing length scales have distinct values, as in the reference study of Gaspar et al (1990). Overall, these modifications impact the average vertical stratification of the Mediterranean Sea, which is intensified near the surface due to the decrease of background mixing coefficients (See Appendix A for further details).

Regarding bottom friction, we start by suppressing the background TKE source associated with tidal currents. Although this background energy is usually defined by the scalar namelist parameter *rn_bfri2*, in NEMOMED12, the source code was modified to use a two-dimensional field. Thus, the bottom TKE background is disabled by setting the namelist boolean *ln_tide_2D* to “False”. Then, we set the bottom friction formulation to the log-layer formulation (*ln_loglayer*=“True”), better suited to handle intense currents near the seafloor. The log-layer formulation is a modified version of the non-linear formulation, in which the drag coefficient is no longer constant but enhanced in the vicinity of the seafloor. The computed adimentional drag coefficient is, however, bounded by minimal and maximal values, specified through the namelist parameters *rn_bfri2* and *rn_bfri2_max*. we set these lower and upper bounds to the typical values of 2.5 10^{-3} and 10^{-1}, respectively (Madec, 2016). Finally, to increase the model stability, we use the implicit formulation of the bottom friction, activated through the namelist boolean *ln_bfrimp*. With respect to the open boundaries and the background mixing coefficient, modification of bottom boundary friction has a much weaker impact on the Mediterranean Sea. The most notable modification is the thickening of the Mediterranean outflow at the SoG, which results in a moderate saltening of the interface between Atlantic and Mediterranean waters masses (See Appendix A for further details).

Darwin Symbol	Complete name	Period (hours)
N_2	Larger lunar elliptic semidiurnal constituent	12.65834751
M_2	Principal lunar semidiurnal constituent	12.4206012
S_2	Principal solar semidiurnal constituent	12
K_2	Lunisolar semidiurnal constituent	11.96723606
Q_1	Larger lunar elliptic diurnal constituent	26.868350
O_1	Lunar diurnal constituent	25.81933871
P_1	Solar diurnal constituent	24.06588766
K_1	Lunisolar diurnal constituent	23.93447213
M_4	Shallow water overtides of principal lunar constituent	6.210300601
M_f	Lunisolar fortnightly constituent	327.8599387
M_m	Lunar monthly constituent	661.3111655

Table 2.5: Tidal harmonics included in the simulations

2.2.4 Tidal forcing

Because of the limited geographical coverage of the NEMOMED12 domain, tides must be prescribed in two different ways. Over the Mediterranean basin, the tides are directly induced by the gravitational forces of the moon and the sun, which consists of a potential in the momentum equations. Over the Atlantic ocean, however, the NEMOMED12 domain is not large enough for tidal waves to develop properly. Thus, the Atlantic tide must be forced as an open boundary condition.

To activate the tidal potential, the NEMO source code must be compiled with an additional CPP key: **key_tide**. The tidal harmonics to consider are specified through a list of strings *clname* in the nam_tide namelist section. Following the operational Iberian Biscay Irish (IBI) Ocean Analysis and Forecasting system (https://doi.org/10.48670/moi-00027), we choose to include the 11 main tidal harmonics listed in Table 2.5. The tidal forcing is then activated by setting the namelist boolean *ln_tide_pot* to “True”.

On the other hand, the Atlantic tide is forced through open boundary conditions on velocities. The prescribed velocities are deduced from reference tidal currents and surface elevations. More specifically, the reference dataset consists of tidal harmonic coefficients obtained from the decomposition of the tidal waves on a cosine and sine basis. Considering a tidal harmonic H as a pure sinusoid, this decomposition follows:

$$\begin{aligned} \eta_H(t) &= A_H\ \cos(\omega_H t + \theta_H) \\ &= A_H\ \cos(\theta_H)\cos(\omega_H t) - A_H\ \sin(\theta_H)\sin(\omega_H t) \\ &= z1\ \cos(\omega_H t) + z2\ \sin(\omega_H t) \end{aligned} \tag{2.1}$$

With A_H the amplitude, ω_H the frequency, and θ_H the phase. $z1$ and $z2$ are the sine and cosine coefficients of the tidal wave.

We create the tidal forcing dataset from the global tidal atlas FES2014 (produced by Noveltis, Legos, and CLS and distributed by Aviso+, with support from

CNES: https://www.aviso.altimetry.fr/). First, the cosine and sine coefficients of the FES2014 sea surface elevation are interpolated on the NEMOMED12 grid following recommendations of Xu (2018). Regarding tidal velocities, even once interpolated onto the NEMOMED12 grid and corrected from the FES2014 grid curvature, they will not necessarily be consistent with the NEMOMED12 bathymetry. Thus, to produce consistent tidal velocities, we perform a yearly barotropic experiment, forced only by FES2014 tidal elevations. We then compute the sine and cosine coefficients of the simulated barotropic tidal currents from instantaneous (non-averaged) hourly outputs using the “Utide” Python package (version 0.2.5). Technical details on the baroclinic simulation setup are provided in Appendix B.

The resulting reference datasets are provided to the NEMO model through the (*nambdy_tide*) namelist section, which is considered by the model when the open boundary parameter *nn_dyn2d_dta* is set to 3. We choose to provide two-dimensional maps of tidal forcing to avoid any mistakes when creating open boundary datasets. We also set the *ln_bdytide_conj* boolean to “True”, which specifies the sign convention used on the tidal sine and cosine coefficients provided to the model.

Finally, in order to assess volume, heat and salt transport across the SoG at the tidal frequency, we implement a new diagnostic in the diawri.F90 module of NEMO. To do so, we diagnose separately the eastward, westward, northward, and southward components of the transport by applying a Heaviside function to velocities at the model time step. Details of modifications performed on the diawri.F90 are displayed in Figure 2.5.

2.3 AGRIF nesting around the SoG

The Adaptive grid refinement in Fortran (AGRIF) package (Debreu et al, 2008, 2012), is a Fortran90 package allowing for the inclusion of adaptive mesh refinement features in existing finite difference codes, such as the NEMO ocean model. Within the NEMO framework, the AGRIF package allows developing nested NEMO configurations, or simply put, coupling a NEMO configuration to one or several others simulating a fraction of the original (parent hereinafter) configuration domain at an equivalent or higher resolution. The AGRIF package is an appealing tool for ocean modeling as it provides a consistent framework for investigating the effect of fine-scale mechanisms on large-scale dynamics or thermodynamics (Biastoch et al, 2008; Chanut et al, 2008; Jouanno et al, 2012; Djath et al, 2014; Talandier et al, 2014; Waldman et al, 2017a).

In this PhD, the AGRIF package allows assessing the sensitivity of the exchanges through SoG to fine-scale dynamics and topography at the SoG as well as the resulting impacts on the Mediterranean region. According to Sannino et al (2014), a 500m resolution is sufficient to simulate the hydraulic properties of the exchange flow through the SoG. To be as close as possible to this resolution, we use a spatial refinement factor of 5, which is the highest possible for numerical stability reasons. In this way, the AGRIF domain reaches a resolution of 1/60° ($\sim$ 1.5km). In the AGRIF configuration, the SoG is 12 grid cells wide at its narrowest section.

```
SUBROUTINE dia_wri( kt )
                              ...
   REAL(wp), POINTER, DIMENSION(:,:)   :: z2d       ! 2D workspace
   REAL(wp), POINTER, DIMENSION(:,:,:) :: z3d, z3d_1, z3d_2, z3d_3       ! 3D workspace
                              ...
   CALL wrk_alloc( jpi , jpj       , z2d )
   CALL wrk_alloc( jpi , jpj, jpk , z3d , z3d_1, z3d_2, z3d_3 )
                              ...
   !------------------
   ! Zonal transports
   !------------------

   IF( iom_use("uoce_m") .OR. iom_use("uocet_m") .OR. iom_use("uoces_m") .OR. &
   &   iom_use("uoce_p") .OR. iom_use("uocet_p") .OR. iom_use("uoces_p") ) THEN
      z3d(:,:,:)   = 0._wp
      z3d_1(:,:,:)  = 0._wp
      z3d_2(:,:,:)  = 0._wp
      z3d_3(:,:,:)  = 0._wp
      DO jk = 1, jpkm1
         DO jj = 2, jpjm1
            DO ji = fs_2, fs_jpim1   ! vector opt.
               ! Westward velocities
               z3d(ji,jj,jk) =  MIN(un(ji,jj,jk),0.)
               ! Eastward velocities
               z3d_1(ji,jj,jk) =  MAX(un(ji,jj,jk),0.)
               ! Sum of T and S at the U cell
               z3d_2(ji,jj,jk) = 0.5 * ( tsn(ji,jj,jk,jp_tem) + tsn(ji+1,jj,jk,jp_tem) )
               z3d_3(ji,jj,jk) = 0.5 * ( tsn(ji,jj,jk,jp_sal) + tsn(ji+1,jj,jk,jp_sal) )
            END DO
         END DO
      END DO
   ENDIF

   ! Write the westward transport outputs
   IF( iom_use("uoce_m") ) CALL iom_put( "uoce_m", z3d(:,:,:) )
   IF( iom_use("uocet_m") ) CALL iom_put( "uocet_m", z3d(:,:,:) * z3d_2(:,:,:) )
   IF( iom_use("uoces_m") ) CALL iom_put( "uoces_m", z3d(:,:,:) * z3d_3(:,:,:) )
   ! Write the eastward transport outputs
   IF( iom_use("uoce_p") ) CALL iom_put( "uoce_p", z3d_1(:,:,:) )
   IF( iom_use("uocet_p") ) CALL iom_put( "uocet_p", z3d_1(:,:,:) * z3d_2(:,:,:) )
   IF( iom_use("uoces_p") ) CALL iom_put( "uoces_p", z3d_1(:,:,:) * z3d_3(:,:,:) )
                              ...
   CALL wrk_dealloc( jpi , jpj       , z2d )
   CALL wrk_dealloc( jpi , jpj, jpk , z3d, z3d_1, z3d_2, z3d_3 )
```

Figure 2.5: Modifications performed on diawri.F90 module to add SoG transport diagnostics at the tidal frequency. Added lines are highlighted in green, deleted lines in red, modified lines in yellow and modification in orange. The added code for meridional velocities is not displayed for the sake of conciseness as it is very similar.

Another point worth mentioning is that nested AGRIF configurations can be used in forced or coupled mode. In the former case, the high-resolution configuration does not provide feedback to the parent configuration, whereas in the latter, the parent solution is restored toward the AGRIF solution at a specific frequency. Since we want to investigate the effect of the SoG fine-scale mechanisms on the Mediterranean region, we use the coupled version of the AGRIF configuration. This is done by specifying the compilation key “#define TWO_WAY” in the agrif_opa_update.F90 module. Once this modification is done, the NEMO code must be compiled with the compilation key **key_agrif**. Note that we choose to update the baroclinic dynamics of the parent configuration at each time-step. The barotropic dynamics are necessarily updated at the parent configuration time step.

In the following, we detail the necessary steps to implement the AGRIF zoom at the SoG. We first discuss the creation of the AGRIF grid and bathymetry. Then, we introduce the external forcing needed by the AGRIF model and how we produced them.

2.3.1 AGRIF domain

The existence of a nested AGRIF configuration and its geographic extent is specified to the NEMO model through a dedicated file: AGRIF_FixedGrids.in. More precisely, each AGRIF configuration to consider is described in three lines. The first line consists of a single number: the number of the AGRIF configuration, starting at 1. The second line contains indices used to set the location of the AGRIF domain in the parent configuration grid. However, these indexes do not directly represent the position of the AGRIF computational domain. Indeed, the edges of the AGRIF domain are shifted northeast, once for the southwest edge and twice for the northeast edge (see Figure 2.6). Furthermore, at the edges of the domain, the first coarse cells are represented by only two fine "ghost cells" starting after or at the middle of the coarse cell, depending on the spatial refinement factor used (see Figure 2.6). Finally, the AGRIF computational domain includes a 2-coarse-points-wide sponge layer. Over this area, the high-resolution dynamics and tracers are relaxed toward the parent solution. Thus, the first AGRIF points free from any relaxation are two coarse points away from the beginning of the computational domain.

With that in mind, we set the western boundary of the AGRIF domain at the western exit of the Gulf of Cadiz ($\sim$ 8.55°W). This location provides a good compromise between the computational cost of the AGRIF configuration and the distance needed for fine-scale physics to fully develop before reaching the SoG. In this regard, we diagnose a rough estimate of the distance over which the spatial spin-up is completed based on Matte et al (2017, Equation 7). Specifically, the spatial spin-up distance is defined as a given number of coarse-resolution grid points depending on the resolution jump between the coarse and fine grids. Considering the spatial spin-up to start at the end of the sponge layer, we diagnose that it ends at $\sim$ 7.75°W, relatively far away from the SoG (see Figure 2.7). Regarding the eastern boundary, we choose to locate it in the center of the Alboran sea ($\sim$ 3°W), allowing for the spatial spin-up to be completed west of $\sim$ 3.78°W. In this way, the Atlantic jet develops at high resolution, and no relaxation area is located over the western Alboran gyre. We choose not to include the Eastern Alboran Gyre (EAG) in the AGRIF domain, as we aim to investigate the effects of the fine-scale dynamics at the SoG, which could be modulated by the EAG. However, to assess the EAG influence on the exchanges through the SoG and the Mediterranean circulation, we develop an alternative version of the AGRIF domain, which extends further east (dashed line rectangle in Figure 2.7). Due to a lack of time, this alternative version will not be discussed in details in this manuscript. However, note that the investigation of simulations performed with the extended AGRIF domain indicates that its main added-value is to improve the realism of the Alboran Sea circulation, with moderate impacts on the rest of the Mediterranean Sea. We create the AGRIF configuration grid file with the NEMO nesting tools, a set of Fortran 95 procedures that aim at facilitating the implementation of AGRIF configurations.

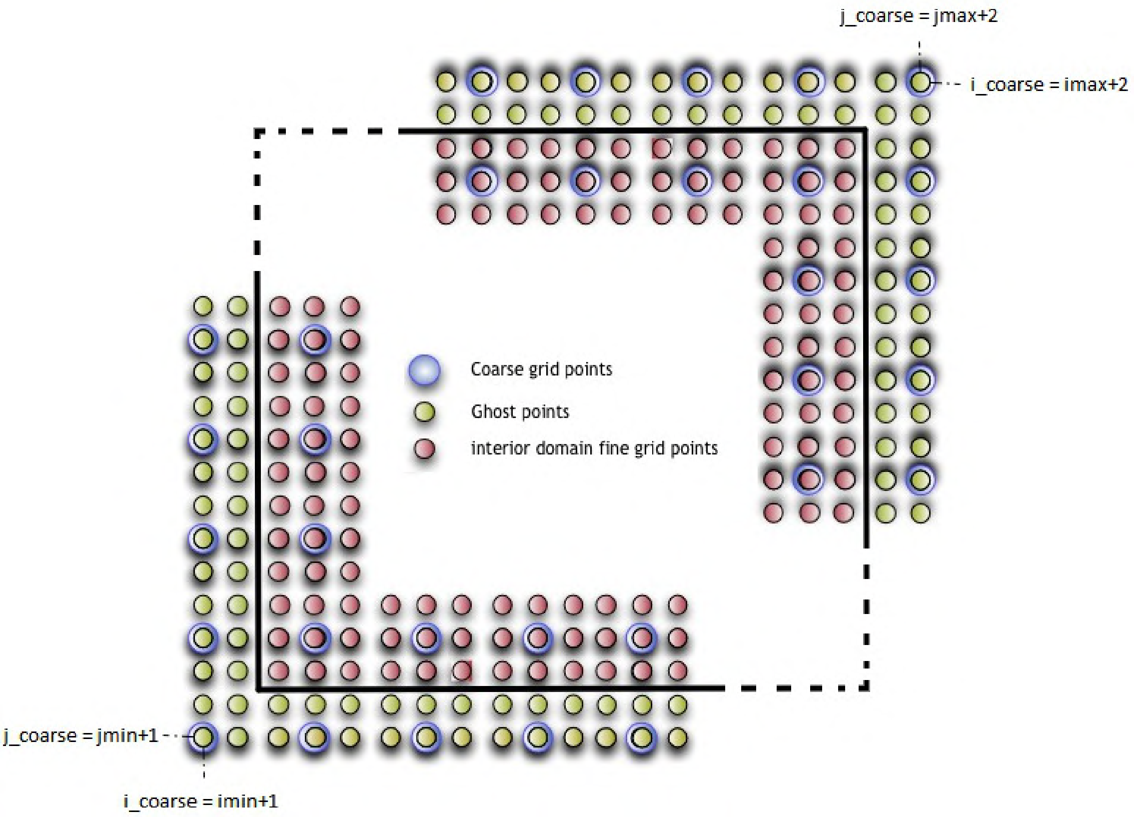

Figure 2.6: Schematic representation of the AGRIF domain, with a spatial refinement factor of three. A black line delimits the computational domain, the points outside are "ghost" points, but the first rows and columns are considered as land. The spatial refinement factor of five is not illustrated for clarity. However, it would display a very similar scheme, the only differences being that the first and last rows and columns of points would not be "coarse" grid points, and coarse grid points inside the computational domain would be at the center of 5-point sides squares instead of 3. Figure adapted from https://forge.ipsl.jussieu.fr/nemo/wiki/Users/SetupNewConfiguration/AGRIF-nesting-tool

2.3.2 High-resolution bathymetry

The complex geometry of the SoG has a strong influence on the fine-scale dynamics at play. Thus, the choice of AGRIF bathymetry is essential in the NEMO-MEDGIB configuration. Furthermore, to properly investigate the effect of fine-scale dynamics at the SoG, the bathymetries of the coarse and AGRIF configurations must retain similar features. In particular, although the SoG geometry will evolve at increasing resolution, the strait section area should remain similar. The coarse and fine resolution bathymetries should, thus, be created from the same dataset with a volume-conservative interpolation method. Unfortunately, this constraint is not achievable with the NEMOMED12 bathymetry, which results from a non-volume-conserving median average operation. Consequently, I have modified the NEMOMED12 bathymetry over the AGRIF domain. The resulting bathymetry will be referred to as the NEMOMEDGIB bathymetry.

For the sake of conciseness, we will discuss only two reference datasets eligible for creating the AGRIF and NEMOMEDGIB bathymetries. The first one is

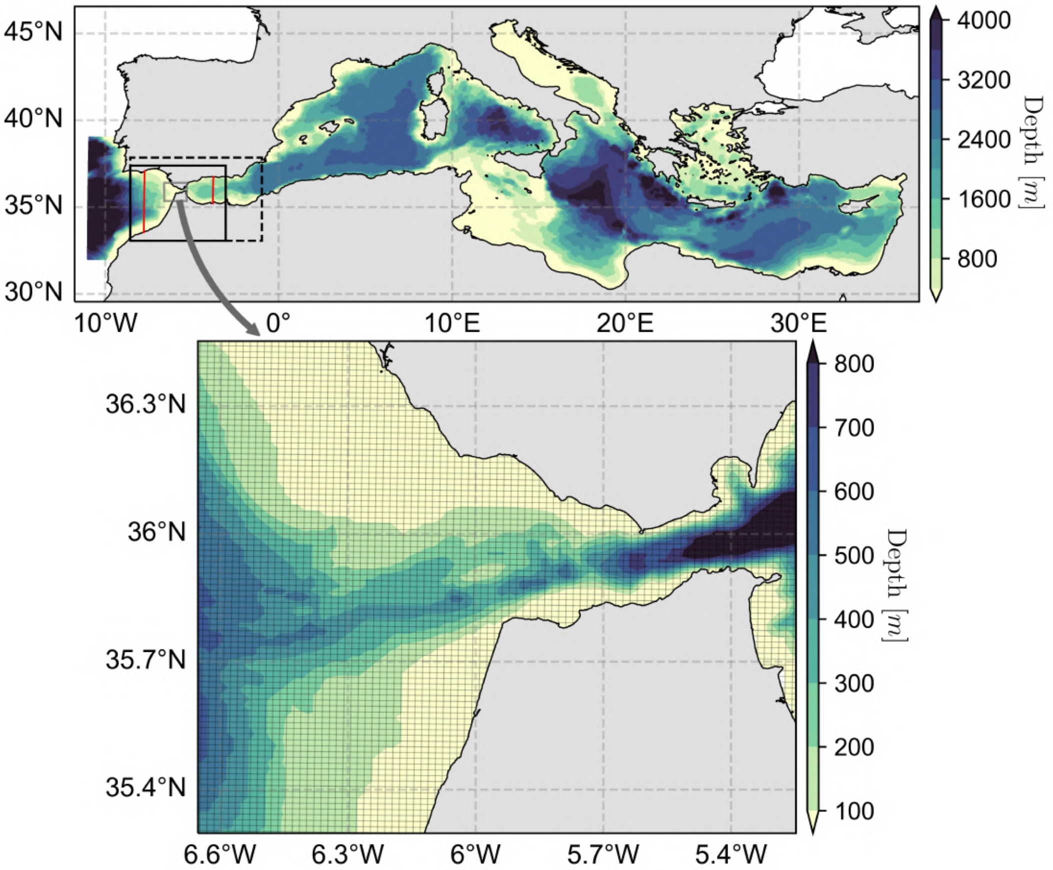

Figure 2.7: NEMOMEDGIB bathymetry (upper panel) and zoom on the grid and bathymetry at the Strait of Gibraltar (lower panel, representing the area framed by the grey rectangle). The black rectangle on the upper panel shows the AGRIF domain. The dashed rectangle displays the extent of the alternative version of the AGRIF domain. The red lines delimit the end of the spatial spin-up zone, diagnosed following Matte et al (2017)

the ML10 dataset, which offers an optimal consistency between the new and old bathymetries as the NEMOMED12 bathymetry was created from it. The second is the 1/960° EMODnet dataset from the EMODnet Bathymetry Consortium (2020; https://doi.org/10.12770/bb6a87dd-e579-4036-abe1-e649cea9881a). The EMODnet bathymetry results from the merging of several bathymetric survey datasets, composite digital terrain models, satellite-derived bathymetry data products, and the GEBCO digital bathymetry (GEBCO Bathymetric Compilation Group, 2022) for areas where no observational product is available.

Because of the large number of observational products included in the EMODnet dataset, we use it to assess the realism of the ML10 bathymetry at the SoG. More specifically, we compare the SoG meridional section area in both datasets. The results, displayed in Figure 2.8, depict significant differences between ML10 and EMODnet east of the Tarifa Narrows at $\sim 5.6°$W, where the SoG is significantly broader in ML10. This difference results from an unrealistically deep seafloor near the coast of Morocco in the ML10 dataset (see Figure 2.9, panels (a) and (b)). In addition, the ML10 bathymetry displays other unrealistic features, including a large cavity north of the Majuan Bank just east of 6.1°W and smaller ones west of the Bay of Algeciras. In light of these results, we consider that the ML10 dataset is not sufficiently accurate at the SoG to derive the AGRIF bathymetry. Thus, we choose to select the EMODnet dataset to create the NEMOMEDGIB and AGRIF bathymetries.

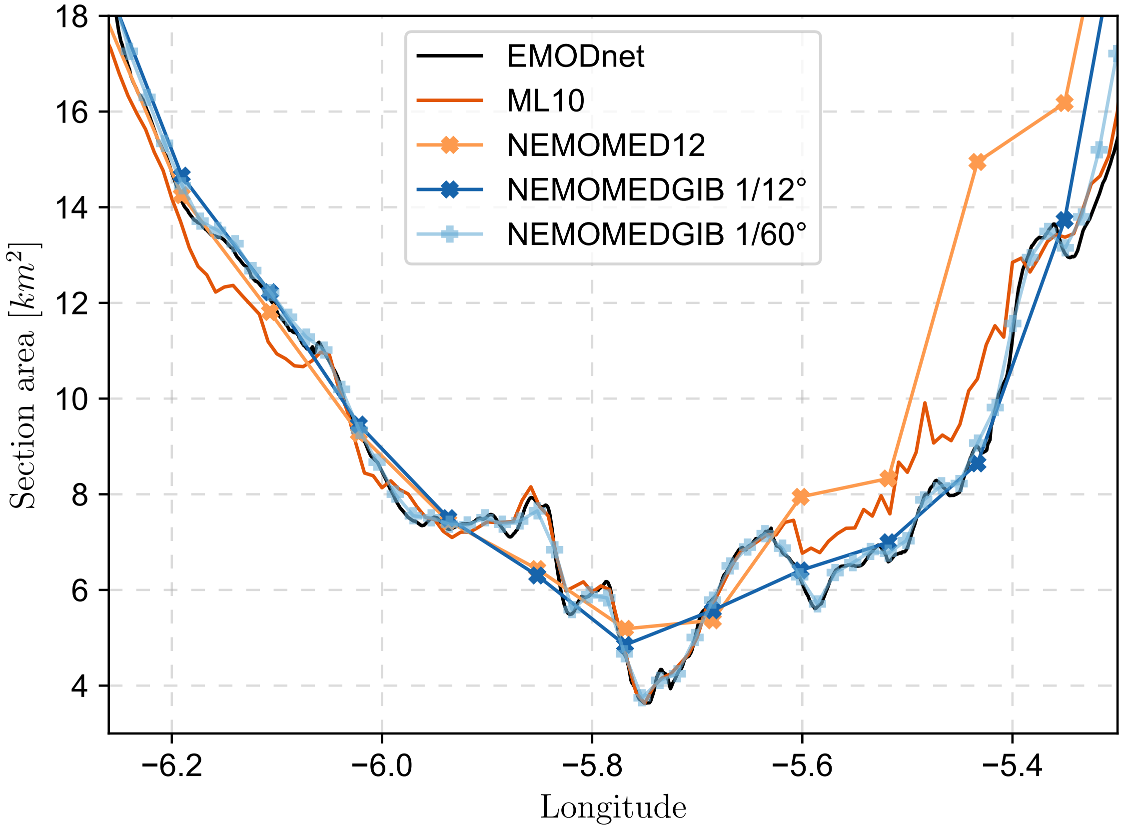

Figure 2.8: Zonal profile of the meridional section area (in km^2) at the SoG, computed from the EMODnet (black) and ML10 (orange) datasets and the bathymetries of the NEMOMED12 (light orange), NEMOMEDGIB (dark blue) and AGRIF (light blue) configurations.

We create the NEMOMEDGIB bathymetry with a modified version of the NEMO nesting tools, which bathymetry module is updated to include a volume-conservative averaging method. At the edges of the AGRIF domain, we do not find any major discontinuity between the NEMOMED12 and NEMOMEDGIB bathymetries. Thus, no modification is made to connect them. However, we ensure the NEMOMEDGIB bathymetry does not include isolated cavities (cells deeper than all their direct neighbors) over the AGRIF sponge layer, where the bathymetries of both configurations must be identical. This step is essential as isolated cavities are “filled” (set to the value of their deepest direct neighbor) at the model initialization for the parent configuration but not for the AGRIF configuration, resulting in inconsistencies between their bathymetries. Indeed in the AGRIF configuration, the coarse bathymetry cavities are represented by 5-points size squares, they are thus not considered isolated. The final NEMOMEDGIB bathymetry provides a realistic representation of the SoG, with meridional section areas consistent with the EMODnet dataset throughout the strait (Figure 2.8). A minimum depth of 240m (29 vertical levels) is reached at the Camarinal Sill (with respect to 270m and 30 vertical levels for NEMOMED12, see Figure 2.9). However, these modifications ask for a re-calibration of the lateral friction coefficients. Based on the latest transports estimates of García-Lafuente et al (2021); Jordà et al (2017a), we find that a lateral friction parameter of 0.9 (*rn_shlat* in NEMO namelist) allows simulating realistic transports in both tidal and non-tidal simulation. For a more extensive validation of the simulated transports, the readers are referred to the following sections.

This modification finalizes the creation of the coarse NEMOMEDGIB configuration, referred to as NT LR in the following. Thus, with respect to NEMOMED12, this new configuration includes open boundary conditions, time-splitting of the barotropic dynamics, explicit tidal forcing (see the previous sections), a modified of the bathymetry at the SoG, and decreased lateral friction coefficient (this section). The impact of bathymetry and lateral friction modifications is extensively detailed in Appendix A. In short, at the SoG, Atlantic and Mediterranean exchanges are enhanced with respect to the NEMOMED12 configuration. In addition, the circulation west of the SoG is moderately modified, resulting in a moderate warming and saltening of the Atlantic water masses crossing the strait. The main impact over the Mediterranean sea is the enhancement of the exchanges between the Eastern and Western Mediterranean basins. This results in a warming and saltening of intermediate layers over the Western Mediterranean, and a cooling and saltening of the upper 150m depth over the Eastern Mediterranean.

Finally, we create the AGRIF bathymetry following the same procedure as for NEMOMEDGIB. As previously mentioned, the AGRIF bathymetry is set to that of NEMOMEDGIB over the sponge layer. In addition, the nesting tools procedures ensure a linear connection between the high and low resolution bathymetries. As displayed in Figure 2.8, the AGRIF bathymetry is highly consistent with the EMODnet dataset. It also realistically reproduces the main topographic obstacles of the SoG, such as the Camarinal and Espartel sills or the Majuan Bank (see Figure 2.7). A minimum depth of 270m (30 vertical levels) is reached at the Camarinal Sill.

Note that I have also developed an alternative version of the AGRIF bathymetry, which consists of bilinear interpolation of the NEMOMEDGIB one. This “smooth” bathymetry will be used in the following chapter to assess the respective effects of refined topography versus fine-scale dynamics on the simulated exchanges at the SoG.

2.3.3 Nesting, forcings, and initial conditions

The AGRIF configuration is forced at its lateral boundaries by NEMOMEDGIB through a two-coarse-cell-wide sponge layer. The intensity of the relaxation is controlled by sponge layer coefficients, set through the namelist parameters *rn_sponge_tra* for tracers and *rn_sponge_dyn* for the dynamics. In order to define these coefficients, we carry out various simulations with different values of *rn_sponge_tra* and *rn_sponge_dyn*. we found that numerical instabilities develop for values higher than $900\text{m}^2.\text{s}^{-1}$. For lower values ($30-600\text{m}^2.\text{s}^{-1}$), the model shows low sensitivity to the coefficients. Finally, we set these coefficients to an intermediate value of $300\text{m}^2.\text{s}^{-1}$ after verifying that internal waves leave the AGRIF domain without spurious reflections against the lateral boundaries.

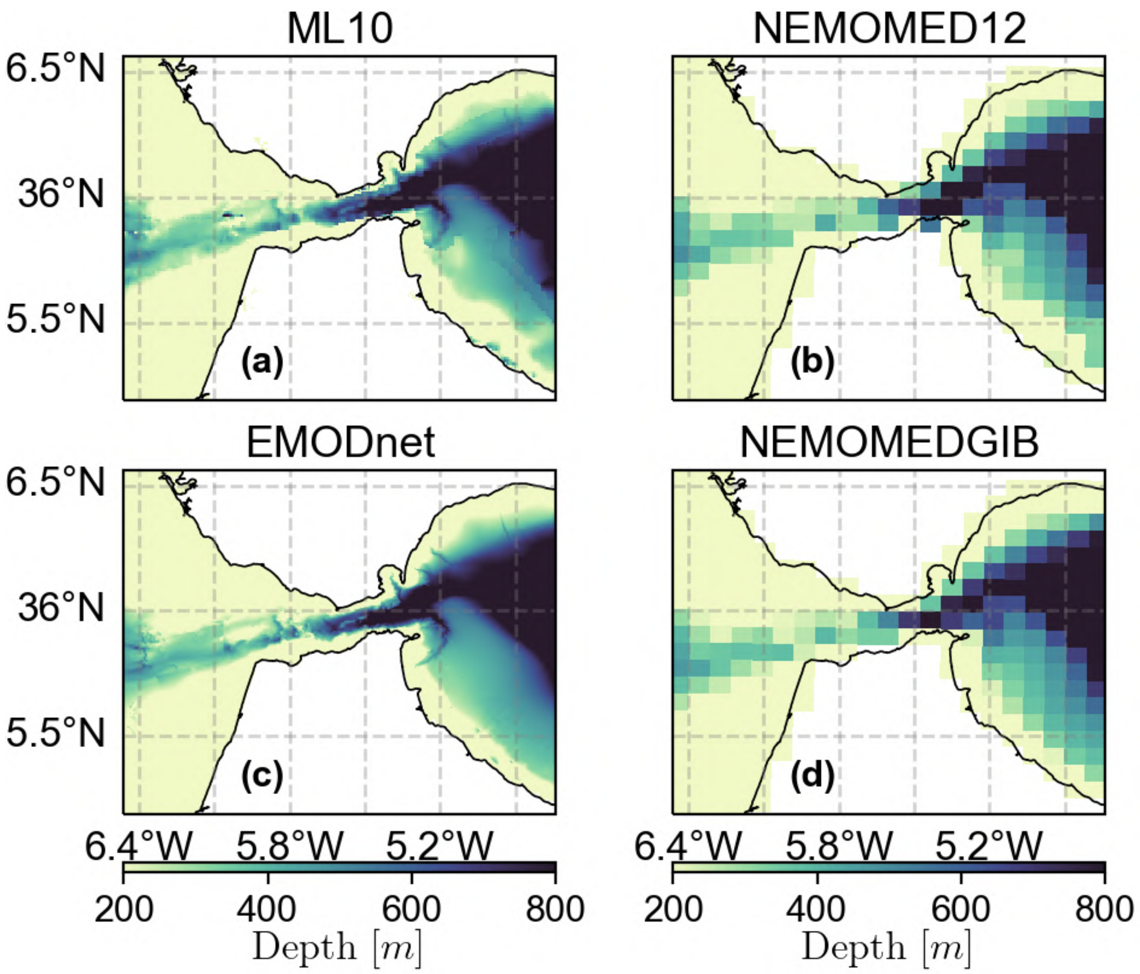

Figure 2.9: From left to right and top to bottom, bathymetry from a) ML10, b) NEMOMED12, c) EMODnet and d) NEMOMEDGIB (coarse grid).

Regarding external forcing datasets, most of them can be created from the NEMOMEDGIB forcing datasets with the NEMO nesting tools. More specifically, the wind stress, solar, heat, and water fluxes, sea surface temperature, and chlorophyll concentration are interpolated on the AGRIF grid with a bicubic scheme. An additional correction is applied to ensure the conservation of the heat, water, and solar fluxes. The interpolation of runoff fields is more complex as they are made of sparse non-zero values. To overcome this issue, we adopt a volume-conservative nearest-neighbor interpolation method using a Python script. Simply put, for each river mouth represented in the parent configuration, we attribute its runoff to the closest coastal point of the AGRIF domain. We do not split the river runoffs over several points as we consider the AGRIF resolution sufficiently coarse to represent river mouths as a single grid cell. For the coastal runoffs (see the previous section about the runoffs in NEMOMED12), their total volume is redistributed over the remaining coastal areas. Thus, the total runoff volume is strictly conserved in the AGRIF configuration.

Finally, the initial state of the AGRIF configuration is also created with the NEMO nesting tools using a bicubic interpolation. However, it happens for a few cells that the interpolation fails, setting a reference value of zero. We attribute to these cells the value of their closest horizontal neighbor using a Python script.

2.3.4 Physical parameters of the AGRIF configuration

Because of its enhanced resolution, some parameters of the AGRIF configuration must be modified with respect to NEMOMEDGIB. A first and essential parameter to modify the simulation time-step. Indeed, the stability of numerical models is linearly related to the ratio between their temporal and spatial resolutions. Thus, for a refinement factor of 5, we divide the time step by 5. Similarly, we divide the horizontal Laplacian eddy diffusivity by 5 (*rn_aht_0* $=12\mathrm{m}^2.\mathrm{s}^{-1}$) and the momentum horizontal bilaplacian eddy viscosity by 5^3 (*rn_ahm_0_blp* $= -10^8\mathrm{m}^4.\mathrm{s}^{-1}$). These multiplicative coefficients are inferred from the theoretical definition of each operator. Indeed, the Laplacian eddy diffusivity is homogeneous to the product of a velocity and a length scale, whereas the bilaplacian eddy viscosity is homogeneous to the product of a velocity and a cubic length scale. Finally, the open boundary conditions are disabled in the AGRIF configuration (namelist parameter *nn_bdy* set to 0), as AGRIF modules directly handle the lateral nesting with the parent configuration.

2.4 Coupled configuration

2.4.1 CNRM-RCSM6: a regional coupled climate model

The CNRM-RCSM6 climate model is a state-of-the-art, fully coupled, regional climate system model developed at CNRM. The model domain covers the Euro-Mediterranean region (see Figure 2.10), including the official Med-CORDEX domain (Ruti et al, 2016). South, the model domain extends to the North of Africa and the Arabian peninsula to include the sources of the main desert dusts transported over the Euro-Mediterranean region. As for NEMOMED12, the CNRM-RCSM6 model results from successive developments (Somot et al, 2008; Sevault et al, 2014; Nabat et al, 2015; Voldoire et al, 2017; Darmaraki et al, 2019; Nabat et al, 2020). It consists of several numerical models coupled at hourly frequency through the OASIS software (Craig et al, 2017) following the strategy described by Voldoire et al (2017). Specifically, CNRM-RCSM6 includes the 12km, 91 levels, atmospheric model of ALADIN v6 (Daniel et al, 2019), coupled to the TACTIC interactive aerosol scheme (Nabat et al, 2020) and the SURFEX v8.0 land surface model (Masson et al, 2013; Voldoire et al, 2017) to which the ISBA-CTRIP land surface system (Decharme et al, 2019) and the Flake lake scheme (Le Moigne et al, 2016) are embedded. Rivers are represented by the CTRIP 50km model (Decharme et al, 2019). Finally, the ocean is simulated through the NEMOMED12 configuration, previously introduced.

Regarding coupling procedures, surface fluxes between the oceanic and atmospheric components are directly computed through boundary conditions. River runoffs are first computed by the SURFEX model and sent to the NEMOMED12 through CTRIP. The Black sea is considered as a river in the NEMOMED12 model. Its runoff is computed as the sum of river discharges over the Black Sea drainage area (58 river mouth) and the Black Sea net surface water flux (evaporation minus

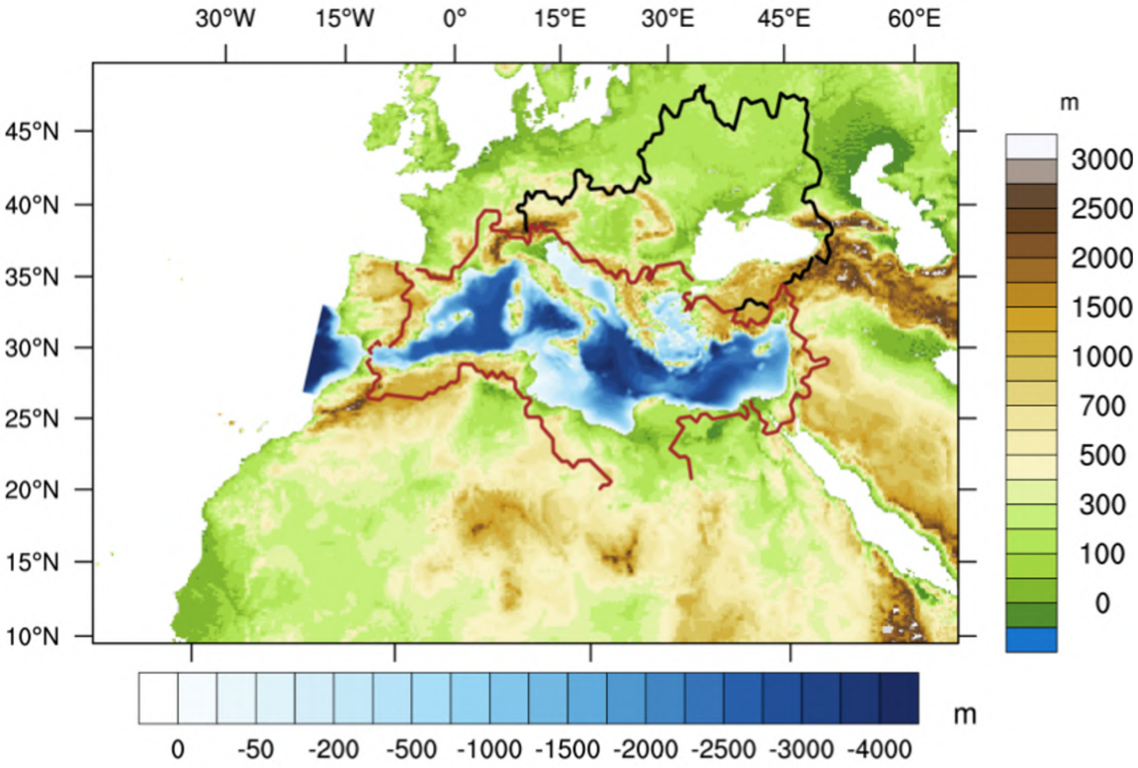

Figure 2.10: CNRM-ALADIN land-sea mask and orography for the AAD12 domain (in meters), and NEMOMED12 bathymetry (in meters). The drainage areas of the Black Sea (in black) and the Mediterranean Sea (in red) are contoured.

precipitation) from the SURFEX model. The Nile river runoff, largely anthropized, is prescribed by a 12-month climatology.

In the so-called hindcast, or evaluation, mode, the coupled model is driven by reanalyses at the lateral boundaries. Namely, the atmosphere is forced by ERA-Interim (Berrisford et al, 2009) and the ocean by ORAS4 (Balmaseda et al, 2013), of which the sea surface elevation is corrected following Adloff et al (2018). In addition, for the atmospheric model, a spectral nudging toward the ERA-Interim dataset is applied over its inner domain (Colin et al, 2010). Outside of the NEMOMED12 domain, namely, over the Atlantic Ocean, the Baltic sea, and the Black sea, the atmospheric model is provided with the sea surface temperature of ERA-INTERIM. Initial conditions are provided by the ERA-Interim dataset for the ALADIN model and the MEDHYMAP dataset (Jordà et al, 2017a) for NEMOMED12.

Note that the coupled model can also be used in historic-scenario mode. In this case, it is driven by the outputs of a free global simulation, forced only by anthropogenetic concentrations of greenhouse gases following historical emissions over the past and a possible pathway of their evolution in the future. I have performed historic-scenario simulations but could not include them in this manuscript due to a lack of time. Thus, in the following, we only discuss simulations performed in hindcast mode.

At the international level, the CNRM-RCSM6 model is part of the Med-CORDEX initiative (Ruti et al, 2016, www.medcordex.eu). It is a useful numerical tool to investigate the Mediterranean Sea climate's past variability and future trends as well as coupled mechanisms at play in the regional climate system, such as that at the ocean-atmosphere interface (Darmaraki et al, 2019) or the land-atmosphere interface.

2.4.2 Inclusion of NEMOMEDGIB into CNRM-RCSM6

In order to activate coupling procedures, the NEMO source code must be compiled with the CPP keys **key_oasis3** and **key_oa3mct_v3**. The coupling is then set through a dedicated namelist section: namsbc_cpl. The namsbc_cpl section comprises two sub-sections: one defines the oceanic fields to be sent to the atmospheric component, and the other the fields received from other model components. A detailed list of the namelist parameters and the associated values is specified in Table 2.6. In the following, we discuss only the ones relevant to the coupled CNRM-RCSM6 configuration.

Regarding the ocean-atmosphere interface, we first adapt the surface boundary conditions to the coupled mode. Specifically, the flux formulation is replaced by the coupled formulation (*ln_flx* set to "False" and *ln_cpl* set to "True"), and the sea surface temperature relaxation is disabled (*ln_ssr* set to "False"). Then, the namsbc_cpl section is set for NEMOMEDGIB to provide sea surface temperature and surface currents to the ALADIN model and receive wind stress, heat, and water fluxes.

Regarding River runoffs, a "mixed" coupling procedure is used (*sn_rcv_rnf* = "mixed") because of the specific treatment applied to the Nile river, which runoff is prescribed through a 12-month climatology. In this way, the Nile river runoff is set in the namsbc_rnf. Specifically, the forcing is specified as climatological, and the associated file is modified to contain only the Nile river runoff climatology. Finally, a file specifying the vertical extent of runoffs at each river mouth must be provided to the NEMO model. Unfortunately, the file used for the simulations studied in this PhD was corrupted due to a runoff conversion error at its creation. Consequently, the simulated runoffs are added only over the top two levels of the water column. However, we diagnosed from a sensitivity test that this error has a negligible impact on the simulations.

2.4.3 CNRM-RCSM6 with NEMOMEDGIB and AGRIF: CNRM-RCSM6-AGIB

In order to make the coupled NEMOv3.6 mode compatible with AGRIF, a few modifications must be made to the source code. Namely, we use a modified version of the step.F90, cpl_oasis3.F90, sbccpl.F90, and geo2ocean.F90 routines, create by Florence Sevault a CNRM. In addition, a new namelist parameter is added to the *namsbc_cpl* namelist section: *ln_use_AGRIF*. This parameter specifies to the NEMO code whether or not the running configuration is nested with an AGRIF config-

Namelist parameter	Formulation	Multiple Categories	Vector Reference	Vector orientation	Vector grids	Field Descripiton
Sent						
snsndtemp	**’oce only’**	**’no’**	**”**	**”**	**”**	**surface temperature**
snsndalb	’none’	’no’	”	”	”	albedo
snsndthick	’none’	’no’	”	”	”	ice/snow thickness
snsndcrt	**’oce only’**	**’no’**	**’spherical’**	**’eastward-northward’**	**’T’**	**surface current**
snsndco2	’none’	’no’	”	”	”	ocean CO2 flux
Received						
snrcvw10m	’none’	’no’	”	”		10m wind module
snrcvtaumod	’none’	’no’	”	”	”	stress module
snrcvtau	**’oce only’**	**’no’**	**’spherical’**	**’eastward-northward’**	**’T’**	**surface stress**
snrcvdqnsdt	’none’	’no’	”	”	”	non-solar heat flux sensitivity
snrcvqsr	**’oce only’**	**’no’**	**”**	**”**	**”**	**solar heat flux**
snrcvqns	**’oce only’**	**’no’**	**”**	**”**	**”**	**non-solar heat flux**
snrcvemp	**’oce only’**	**’no’**	**”**	**”**	**”**	**freshwater budget**
snrcvrnf	**’mixed’**	**’no’**	**”**	**”**	**”**	**runoffs**
snrcvriv	**’coupled’**	**’no’**	**”**	**”**	**”**	**rivers**
snrcvcal	’none’	’no’	”	”	”	calving
snrcviceflx	’none’	’no’	”	”	”	sea ice heat fluxes
snrcvco2	’none’	’no’	”	”	”	atmospheric CO2

Table 2.6: Parameters of the coupling namelist section (namsbc_cpl). The coupled fields are displayed in bold. The coupling formulation is set to ‘none’ for uncoupled fields.

uration. In this way, the *ln_use_AGRIF* is set to “True” in the NEMOMEDGIB namelist and “False” in the AGRIF namelist.

As a final step, we adapt the AGRIF coupling namelist to ensure that the ALADIN model receives feedback from a single ocean configuration. Since the AGRIF solution is constantly prescribed to NEMOMEDGIB, we send only the NEMOMEDGIB fields to the ALADIN model. However, the AGRIF configuration does receive the wind stress, heat, and water fluxes from ALADIN and the river runoffs from CTRIP. In the end, with respect to the NEMOMEDGIB namelist, we only set the parameters *sn_snd_temp* and *sn_snd_crt* to ‘none’. In the following, we will refer to the NEMOMEDGIB version of CNRM-RCSM6 as CNRM-RCSM6-GIB and the AGRIF NEMOMEDGIB version of CNRM-RCSM6 as CNRM-RCSM6-AGIB.

2.5 Simulations investigated in the PhD

To conclude this chapter, we now introduce the simulations investigated in this PhD and the scientific questions they will allow us to investigate. We make use of two main sets of simulations.

The first set consists of four coupled simulations, displayed in Table 2.7 (NT LR, T LR, NT HR, and T HR). These simulations are run over 1979/08/01 - 2017/12/31 using realistic physical forcings following the historical chronology (so-called hindcast mode, see previous sections) after a 19.5-year spin-up. For the spin-ups, we use annual forcing datasets (starting in August) taken randomly over 1979/07/01 - 1986/07/31. The goal is for the coupled model to reach a stable state, representative of the 1980s climate. The initial conditions used in the spin-ups, common to all simulations, are the outputs from a preliminary 10-year coupled spin-up with the CNRM-RCSM-GIB model. For this spin-up, initial conditions are provided by the ERA-Interim dataset for the ALADIN model and the output of a forced NEMOMED12 spin-up over 1979 - 1982 using a 3D relaxation toward the MEDHYMAP dataset for the NEMOMEDGIB model (this allows initializing the ocean circulation without altering water masses).

The second set of simulations, also displayed in Table 2.7, consists of 7 forced, 19.5-year ocean spin-ups, performed following the same protocol as for coupled simulations. We use these simulations to investigate questions that do not require ocean-atmosphere coupling. They are not extended over the historical period, as they only aim at investigating short-term and direct effects.

Those two sets of simulations can be considered as the main numerical material of the fourth and fifth chapters of this PhD. In the third chapter, we first conduct a preliminary study investigating tidal mixing mechanisms in high-resolution simulations of the SoG with the MITgcm model. Then, in the fourth chapter, we use coupled simulations to investigate the respective roles of tidal and fine-scale dynamics on exchanges at the SoG and their impact on the Mediterranean Sea and its interactions with the atmosphere. Finally, in the fifth chapter, we use forced simulations to investigate an alternative to high-resolution and explicit tidal forcing at

Simulation	Tides	Grid nesting	SoG Bathymetry	Coupled run: Hindcast mode (1980-2017)	Forced run: Spin-up mode (20 year-long)
Main Simulations					
NT LR	No	No	Realistic	Yes	Yes
pT LR	Parameterized	No	Realistic	No	Yes
T LR	Yes	No	Realistic	Yes	Yes
NT HR	No	Yes	Realistic	Yes	Yes
T HR	Yes	Yes	Realistic	Yes	Yes
Sensitivity tests					
NT sHR	No	Yes	Smoothed	No	Yes
T sHR	Yes	Yes	Smoothed	No	Yes

Table 2.7: Simulations used to investigate the influence of the SoG on the Mediterranean climate and how to represent in numerical models. The last two simulations allow assissing the respective influence of fine-scale topography and dynamics on the exchanges trhough the strait.

the SoG for use in lower resolution ocean models (pT LR in Table 2.7).

Appendices

A From NEMOMED12 to NEMOMEDGIB: Overview of the differences between both configurations

In this appendix, we compare the NEMOMEDGIB configuration in non-tidal and non-nested mode (NT LR, as referred to in the following chapters of this manuscript) to the NEMOMED12 configuration available at CNRM at the start of this PhD (NM12 hereinafter). The goal is to assess the effects of the modifications performed on NM12 in the scope of the NEMOMEDGIB implementation. To do so, we rely on a set of four decadal forced oceanic simulations (see Table A.8), which can be considered as intermediate versions between NM12 and NT LR, progressively including the modifications related to: time-splitting and open boundary conditions (NM12 OB TS), vertical mixing (NM12 OB TS bg mix), bottom mixing (NM12 OB TS bg bot mix), and finally, bathymetry and lateral friction coefficients (NT LR). The simulations, initialized in August 1979 from the outputs of a preliminary decadal NEMOMEDGIB simulation, use identical realistic forcings, which do not follow the historical climatic chronology. Specifically, the forcings consist of annual datasets (starting in August) taken randomly over 1979/07/01 - 1986/07/31. The aim is to simulate a relatively steady climate free of transient climatic trends. In this way, the simulations only differ by the aforementioned numerical modifications.

Simulation	Specificity with respect to preceding simulation
NM12	NEMOMED12 original configuration
NM12 OB TS	Addition of open boundaries and activation of time-splitting
NM12 K_z^{min}	Decrease of the background mixing coefficients and modification of the TKE closure scheme mixing length scale formulation
NM12 K_z^{bot}	Logarithmic bottom friction, deletion of parameterized tidal bottom friction, and implicit bottom friction formulation
NT LR	Modified bathymetry at the Strait of Gibraltar and increased partial free-slip lateral boundaries

Table A.8: Simulations used to assess the effect of the modifications performed on the NEMOMED12 configuration

A.1 Exchanges through the Strait of Gibraltar

The NM12 and NT LR configurations primarily differ in modeling choices related to the Strait of Gibraltar (SoG hereinafter). Thus, dynamic and hydrographic properties of the exchanged flows through the strait constitute a relevant starting point to compare both configurations. We display on the upper panels of Figure A.1 the NM12 and NT LR average vertical profiles of temperature, salinity, and velocity in the vicinity of the SoG (6.1°W-5.25°W, black lines in Figure A.2). They depict a typical picture of the two-layer exchange flow through the strait, with a relatively warm and fresh surface layer advected toward the Mediterranean Sea and a colder and saltier deeper layer advected toward the Atlantic Ocean. The climatological mean zero velocity interface is approximately 140m deep.

Despite the overall structure just described, NM12 and NT LR display substantial dynamic and hydrographic differences, illustrated on the lower panels of Figure A.1. With respect to NM12, NT LR simulates a cooler (up to $-1°C$) and fresher (up to $-0.15‰$) Atlantic layer and a saltier Mediterranean layer (up to $+0.15‰$). In terms of dynamics, in NT LR, the exchanged flow intensifies in both directions, and the climatological zero-velocity interface moderately shoals, indicating a thickening of the Mediterranean layer. To shed light on these anomalies, we decompose them into four components corresponding to the main physical differences between NM12 and NT LR. The resulting vertical profiles, displayed on the lower panels of Figure A.1, reveal that NT LR primarily differs from NM12 through the use of open boundaries and time splitting (orange lines) and the modified bathymetry and bottom friction (brown lines). However, interpretation of the associated anomalies and their combination is not straightforward.

Regarding hydrographic properties, the intense cooling and freshening of surface Atlantic water masses in NT LR mainly results from replacing the Atlantic buffer zone with open boundaries, which largely influences the Gulf of Cadiz circulation. in NM12, the Atlantic inflow through the SoG is mainly fed by a coastal northward current along the northern coast of Morocco. This dynamical structure is unrealistic with respect to the literature (Peliz et al, 2007, 2009, 2013), advecting

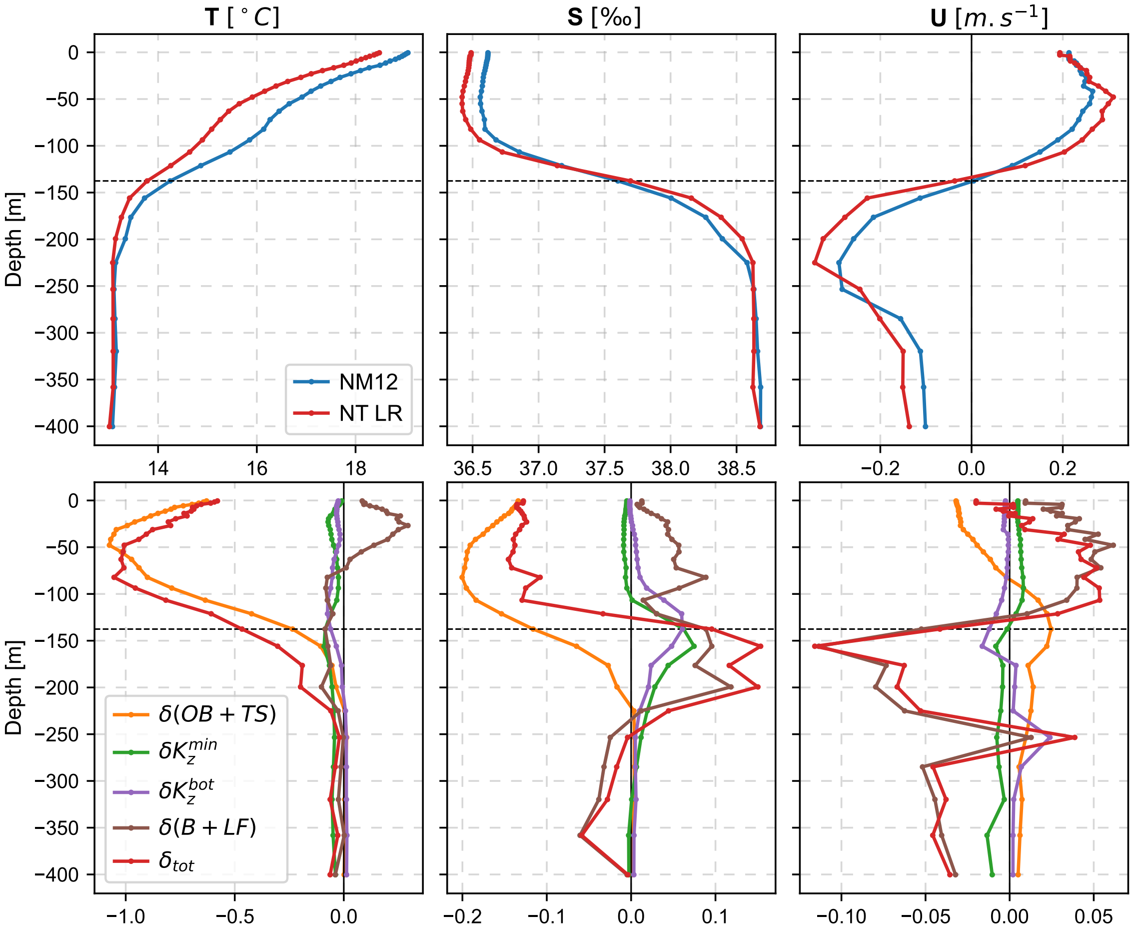

Figure A.1: Upper panels display vertical profiles of temperature, salinity, and zonal velocity for NEMOMED12 (NM12) and NEMOMEDGIB (NT LR) simulations, averaged at the SoG (6.1°W-5.25°W). Lower panels display the anomaly NT LR - NM12 (δ_{tot}) and its decomposition into four components, associated with the main physical differences between both configurations. We consider four main steps of the NEMOMED12 modifications: the replacement of the Atlantic buffer zone with open boundary conditions and the addition of time splitting (OB + TS), the decrease of background vertical mixing coefficients and the modification of the TKE mixing length-scales formulation (K_z^{min}), the removal of background tidal TKE energy and the activation of logarithmic bottom friction formulation (K_z^{bot}), the modification of NEMOMED12 bathymetry at the SoG and the decrease of lateral friction (B+ LF). The total anomaly between both configurations is displayed in red (δ_{tot}). The horizontal dashed line represents the depth of the zero velocity interface in the NEMOMED12 simulation.

abnormally warm and salty water masses into the SoG. On the other hand, in NT LR, the Atlantic inflow is fed by an offshore northward current from the south of the Gulf of Cadiz, an eastward current from the center of the Gulf of Cadiz, and to a lesser extent, by the Gulf of Cadiz slope current along the Iberian coast (Peliz et al, 2007), transporting colder and fresher water masses. These currents are relatively consistent with the literature, except for the low intensity of the Gulf of Cadiz slope current.

To a lesser extent, the inflowing vein of Atlantic water masses is also altered by the modification of lateral friction (brown lines in Figure A.1). Specifically, the reduction of lateral friction strengthens the northward current west of the strait and weakens the Gulf of Cadiz slope current (not shown), allowing warmer and saltier Atlantic water masses to enter the SoG. Note that over $\sim 100-200$m depth, this warm and salty anomaly combines with a cold and salty anomaly associated with the shoaling of the Mediterranean layer in NT LR, which seafloor is shallower than that of NM12 at the center and the eastern entrance of the strait. Conversely, the fresh anomaly below 225m depth is due to the greater breadth of the western entrance of the SoG in NT LR, where the Mediterranean outflow mixes with fresher Atlantic water masses.

Finally, the modification of bottom friction and vertical mixing moderately influences hydrographic properties. The anomalies associated with bottom friction (purple lines in Figure A.1) are mainly related to the use of the logarithmic bottom friction formulation in NT LR, which allows for a more intense drag above the seafloor and results in a shoaling of the Mediterranean layer. The modifications of vertical mixing (green lines in Figure A.1) induce a moderate saltening of the upper Mediterranean layer, which results from a strengthening of the western Mediterranean stratification, analyzed in the following section

In terms of dynamics, the differences between NM12 and NT LR mainly result from bathymetry and lateral friction modifications. In particular, the intense currents simulated in NT LR are consistent with the is narrower and shallower geometry of NT LR and the decrease of lateral friction, tuned to obtain consistent volume transports through the SoG with respect to the latest available estimates (García-Lafuente et al, 2021; Jordà et al, 2017b). Replacing the Atlantic buffer zone with open boundaries also influences the zonal velocity profile at the SoG, however, to a lesser extent. Specifically, it induces a dipole anomaly over the surface Atlantic layer, which can be explained by both a less intense flow of Atlantic water west of the SoG (see Figure A.2) and the weakening of the Atlantic layer stratification between $\sim 50-150$m depth. More precisely, the weakened stratification allows for greater turbulent viscosity, resulting in a homogenization of the zonal velocity profile between $\sim 50-150$m depth and a reduced flow of Atlantic water masses through the strait. As for hydrographic properties, the modification of bottom and background mixing coefficients has a moderate impact. The anomaly pattern induced by the bottom friction modification is consistent with intensified friction near the seafloor, forcing a shoaling of the Mediterranean layer. On the other hand, the dipole anomaly induced by the modification of vertical mixing provides a clear picture of vertical shear intensification consistent with the reduction of turbulent viscosity.

Transports through the SoG are displayed in Figure A.3. Both NM12 and NT LR display realistic values. Specifically, the simulated net volume, heat, and salt transports fall within the uncertainty range 0.04 ± 0.02Sv, 4.5W.m^2, and $0.1 \pm 0.3 10^6$kg.s^{-1} from Jordà et al (2017b, Tables 10, 11, 12), respectively. The simulated inflows also within the confidence interval of 0.86 ± 0.1Sv from Jordà et al (2017b, Table 3), with notable improvements in NT LR. The outflows are outside the estimation interval of -0.85 ± 0.03Sv from Sammartino et al (2015) for interannual timescales. However, they display reasonable values, particularly for the NT LR simulation. In addition,

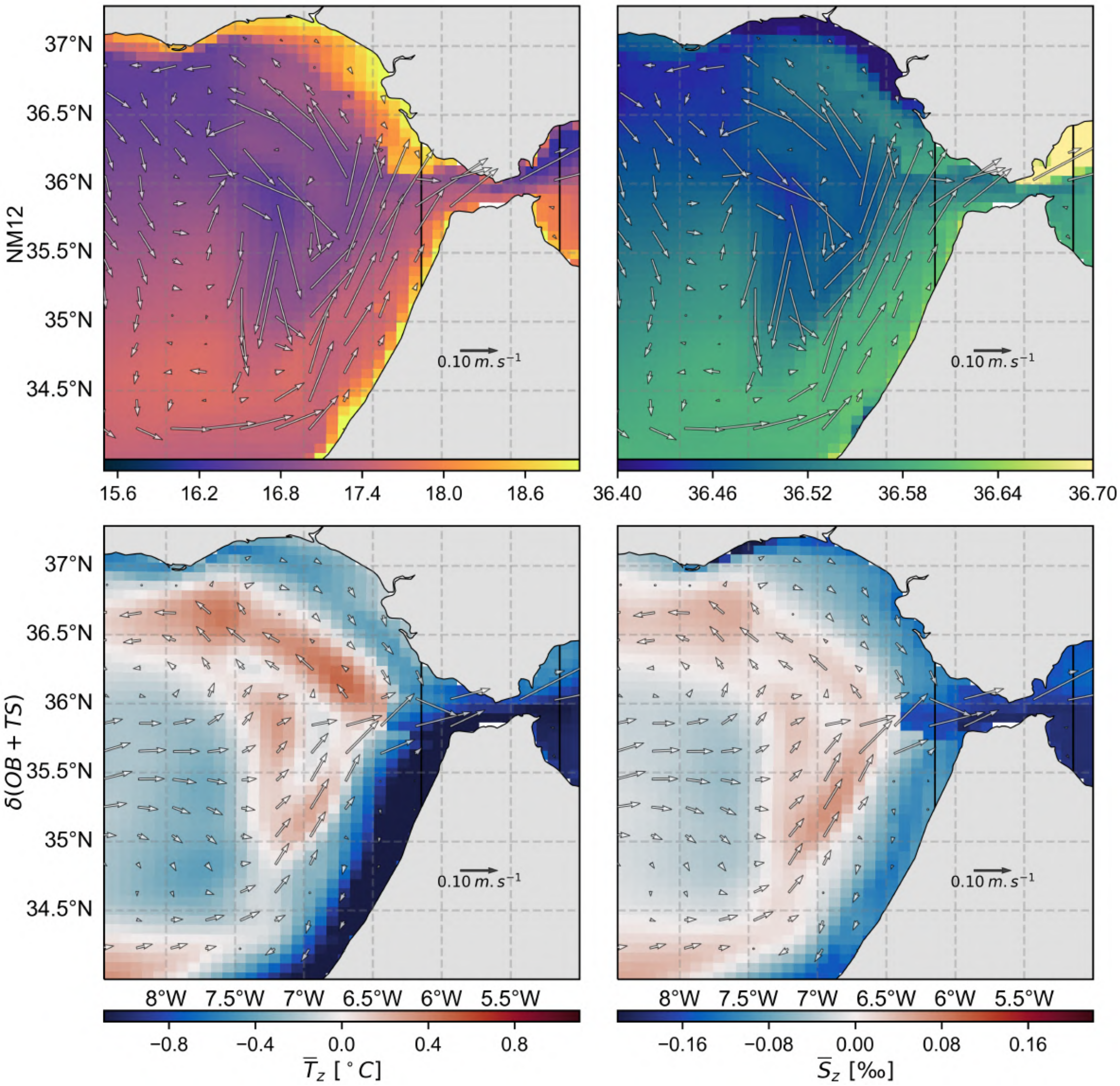

Figure A.2: The upper panels display the NEMOMED12 surface 100m depth average temperature (left), salinity (right), and horizontal currents (arrows). The lower panel displays the anomaly induced by replacing the NEMOMED12 buffer zone with open boundary conditions. The currents displayed are that of the modified NEMOMED12 simulation with open boundaries.

the computed heat and salt transport are within the range of values commonly obtained with similar numerical models (Jordà et al, 2017b).

In NT LR, the volume transports through the SoG significantly increase with respect to NM12. This enhanced advection directly results from the modification of lateral friction, calibrated to obtain consistent volume transport with respect to Sammartino et al (2015) and Jordà et al (2017b, Table 3). Because of their large sensitivity to volume advection, heat and salt transports follow similar variations to that of volume transports, primarily driven by the modification of lateral friction. The picture is more complex for the net heat and salt transports as hydrographic modulations interfere with the dynamics. The net heat transport substantially decreases in NT LR due to the cooling of the surface Atlantic water masses. The

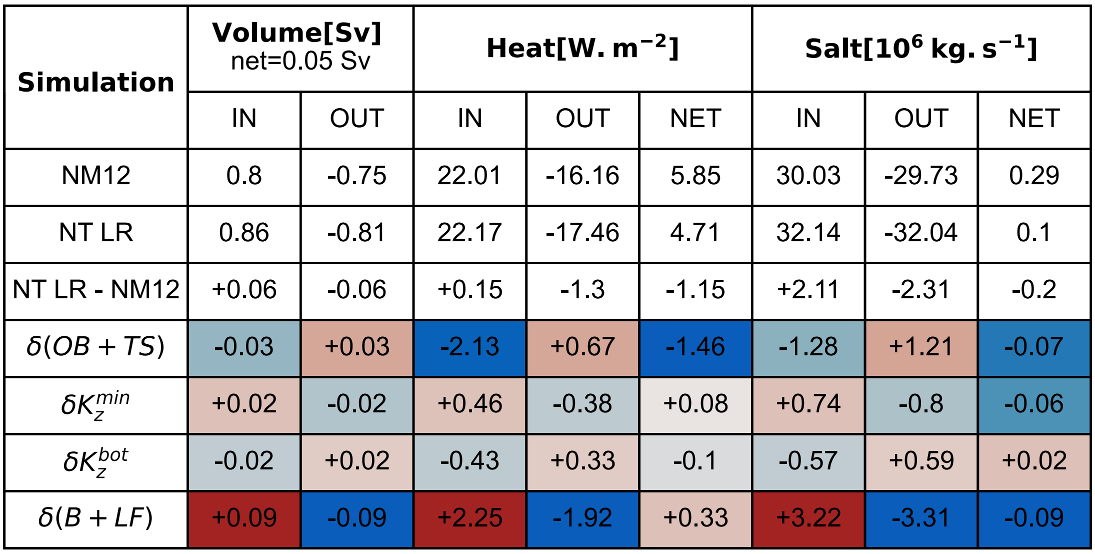

Simulation	**Volume[Sv]** net=0.05 Sv		**Heat[W. m^{-2}]**			**Salt[10^6 kg. s^{-1}]**		
	IN	OUT	IN	OUT	NET	IN	OUT	NET
NM12	0.8	-0.75	22.01	-16.16	5.85	30.03	-29.73	0.29
NT LR	0.86	-0.81	22.17	-17.46	4.71	32.14	-32.04	0.1
NT LR - NM12	+0.06	-0.06	+0.15	-1.3	-1.15	+2.11	-2.31	-0.2
$\delta(OB + TS)$	-0.03	+0.03	-2.13	+0.67	-1.46	-1.28	+1.21	-0.07
δK_z^{min}	+0.02	-0.02	+0.46	-0.38	+0.08	+0.74	-0.8	-0.06
δK_z^{bot}	-0.02	+0.02	-0.43	+0.33	-0.1	-0.57	+0.59	+0.02
$\delta(B + LF)$	+0.09	-0.09	+2.25	-1.92	+0.33	+3.22	-3.31	-0.09

Figure A.3: Average transports of volume, heat, and salt through the SoG. Positive values are oriented toward the Mediterranean Sea. As in Figure A.1, anomalies between the NEMOMED12 and NEMOMEDGIB configurations are decomposed into four components associated with the main differences between both simulations. Inflowing and outflowing transports are computed from time-step averages of the eastward and westward velocities, applying a Heaviside function on each velocity sign. As traditionally done for comparison purposes with the surface forcing, we convert the heat flux into an equivalent surface flux over the whole Mediterranean Sea, in W.m^{-2}, considering the Mediterranean area to be $2.5 \cdot 10^{12}$m^2, following Sanchez-Roman et al (2018).

net salt transport also decreases, but this time, because of the cumulative effects of open boundaries, vertical mixing, and lateral friction modifications. The lateral friction modification drives the largest decrease, resulting from the volume exchange intensification, which further enhances the outflowing salt transport carrying saltier Mediterranean water masses. The net salt flow further decreases due to Atlantic inflow freshening, induced by the open boundaries, and the Mediterranean outflow saltening due to the modification of vertical mixing over the Mediterranean Sea.

A.2 Impact on the Mediterranean Sea

Although the modifications performed on NM12 mainly focus on mechanisms at stake within the SoG, some of them apply to the whole Mediterranean Sea. This is the case for the modification of background vertical mixing (NM12 OB TS bg mix), background tidal TKE above the seafloor, bottom friction formulation (NM12 OB TS bg bot mix), and lateral friction (NT LR). In addition, it is important to assess the influence of the dynamical and hydrographic modulations of the exchange flow through the SoG on the Mediterranean Sea. To do so, we display in Figure A.4 the NM12 and NT LR vertical profiles of temperature and salinity, averaged over the western, eastern, and whole Mediterranean Sea, as well as the anomalies associated with the modifications decomposed as in the previous section. As a reference, we include the vertical profile of the MEDHYMAP dataset averaged over the period considered in the forcing dataset (1979/07/01 - 1986/07/31). NM12 and

NT LR are in relatively good agreement with the MEDHYMAP dataset, displaying reasonable errors comparable to other state-of-the-art Mediterranean regional simulations (Sannino et al, 2022). Basin-scale temperature absolute errors with respect to MEDHYMAP are relatively similar over the Eastern and Western Mediterranean Basins, with higher errors over the eastern Mediterranean in NM12 and the western Mediterranean in NT LR. Basin-scale salinity absolute errors mainly arise over the Western Mediterranean Basin, where the simulations display a large fresh bias.

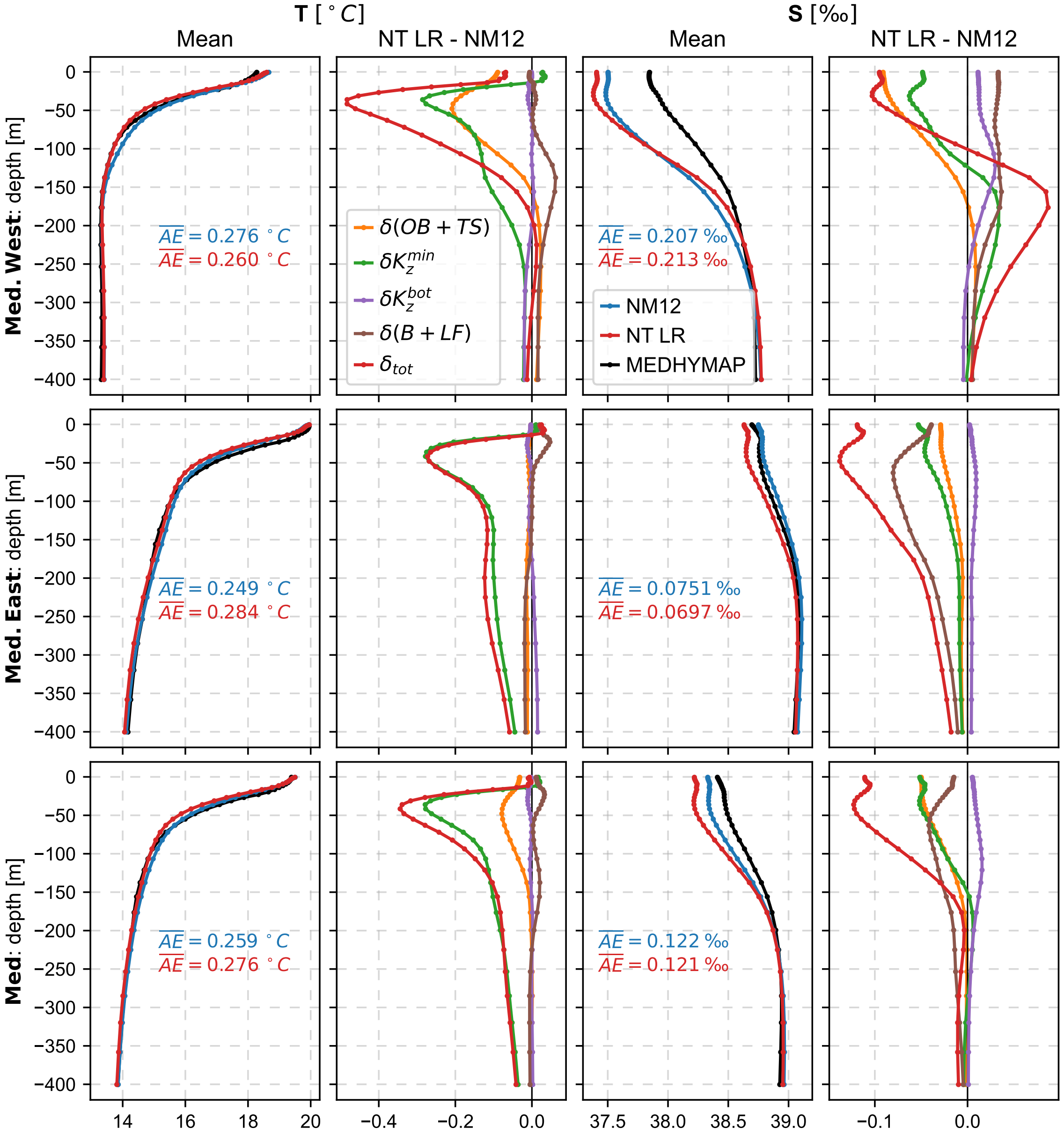

Figure A.4: Vertical temperature and salinity profiles for NEMOMED12 and NEMOMEDGIB simulations and associated anomalies. As in Figure A.1, anomalies between NEMOMED12 and NEMOMEDGIB configurations are decomposed into four components, associated with the main differences between both simulations. From top to bottom, we display the averages and anomalies over the Western Mediterranean Basin, the Eastern Mediterranean Basin, and the whole Mediterranean Sea.

The vertical temperature and salinity profiles of NM12 and NT LR display notable differences over the Eastern and Western Mediterranean Basins. Regarding the Western Mediterranean Basin, with respect to NM12, the upper 200m of NT LR are cooled (up to $-0.5°$C at 50m depth) and characterized by an enhanced salinity stratification. Due to the proximity with the SoG, these anomalies result from both basin-scale and local modifications within the strait. The influence of the SoG is particularly evident on the temperature and salinity anomalies, mainly resulting from the replacement of the Atlantic buffer zone with open boundaries (orange lines in Figure A.4). Consistently with the modification of the inflowing Atlantic water masses at the SoG, the upper 150m depth of the Western Mediterranean Basin are cooled and freshened, with a maximal anomaly at 50m depth for the temperature ($-0.2°$C) and at the surface for the salinity (-0.1‰).

Basin-scale effects over the western Mediterranean are mainly driven by the modification of vertical mixing coefficients (green lines in Figure A.4), which cools the upper 200m depth and induces a salt dipole anomaly centered on $\sim$ 125m depth. These anomalies are mainly related to the decrease of background vertical mixing coefficients. For the temperature, the weakening of vertical mixing allows for less intense ventilation of the surface layer. Consequently, the seasonal cycle of sea surface temperature is significantly enhanced (not shown), resulting in a reduced ocean heat uptake in summer. Over long periods, this leads to a cooling of deeper layers, up to 200m depth. Regarding salinity, since atmospheric fluxes have a lesser influence, the reduced vertical mixing results in a simple intensification of the stratification. Besides vertical mixing and open boundaries, the modification of bathymetry and lateral friction (brown lines in Figure A.4) induces less intense but notable hydrographic anomalies. Over the upper 100m depth, the relatively homogeneous salt anomaly is consistent with the saltening of the Atlantic water masses at the SoG. Deeper, the 100-200m layer is warmed and saltened with respect to NM12. This anomaly can be related to intensified transports with the Eastern Mediterranean Basin, displayed in Table A.5. Finally, bottom friction has a more mitigated influence. It mainly consists of a salt anomaly centered between 100-150m depth, consistent with the saltening of inflowing Atlantic water masses at the SoG.

Over the Eastern Mediterranean Basin, with respect to NM12, the upper 400m depths are colder and fresher in NT LR, with maximal differences at 50m depth. The cooling of the water column almost uniquely results from the decrease of background vertical mixing coefficients through the same mechanism as detailed for the Eastern Basin. Regarding salinity, the freshening of the upper 400m depth is mainly related to the decrease of lateral friction (brown lines in Figure A.4), which allows for a substantially larger volume of Western Mediterranean surface water masses to enter the Eastern Basin (see Table A.5). The freshening is further enhanced by the modified vertical mixing, which has a more moderate effect than over the western basin due to the reduced vertical salt stratification. In fact, this effect is partly indirect, resulting from the advection of the freshened Western Mediterranean water masses, as evidenced by the reduced salt inflow toward the Western Mediterranean Basin (Table A.5). Finally, open boundaries, time-splitting, and bottom mixing modification moderately impact the Eastern Mediterranean.

Considering the Mediterranean Sea in its entirety, the various effects previously

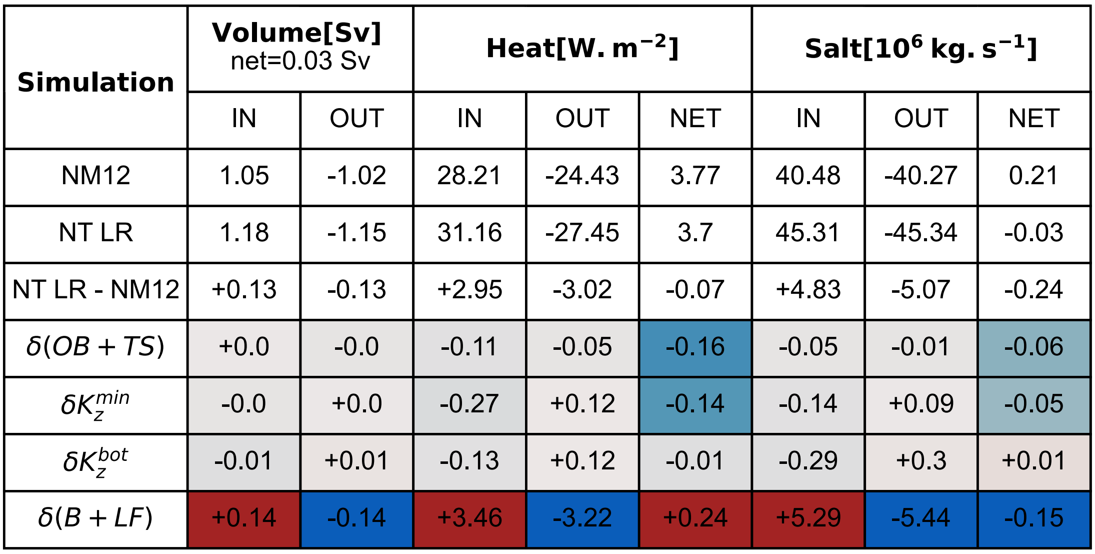

Simulation	**Volume[Sv]** net=0.03 Sv		**Heat[$\mathbf{W.m^{-2}}$]**			**Salt[$\mathbf{10^6\,kg.s^{-1}}$]**		
	IN	OUT	IN	OUT	NET	IN	OUT	NET
NM12	1.05	-1.02	28.21	-24.43	3.77	40.48	-40.27	0.21
NT LR	1.18	-1.15	31.16	-27.45	3.7	45.31	-45.34	-0.03
NT LR - NM12	+0.13	-0.13	+2.95	-3.02	-0.07	+4.83	-5.07	-0.24
$\delta(OB + TS)$	+0.0	-0.0	-0.11	-0.05	-0.16	-0.05	-0.01	-0.06
δK_z^{min}	-0.0	+0.0	-0.27	+0.12	-0.14	-0.14	+0.09	-0.05
δK_z^{bot}	-0.01	+0.01	-0.13	+0.12	-0.01	-0.29	+0.3	+0.01
$\delta(B + LF)$	+0.14	-0.14	+3.46	-3.22	+0.24	+5.29	-5.44	-0.15

Figure A.5: Average volume, heat, and salt transports between the Western and Eastern Mediterranean Basins (Straits of Sicily and Messina). Positive values are oriented toward the Eastern Mediterranean Basin. As in Figure A.1, anomalies between NEMOMED12 and NEMOMEDGIB configuration are decomposed into four components, associated with the main differences between both simulations. Inflowing and outflowing transports are computed from time-step averages of the eastward, westward, southward, and northward velocity components, applying a Heaviside function on each velocity sign. As traditionally done for comparison purposes with surface forcing, we convert the heat flux into an equivalent surface flux over the whole Mediterranean Sea, in W.m^{-2}, considering the Mediterranean area to be $2.5 \cdot 10^{12}$m^2, following Sanchez-Roman et al (2018).

analyzed add up. The resulting vertical profiles, displayed on the lower panels of Figure A.4, highlight that the temperature and salinity differences between NM12 and NT LR mainly result from the modification of vertical mixing, the use of open boundaries, and the modification of lateral friction for salinity.

B Setup of the barotropic experiment

To setup the barotropic simulation, a few modifications have to be carried out on the NEMO source code. We add a new namelist entry, *ln_bdytide_no_u2d*, in the bdytides.F90 module (bdytide_init routine, see Figure A.6). This namelist parameter is then used in the bdydyn2d.F90 module, by the bdy_dyn2d_fla and bdy_ssh routines. Specifically, we modify the bdy_dyn2d_fla routine to force the tangential velocities at the open boundary to be equal to the first interior point (lines 208 and 228 in Figure A.7). In the bdy_ssh routine, we set directly the sea surface elevation to the tidal elevation provided by the forcing files, instead of computing it from both the tidal elevation and velocities (line 303 in FigureA.7). Note that we thus need to provide the forcing data to the bdy_ssh routine (line 280 in FigureA.7). The call to this routine is modified in the rest of the code. To do so, we modify the dyn_spg_ts.F90 and sshwzv.F90 routines to provide the forcing dataset to the bdy_ssh routine (for dyn_spg_ts.F90, we add the “USE bdy_oce” at the beginning of the code in order to include the forcing dataset).

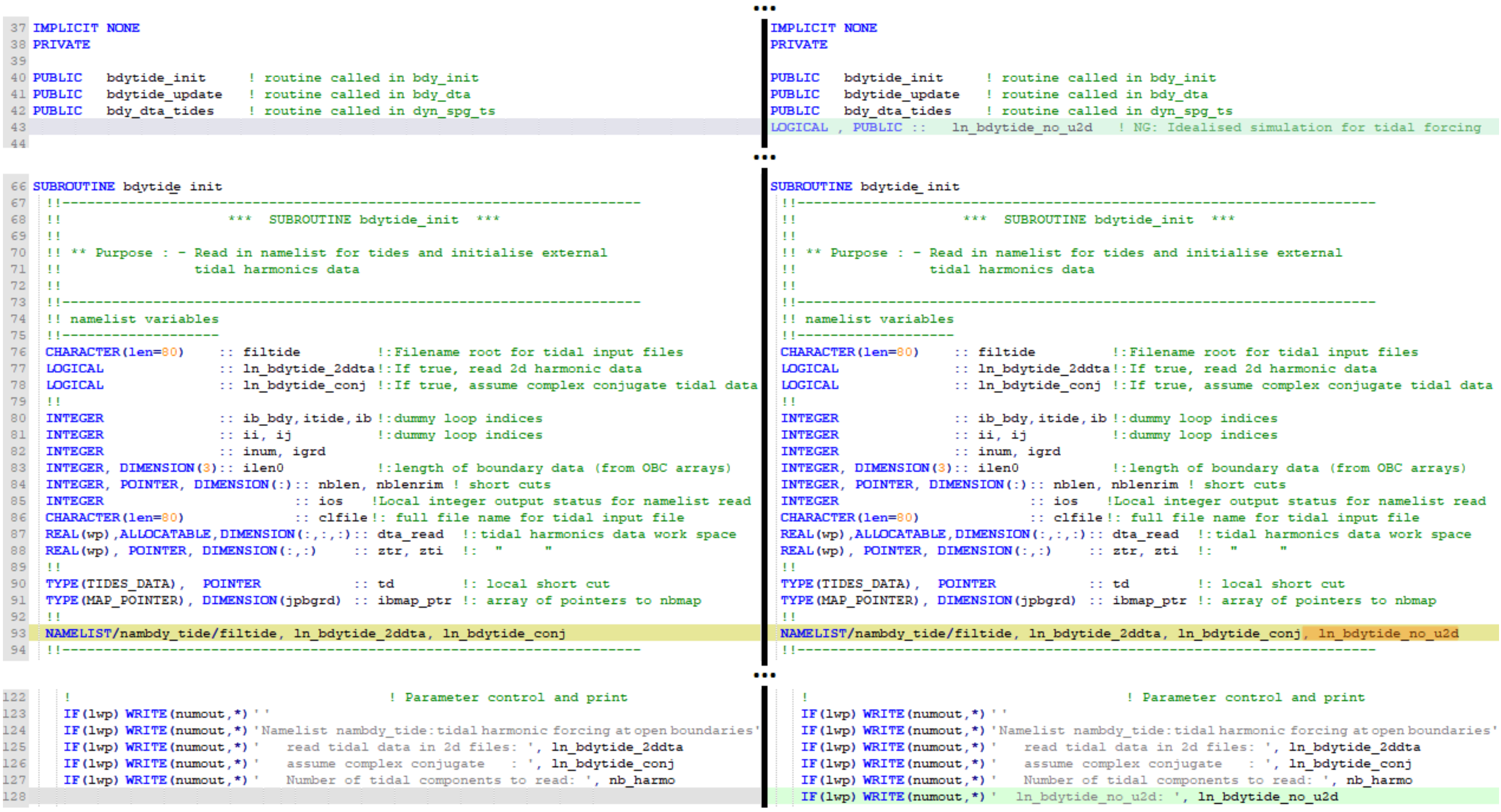

```fortran
...
IMPLICIT NONE
PRIVATE

PUBLIC   bdytide_init     ! routine called in bdy_init
PUBLIC   bdytide_update   ! routine called in bdy_dta
PUBLIC   bdy_dta_tides    ! routine called in dyn_spg_ts


...
SUBROUTINE bdytide_init
  !!----------------------------------------------------------------------
  !!                   ***  SUBROUTINE bdytide_init  ***
  !!
  !! ** Purpose : - Read in namelist for tides and initialise external
  !!                tidal harmonics data
  !!
  !!----------------------------------------------------------------------
  !! namelist variables
  !!-------------------
  CHARACTER(len=80)     :: filtide          !:Filename root for tidal input files
  LOGICAL               :: ln_bdytide_2ddta !:If true, read 2d harmonic data
  LOGICAL               :: ln_bdytide_conj  !:If true, assume complex conjugate tidal data
  !!
  INTEGER               :: ib_bdy, itide, ib !:dummy loop indices
  INTEGER               :: ii, ij           !:dummy loop indices
  INTEGER               :: inum, igrd
  INTEGER, DIMENSION(3):: ilen0             !:length of boundary data (from OBC arrays)
  INTEGER, POINTER, DIMENSION(:):: nblen, nblenrim ! short cuts
  INTEGER                        :: ios    !Local integer output status for namelist read
  CHARACTER(len=80)              :: clfile !: full file name for tidal input file
  REAL(wp),ALLOCATABLE,DIMENSION(:,:,:):: dta_read  !:tidal harmonics data work space
  REAL(wp), POINTER, DIMENSION(:,:)    :: ztr, zti  !:  "     "
  !!
  TYPE(TIDES_DATA),  POINTER           :: td        !: local short cut
  TYPE(MAP_POINTER), DIMENSION(jpbgrd) :: ibmap_ptr !: array of pointers to nbmap
  !!
  NAMELIST/nambdy_tide/filtide, ln_bdytide_2ddta, ln_bdytide_conj
  !!----------------------------------------------------------------------
...
    !                                   ! Parameter control and print
    IF(lwp) WRITE(numout,*) ' '
    IF(lwp) WRITE(numout,*) 'Namelist nambdy_tide:tidal harmonic forcing at open boundaries'
    IF(lwp) WRITE(numout,*) '   read tidal data in 2d files: ', ln_bdytide_2ddta
    IF(lwp) WRITE(numout,*) '   assume complex conjugate   : ', ln_bdytide_conj
    IF(lwp) WRITE(numout,*) '   Number of tidal components to read: ', nb_harmo
```

```fortran
...
IMPLICIT NONE
PRIVATE

PUBLIC   bdytide_init     ! routine called in bdy_init
PUBLIC   bdytide_update   ! routine called in bdy_dta
PUBLIC   bdy_dta_tides    ! routine called in dyn_spg_ts
LOGICAL , PUBLIC ::   ln_bdytide_no_u2d   ! NG: Idealised simulation for tidal forcing
...
SUBROUTINE bdytide_init
  !!----------------------------------------------------------------------
  !!                   ***  SUBROUTINE bdytide_init  ***
  !!
  !! ** Purpose : - Read in namelist for tides and initialise external
  !!                tidal harmonics data
  !!
  !!----------------------------------------------------------------------
  !! namelist variables
  !!-------------------
  CHARACTER(len=80)     :: filtide          !:Filename root for tidal input files
  LOGICAL               :: ln_bdytide_2ddta !:If true, read 2d harmonic data
  LOGICAL               :: ln_bdytide_conj  !:If true, assume complex conjugate tidal data
  !!
  INTEGER               :: ib_bdy, itide, ib !:dummy loop indices
  INTEGER               :: ii, ij           !:dummy loop indices
  INTEGER               :: inum, igrd
  INTEGER, DIMENSION(3):: ilen0             !:length of boundary data (from OBC arrays)
  INTEGER, POINTER, DIMENSION(:):: nblen, nblenrim ! short cuts
  INTEGER                        :: ios    !Local integer output status for namelist read
  CHARACTER(len=80)              :: clfile !: full file name for tidal input file
  REAL(wp),ALLOCATABLE,DIMENSION(:,:,:):: dta_read  !:tidal harmonics data work space
  REAL(wp), POINTER, DIMENSION(:,:)    :: ztr, zti  !:  "     "
  !!
  TYPE(TIDES_DATA),  POINTER           :: td        !: local short cut
  TYPE(MAP_POINTER), DIMENSION(jpbgrd) :: ibmap_ptr !: array of pointers to nbmap
  !!
  NAMELIST/nambdy_tide/filtide, ln_bdytide_2ddta, ln_bdytide_conj, ln_bdytide_no_u2d
  !!----------------------------------------------------------------------
...
    !                                   ! Parameter control and print
    IF(lwp) WRITE(numout,*) ' '
    IF(lwp) WRITE(numout,*) 'Namelist nambdy_tide:tidal harmonic forcing at open boundaries'
    IF(lwp) WRITE(numout,*) '   read tidal data in 2d files: ', ln_bdytide_2ddta
    IF(lwp) WRITE(numout,*) '   assume complex conjugate   : ', ln_bdytide_conj
    IF(lwp) WRITE(numout,*) '   Number of tidal components to read: ', nb_harmo
    IF(lwp) WRITE(numout,*) '  ln_bdytide_no_u2d: ', ln_bdytide_no_u2d
```

Figure A.6: Modifications performed on bdytides.F90 module for the barotropic experiment setup. Added lines are highlighted in green, modified in yellow and modifications in orange.

```
•••
USE dynspg_oce      ! for barotropic variables





USE phycst          ! physical constants
•••
 REAL(wp), DIMENSION(:,:), INTENT(inout) :: pua2d, pva2d
 REAL(wp), DIMENSION(:,:), INTENT(in) ::   pssh, phur, phvr

 INTEGER  ::   jb, igrd                         ! dummy loop indices
 INTEGER  ::   ii, ij, iiml, iipl, ijml, ijpl   ! 2D addresses
•••
 DO jb = 1, idx%nblenrim(igrd)
    ii  = idx%nbi(jb,igrd)
    ij  = idx%nbj(jb,igrd)
    flagu => idx%flagu(jb,igrd)

    iiml = ii + MAX( 0, INT( flagu ) )   ! T pts i-indice inside the boundary
    iipl = ii - MIN( 0, INT( flagu ) )   ! T pts i-indice outside the boundary
    !
    zcorr = - flagu * SQRT( grav * phur(ii, ij) )*(pssh(iiml, ij)-spgu(iipl,ij))

    ! jchanut tschanges: Set zflag to 0 below to revert to Flather scheme
    ! Use characteristics method instead
    zflag = ABS(flagu)

    zforc = dta%u2d(jb) * (1._wp - zl_2*zflag) + zl_2 * zflag * pua2d(iiml,ij)
    pua2d(ii,ij) = zforc + (1._wp - zl_2*zflag) * zcorr * umask(ii,ij,1)






 END DO
 igrd = 3       ! Flather bc on v-velocity
 !              ! remember that flagv=-1 if normal velocity direction is outward
 DO jb = 1, idx%nblenrim(igrd)
•••
    ! jchanut tschanges: Set zflag to 0 below to revert to std Flather scheme
    ! Use characteristics method instead
    zflag = ABS(flagv)

    zforc  = dta%v2d(jb) * (1._wp - zl_2*zflag) + zl_2 * zflag * pva2d(ii,ijml)
    pva2d(ii,ij) = zforc + (1._wp - zl_2*zflag) * zcorr * vmask(ii,ij,1)
•••
SUBROUTINE bdy_ssh( zssh )
•••

 REAL(wp), DIMENSION(:,:), INTENT(inout) ::   zssh ! Sea level
 !!
 INTEGER  ::   ib_bdy, ib, igrd                        ! local integers
 INTEGER  ::   ii, ij, zcoef, ip, jp   !   "         "

 igrd = 1                        ! Everything is at T-points here

 DO ib_bdy = 1, nb_bdy
   DO ib = 1, idx_bdy(ib_bdy)%nblenrim(igrd)
    ii = idx_bdy(ib_bdy)%nbi(ib,igrd)
    ij = idx_bdy(ib_bdy)%nbj(ib,igrd)
    ! Set gradient direction:
    zcoef=bdytmask(ii-1,ij)+bdytmask(ii+1,ij)+bdytmask(ii,ij-1)+bdytmask(ii,ij+1)
    IF ( zcoef == 0 ) THEN
       zssh(ii,ij) = 0._wp
    ELSE





          ip = bdytmask(ii+1,ij   ) - bdytmask(ii-1,ij   )
          jp = bdytmask(ii   ,ij+1) - bdytmask(ii   ,ij-1)
          zssh(ii,ij) = zssh(ii+ip,ij+jp) * tmask(ii+ip,ij+jp,1)

       ENDIF
    END DO
```

```
•••
USE dynspg_oce      ! for barotropic variables

#if defined key_tide
USE tideini
USE bdytides   , ONLY : ln_bdytide_no_u2d
#endif
USE phycst          ! physical constants
•••
 REAL(wp), DIMENSION(:,:), INTENT(inout) :: pua2d, pva2d
 REAL(wp), DIMENSION(:,:), INTENT(in) ::   pssh, phur, phvr

 INTEGER  ::   jb, igrd, iuint, jvint           ! dummy loop indices
 INTEGER  ::   ii, ij, iiml, iipl, ijml, ijpl   ! 2D addresses
•••
 DO jb = 1, idx%nblenrim(igrd)
    ii  = idx%nbi(jb,igrd)
    ij  = idx%nbj(jb,igrd)
    flagu => idx%flagu(jb,igrd)
    IF (.NOT. ln_bdytide_no_u2d) THEN
       iiml = ii + MAX( 0, INT( flagu ) )   ! T pts i-indice inside the boundary
       iipl = ii - MIN( 0, INT( flagu ) )   ! T pts i-indice outside the boundary
       !
       zcorr = - flagu * SQRT( grav * phur(ii, ij) ) * (pssh(iiml, ij)-spgu(iipl,ij))

       ! jchanut tschanges: Set zflag to 0 below to revert to Flather scheme
       ! Use characteristics method instead
       zflag = ABS(flagu)
       iuint = ii+INT(flagu)
       zforc = dta%u2d(jb) * (1._wp - zl_2*zflag) + zl_2 * zflag * pua2d(iuint, ij)
       pua2d(ii,ij) = zforc + (1._wp - zl_2*zflag) * zcorr * umask(ii,ij,1)
    ELSE
       IF (flagu == 0 ) THEN
          !juint = ij+1
          pua2d(ii,ij) = pua2d(ii, ij+1) !juint
       ENDIF
    ENDIF
 END DO
 igrd = 3       ! Flather bc on v-velocity
 !              ! remember that flagv=-1 if normal velocity direction is outward
 DO jb = 1, idx%nblenrim(igrd)
•••
    ! jchanut tschanges: Set zflag to 0 below to revert to std Flather scheme
    ! Use characteristics method instead
    zflag = ABS(flagv)
    jvint = ij+INT(flagv)
    zforc  = dta%v2d(jb) * (1._wp - zl_2*zflag) + zl_2 * zflag * pva2d(ii, jvint)
    pva2d(ii,ij) = zforc + (1._wp - zl_2*zflag) * zcorr * vmask(ii,ij,1)
•••
SUBROUTINE bdy_ssh( zssh, dta )
•••
 TYPE(OBC_DATA) , DIMENSION(jp_bdy), TARGET      ::   dta
 REAL(wp), DIMENSION(:,:), INTENT(inout) ::   zssh ! Sea level
 !!
 INTEGER  ::   ib_bdy, ib, igrd                        ! local integers
 INTEGER  ::   ii, ij, zcoef, ip, jp   !   "         "

 igrd = 1                        ! Everything is at T-points here

 DO ib_bdy = 1, nb_bdy
   DO ib = 1, idx_bdy(ib_bdy)%nblenrim(igrd)
      ii = idx_bdy(ib_bdy)%nbi(ib,igrd)
      ij = idx_bdy(ib_bdy)%nbj(ib,igrd)
      IF (ln_bdytide_no_u2d) THEN


         zssh(ii,ij) = dta(ib_bdy)%ssh(ib)
      ELSE
        ! Set gradient direction:
        zcoef=bdytmask(ii-1,ij)+bdytmask(ii+1,ij)+bdytmask(ii,ij-1)+bdytmask(ii,ij+1)
        IF ( zcoef == 0 ) THEN
           zssh(ii,ij) = 0._wp
         ELSE
            ip = bdytmask(ii+1,ij   ) - bdytmask(ii-1,ij   )
            jp = bdytmask(ii   ,ij+1) - bdytmask(ii   ,ij-1)
            zssh(ii,ij) = zssh(ii+ip,ij+jp) * tmask(ii+ip,ij+jp,1)
         ENDIF
       ENDIF
    END DO
```

Figure A.7: Modifications performed on the bdy_dyn_2d.F90 module for the barotropic experiment setup. Added lines are highlighted in green, deleted lines in red, modified lines in yellow and modification in orange. Some lines may be interpreted as deleted, but are only displaced.

Chapter 3

Understanding tidal mixing at the Strait of Gibraltar: a high-resolution model approach

N. Gonzalez, R. Waldman, G. Sannino, H. Giordani, S. Somot

This chapter is a published article in *Progress in Oceanography* (`https://doi.org/10.1016/j.pocean.2023.102980`). I did not modify the corpus here. The organisation is the same, with the appendices and supplementary material at the end of the chapter. I have simply modified the layout such that it stays coherent with the rest of the document. Some elements of the introduction and methodology section can be redundant with the previous chapters.

Résumé en Français

Ce chapitre vise à étudier le mélange diapycnal induit par les courants de marée au détroit de Gibraltar (mélange de marée ci-après), un mécanisme contrôlant les transformations de masses d'eau au travers du détroit. À cette fin, nous étudions le mélange de marée représenté par deux simulations annuelles, différant seulement par l'inclusion ou l'omission de courants de marée. Ces simulations sont réalisées à partir d'une configuration régionale du modèle numérique tridimensionnel MITgcm, utilisant une haute résolution spatiale autour du détroit de Gibraltar (1/200°, 100 niveaux verticaux). Spécifiquement, nous étudions le mélange diapyncal simulé au travers du schéma de fermeture de la turbulence du modèle, basé sur un bilan d'énergie cinétique turbulente.

En accord avec la littérature, nous trouvons que les marées intensifient le mélange diapycnal et l'advection verticale au détroit. Nous démontrons ensuite que ce mélange repose sur deux ingrédients principaux : un cisaillement vertical intense des courants horizontaux et un affaiblissement local de la stratification. Dans la couche Méditerranéenne, le premier mécanisme contrôle le mélange près du plancher océanique alors que second contrôle le mélange dans des zones moins profondes, particulièrement au-dessus des seuils du Camarinal et d'Espartel. Dans la couche Atlantique, les deux mécanismes sont impliqués dans le mélange diapycnal, qui se développe le long de le sillage d'une onde interne générée au seuil de Camarinal, advectée vers la Méditerranée. À haute fréquence, l'affaiblissement local de la stratification résulte de la création de zones de convergence et divergence, qui alimentent des cellules de recirculation entre les couches Atlantiques et Méditerranéenne. De plus, nous soulignons que le mélange diapycnal se développe principalement dans la couche Méditerranéenne pendant la phase de marée descendante et dans la couche Atlantique pendant la phase de marée montante.

Nous concluons en proposant un schéma conceptuel du mélange de marée au détroit de Gibraltar, où les cellules de recirculation induites par la marée jouent un rôle prépondérant dans la transformation des masses d'eau échangées. De manière plus générale, cette étude souligne la pertinence d'une représentation réaliste des marées et de la topographie pour simuler les échanges au détroit de Gibraltar et plaide pour l'utilisation de paramétrisations lorsque cela n'est pas possible.

3.1 Introduction

The Strait of Gibraltar (SoG hereinafter, illustrated in Figure 3.1) is a narrow and shallow channel, about 15km wide at its narrowest point and 300m deep at its shallowest sill of Camarinal (CS hereinafter). It is the main connection between the Mediterranean Sea and the open Ocean. Along this approximately 60km long pathway, in the upper $\sim$ 150m depth, warmer and fresher Atlantic waters are advected into the Mediterranean Basin, whereas underneath, colder and saltier Mediterranean waters are exported to the Atlantic Ocean. This two-way exchange closes the Mediterranean Basin heat and water budgets, which, at the surface, are in deficit of 4.5 ± 4.1W.m^{-2} and 0.5 ± 0.2m of annual equivalent sea level, respectively (Jordà et al, 2017b). Besides the thermohaline budget, the water exchange at the SoG is also essential for the biogeochemical balance of the basin (Huertas et al, 2012b), as the Atlantic inflow is one of the primary nutrient sources for the Mediterranean Sea (Ramírez-Romero et al, 2014).

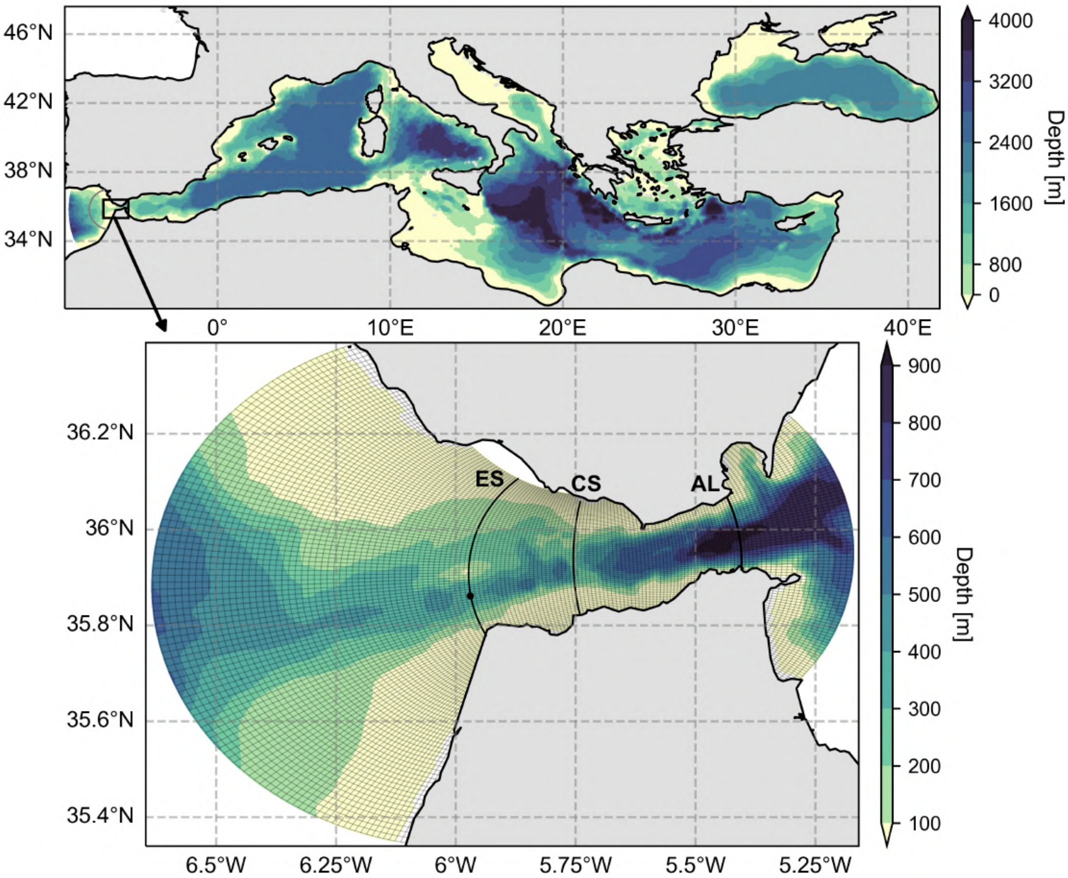

Figure 3.1: MITgcm model bathymetry (upper panel) and zoom on the grid and bathymetry at the SoG (lower panel). The gray line in the upper panel displays the end of the model western boundary relaxation zone. In the lower panel, meridional sections "ES", "CS", and"AL", displayed in black, refer to the Espartel Sill, the Camarinal Sill, and the entrance of the Alboran Sea, respectively. The black dot on the ES section indicates the velocity profile measurement station (INGRES project Sammartino et al, 2015).

Great levels of tidal energy further characterize the SoG. By interacting with ocean stratification and rough topography, tides give rise to various non-linear processes and unique mechanisms, which motivated observation campaigns in the 1980s and 1990s. At several locations across the strait, tidal currents and channel shrinkage were found to submit the flow to hydraulic control (Farmer and Armi, 1985; Farmer et al, 1988). These control points modulate the size of the volume exchanges (Bryden and Stommel, 1984) and release large internal waves, mainly toward the Mediterranean Sea (Lacombe and Richez, 1982; Wesson and Gregg, 1988; Pettigrew and Hyde, 1990), but also toward the Atlantic Ocean (Farmer et al, 1988), and across the strait (Watson and Robinson, 1990; Richez, 1994). During the Gibraltar Experiment (Bryden and Kinder, 1986), turbulence observations evidenced intense diapycnal mixing on both sides of the CS and along the trail of the eastward internal bore released at the CS (Wesson and Gregg, 1988, 1994). In addition, cross-strait hydrographic sections allowed oceanographers to examine the interface between Atlantic and Mediterranean water masses and to describe it as a distinct layer. This intermediate layer, resulting from the intense tidal mixing occurring within the strait, is advected toward the Mediterranean Sea east of the CS and toward the Atlantic Ocean west of the CS (Bray et al, 1995). It motivates the characterization of exchanges through the strait as a three-layer flow rather than an idealized two-layer flow.

More recently, high-resolution simulations using realistic physical forcing have emerged (Sannino et al, 2004, 2007; Sanchez-Garrido et al, 2011; García Lafuente et al, 2013; Sannino et al, 2014; Sanchez-Roman et al, 2018; Álvarez et al, 2019), allowing ocean modelers to reproduce and analyze in detail the main characteristics of the exchange flow through the SoG. While the eastward barotropic tide deepens and thickens the interface layer separating the Atlantic inflow from the Mediterranean outflow, the westward barotropic tide uplifts and shoals it, powering a periodic oscillation of the stratification and driving entrainment between both layers (Sannino et al, 2007; García Lafuente et al, 2013). At the CS, the interface sinking is accompanied by the relaxation of a hydraulic control point previously formed by the westward tidal currents. This hydraulic transition releases large-amplitude internal waves toward the Mediterranean Sea and produces an intense turbulent mixing (Brandt et al, 1996; Vázquez et al, 2006; Vlasenko et al, 2009; Sánchez-Román et al, 2012; García Lafuente et al, 2013; Hilt et al, 2020). Significant temperature and salinity anomalies result from this tide-induced dynamic and mixing, cooling, and saltening by up to 1°C and 0.5 psu the inflowing Atlantic water (Sannino et al, 2015).

On a larger scale, tidal influence at the SoG impacts the Mediterranean basin-scale heat and salt budgets. By acting simultaneously on currents and thermohaline properties, tides were found to increase the net salt transport through the strait by 25% and decrease the net heat transport by 10% (Sanchez-Roman et al, 2018, Table 4 and 6). In the western Mediterranean Basin, the significant transformation of the Atlantic inflow by tidal mixing has been shown to affect the production of deep waters (Naranjo et al, 2014; Sannino et al, 2015). Over long periods (50-year simulations), Harzallah et al (2014) reported that tides induce a general cooling (0.08°C) and saltening (0.012 psu) of the Mediterranean Sea, mainly in the upper 150m depth. In the context of global warming scenario simulations, it is essential to accurately model the SoG, which can be considered as a heat and salt anomaly filter between the Atlantic Ocean and the Mediterranean Sea (Potter and Lozier, 2004; Somot et al, 2006; Soto-Navarro et al, 2020; Parras-Berrocal et al, 2022), as well as a variable nutrient source for the Mediterranean Sea (Richon et al, 2019).

Thus, both observational and numerical studies have stressed the key role of tides in the exchanges at the SoG. However, although some aspects of tidal mixing have already been highlighted, such as variability (Wesson and Gregg, 1994; Macias et al, 2006), connection to internal waves (Wesson and Gregg, 1988; Pettigrew and Hyde, 1990; Send and Baschek, 2001; Vázquez et al, 2006) and convergence patterns within the strait (Bruno et al, 2013), the detailed mechanisms driving it remain unclear. In the literature, tidal mixing is often related to either hydraulic transitions, intensification of the vertical shear of horizontal currents, or both (Wesson and Gregg, 1994; Sannino et al, 2009a; Sanchez-Garrido et al, 2011; García Lafuente et al, 2013), but no study has allowed delineating the respective importance of these phenomena throughout the strait. Other than improving our understanding of the physical mechanisms at stake at the SoG, a more extensive appreciation of tidal mixing is needed in numerical models. It would allow the development of valid alternatives to high-resolution and explicit tidal forcing at the SoG, which are often renounced in regional models of the Mediterranean Sea (Harzallah et al, 2014; Soto-Navarro et al, 2015; Sannino et al, 2015; Harzallah et al, 2018; Llasses et al, 2018; Soto-Navarro et al, 2020) because of the challenges and numerical cost associated with these developments. Recently, tidal mixing parameterizations have been developed for models that do not explicitly resolve tidal currents (de Lavergne et al, 2020). However, significant uncertainties result from the complex cascade of tidal energy to dissipation scales (Osborn, 1980; Jackson and Rehmann, 2014; Bouffard and Boegman, 2013; de Lavergne et al, 2016).

Therefore, the present work addresses the need for a deeper understanding of tidal mixing at the SoG. To this end, we analyze the processes driving turbulent mixing in ocean simulations of the Mediterranean Sea, including or not an explicit tide. Among the currently available numerical tools, we use a non-hydrostatic kilometric model resolution, which allows a faithful 3D representation of the exchange flow through the SoG and the largest internal waves at work (Sannino et al, 2014; Álvarez et al, 2019; Hilt et al, 2020). We consider that it provides an adequate framework to study the main mechanisms driving diapycnal mixing within the strait. In section 2, we introduce the model, simulations, and analysis frameworks. In section 3, we present the model validation, we characterize the effect of tides on diapycnal mixing, and we explain how it relates to tidal circulation patterns within the strait. Finally, we draw the main conclusions and discuss our results in section 4.

3.2 Model and methods

3.2.1 Model description

We use a numerical model based on the three-dimensional z-coordinate Massachusetts Institute of Technology general circulation model (MITgcm; Marshall et al, 1997a,b) adapted to the Mediterranean region. The model solves the fully non-linear hydrostatic Navier–Stokes equations under the Boussinesq approximation using a spatial finite-volume discretization. It is run with partial step topography, rescaled vertical height (z*) coordinate (Adcroft (Adcroft et al, 1997), with an implicit non-linear surface based on Campin et al (2004). The source code and documentation are available at the following website: https://github.com/MITgcm/MITgcm (last access: 10 October 2022).

The model domain extends over the whole Mediterranean Sea and part of the Atlantic Ocean. The horizontal grid is a non-uniform and curvilinear Arakawa-C grid composed of 1040 × 320 points, reaching a resolution of approximately 1/200° × 1/200° ($\sim$ 500m) at the SoG (Figure 3.1) and the Bosphorus Strait, and 1/50° × 1/50° ($\sim$ 2km) at the Straits of Dardanelles. It is smoothly degraded down to a regular 1/16° × 1/16° grid ($\sim$ 6km) in the Mediterranean Sea. The vertical grid comprises 100 unevenly spaced z*-levels, rescaled as suggested by Adcroft and Campin (2004). The (vertical) cell thicknesses vary between 2m at the top to 100m at the bottom. We use a time step of 20 seconds.

Three datasets compose the bathymetry: the European Marine Observation and Data Network (EMODnet) 2016 dataset (https://www. emodnet-bathymetry.eu) for the Mediterranean Basin and the Black Sea, the very high-resolution digitalized chart of Sanz et al (1991) for the SoG, and a high-resolution bathymetry for the Bosphorus and Dardanelles Straits made available by Erkan Gökaşan (Gökaşan et al, 2005, 2007), with the permission of the Turkish Navy, Navigation, Hydrography, and Oceanography Office. The datasets were combined through a bilinear interpolation on the computational grid. In addition, a handmade check has been made for isolated points, islands, and narrow passages (see Sannino et al, 2015, 2017).

We use a third-order direct space-time flux-limited advection scheme for tracers (temperature, salinity), with a constant horizontal Laplacian diffusivity coefficient of $2\text{m}^2.\text{s}^{-1}$. The vertical eddy viscosity and diffusivity coefficients are computed from the 1.5 order Turbulent Kinetic Energy (TKE) closure scheme (Gaspar et al, 1990), adapted from the atmospheric case developed by Bougeault and Lacarrere (1989). The TKE scheme was chosen for its straightforward physical interpretation and its few parameters to configure. We set the background vertical eddy viscosity and diffusivity coefficients to their molecular values of $1.5 \cdot 10^{-6}\text{m}^2.\text{s}^{-1}$ and $10^{-7}\text{m}^2.\text{s}^{-1}$ for momentum and tracers, respectively. We impose a maximal diffusivity of $100\text{m}^2.\text{s}^{-1}$ to avoid the use of an enhanced diapycnal mixing parameterization of convection. At the lateral and bottom solid boundaries, we use no-slip conditions along with a quadratic bottom drag. The latter is calculated as a function of the velocity near the bottom, with a dimensionless coefficient of $2.5 \cdot 10^{-3}$.

3.2.2 Numerical simulations

We focus on two hindcast numerical simulations, differing only by the inclusion (ExpT) or omission (ExpNT) of tidal forcing. The simulations are initialized with the MEDHYMAP climatology (Jordà et al, 2017b) in August 1980 and run until December 31^{st} 1981.

The simulations are forced with a modified ORAS4 climatology at the Atlantic open boundary through a 3D relaxation of salinity and temperature. The relaxation time varies linearly from 2 hours at the western limit of the domain to 30 days over the first 30 grid points (gray line in the upper panel of Figure 3.1). Over the rest of the domain, the river runoff discharge is obtained according to Struglia et al (2004) for the 68 main catchments and applied in conjunction with the non-linear free surface numerical scheme, see Sannino et al (2015). The surface forcing is derived from dynamically downscaled regional atmospheric fields, produced by the Rossby Centre regional atmospheric model RCA4 (Strandberg et al, 2014), at 0.11° resolution ($\sim$ 11km). The downscaling is performed over the EURO-CORDEX domain (Giorgi et al, 2009) with boundary conditions provided by the ERA-Interim reanalysis. Three-hourly shortwave radiation and cloud cover are directly extracted from the atmospheric model, while long-wave radiation is computed following the parameterization of Bignami et al (1995). Three-hourly latent heat flux and sensible heat flux, and six-hourly wind stress are calculated according to the bulk formula of Large and Yeager (2004). Evaporation is computed from the latent heat. The net freshwater flux is prescribed from the net balance of evaporation, precipitation (taken from the atmospheric model), and river discharge. The model is also forced with atmospheric pressure, taken from the atmospheric model.

The explicit tidal forcing used in ExpT is the same as in Palma et al (2020). It includes an equilibrium tide, acting as a potential in the momentum equations, and the Atlantic tide propagating from the western open boundary, where it is prescribed as an open boundary condition on the dynamic sea level. The equilibrium tide is composed of four tidal components : M2, O1, S2, K1, namely, the semidiurnal and diurnal principal lunar tides, the principal semidiurnal solar tide, and diurnal lunisolar declination tide. The tidal values used to prescribe the Atlantic tide are derived from the Oregon State University Tidal inversion software (OTIS hereinafter, Egbert and Erofeeva, 2002). In ExpNT, the equilibrium and Atlantic tides are removed.

For both ExpT and ExpNT, the first five months of simulation (01/08/1980 – 31/12/1980) are used as a spin-up for the exchange flow through the SoG to reach a steady state. At the end of the spin-up phase, we diagnose the drift of temperature and salinity over the domain defined in Figure 3.1 in three specific layers: the Atlantic layer (58m – 163m), the upper Mediterranean layer (163m – 371m) and the lower Mediterranean layer (371m – 670m). To do so, we fit an exponential decay to the temperature and salinity drift in each layer, and we determine their e-folding time. We find e-folding times between 20 – 40 days so that at the end of the five-month spin-up period, over 98% of the drift has occurred.

In the following, we use hourly-averaged outputs over January 1981 to perform a detailed analysis of the tidal mixing throughout a tidal cycle and yearly-averaged outputs over 1981 for an annual mean analysis. We consider that one year of simulation is sufficient to study diapycnal mixing at the SoG because the interannual variability of the transports through the strait is low compared to the tidal and subinertial variability (Boutov et al, 2014; Sanchez-Roman et al, 2018, Figures 3 and 4).

3.2.3 Definition of volume, heat, and salt transport at the SoG

We define the transports through the SoG in the framework of a two-way exchange flow between the Mediterranean Sea and the Atlantic Ocean. Net volume, heat, and salt transports are computed by integrating the currents, heat, and salt fluxes over a section of interest:

$$\begin{aligned}
\overline{Q_{net}}(x) &= \int_{South}^{North} \int_{bottom}^{\eta} \overline{u}\, dzdy \\
\overline{QH_{net}}(x) &= \int_{South}^{North} \int_{bottom}^{\eta} \rho_0 C_w \overline{u\theta}\, dzdy \\
\overline{QS_{net}}(x) &= \int_{South}^{North} \int_{bottom}^{\eta} \overline{uS}\, dzdy
\end{aligned} \tag{3.1}$$

With η the sea surface elevation, u the velocity normal to the section, $\rho_0 = 1025\text{kg.m}^{-3}$ a reference sea water density, $C_w = 3850\ J\,kg^{-1}\,{}^{\circ}C^{-1}$ the specific heat of seawater, θ the potential temperature and S the practical salinity of seawater (as defined in the modified UNESCO formula by Jackett and Mcdougall, 1995). The overline denotes the time-average operator. Second-order terms (product of velocity with salinity or temperature) are averaged at the model time step.

Eastward and westward transports (hereinafter referred to as inflow and outflow, respectively) are more complex to estimate as they require distinguishing the two flows at high-frequency. Several definitions of the inflowing Atlantic and outflowing Mediterranean layers have been used in the literature. In this study, we will use two different definitions, the first one to validate the simulated transports against observational-based estimates and the second to depict the full extent of the tidal influence on the water masses dynamic.

To validate the simulated transports, we follow the framework used by Sammartino et al (2015) to estimate of the Mediterranean outflow. In this way, we define the interface between inflowing and outflowing waters as the isohaline that maximizes the outflowing volume transport (Sammartino et al, 2015, section 7.3). Due to the large amount of data required to perform this computation at high-frequency, the inflowing and outflowing transports are computed from hourly-averaged outputs over the same period as for the detailed analysis of tidal mixing, that is, January 1981. We address the uncertainty related to the time coverage of the resulting estimates in section 3. We calculate the inflows at the entrance of the Alboran Sea (AL section, see Figure 3.1) and outflows at the Espartel Sill (ES section), where their estimation is more robust (Jordà et al, 2017b). Under this specific benchmark, we find the isohaline that maximizes the outflow to be 36.6 psu, close to the value used in (Sammartino et al, 2015; Naranjo et al, 2014), and the isohaline that maximizes the inflow to be 37.8 psu, close to the values used in (Lafuente et al, 2000; Baschek et al, 2001; Vargas et al, 2006).

To fully account for the advective properties of tides on the transports through the SoG, we refer to the framework introduced in Sanchez-Roman et al (2018). The affiliation of a cell to a flow or the other is determined only by the sign of its pseudo-zonal velocity (model grid-oriented). In this way, we compute the inflow and outflow transports by integrating the velocities of the water masses flowing in each direction:

$$\begin{aligned} Q_{in}^{max}(x,t) &= \int_{South}^{North} \int_{bottom}^{\eta} u\, H(u)\, (x,y,z,t)\, dzdy \\ Q_{out}^{max}(x,t) &= \int_{South}^{North} \int_{bottom}^{\eta} u\, H(-u)\, (x,y,z,t)\, dzdy \end{aligned} \tag{3.2}$$

With H the Heaviside step function ; $H(u) = 1$ if $u > 0$; $H(u) = 0$ otherwise. The main difference with the previous definition is that water masses from a given layer consistently flow in the same direction. Indeed, this may not be the case with the halocline interface, which allows a form of transport compensation due to the occasional presence of counter-flowing water masses in each layer. Q_{in}^{max} and Q_{out}^{max} may be considered as maximal estimates of the transport through the SoG. Note that we compute these estimates at the simulations time-step to avoid transports compensations from averaging opposite velocities.

3.2.4 Theoretical framework: TKE turbulent closure scheme

In a numerical model, diapycnal mixing occurs explicitly through horizontal and vertical mixing parameterizations and implicitly due to numerical discretization errors. We assume the latter source of mixing to be weak at the SoG in our simulations because of the high resolution. We have also estimated horizontal mixing using the constant horizontal Laplacian diffusivity coefficient and hourly-averaged outputs of temperature and salinity over January 1981. We found it to be, on average, five times weaker than its vertical counterpart (not shown). Therefore, we will henceforth focus on explicit vertical mixing, parameterized using vertical eddy diffusivity and viscosity coefficients (K_t and K_m, respectively), representing passive tracers and momentum diffusion by unresolved eddies. Following the mixing length theory (Prandtl, 1949), these coefficients are expressed as the product of a turbulent velocity deduced from the squared root of the TKE, a mixing length, and a mixing efficiency coefficient as follows:

$$K_m = K_t P_{rt} = c_k\, l_k\, \mathrm{TKE}^{1/2} \tag{3.3}$$

With :

- c_k The mixing coefficient, controlling the efficiency of turbulent mixing. Following Gaspar et al (1990), $c_k = 0.1$.

- l_k The characteristic mixing length scale. Following Gaspar et al (1990), $l_k = \max(10^{-9}, \min(l_u, l_d))$. l_u and l_d are introduced in Bougeault and Andre (1986), they can be interpreted as the unresolved eddies size in the upward and downward directions. In our model configuration, for a given cell, $l_u = l_d = l = \sqrt{2}\mathrm{TKE}^{1/2}N^{-1}$ as long as l does not exceed the cell thickness. Once that threshold is exceeded, $l_u = l_u^{max} \neq l_d = l_d^{max}$, where l_u^{max} and l_d^{max} depend on the upper and lower tracer cell thickness.

- P_{rt} The Prandtl number, quantifying the ratio between momentum and tracer diffusivity. $P_{rt} = \min\left(\max(1, 5R_i), 10\right)$, with R_i the bulk Richardson number that measures the ratio between the TKE destruction by stratification and its production by the vertical shear of horizontal currents. $R_i = \frac{N^2}{(\partial_z u)^2 + (\partial_z v)^2}$, where N is the Brunt-Väisälä frequency and ∂_z the partial derivative operator associated to the vertical axis.

Vertical mixing is thus defined through the TKE by the 1.5 order TKE closure scheme. This scheme resolves the TKE tendency under the assumption of horizontal homogeneity, using the dissipation parameterization of Kolmogorov (1942). It follows:

$$\begin{aligned}\partial_t \mathrm{TKE} = \underbrace{\partial_z(K_m\,\partial_z \mathrm{TKE})}_{\text{turbulent transport } T} + \underbrace{K_m\left[(\partial_z u)^2 + (\partial_z v)^2\right]}_{\text{dynamic shear production } S} \\ - \underbrace{K_t N^2}_{\text{buoyancy flux } B} - \underbrace{\frac{c_\epsilon \mathrm{TKE}^{3/2}}{l_\epsilon}}_{\text{dissipation } \epsilon}\end{aligned} \tag{3.4}$$

Where l_ϵ is the TKE characteristic dissipation length and c_ϵ an associated dissipation coefficient. Following Gaspar et al (1990): $l_\epsilon = \max(10^{-9}, \sqrt{l_u l_d})$ and $c_\epsilon = 0.7$. The four contributions to the TKE tendency are:

- The turbulent transport T (computed implicitly). Under the assumption of horizontal homogeneity, it represents only the convergence or divergence of the TKE vertical flux, which is parameterized using the concept of eddy diffusivity.

- The dynamic shear production S. It is always a source of TKE. Its contribution to the TKE tendency relies on the vertical eddy viscosity coefficient (inherited from the parameterization of the turbulent horizontal momentum vertical flux) and the vertical shear of horizontal velocities. On a climatological scale, S is the main source of TKE.

- The buoyancy flux B. It represents the TKE destruction (production) by the positive (negative) stratification. B also gives an estimate of diapycnal mixing as the vertical mixing tendency of tracers is equal to its convergence or divergence.

- The TKE dissipation ϵ (computed implicitly). It is always a sink of TKE. It represents the TKE destruction by molecular viscosity and is parameterized according to Kolmogorov (1942). On a climatological scale, ϵ is the main sink of TKE.

This study will mainly focus on the dynamic shear production, directly impacted by tidal forcing through vertical shear intensification or reduction. Special attention will also be paid to the buoyancy flux as a proxy for diapycnal mixing and for its ability to produce TKE in the presence of negative stratification. Note that the terms computed implicitly cannot be separated. They will be analyzed as one and referred to as the implicit TKE tendency: $I = T - \epsilon$.

3.3 Results

3.3.1 Model Validation

The tidal forcing used in ExpT has been validated over the Mediterranean Sea by Palma et al (2020) and Sannino et al (2015) with similar model configurations. The authors performed a one-year simulation with a barotropic version of the model and separated the tidal constituents through a harmonic analysis of the surface elevation (Foreman, 1977; Pawlowicz et al, 2002). The amplitude and phase of the modeled tides were validated against the OTIS global tide inverse model, and the simulation correctly reproduced the main zero amplitude points for the M2 tidal component in the Mediterranean Sea (Tsimplis et al, 1995). Palma et al (2020) also validated the tidal forcing against maps from more recent tidal simulations (Ferrarin et al, 2018). In this study, we carry out further validations specific to the SoG by comparing the simulated tides to reference tidal models and observations, as well as transports and velocities against observational estimates and datasets. Regarding transports and velocities, when available, we indicate the interannual variability of the estimates. Otherwise, we provide their uncertainties, which are larger than the interannual variability of the estimated quantities.

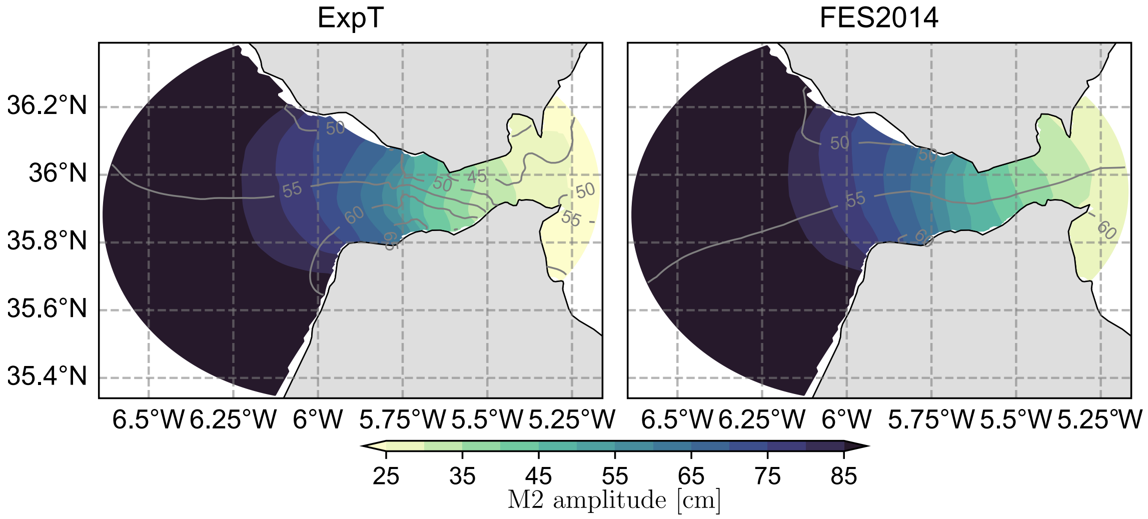

Figure 3.2: In shades, M2 tidal elevation amplitude, in contours, M2 tidal elevation. On the left is the MITgcm simulation, and on the right is the global tidal atlas FES2014. For ExpT, tidal amplitudes and phases are estimated from hourly outputs of instantaneous (not averaged) sea level elevation over January 1981 using the “Utide” Python package (version 0.2.5). FES2014 fields are interpolated on the MITgcm model grid through bilinear interpolation, following Xu (2018).

To begin with, we will first assess the realism of the simulated tidal elevations against the observation-based charts of Candela et al (1990) and Lafuente et al (1990) (CA90 and GL90 hereinafter). We also refer to the global tidal atlas FES2014 (produced by Noveltis, Legos, and CLS and distributed by Aviso+, with support from CNES: https://www.aviso.altimetry.fr/) as a reference numerical dataset. In the following, differences between the charts of CA90 and GL90 provide an observational estimate of the tidal amplitude and phase. They display very similar amplitude patterns, mainly differing at the center of the strait near the Tarifa Narrow (between 5.5°W - 5.75°W), where they approximately differ by 5-8cm. On the other hand, the tidal phase patterns display larger differences, peaking at the center of the strait, near the Tarifa Narrow, where they exceed 10°. With that in mind, the amplitude and phase simulated by ExpT and FES2014 are both in good agreement with the former observations-based charts. As depicted in Figure 3.2, the M2 amplitude is characterized by a well-known abrupt zonal decrease from west ($\sim$ 90 cm) to east ($\sim$ 25 cm) and its phase by a meridional decrease from south to north (Candela et al, 1990; Lafuente et al, 1990). More specifically, regarding tidal amplitude, ExpT is in very good agreement with GL90, whereas FES2014 is more consistent with CA90. The zonal decrease of tidal amplitude is more intense in ExpT; however, the differences are within the range of the observation-based estimates uncertainty. Regarding the tidal phase, ExpT is in better agreement with CA90 and GL90 than FES2014. The main differences with respect to CA90 and GL90 fall within the uncertainty of the observation-based estimates. The validation of K1 and O1 harmonics against GL90 detailed in Appendix A gives further confidence in the realism of the simulated tidal elevation at the SoG.

To assess the baroclinic structure of the simulated tides, we refer to in situ Doppler current profiler measurements collected at the ES in the framework of the INGRES projects (more details in Sánchez-Román et al, 2008, 2009; Sammartino et al, 2015). We display in Figure 3.3 the vertical profile of M2 tidal ellipses extracted from the INGRES in situ data and the simulated velocity fields at the closest point to the measurement station. The tidal ellipses synthesize the evolution of horizontal tidal currents along the tidal cycle. Simulation-based and observation-based ellipses are in overall good agreement. They depict intense tidal currents with a dominant zonal component (up to 0.55m.s^{-1}) of almost constant amplitude in the upper 220m depth. Below, the zonal component progressively decreases, whereas its meridional counterpart increases. The simulated zonal currents are overestimated within the upper 220m (average bias of 0.1 m.s^{-1}), and underestimated below (average bias of -0.06m.s^{-1}). Regarding the tidal phase, the simulated currents are characterized by a mean absolute phase bias of 2°. Note that for a few ellipses, the rotation direction is reversed with respect to the observed currents (the rotating direction is indicated by ”x” and ”+” signs in Figure 3.3). However, these ellipses all depict very low meridional currents and consistent phases with respect to the observations. Thus, the rotating direction has a low impact on the associated tidal currents.

To conclude on the tidal validation, in light of the reasonable biases highlighted by the former analyses and the consistency with available references, we consider the simulated tides relevant to study the processes involved in tidal mixing at the SoG.

To evaluate the simulated velocities at the SoG, we refer again to in situ Doppler current profiler measurements collected in the framework of the INGRES projects. Specifically, to assess the average vertical profile of zonal velocities, we compare 2005 – 2015 measured velocities to 1981 simulated velocities at the closest point to the measurement station (black dot in Figure 3.1). In addition, we assess the associated temporal variability by comparing the hourly standard deviation of mea-

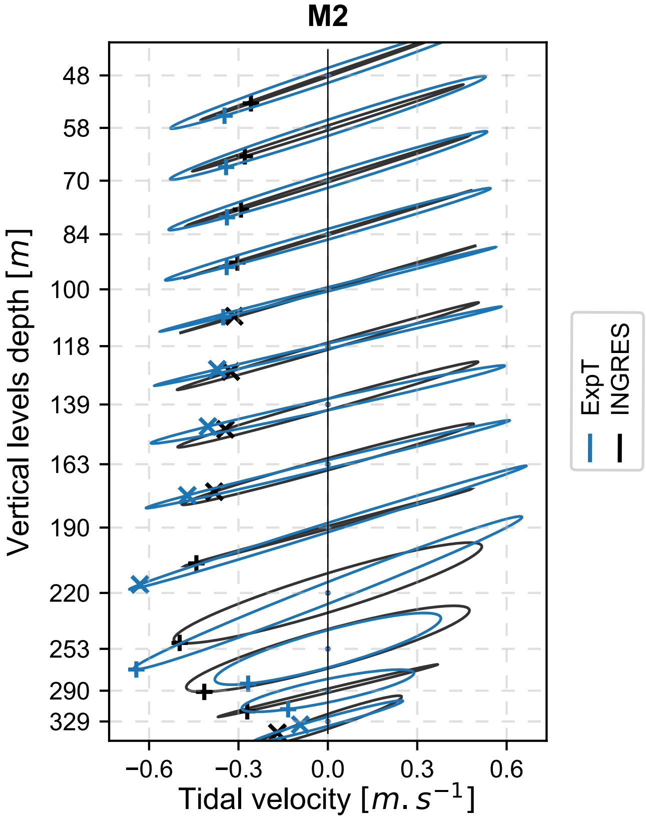

Figure 3.3: Vertical profile of tidal ellipses associated with the M2 horizontal tidal harmonic at the INGRES location ($\simeq 35.86°N,\ 5.97°W$; black dot in Figure 3.1). In blue, MITgcm simulation (ExpT), in black, in situ Doppler current profiler measurements from the INGRES project. Meridional currents (along the y-axis) are stretched by a factor of three for the sake of readability. The location of the current vector at the zero Greenwich phase is indicated by the symbols "+" (counterclockwise) and "x" (clockwise). Tidal ellipse parameters are computed using the "Utide" Python package (version 0.2.5) from hourly-averages of horizontal currents over January 1981 for ExpT, and instantaneous 30-minute measurements over January 2004-2015 for the INGRES dataset. For ExpT, horizontal velocities are obtained by projecting the model outputs onto the zonal and meridional directions. Measurements are linearly interpolated onto the model vertical grid.

sured velocities over January 2005 – 2015 to that of the simulated velocities over January 1981. The results are displayed in Figure 3.4. For both simulations, mean velocities are in good agreement with measurements, exhibiting vertical correlation coefficients of 0.997 and 0.987, along with root-mean-square errors (RMSE hereinafter) of 0.07m.s^{-1} and 0.15m.s^{-1} for ExpT and ExpNT, respectively. The simulated currents are underestimated in ExpNT between 50m – 150m depth and overestimated in both simulations below 190m depth, with a notable improvement in ExpT. With respect to measurements, the zero-velocity interface only differs by ∼ 10m, with a notable improvement in ExpT. As expected, the non-tidal simulation largely underestimates the zonal velocity variability at high-frequency. With respect to INGRES measurements, the hourly standard deviation of zonal velocity depicts a RMSE of 0.29m.s^{-1}, with a minimal amplitude at 220m depth, just below the mean zero-velocity interface. The addition of tidal forcing substantially corrects this bias, decreasing the RMSE to 0.09m.s^{-1} in ExpT. Consistently with the results

		Volume: $\overline{Q}$ ($Q^{\max}$) [Sv]	Heat: $\overline{QH}$ [$W.m^{-2}$]	Salt: $\overline{QS}$ [$10^6 kg.s^{-1}$]
$\mathrm{IN}_{\mathrm{AL}}$ 1981/01	ExpT	0.81 (1.63)	19.3	29.4
	ExpNT	0.79 (0.87)	19.3	28.6
	Jordà et al (2017b), Table 3	0.86±0.10	-	-
$\mathrm{OUT}_{\mathrm{ES}}$ 1981/01	ExpT	-0.86 (-1.45)	-18.4	-32.6
	ExpNT	-0.86 (-0.96)	-18.14	-32.72
	Sammartino et al (2015)	-0.85±0.08	-	-
$\mathrm{NET}_{\mathrm{CS}}$ 1981	ExpT	0.06	4.77	0.68
	ExpNT	0.06	5.00	0.55
	Jordà et al (2017b)	0.04±0.02	4.5±4.1	0.1±0.3

Table 3.1: Average pseudo-zonal transports of volume, heat, and salt for the MITgcm model simulations ExpT and ExpNT. AL, CS, and ES stand for the Alboran, Camarinal Sill, and Espartel Sill sections, respectively (see Figure 3.1). The inflow and outflow (in Sverdrups) are computed over January 1981 from hourly outputs at the AL and ES sections (Figure 3.1), respectively. Net transports are computed over 1981 at the CS section (Figure 3.1). For the volume transports, we indicate an alternative, maximal estimate in brackets, which accounts for high-frequency flow variations over 1981. When available, references are given in the third row. As traditionally done for comparison purposes with surface forcing, we convert the heat flux into an equivalent surface flux over the whole Mediterranean Sea, in W.m^{-2}, considering the Mediterranean area to be $2.5 \cdot 10^{12}$m^2, following Sanchez-Roman et al (2018).

from the tidal validation, ExpT overestimates the variability of zonal velocities over the upper 220m depth and underestimates it below.

Table 3.1 summarizes the main characteristics of transports through the SoG. To be as consistent as possible with observations, we calculate the inflows (outflows) at the AL (ES) section, where their estimation is more robust (Jordà et al, 2017b) (see Figure 3.1). For both ExpT and ExpNT, the computed volume inflow and outflow fall within the confidence interval of Jordà et al (2017b, Table 3) and the estimation interval of Sammartino et al (2015) for sub-annual timescales, respectively. Although simulations estimates are only computed over January 1981, their consistency over longer periods can be assessed by considering the monthly variability of the Mediterranean outflow as an uncertainty range. The latter is estimated at 0.08Sv by Sammartino et al (2015). Note also that the computed heat and salt transport are within the range of the values commonly obtained with similar numerical models (Jordà et al, 2017b). Regarding the net transports (computed over 1981 at the CS, although they are uniform throughout the strait), the volume and heat transports are consistent with the accepted range defined by Jordà et al (2017b). For the salt transports, the simulations are out of the indirect estimate range from Jordà et al (2017b). However, they remain relatively close to it, given its high uncertainty and the high sensitivity of net salt transports to interannual variations of the inflow and outflow.

The effect of tidal forcing is evident in the maximal transport estimates $Q^{\max}$. For ExpT, $Q^{\max}$ displays large values, twice as high as $\overline{Q}$, whereas for ExpNT,

$Q^{\max}$ and $\overline{Q}$ are relatively similar. This reflects that tidal forcing induces intense high-frequency variations of zonal advection, which is consistent with water mass recirculation and periodic reversals of the exchange flow (Candela et al, 1990; Bryden et al, 1994; Lafuente et al, 2000). These results are in line with Sanchez-Roman et al (2018), who highlighted that inclusion of tidal forcing intensifies the exchanges through the SoG, however, to a much lesser extent. The substantial values highlighted here can be attributed to the computation of $Q^{\max}$ at the simulation timestep, in contrast to the use of 3-hourly averages in Sanchez-Roman et al (2018), which allows transports compensations from averaging opposite velocities. Tidal forcing also influences the net heat and salt transport through the strait, which decreases by 5% and increases by 24% in ExpT, respectively. These modifications are similar to what is reported in Sanchez-Roman et al (2018). It is important to note that they are significant, especially for the net salt transport, whose observed estimate is, however, highly uncertain (Jordà et al, 2017b). In longer simulations, such changes would likely impact the heat and salt contents of the Mediterranean Basin after a few years of integration.

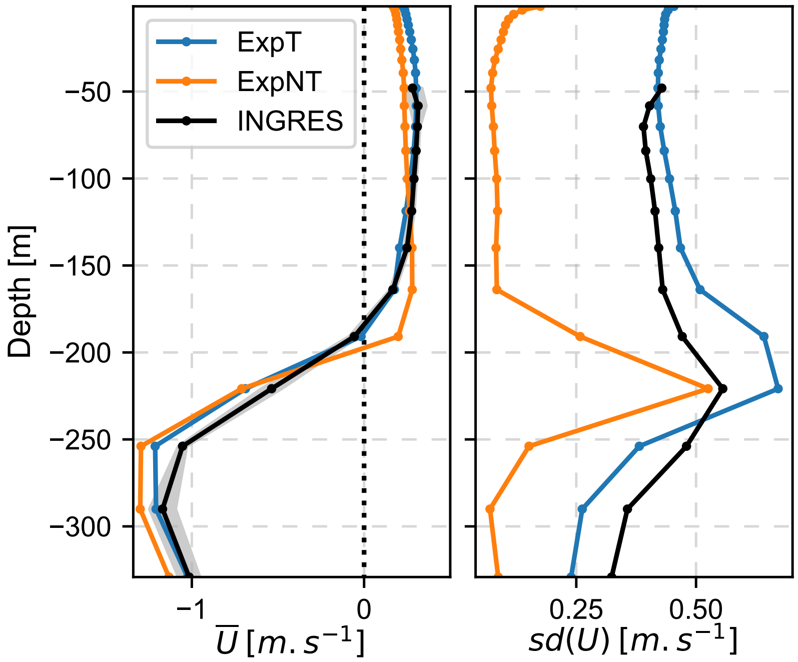

Figure 3.4: Mean (left) and hourly standard deviation (right) of the zonal velocity profile at the Espartel Sill (see Figure 3.1). In black, 2005 – 2015 mean in situ Doppler current profiler measurements from the INGRES project, with a sampling interval of 30 minutes (Sammartino et al, 2015). Dark shades represent the interannual variability computed from the measured data. In blue and orange, 1981 mean simulated zonal velocity, taken at the closest point to the measurement station ($\simeq 35.86°N,\ 5.97°W$; black dot in Figure 3.1), for ExpT and ExpNT, respectively. Hourly standard deviations are computed considering only the month of January. The zonal velocities are obtained by projecting the model outputs onto the zonal direction. Measurements are linearly interpolated onto the model vertical grid.

3.3.2 Characterization of Tidal Mixing Within and Around The SoG

Several studies have already investigated the impact of tidal forcing on the currents and water masses at the SoG (Sanchez-Roman et al, 2018; Sannino et al, 2015; Naranjo et al, 2014; Harzallah et al, 2014). The following discussion reinforces the results highlighted in these studies and gives further details on the tidal mixing intensity and location.

Figure 3.5 displays the model mean temperature, salinity, westward and eastward velocity, vertical eddy diffusivity coefficient, and absolute vertical buoyancy flux, averaged along the model pseudo-meridional direction for the domain illustrated in Figure 3.1. In panels (a) and (b), we can readily distinguish the relatively warm and fresh Atlantic layer ($\sim$ 15°C – 17.5°C and 36 psu – 37 psu), flowing toward the Mediterranean Sea, from the cold and salted Mediterranean layer ($\sim$ 13°C – 14°C and 37.5 psu – 38.5 psu), flowing toward the Atlantic Ocean. The zero-velocity interface separating these two layers (black line in Figure 3.5) is almost flat within the strait, around 150m depth, and sinks to 300m depth to the west, following the Mediterranean outflow. At fixed depths, the water masses depict noticeably different characteristics along the strait, indicating the occurrence of intense diapycnal mixing and water masses recirculation. This is particularly striking near the depth of the inflowing and outflowing layers interface, where temperature and salinity vary by up to 1°C and 1 psu along the strait. Comparison with ExpNT reveals that tides induce intense temperature and salinity anomalies within the strait (colored contours in Figure 3.5 (a) and (b)). These anomalies organize as vertical dipoles, indicating a vertical redistribution of heat and salt. Regarding temperature, tides significantly cool the surface above 50m depth, especially east of the CS, where mean temperature anomalies reach -0.5°C. Underneath, Atlantic and Mediterranean water masses are warmed less intensely (up to $+0.3$°C). Note that the temperature dipole is not centered on the interface between the inflowing and outflowing layers, as it results from the impact of tides on the warm ocean surface in summer. At that time, tidal motions mainly flux heat to depth, cooling the top fifty meters by up to -1°C and warming less intensely the water masses below (not shown). Regarding salinity, the tide-induced anomalies provide a vivid picture of diapycnal mixing and vertical displacement of the interface between Mediterranean and Atlantic water masses (Figure 3.5 (b)). Above the velocity interface, mean salinity increases by up to 0.2 psu, whereas below, it decreases by up to 0.15 psu.

The mean westward and eastward velocities (Figure 3.5 (c) and (d)) illustrate the remarkable intensity of the exchange flow through the SoG, as well as the intense vertical shear that characterizes it. After crossing the CS, the Atlantic and Mediterranean layers become narrower, forcing the water masses to accelerate up to $1\,\mathrm{m.s^{-1}}$. Overall, tidal forcing increases both eastward and westward advection (colored contours in Figure 3.5 (c) and (d)), reflecting a periodic reversal of the inflowing and outflowing layers (Candela et al, 1990; Bryden et al, 1994; Lafuente et al, 2000). Local decreases in the velocity fields can be explained by tidal recirculation patterns above the main topographic obstacles of the strait (Sanchez-Roman et al, 2018). In this way, the weakening of westward currents at the crest of the CS and west of

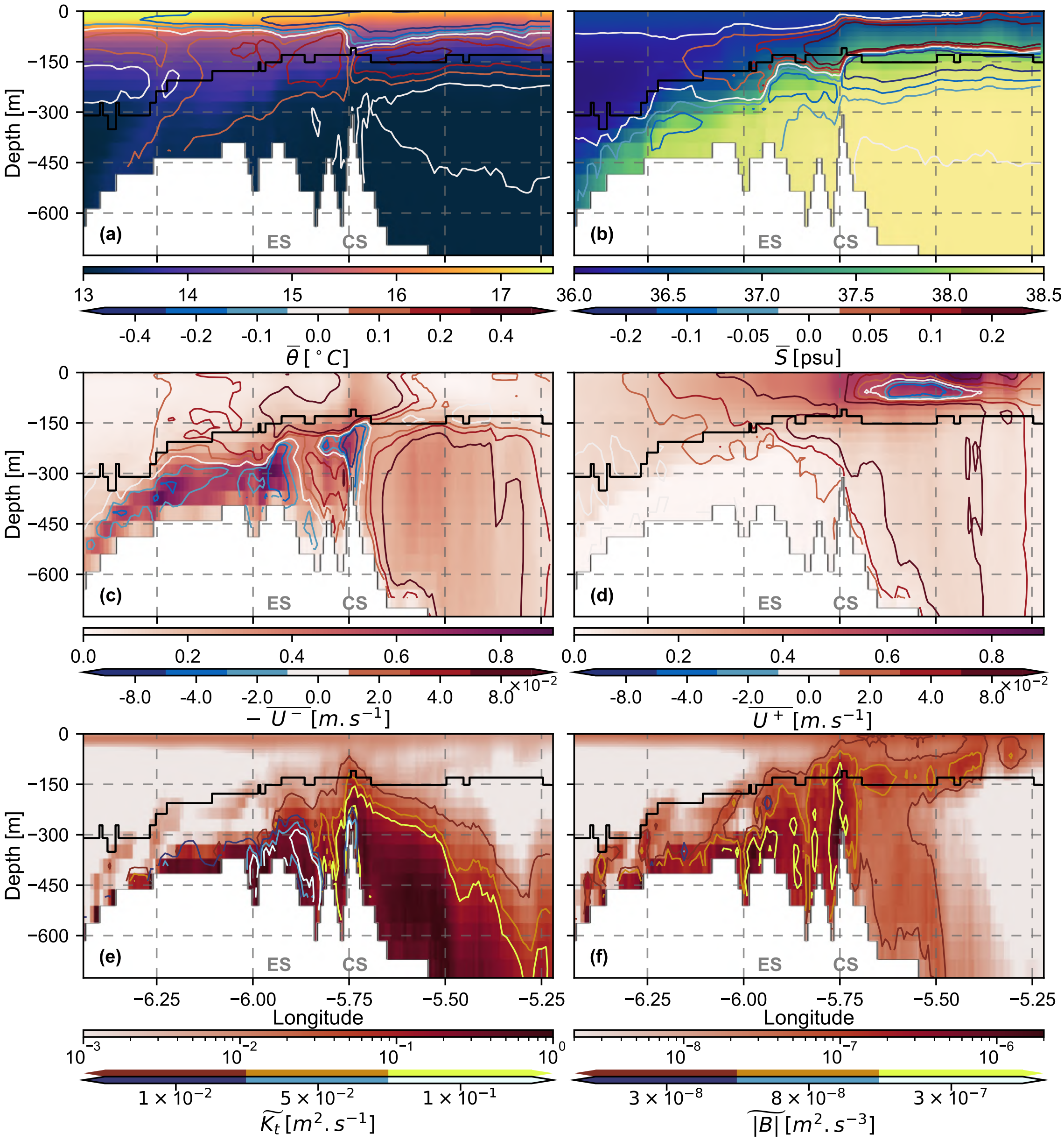

Figure 3.5: From (a) to (f): Model 1981 mean temperature, salinity, eastward velocity U^+, westward velocity U^-, vertical eddy diffusivity coefficient K_t, and absolute vertical buoyancy flux $|B|$ in ExpT (shades). The fields are spatially averaged over pseudo-latitudes (following the model grid) of the domain illustrated in Figure 3.1, excluding coastal areas (shallower than 100m depth). Anomalies with respect to ExpNT (ExpT-ExpNT) are represented in contours, with colors defined according to the lower color bars below the figure. For panels (e) and (f), in which we use a logarithmic scale, negative anomalies are indicated in dark to light-blue shades and positive anomalies in brown to yellow shades. The black line marks the 1981 average interface depth between the inflowing Atlantic waters and outflowing Mediterranean waters. It is defined in a vertical integral sense as follows: $_{d\in[0;bot]}\int_d^0 \bar{U}\ dz$. The acronyms "ES" and "CS" in gray refer to the Espartel Sill and the Camarinal Sill, respectively. The mean eddy diffusivity coefficient and buoyancy flux are geometrically averaged over pseudo-latitudes to filter out isolated large values and highlight the most meridionally-consistent patterns using the following operator: $log_{10}\left(\widetilde{X}\right) = \frac{\int log_{10}(X)\,dzdy}{\int dzdy}$. Note that the illustrated seafloor represents the maximum of the model bathymetry. Thus, bottom anomalies related to shallower regions may appear a few hundred meters above

the ES is consistent with the recirculation of the Mediterranean outflow. Given the reduction of the ExpT near-bottom velocity bias at the ES with respect to INGRES measurements (Figure 3.4), this suggests that tidal currents act as a mitigator of the zonal Mediterranean jet intensity. Conversely, the local intensification of westward velocities between the CS and ES is consistent with Atlantic water recirculation, also evidenced by the decrease of eastward velocities above 100m depth east of the CS.

The vertical eddy diffusivity coefficient (Figure 3.5 (e)) is averaged at each time step of the simulation before no-slip conditions modify it. It is, thus, fully defined by the TKE closure scheme and the wind stress at the surface (used as a boundary condition for the TKE). At the SoG, vertical diffusivities reach a maximum near the seafloor. They are also noticeably strong, although to a lesser extent, above 50m depth, between 50m – 300m depth just east of the CS, and near the zero-velocity interface. Overall, tides mainly influence eddy diffusivities near the seafloor, where they modify the stratification and the vertical shear of horizontal currents (Equations 3.3 and 3.4). Given the intense temperature and salinity anomalies above 300m depth (Figure 3.5, (a) and (b)), the former analysis reveals that the vertical eddy diffusivity coefficient is not adequate to draw an accurate picture of diapycnal mixing, although it is commonly used to do so (Sannino et al, 2015, Figure 11). Indeed, eddy diffusivities can be seen as a measure of the tracer gradient diffusion rate, and thus, they must be interpreted in conjunction with the background stratification. A good illustration is that for a given level of turbulence (TKE_{ref}), the eddy diffusivity coefficient is more intense in well-mixed areas than in strongly stratified areas ($K_t \propto \mathrm{TKE}_{ref} N^{-1}$ in Equation 3.3). Conversely, in this scenario, diapycnal mixing increases with stratification. In the following, we will use the absolute buoyancy flux $|B|$ as a measure of diapycnal mixing since it accounts for both diffusivity and stratification (Equation 3.4) and relates directly to the tracer mixing trends. We consider the absolute value to capture the total amount of diapycnal mixing, whether it is produced in the presence of stable ($N^2 > 0$) or unstable ($N^2 < 0$) stratification.

As expected, $|B|$ is intense in areas of strong vertical shear (Figure 3.5 (f)), such as the upper 50m, above the seafloor, and near the zero-velocity interface. It also reaches high values east of the CS in the Atlantic layer, between the zero-velocity interface and the surface, reflecting the occurrence of turbulent mixing. $|B|$ is minimal west of $6°W$ below 50m depth in the Atlantic layer and east of $5.5°W$ in the Mediterranean layer, respectively. This indicates that both water masses experience turbulent mixing upon crossing the CS. East of the CS above the seafloor, the buoyancy flux is moderate despite the intense viscosity (Figure 3.5 (e)). It illustrates that in weakly stratified areas, high diffusivities do not reflect strong diapycnal mixing. Tides mainly strengthen $|B|$ above the CS up to the surface, between the CS and ES in the Mediterranean layer, at the bottom of the Atlantic layer east of the CS, and to a lesser extent, at the eastern flank of the CS (colored contours in Figure 3.5 (f)). These intensification patterns are consistent with enhanced mixing near the seafloor and between the Atlantic and Mediterranean layers, as well as the incorporation of recirculating water masses within each layer. However, differences with respect to tidal temperature and salinity anomalies (Figure 3.5 (a) and (b)) suggest that the latter mainly reflects the periodic vertical advection of the interface between both layers.

Figure 3.6 illustrates the vertical average of $|B|$ over the same domain as the one considered in Figure 3.5. It gives a horizontal perspective on the diapycnal mixing intensity and location. Once again, the CS stands out as a location of intense buoyancy fluxes. Further west, $|B|$ is enhanced by the Mediterranean outflow, which drives vertical shear and turbulent mixing near the bottom. At the eastern side of the strait, the vertical average of $|B|$ is much lower (with respect to the west) due to the absence of solid obstacles on the path of the Atlantic jet. As expected, tides intensify diapycnal mixing within most of the strait, except along the Mediterranean outflow pathway, where both increased and reduced mixing are evident (Figure 3.5 (e)).

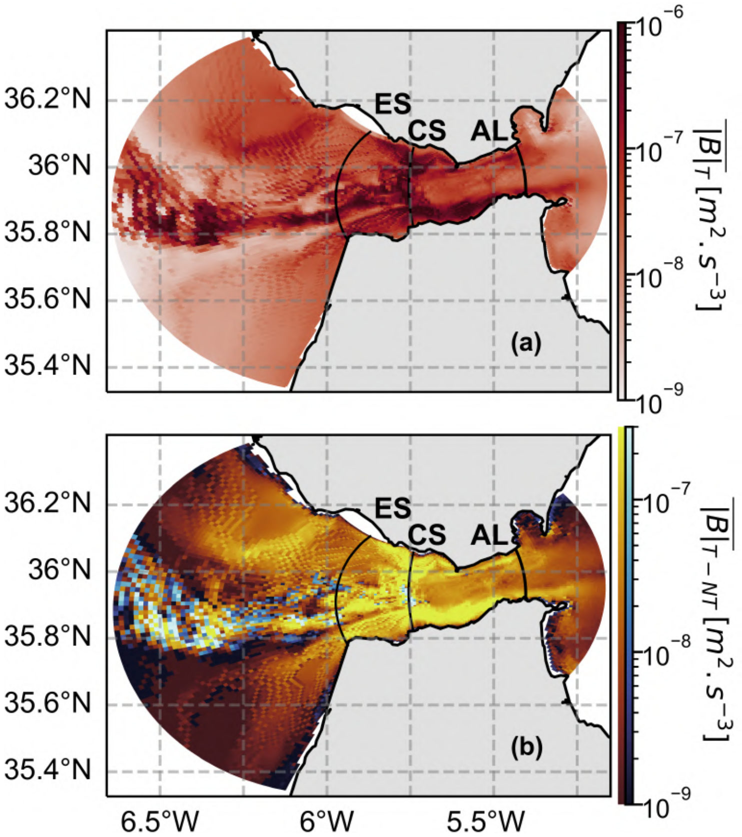

Figure 3.6: Depth average absolute vertical buoyancy flux $|B|$ in 1981 from ExpT (a), and anomalies with respect to ExpNT (b) (ExpT-ExpNT). Because of the logarithmic scale, negative anomalies are indicated in dark to light-blue shades and positive anomalies in brown to yellow shades. The acronyms "ES", "CS", and "AL" in black refers to the Espartel Sill, the Camarinal Sill, and the entrance of the Alboran Sea, respectively.

Thus, the addition of tidal forcing leads to significant changes in the mean characteristics of the exchange flow through the SoG. Analysis of vertical buoyancy fluxes indicates that diapycnal mixing substantially increases within the strait, and provides insight into its location and intensity. However, investigation of the related mechanisms is limited by the analysis of long-term averages, which depict large residual anomalies from periodic reversals of the exchange flow and vertical displacements of the Atlantic and Mediterranean water masses. This emphasizes the need to investigate the tidal dynamics and associated mixing at high-frequency.

3.3.3 Insight Into Turbulent Mixing at the SoG

In the previous section, we have detailed the effect of tides on water masses and currents at the SoG. We have then related these effects to diapycnal mixing patterns. We will now investigate the processes driving diapycnal mixing within the strait by analyzing TKE production ($\partial_t TKE > 0$) and destruction ($\partial_t TKE < 0$) at high frequency. We assume here that a large production of TKE reflects the occurrence of diapycnal mixing. Indeed, the increase of TKE is a necessary condition for the occurrence of intense diapycnal mixing (not a sufficient condition, as the buoyancy flux $B \propto TKE\, N$; Equations 3.3 and 3.4).

Figure 3.7 displays the evolution along the tidal cycle of the TKE tendency terms, integrated between ES and AL sections (Figure 3.1). The considered period starts at spring tides and ends at neap tides in order to capture the influence of the fortnightly tidal cycle on the TKE. As expected, the dynamic shear production (S) and the implicit TKE tendency ($I = T - \epsilon$, representing the terms of the TKE prognostic equation computed implicitly) are the dominating terms of the tendency (Figure 3.7, upper panel). Both share the same order of magnitude and follow similar variations, reaching their maximum during spring tides and their minimum during neap tides. Note that the integral of I is always negative over the domain and period examined. It indicates that TKE dissipation is the main contributor to I. Overall, the inclusion of tidal forcing substantially enhances S and I. Consistently with observations from Wesson and Gregg (1994), at hourly frequency, tides induce large oscillations in the intensity of S and I, reflecting a periodic intensification of the TKE and, thus, the occurrence of diapycnal mixing. To investigate the source of this tide-induced turbulence, we can look at the respective contributions of the TKE tendency terms. The buoyancy flux B (Figure 3.7, middle panel), always negative, is less variable and less intense than S and I. It correlates poorly with the total tendency (correlation coefficient of 0.06), which may be surprising since we have just described B as a good indicator of diapycnal mixing. However, it is essential to remind that B is related to the TKE and thus, not directly to its tendency. In fact, the poor correlation between B and the TKE tendency only suggests that B does not drive it but may occasionally alter it. On the contrary, the sum of I and S depicts a strong correlation with the TKE tendency (coefficient of 0.92), which points out that within the strait, the main drivers of TKE are dynamic shear production and dissipation.

In order to identify the physical mechanisms driving the TKE intensification through S, we will first shed light on the conditions required to trigger TKE production. Let us consider an initial state before the emergence of turbulence. We can argue that stratification is strong with respect to the TKE such that mixing and dissipation length scales are defined by: $l_k = l_\epsilon = l = \sqrt{2} N^{-1} \mathrm{TKE}^{1/2}$ (l is lower than the cells thickness). Focusing on the terms able to create or dissipate TKE, we can write from Equations 3.3 and 3.4:

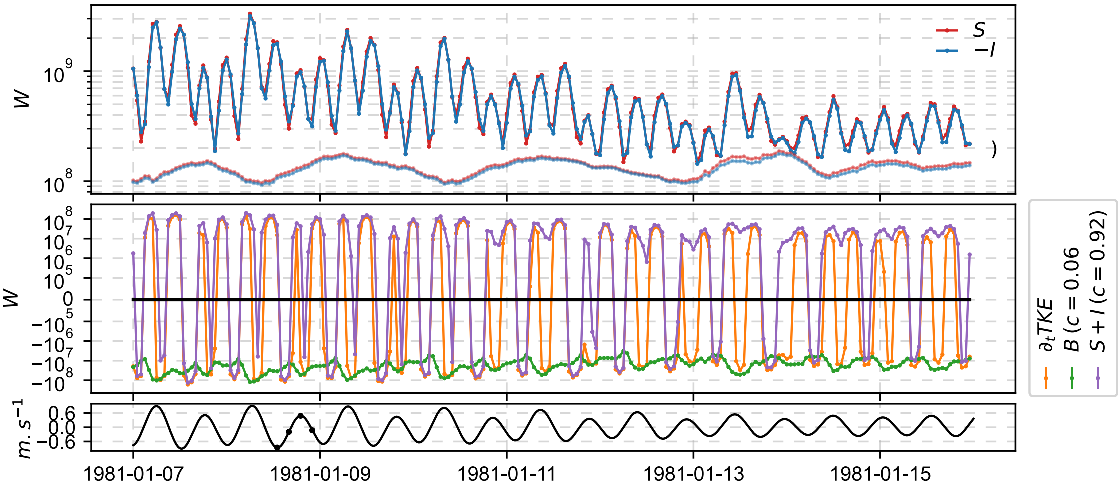

Figure 3.7: Hourly time series of the TKE tendency terms integrated between ES and AL sections (Figure 3.1) in ExpT. The period considered includes spring tide (01/07 – 01/12) and neap tide (01/12 – 01/16). The upper panel illustrates the dynamic shear production (in red) and the terms of the TKE prognostic equation computed implicitly (in blue, it includes TKE dissipation, vertical transport, and boundary conditions). The light-colored lines show the value of these terms in ExpNT. On the middle panel, we display the total tendency of TKE (in orange), the buoyancy flux (in green), and the sum of dynamic shear production and implicit TKE tendency (in purple). The correlation coefficient with the total tendency is given in the legend. The lower panel illustrates the pseudo-zonal (following the model grid) barotropic tidal currents, estimated from the simulated pseudo-zonal and pseudo-meridional velocities, using the "Utide" Python package (version 0.2.5). The four black dots represent the time of the hourly averages displayed in Figures 3.9 and 3.10

$$\partial_t \mathrm{TKE} - T = \sqrt{2} N^{-1} \mathrm{TKE} \left(c_k \mathrm{Sh} - N^2 \left(\frac{c_k}{P_r} + \frac{c_\epsilon}{2} \right) \right) \tag{3.5}$$

with Sh the squared vertical shear of horizontal currents. Thus, the balance between TKE production and dissipation only depends on vertical shear and vertical stratification (N^2). Going further in this argument, we can show (Appendix B, Equation 7) that TKE production is triggered when the bulk Richardson number decreases below a critical value $R_{i_c} \simeq 0.23$, close to the value commonly used to indicate the development of Kelvin-Helmholtz instabilities: $R_g = 0.25$ (Fernando, 1991). Simply put, for turbulence to develop, the vertical stratification must be sufficiently weak relative to the vertical shear of horizontal currents. We can conclude that tide-induced turbulence at the SoG must rely on either a local weakening of stratification or an intensification of vertical shear, or both.

To determine which of the former processes drives TKE production, we display in Figure 3.8 (a-b) the 1981 mean pseudo-meridional average correlation coefficient of the dynamic shear production S with the vertical shear Sh and vertical stratification N^2. Since the variables of interest vary exponentially and the function relating them is not linear, we investigate their correlation using the Spearman rank correlation coefficient (Schober et al, 2018). The results reflect a strong correlation between S and Sh within most of the strait. However, in areas where S is high

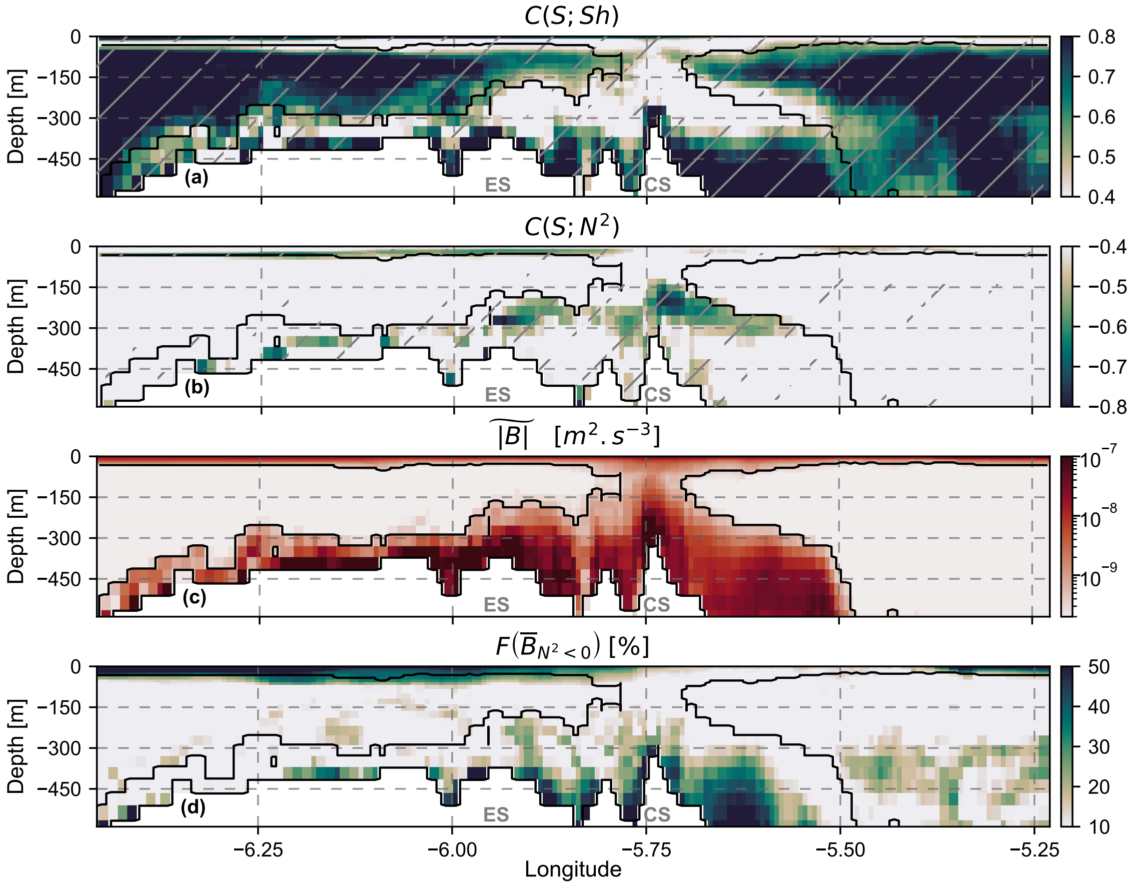

Figure 3.8: Panels (a) and (b) represent the pseudo-meridional average (following the model grid) Spearman rank correlation coefficient of dynamic shear production (S) with the squared vertical shear of horizontal currents (Sh) and stratification (N^2), respectively. Hatches mark areas where the correlation significance level is above 95% according to Student's T-test. Panels (c) and (d) show the time and pseudo-meridional geometric average of the absolute vertical buoyancy flux $|B|$ and the fraction of buoyancy flux oriented downward, respectively. Black contour lines delimit areas where dynamic shear production is consistently intense over time (i.e., where its time and pseudo-meridional geometric average is greater than $2\,10^{-9}\mathrm{m}^2\mathrm{s}^{-3}$). We use hourly outputs over 1981/01/01 – 1981/02/01 to compute time averages and correlation coefficients. The spatial domain considered is represented in Figure 3.1. The acronyms "ES" and "CS" refer to the Espartel Sill and the Camarinal Sill, respectively (see Figure 3.1).

(black contour in Figure 3.8), the correlation decreases as we move away from the seafloor. Conversely, N^2 depicts significant negative correlation patterns in these areas, particularly above topographic obstacles, and a poor correlation over the rest of the strait. Note that the correlation patterns of N^2 and Sh do not fully overlap, leaving areas where both are low. At these locations, we can deduce that N^2 and Sh equally contribute to the generation of vertical mixing. Thus, the former analysis emphasizes that although vertical shear drives TKE production in moderately turbulent areas, its influence in energetic areas is confined to the seafloor as stratification plays a greater role at shallower depths. In this way, tidal mixing at the SoG relies not only on an intensification of vertical shear by tidal currents but also on the work these currents exert against vertical stratification.

In order to relate TKE production to diapycnal mixing, we now investigate the buoyancy flux generated at the SoG and its relation to TKE production. To focus on areas where the buoyancy flux is consistently strong, we display in the panel (c) of Figure 3.8 the absolute buoyancy flux pseudo-meridional geometric average in 1981/01, representing the temporal and spatial average of its order of magnitude. As previously hypothesized, a significant buoyancy flux develops in areas of intense TKE production, namely, along the path of Mediterranean outflow west of the CS, above the CS, and east of the CS above 60m depth and below 300m depth. Between 150-300m depth above the main topographic obstacles, where stratification drives the TKE, the intense buoyancy flux indicates that TKE production is strong enough to induce diapycnal mixing, even if stratification has weakened ($B \propto TKE\ N$). Thus, stratification weakening acts as a trigger, allowing turbulence to develop and eventually produce diapycnal mixing.

An alternative mechanism to that described in Equation 3.5 is the generation of static instabilities ($N^2 < 0$), which result from the advection of dense water over lighter water. In this scenario, the conditions for TKE production change as the characteristic mixing lengths reach their threshold values ($l_k^{max} \neq l_\epsilon^{max}$). It can be shown (Appendix B, Equation 6) that TKE production then requires the vertical shear and/or the (negative) stratification to be sufficiently strong, relatively to the TKE: $\frac{c_k}{c_\epsilon}\, l_k^{max}\, l_\epsilon^{max}\, (\mathrm{Sh} - N^2) >$TKE. Thus, either (negative) stratification, vertical shear, or both can power great diapycnal mixing. To investigate this mechanism, we display in panel (d) of Figure 3.8 the pseudo-zonal average fraction of downward buoyancy flux over January 1981. Over the top 50m depth west of $5.75°W$, and close to the seafloor, a significant fraction of the buoyancy flux is oriented downward (at least 20%). In low turbulence areas, occasional static instabilities can account for a large fraction of the mean buoyancy flux. However, in areas of intense TKE production, such as near the seafloor between $6.25°W$ and $5.5°W$, the significant fraction of downward buoyancy flux suggests the frequent occurrence of large static instabilities. Since stratification does not strongly correlate with S in this area, we can assume that these instabilities act as an unsteady mixing source of variable intensity and location. Such mechanism is consistent with the unstable structures observed by Farmer et al (1988, Figure 13.1) and Wesson and Gregg (1994) near the crest and the west flank of the CS, respectively. On the other hand, the absence of significant negative buoyancy flux above 300m east of the CS indicates that diapycnal mixing mainly develops in a stably stratified sheared flow there.

3.3.4 Tidal Recirculation Patterns

We have just shown that besides vertical shear, tidal mixing at the SoG relies on the local weakening or reversal of stratification, suggesting the presence of strong tidal recirculation patterns within the strait. We will now describe these patterns throughout a tidal cycle and investigate how they relate to diapycnal mixing. Although not discussed in this section, the mixing induced by horizontal eddy diffusion is briefly investigated in Appendix C.

Figures 3.9 and 3.10 show the evolution of practical salinity (panels (a)), absolute buoyancy flux (panels (b)), circulation (panels (a) and (b), arrows), and absolute buoyancy flux variations with respect to the previous tidal phase (panels (c) and (d)) throughout different tidal phases on 1981/01/08. Namely, we display in Figure 3.9 the peak of the outflowing phase and the rise of the inflow, and in Figure 3.10 the peak of the inflowing phase and the rise of the outflow. In each panel, we also display isopycnals to track deeper density variations. Panels (d) specify the mechanism driving absolute buoyancy flux variations. This diagnostic is based on the detection of meridionally consistent variations of stratification and vertical shear. It relies on the hypothesis that TKE drives hourly buoyancy flux variations ($B \propto \text{TKE}\, N$; see Appendix E). The reader wishing to examine buoyancy flux and stratification variations is referred to the annex Figures C.1 and C.2, which also display a budget for the stratification tendency.

Throughout all periods illustrated in Figures 3.9 and 3.10, fresher Atlantic waters are readily distinguishable from saltier Mediterranean waters (panels (a)). The large zonal variations of salinity along the strait (up to 2psu near 150m depth) indicate the occurrence of diapycnal mixing and vertical advection associated with water masses recirculation. These are more directly reflected by intense buoyancy fluxes (panels (b)) and significant volume transport variations (upper line plots panels). In the course of the tidal cycle, absolute buoyancy flux variations (panels (c)) depict an alternation of intense and moderate mixing phases, with a 6-hour phase lag between the inflowing and outflowing layers. In moderately turbulent areas, these variations are mainly driven by the vertical shear of horizontal currents (panels (d)). In energetic areas, the complex mechanisms at play ask for a more detailed analysis.

At the peak of the outflow (Figure 3.9 (1), 1 p.m.), westward advection greatly intensifies, and the Atlantic inflow reverses between $6.25 - 5.50°W$. On the other hand, the Mediterranean outflow reaches the CS with high velocity, where it is blocked and forced to diverge. This is evidenced by an intense upwelling of dense water masses against the CS (the 1029 isopycnal locally shoals up to $\sim$ 150m depth) and a meridional transport from the center of the strait towards the land (not shown). The diverging water masses mainly converge west of the sill, where they force intense downward currents, completing the mechanism described in Bruno et al (2013). East of the CS, the divergent flow forces surface Atlantic and intermediate Mediterranean water masses to flow toward the Mediterranean Sea. Following Sanchez-Roman et al (2018), the resulting structure may be described as a vertical recirculation cell, identifiable by an intensification of volume transports east of the CS (upper panel of Figure 3.9 (1)). During this first tidal phase, diapycnal mixing is mainly intensified in the upwelled Mediterranean layer. West of the CS, this intensification results from vertical shear strengthening above the seafloor. On the contrary, above and east of the CS, as vertical shear diminishes with respect to the previous tidal phase, it is the stratification weakening by vertical tidal advection that allows diapycnal mixing to develop. Diapycnal mixing is also enhanced by static instabilities near the crest of the CS, consistently with observations from Farmer et al (1988, Figure 13.1), and at the eastern flank of the sill.

At the rise of the inflow (Figure 3.9 (2), 4 p.m.), the Mediterranean outflow intensity diminishes but maintains the recirculation cell previously described. East of

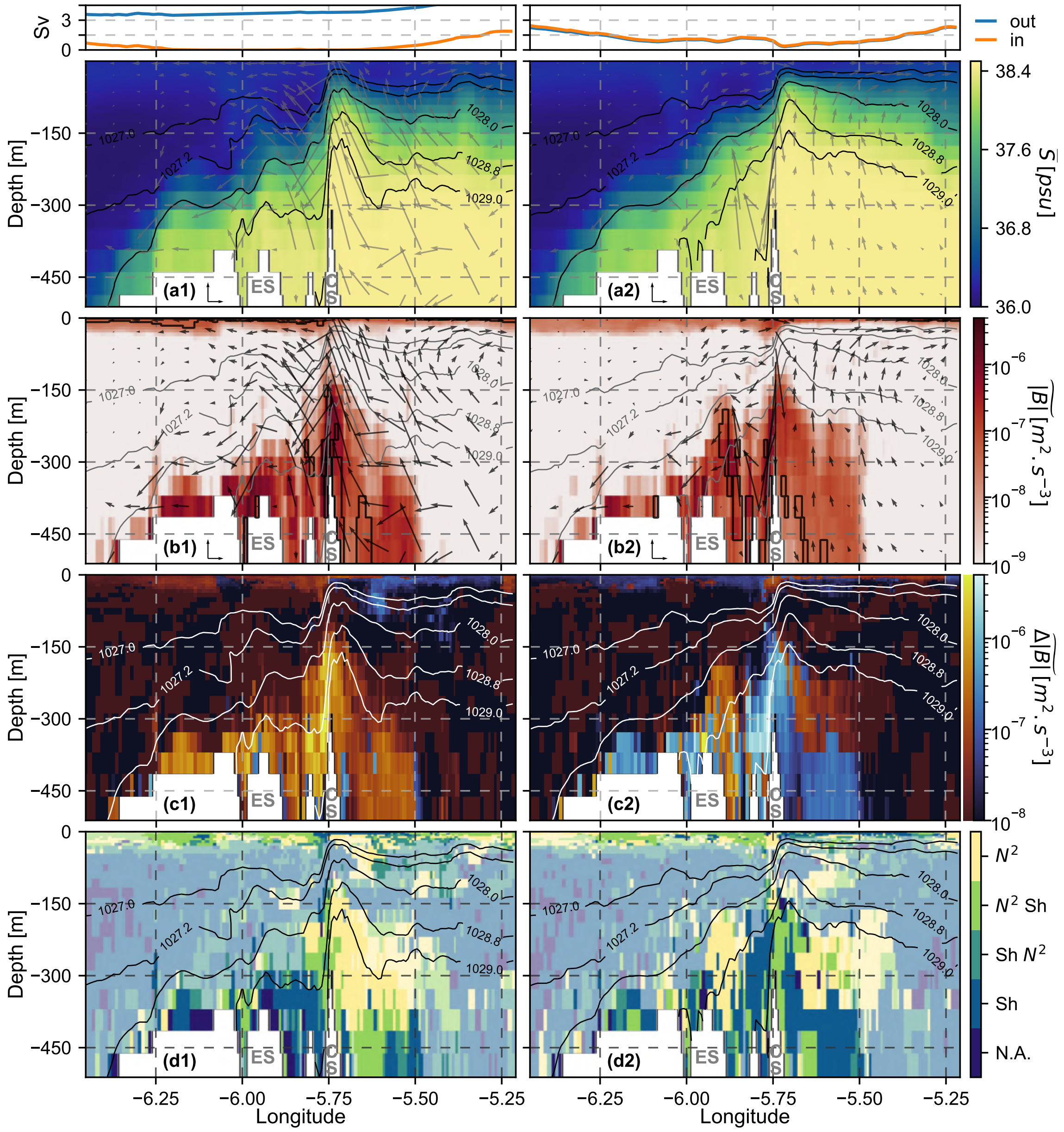

Figure 3.9: In shades, from top to bottom: pseudo-meridional average (a) practical salinity, (b) absolute vertical buoyancy flux $|B|$, (c) $|B|$ variation with respect to the previous tidal phase (three hours before), and (d) processes driving $|B|$ variations. The colors of panels (d) stand for stratification (N^2), both stratification and vertical shear, with a dominant influence for stratification (N^2 Sh) or vertical shear (Sh N^2), vertical shear (Sh), and non-identified process (N.A., see Appendix E). The fields are hourly-averaged outputs, extracted on 1981/01/08 at 1 p.m. (1), 4 p.m. (2) (black dots in Figure 3.7). The top blue and orange line plots represent the westward and eastward volume transport (in Sverdrups), respectively, computed from hourly-averaged outputs of zonal velocity. In panels (a) and (b), arrows represent the velocity direction and norm. Reference arrows (0.5m.s^{-1}, 0.005m.s^{-1}) and are displayed next to the image labels. Black contours in panels (b) outline areas where the average of the buoyancy flux is oriented downward and the absolute buoyancy flux higher than 5 10^{-8} m^2.s^{-3}. The 1027kg.m^{-3},1027.2kg.m^{-3}, 1028kg.m^{-3}, 1028.8kg.m^{-3}, and 1029kg.m^{-3} isopycnal surfaces are illustrated in contours for all panels. For panels (d), areas where the absolute buoyancy flux variations are lower than 2.5 10^{-8} m^2.s-4 in absolute value are made transparent. The acronyms "ES" and "CS" in gray refer to the Espartel Sill and the Camarinal Sill, respectively (see Figure 3.1). Time and spatial averages of the buoyancy flux are performed as detailed in Figure 3.5. For $\Delta|B|$, the meridional average only considers the cells driving meridionally dominant variations (see Appendix E).

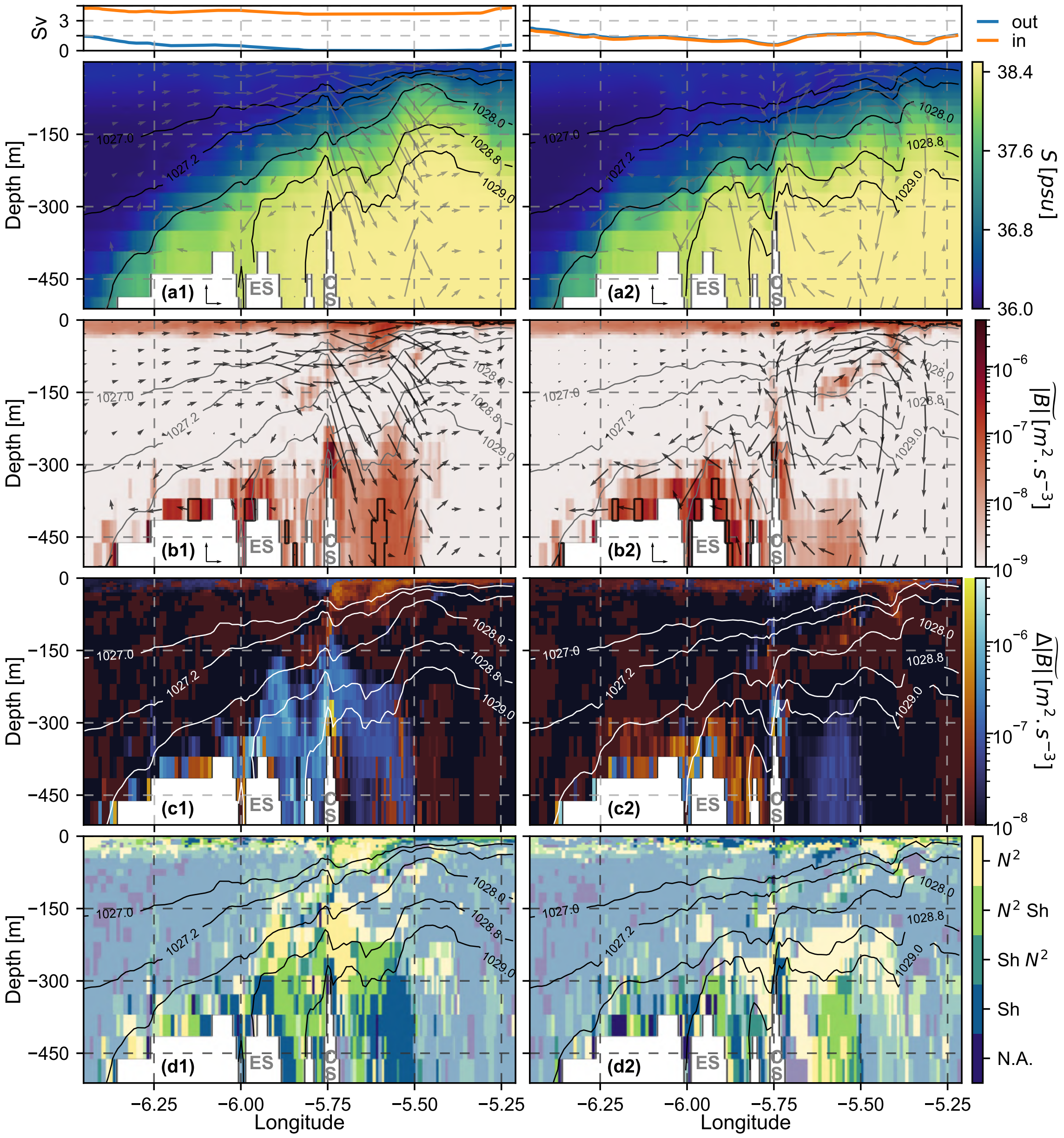

Figure 3.10: Same as Figure 3.9 for hourly outputs extracted at 7 p.m. (1) and 10 p.m. (2) (black dots in Figure 3.7).

the CS, the 1028.8kg.m^{-3} isopycnal flattens and rises above 150m depth, reflecting a shoaling and widening of the tongue of upwelled Mediterranean waters. In addition, the intensified eastward advection forces the upwelled water masses to flow toward the Alboran Sea, marking the release of the well-known internal bore at the CS (Ziegenbein, 1969, 1970; Farmer et al, 1988; Richez, 1994; Morozov et al, 2002). West of the CS, the intensified Atlantic inflow maintains the convergence area above the CS and partially recirculates along the western flank of the sill. This recirculation pattern is, to some extent, closed at the ES by a less intense recirculation of outflowing water masses. The overall structure is evidenced by a local increase in volume transports between the ES and CS. During this intermediate tidal phase, with respect to the outflowing phase, diapycnal mixing has reduced above the seafloor as vertical shear progressively diminishes, and tidal advection restores the stratification near the CS. Conversely, diapycnal mixing intensifies between $\sim 300-150$m depth east of the ES and the CS, where upward and westward advection weakens the stratification. Above the ES, the turbulence is further enhanced by the occurrence of static instabilities, which may be related to the unstable structures observed by Wesson and Gregg (1994) and simulated by various numerical models (Hilt et al, 2020; García Lafuente et al, 2013; Sanchez-Garrido et al, 2011).

At the peak of the inflowing phase (Figure 3.10 (1), 7 p.m.), the recirculation cells east of the CS and ES vanish as the Mediterranean outflow reverses. West of the CS, intense eastward tidal currents continue to force water mass convergence toward the center of the strait, as evidenced by the active Atlantic recirculation cell. The internal bore released during the previous tidal phase propagates eastward, and the inflowing Atlantic water masses following it restore stratification. Diapycnal mixing is significantly reduced in the Mediterranean layer. Indeed, above and around the CS, the deepening of the Atlantic layer increases stratification and, thus, prohibits diapycnal mixing. In addition, on both sides of the CS, the reduced vertical shear above the seafloor allows for a less intense mixing to develop. Conversely, diapycnal mixing intensifies in the thickened Atlantic layer east of the CS, where stratification weakens and vertical shear intensifies in the trail of the released bore.

At the rise of the new outflowing phase (Figure 3.10 (2), 10 p.m.), eastward advection diminishes but retains enough intensity to maintain the convergence area west of the CS, where the Atlantic inflow partly recirculates. On the other hand, the intensified Mediterranean outflow is forced to diverge against the eastern flank of the CS, forming the previously described recirculation cell. Further east, the internal bore propagates toward the Alboran Sea. The convergence area that follows it produces an intense recirculation opposing that on the eastern flank of the CS. Smaller waves develop along the trail of the internal bore. Among these structures, the vertical velocity dipole between $5.75 - 5.50°W$ indicates the propagation of a second-mode internal wave, observed by Farmer et al (1988); Vázquez et al (2006). These waves power a moderate diapycnal mixing in the Atlantic layer and at the interface with the Mediterranean layer through their local influence on vertical shear and stratification. In the Mediterranean layer, diapycnal mixing vanishes between $5.75 - 5.50°W$ due to the strengthening of stratification by vertical currents. Conversely, west of the CS, diapycnal mixing intensifies as the vertical shear increases with the Mediterranean outflow intensity.

Overall, these results explicitly reveal the tidal recirculation patterns at SoG and their connection to diapycnal mixing. They highlight that besides vertical shear near the seafloor, tidal mixing at the SoG strongly relies on the upwelling of dense Mediterranean water masses against the CS, favoring TKE production at the top of the Mediterranean layer, where stratification weakens, and producing an internal bore in the Atlantic layer, which locally weakens stratification and enhances vertical shear .

3.3.5 Synthetic mechanism

Although the exact location and intensity of diapycnal mixing at the SoG are highly variable, in this section, we propose a synthetic view of the different steps driving its occurrence in the course of the tidal cycle (Figure 3.11).

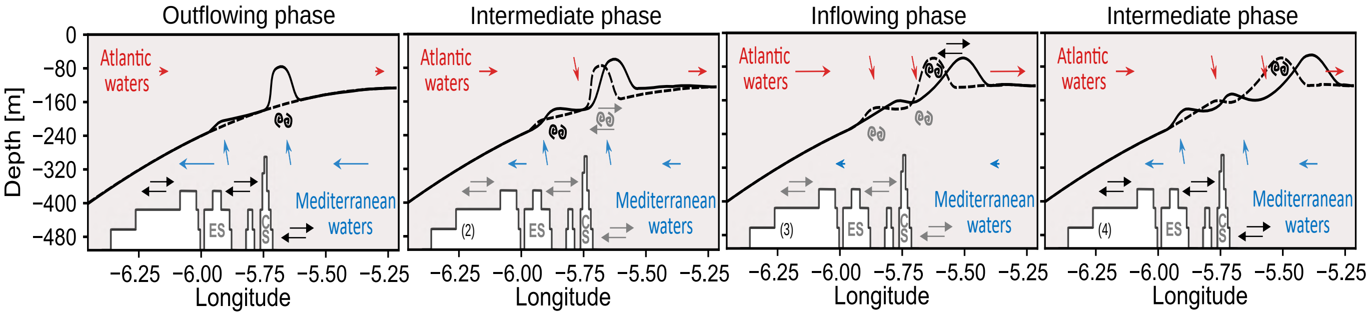

Figure 3.11: Synthetic schematic of tidal mixing at the Strait of Gibraltar. Advection of Atlantic and Mediterranean waters is indicated with red and blue arrows, respectively. Diapycnal mixing is illustrated by opposite horizontal arrows when driven by vertical shear, by spirals when driven by stratification, and a combination of these symbols when driven by both. Black symbols reflect the occurrence of intense diapycnal mixing. Gray symbols indicate a significant but decreasing diapycnal mixing. Acronyms "ES" and "CS" in gray refer to the Espartel Sill and the Camarinal Sill, respectively (see Figure 3.1). The interface between the Mediterranean and Atlantic layers is indicated by the solid (current location) and dashed lines (previous location). The idealized scenario starts in panel (1) with a relaxed interface between the Mediterranean and Atlantic layers. The interface is then deformed during the outflowing tidal phase (solid line), and diapycnal mixing develops in the Mediterranean layer where stratification weakens and vertical shear intensifies. During the intermediate (panel 2) and inflowing tidal phases (panel 3), diapycnal mixing progressively diminishes in the Mediterranean layer and increases in the Atlantic layer. In panel (4), during a final inflowing phase, diapycnal mixing continues to develop in the Atlantic layer along the trail of the eastward internal bore.

We consider an initial state in which the interface between the Atlantic and Mediterranean layers is relaxed (dashed line in Figure 3.11 (1)). As in ExpNT, it is smoothly slanted downward toward the Atlantic, characterized by an intense vertical shear, but also a strong stratification, such that $R_i > R_{i_c}$ and limited mixing occurs. Let us now consider the action of the outflowing tide on the system (solid line in Figure 3.11 (1)). East of the CS, the local upwelling of Mediterranean waters forms a recirculation cell between the Atlantic and Mediterranean layers. Stratification locally weakens above the CS, favoring TKE production and diminishing its dissipation (Equation 3.4). Once stratification is low enough relative to the vertical shear of horizontal currents ($R_i < R_{i_c}$), turbulence develops, progressively strengthening diapycnal mixing. As long as strong vertical shear persists, the recirculation cell continuously powers diapycnal mixing on the top of the Mediterranean layer by extracting available potential energy from the upwelled Mediterranean water masses. Diapycnal mixing also develops near the seafloor, where the Mediterranean outflow intensifies the vertical shear.

During an intermediate tidal phase (Figure 3.11 (2)), eastward velocities increase, whereas westward velocities progressively diminish. Above the seafloor, the intense diapycnal mixing progressively decreases as the Mediterranean outflow slows down. Similarly, diapycnal mixing diminishes above the CS, where the vertical shear decreases, and the released eastward internal bore restores the stratification. Just west of the CS, the convergence of water masses induces a second recirculation cell. The latter transports relatively light Atlantic water masses deeper into the Mediterranean layer west of the CS, where static instabilities form. These unstable structures further enhance diapycnal mixing, which is powered by the upwelling of dense water masses against the ES.

During the inflowing tidal phase (Figure 3.11 (3)), east of the CS, the recirculation cell vanishes due to the low intensity of the Mediterranean outflow. Above the CS, in the Mediterranean layer, stratification is restored, and diapycnal mixing is inhibited. Specifically, TKE shear production decreases while dissipation increases, reversing the TKE tendency (Equation 3.5). Conversely, east of the CS, the weakened stratification and intensified vertical shear along the trail of the internal bore allow the development of diapycnal mixing in the Atlantic layer.

During a last intermediate tidal phase (Figure 3.11 (4)), eastward velocities decrease, whereas westward velocities progressively intensify. Diapycnal mixing continues to develop along the trail of the internal bore. Over time, the internal bore disintegrates into smaller waves, which may produce further mixing by modifying the local stratification and vertical shear. Above the seafloor, diapycnal mixing increases as the vertical shear progressively strengthens with the Mediterranean outflow.

This synthetic view stresses the instrumental role of tidal recirculation cells and internal waves released at the CS in powering diapycnal mixing at the Strait of Gibraltar.

3.4 Conclusions and Discussions

This study characterizes tidal mixing at the Strait of Gibraltar (SoG hereinafter), a key phenomenon controlling water mass transformations across the strait. To do so, we analyze and compare twin tidal and non-tidal yearly MITgcm simulations over the Mediterranean Sea, with high-resolution at the SoG (1/200°, 100 vertical levels). Our analysis focuses on mechanisms driving explicit vertical mixing, defined by the 1.5-order turbulent kinetic energy closure scheme. We strongly emphasize that eddy diffusivity coefficients are irrelevant for measuring such mixing, which is better depicted by the vertical buoyancy flux.

The simulated tides are in good agreement with available observation-based references. In addition, both tidal and non-tidal simulations compare well to velocity measurements at the Espartel Sill (ES hereinafter) and transport estimates through the strait, with a notable improvement of the simulated velocities in the tidal simulation. As expected, tidal currents strengthen diapycnal mixing and induce considerable recirculation patterns across the strait, which are controlled by the main topographic obstacle: the Camarinal Sill (CS hereinafter). On an annual scale, tidal hydrographic anomalies mainly result from water mass recirculation and vertical displacements of the interface between the Atlantic and Mediterranean layers. East of the CS, the upper 150m depth, advected on average toward the Mediterranean sea, are cooled by up to 0.5°C and saltened by up to 0.2 psu. On the contrary, west of the CS, the water masses below 150m, flowing on average toward the Atlantic Ocean, are warmed by up to 0.2°C and freshened by up to 0.15 psu. Regarding the net transports, tide-induced currents and mixing decrease the net heat transport through the SoG by 5% and increase the net salt transports by 24%, which is consistent with the results reported in Sanchez-Roman et al (2018, Table 4 and 6). In agreement with the previous literature (Naranjo et al, 2014; Harzallah et al, 2014; Sannino et al, 2015), these results further highlight the significant influence of tides on the thermohaline exchanges through the SoG. They emphasize the relevance of modeling tidal currents at the SoG for the thermohaline balances of the Mediterranean Basin and, to a lesser extent, the Atlantic Ocean.

Investigation of diapycnal mixing shows it is intense above the seafloor throughout the strait and in the Atlantic layer east of the CS. Tides substantially strengthen diapycnal mixing within the strait, particularly west of the CS above the seafloor, above the CS up to the surface, and east of the CS in the Atlantic layer. We then investigate the Turbulent Kinetic Energy (TKE) scheme to identify the mechanisms of tidal mixing at the SoG. As expected, it reveals that the vertical shear of horizontal currents drives TKE production near the seafloor. However, at intermediate depths above the main topographic obstacles, turbulence is mainly driven by modulations of the stratification. It then relies on two mechanisms:

- Stratification weakening in areas of strong vertical shear of horizontal currents, particularly near the interface between the Atlantic and Mediterranean layers; this condition is reached when the bulk Richardson number, which measures the ratio between vertical stratification and shear, decreases below a critical value: $R_{i_c} \simeq 0.23$.
- The reversal of stratification, which mainly occurs in the Mediterranean layer close to the main topographic obstacles, due to water masses recirculation.

At shallower depths, in the Atlantic layer, diapycnal mixing is powered by eastward internal waves released at the CS through their impact on stratification and vertical shear.

Finally, we relate these mechanisms to circulation patterns within the strait. We show that the diapycnal mixing intensifies during different tidal phases for the Mediterranean and Atlantic layers, with a 6-hour time lag. In the Mediterranean layer, diapycnal mixing intensifies during the outflowing tidal phase, when vertical advection weakens stratification, and westward advection increases vertical shear near the seafloor. In the Atlantic layer, mixing intensifies during the inflowing tidal phase. It develops along the trail of the eastward internal bore of upwelled Mediterranean water masses released at the CS, where stratification locally weakens and vertical shear intensifies. Consistently with Sanchez-Roman et al (2018), these results emphasize that water mass transformations throughout the SoG strongly rely on vertical tidal motions at the CS. In addition, we explicitly show tidal recirculation cells between the Atlantic and Mediterranean layers, and large static instabilities near the main topographic obstacles of the strait.

As a further step in understanding tidal mixing at the SoG, this study would gain from comparison with a very-high-resolution non-hydrostatic counterpart, allowing to investigate the role played by high-order internal wave baroclinic modes, which are a key component of the energy cascade over abrupt topography (Lahaye et al, 2020). Although the mechanisms highlighted in this study should remain consistent, fine-scale and non-hydrostatic features, such as short internal solitary waves formed along the trail of the eastward internal bore released at the CS, should affect the intensity and location of diapycnal mixing (Hilt et al, 2020; Álvarez et al, 2019; Sannino et al, 2014). Such study could also assess the consistency of the highlighted recirculation cells to the relaxation of the hydrostatic assumption. Regarding turbulence closure schemes, a similar work based on an alternative scheme to that of the TKE (Umlauf and Burchard, 2005) would be very instructive. In particular, the use of 3D turbulence schemes would allow assessing the consistency of the classical horizontal homogeneity assumption at increasingly high resolution.

In the meantime, this study emphasizes the key role that both tides and abrupt topography play in controlling the exchanges at the SoG. In addition to tidal forcing, accurate representation of the seafloor, in particular the CS, appears as a necessary condition to resolve tidal mixing. Similarly, the magnitude of the fine-scale mechanisms suggests that a kilometric model resolution is also essential. Hence, our results question the reliability of coarse numerical models in representing the exchange flow through the SoG, even when tides are explicit (Harzallah et al, 2014). Regarding tidal mixing parameterizations, the magnitude of diapycnal mixing at the SoG is unlikely to be matched by current parameterizations, which present a significant energy loss in high turbulence regimes due to water column homogenization assumptions under energetic regimes (de Lavergne et al, 2016). However, these results should not stand in the way of improving such parameterizations, which are a low numerical cost alternative for non-tidal and low-resolution simulations. For example, implementing a specific tidal mixing parameterization for the SoG could be the key to notable improvements in the modeling of the Mediterranean Sea and the Atlantic Ocean at climatic scales. To this aim, the simple parameterization introduced in Sanchez-Roman et al (2018) would be a promising start.

Regarding observational validation, so far, past field measurements have been too scarce to validate the modeled tidal mixing mechanism. However, multiple observational campaigns at the SoG have shown large vertical displacements of the interface between the Atlantic and Mediterranean layers, as well as deep Mediterranean water suction above the strait, all related to the tidal cycle (Farmer and Armi, 1985; Farmer et al, 1988; Kinder and Bryden, 1990; Wesson and Gregg, 1994; García Lafuente et al, 2002; Sánchez-Román et al, 2012). In light of these observations, the mechanisms highlighted in this study are reasonable. Their field investigation would require microstructure turbulence measurements, together with hydrographic and velocity measurements at the SoG, throughout the main semidiurnal tidal cycle.

Finally, it is worth noting that the results highlighted in this study may be transferable to other straits of the world, provided that they include shallow sills and are subject to strong tidal currents.

Acknowledgements

This work is part of the Med-CORDEX initiative (www.medcordex.eu) and in particular of the CORDEX Flagship Pilot Study on an improved representation of small-scale oceanic processes and air-sea coupling in the region climate system models (CORDEX FPS-airsea).

Appendices

A Validation of K1 and O1 tidal elevations at the SoG

In this appendix, we validate the K1 and O1 tidal amplitudes at the SoG against available observation-based datasets and reference simulations.

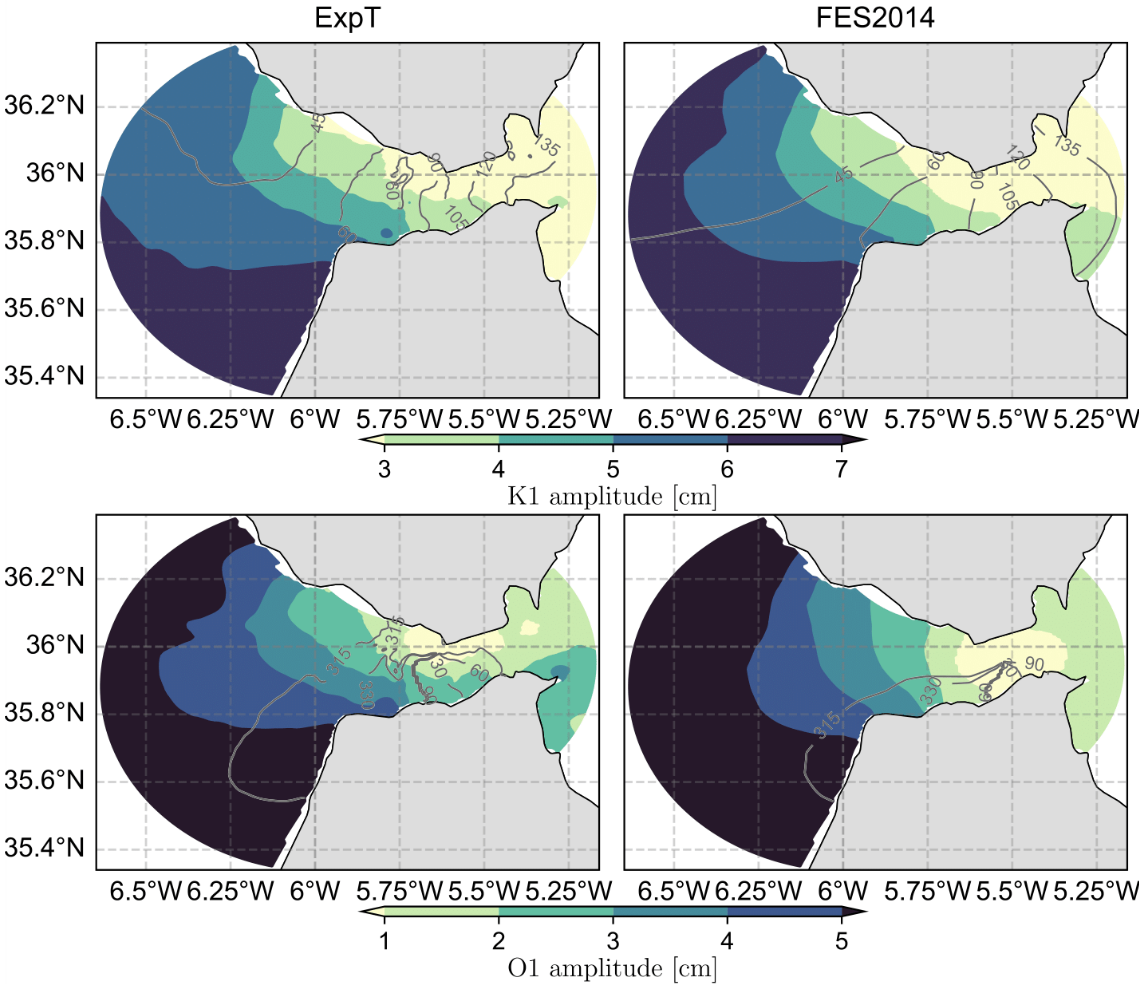

Figure A.1: Same as Figure 3.2 for the K1 and O1 tidal harmonics.

We display in Figure A.1 the amplitude and phase of the simulated K1 and O1 tidal elevation patterns in the vicinity of the SoG. As reference datasets, we consider the observation-based charts of Lafuente et al (1990) (GL90 hereinafter). In addition, we include in Figure A.1 the tidal amplitudes and phases from the global tidal atlas FES2014 as a reference numerical tidal model.

With respect to the aforementioned references, ExpT displays realistic tidal elevations within the SoG. Specifically, the simulation captures the north-eastward decrease of tidal amplitudes and zonal variation of tidal phases from the GL90 charts. The O1 amphidromic point near Tarifa is also well reproduced, although it is shifted southward. FES2014 displays relatively similar K1 elevations to ExpT, but it is less consistent with GL90 for the O1 harmonic. In terms of biases, ExpT elevation patterns display moderate differences with respect to GL90, typically less than one centimeter, with an overall better consistency than FES2014 for the O1 harmonic. The associated tidal phases are subject to larger biases due to their significant variability. However, they remain largely consistent with GL90. Therefore, we consider that the ExpT simulation satisfactorily represents the K1 and O1 tidal elevations within the SoG.

B On the conditions for TKE production

In this appendix, we derive from the TKE tendency equation necessary and sufficient conditions for the production of TKE. Consistently with our simulations, we consider the following numerical parameters: $c_k = 0.1$; $c_\epsilon = 0.7$; $P_r = \max(1, \min(10, 5R_i))$; $R_i = \frac{N^2}{(\partial_z u)^2 + (\partial_z v)^2}$. Also, we refer to the squared vertical shear of horizontal currents as Sh.

We search for a condition for the production of TKE. From Equation 3.4, we have:

$$\begin{aligned}
\partial_t \mathrm{TKE} - T &\geq 0 \\
\Rightarrow c_k l_k \mathrm{TKE}^{1/2}\mathrm{Sh} - c_k l_k \mathrm{TKE}^{1/2}\frac{N^2}{P_r} - c_\epsilon \frac{TKE^{3/2}}{l_\epsilon} &\geq 0 \\
\Rightarrow c_k l_k \mathrm{TKE}^{1/2}\left(\mathrm{Sh} - \frac{N^2}{P_r}\right) - c_\epsilon \frac{TKE^{3/2}}{l_\epsilon} &\geq 0 \\
\Rightarrow \frac{c_k}{c_\epsilon} l_k\, l_\epsilon \left(\mathrm{Sh} - \frac{N^2}{P_r}\right) &\geq TKE
\end{aligned} \tag{6}$$

We must now distinguish two cases, depending on whether the mixing and dissipation length scales have reached their threshold values or not. In the latter case (i.e. $l_k = l_\epsilon = \sqrt{2}N^{-1}TKE^{1/2}$):

$$\begin{aligned}
\frac{c_k}{c_\epsilon} 2\left(\mathrm{Sh}N^{-2} - \frac{1}{P_r}\right) &\geq 1 \\
\Rightarrow \frac{c_k}{c_\epsilon} 2\left(\frac{1}{R_i} - \frac{1}{P_r}\right) &\geq 1
\end{aligned}$$

From the definition of the Prandtl number, we distinguish three conditions:

- if $R_i \geq 2$ (i.e. $P_r = 10$) :

$$\frac{c_k}{c_\epsilon}2\left(\frac{1}{R_i}-\frac{1}{10}\right)\leq\frac{c_k}{c_\epsilon}2\left(\frac{1}{2}-\frac{1}{10}\right)<1$$

- if $2 > R_i > 0.2$ (i.e. $P_r = 5R_i$) :

$$\begin{aligned}&\frac{c_k}{c_\epsilon}2\left(\frac{1}{R_i}-\frac{1}{5R_i}\right)\geq 1\\ \Rightarrow\ &\frac{c_k}{c_\epsilon}2\frac{4}{5}=R_{i_c}=0.23\geq R_i\end{aligned}$$

- if $R_i \leq 0.2$ (i.e. $P_r = 1$) :

$$\frac{c_k}{c_\epsilon}2\left(\frac{1}{R_i}-1\right)>8\frac{c_k}{c_\epsilon}>1$$

Finally:

$$\begin{aligned}&\partial_t\text{TKE}-T\geq 0\\ &\Rightarrow R_i\leq R_{i_c}\end{aligned}\tag{7}$$

Thus, when the mixing and dissipation length scales have not reached their threshold values (strong stratification and/or low TKE), TKE variations evenly impact the terms of the tendency (Figure A.2 (1)). The TKE production is then triggered by strong vertical shear relative to the stratification, i.e. when the bulk Richardson number R_i decreases below $R_{i_c} \simeq 0.23$ (Equation 7). On the other hand, when the mixing and dissipation length scales reach their threshold values (weak stratification and/or great TKE), they become disconnected from the TKE, which becomes a net source of dissipation (Figure A.2 (2)). The TKE production then requires strong vertical shear of horizontal currents and low stratification relative to the TKE (Equation 6).

C Overview of the horizontal buoyancy flux at hourly frequency

This appendix provides an overview of the diapycnal mixing produced by the horizontal buoyancy flux $|K_hM^2| = K_h\sqrt{(\partial_x^2\rho)^2 + (\partial_y^2\rho)^2}$ during the period analysed in section 3.4 “Tidal Recirculation Patterns”, that is January 8, 1981, 1:00 p.m. - 11:00 p.m.. The pseudo-meridional average of $|K_hM^2|$ during this period is displayed in Figure B.1. First, it is important to note that although $|K_hM^2|$ is higher than $|B|$ (Figures 3.9 and 3.10, panels (b)), it powers a less intense diapycnal mixing. Indeed, over the domain represented in Figure 3.1, $\int|\nabla\cdot K_hM^2|\,dV$ is, on average, five-time inferior to $\int|\partial_zB|\,dV$ during the period considered in Figure B.1. With that in mind, $|K_hM^2|$ provides meaningful information about the location and intensity of the diapycnal mixing powered by the horizontal eddy diffusivity. Unlike $|B|$, which is mainly intensified within the Atlantic and Mediterranean layers, $|K_hM^2|$ is more

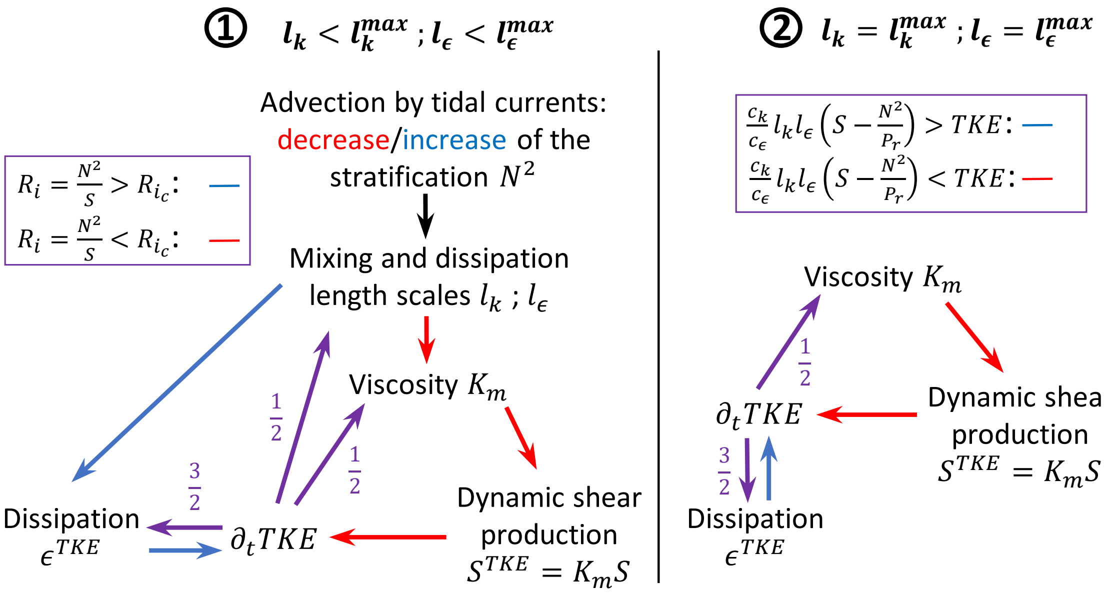

Figure A.2: Conceptual diagram of the mechanisms controlling TKE production and destruction. On the left (1) behavior of the TKE tendency in the presence of strong stratification and/or low TKE. On the right (2) behavior of the TKE tendency in the presence of weak stratification and/or high TKE. Red and blue arrows denote positive and negative feedback, respectively. When tidal currents reduce the stratification, the black arrow represents the positive feedback on the mixing and dissipation length scales; otherwise, it represents negative feedback. Purple arrows represent either positive or negative feedback. The conditions in the purple frame define their color. R_i refers to the bulk Richardson number, the ratio between stratification and vertical shear of zonal currents. $R_{i_c} \simeq 0.23$ is a bulk Richardson critical value. $Pr = min(10, max(1, 5 * R_i))$ refers to the Prandtl number. The number next to the purple arrows represents the order of the TKE in the other terms. We do not represent the buoyancy flux in the diagram, but we consider it in the conditions for the production or destruction of TKE.

homogeneous and reaches its maximum at the interface between the Atlantic and Mediterranean layers. More specifically, over the period analyzed, $|K_h M^2|$ is high between the 1029 - 1027 kg.m^{-3} isopycnals, which are sheared by tidal circulation patterns. Thus, the absolute horizontal buoyancy flux can be considered a less intense but complementary source of diapycnal mixing at the SoG.

D Vertical shear and stratification variations along the tidal cycle

In this appendix, we provide additional or supporting information for section 3.4 “Tidal Recirculation Patterns”. More specifically, we outline the variations of the vertical shear of horizontal currents Sh and the vertical stratification N^2 along the tidal cycle on January 8, 1981, and provide insights into the mechanism driving N^2 variations.

Regarding the vertical shear variation ΔSh, displayed in the panels (a) of Fig-

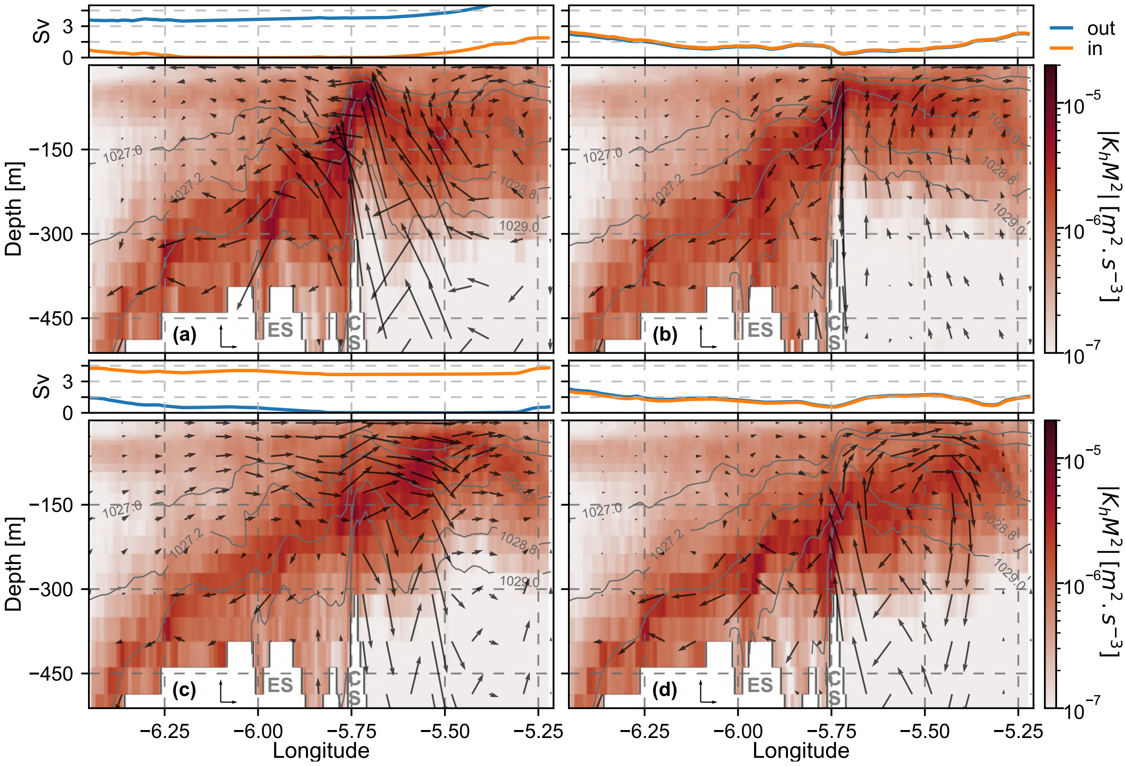

Figure B.1: Pseudo-meridional average of horizontal buoyancy fluxes $|K_h M^2| = K_h\sqrt{(\partial_x^2\rho)^2 + (\partial_y^2\rho)^2}$, with $K_h = 2\text{m}^2.\text{s}^{-1}$ the horizontal Laplacian diffusivity coefficient. The fields are hourly outputs, extracted on 1981/01/08 at 1 p.m. (1), 4 p.m. (2), 7 p.m. (3) and 10 p.m. (4) (black dots in Figure 3.7). The top blue and orange line plots represent the westward and eastward volume transport (in Sverdrups), respectively, computed from hourly outputs of zonal velocity. The 1027kg.m^{-3},1027.2kg.m^{-3}, 1028kg.m^{-3}, 1028.8kg.m^{-3}, 1029kg.m^{-3} isopycnal surfaces are illustrated in contours for all panels. The acronyms "ES" and "CS" in gray refer to the Espartel Sill and the Camarinal Sill, respectively (see Figure 3.1). Spatial averages are performed as detailed in Figure 3.5.

ures C.1 and C.2, above the seafloor, it is mainly consistent with the intensification or weakening of the Mediterranean outflow, except at the CS and ES, where tidal reticulation patterns influence Sh. In the Atlantic layer, ΔSh is more complex to interpret. However, it provides insights into the influence of the eastward internal bore released at the CS, which mainly intensifies Sh along its trail (Figure C.2). Stratification variations, displayed in panels (b) of Figures C.1 and C.2, are organized in dipoles, reflecting, on the one hand, a stretching of the isopycnals ($\Delta N^2 < 0$), and on the other hand, a squashing of the isopycnals ($\Delta N^2 > 0$). In panels (c), we indicate the mechanism that contributes the most to the mean stratification tendency based on the vertical stratification tendency equation (see Appendix F for the full derivation). Three processes are involved in this tendency: turbulent buoyancy diffusion (D^{N^2}), frontogenesis (F^{N^2}), and advection of stratification (T^{N^2}). Strong tendencies are mainly due to vertical or zonal advection. For weaker tendencies, the balance is mitigated as zonal and vertical frontogenesis can locally dominate. Finally, turbulent buoyancy diffusion, meridional frontogenesis, and meridional advection play a minor role (the two latter are not displayed in Figures C.1 and C.2).

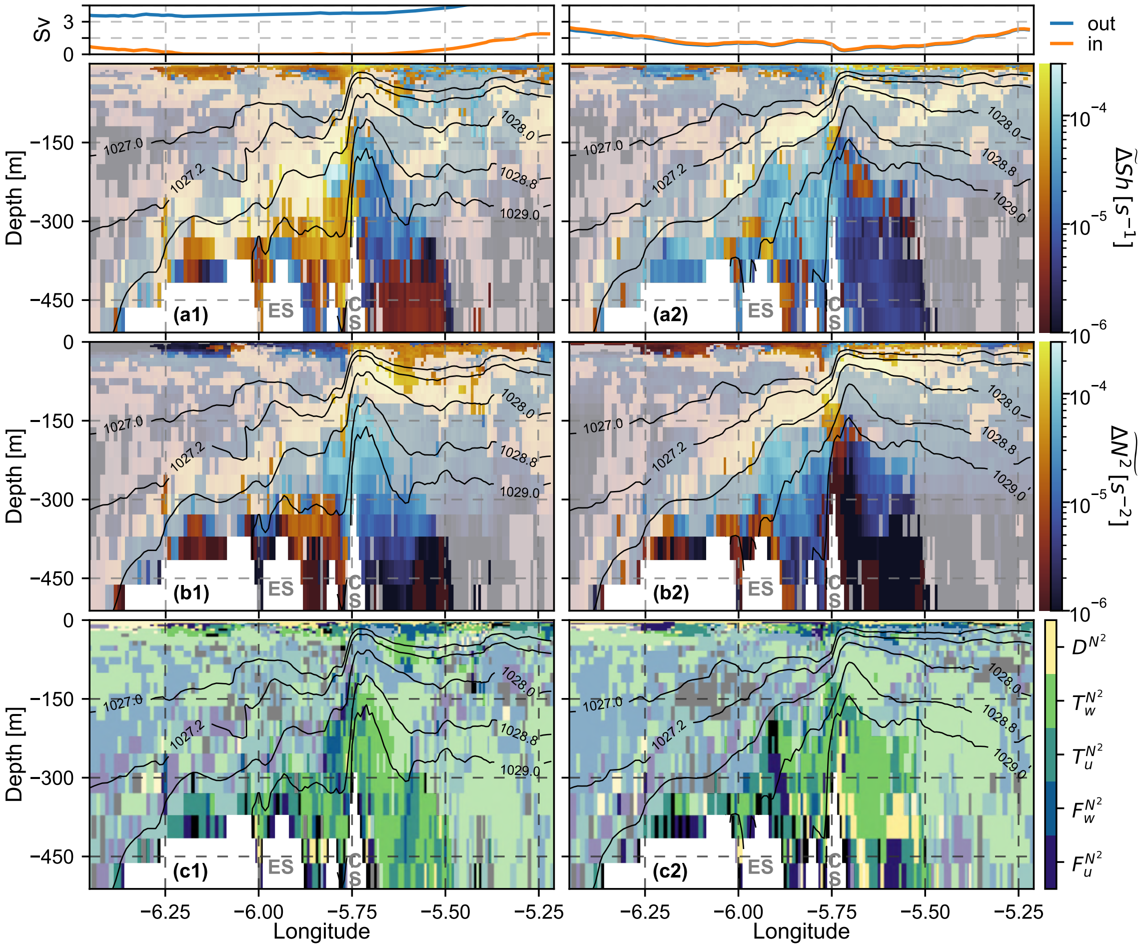

Figure C.1: In shades, from top to bottom: (a) pseudo-meridional average of vertical shear (Sh) and (b) stratification (N^2) variation with respect to the previous tidal phase, and (c) processes dominating the stratification tendency (the term with the maximum absolute value). In panels (c), the considered mechanisms are turbulent buoyancy diffusion (D^{N^2}), vertical and zonal advection of stratification ($T_W^{N^2}$ and $T_U^{N^2}$, respectively), vertical and zonal frontogenesis ($F_W^{N^2}$ and $F_U^{N^2}$, respectively). For the sake of readability, we shade the areas where other mechanisms drive the stratification tendency in black. The fields are hourly outputs, extracted on 1981/01/08 at 1 p.m. (1), 4 p.m. (2) (black dots in Figure 3.7). The top blue and orange line plots represent the westward and eastward volume transport (in Sverdrups), respectively, computed from hourly outputs of zonal velocity. The 1027kg.m^{-3},1027.2kg.m^{-3}, 1028kg.m^{-3}, 1028.8kg.m^{-3}, 1029kg.m^{-3} isopycnal surfaces are illustrated in contours for all panels. Areas where the absolute buoyancy flux variations are lower than $2.5\,10^{-8}$ m^2.s^{-4} in absolute value are made transparent to make the figure clearer. The acronyms “ES” and “CS” in gray refer to the Espartel Sill and the Camarinal Sill, respectively (see Figure 3.1). Spatial averages of the vertical shear and stratification are performed as detailed in Figure 3.5 considering only the cells driving the mean meridional variation computed as described in Appendix E.

E On the diagnostic of buoyancy flux variations

This appendix details the method used to diagnose the mechanisms driving absolute buoyancy flux ($|B| = |K_t N^2|$) variations at the SoG. The method mainly relies on the straightforward influence of stratification and vertical shear on the production of TKE (Appendix B). Namely, the production of TKE increases as stratification

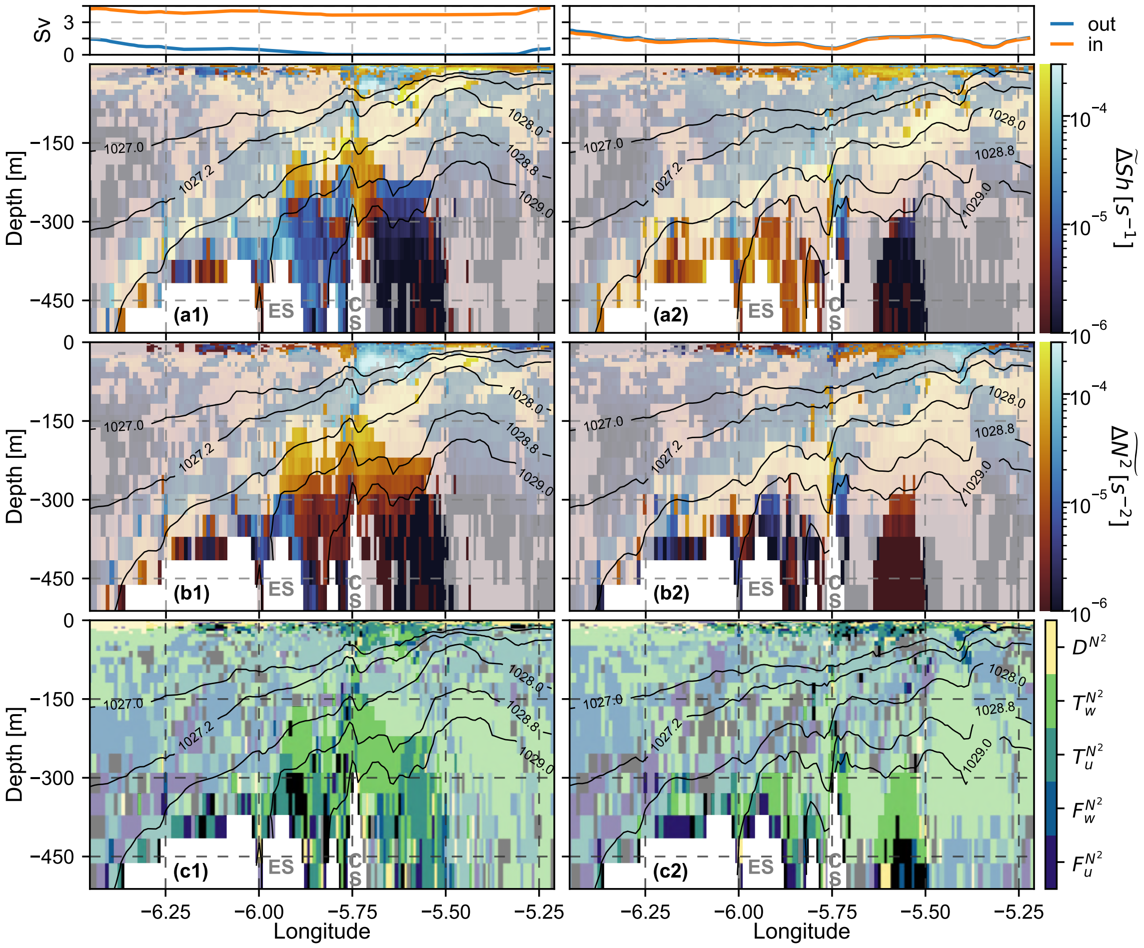

Figure C.2: Same as Figure C.1 for hourly outputs extracted at 7 p.m. (1) and 10 p.m. (2) (black dots in Figure 3.7).

weakens and vertical shear intensifies. However, to extend this simple reasoning to $|B|$, we must first verify that the TKE tendency drives its tendency. Since the buoyancy flux has a limited influence on the TKE at the SoG (see section 3.3), we can have a qualitative idea of the hypothesis validity by comparing meridionally consistent patterns of TKE and $|B|$ variations. To do so, we use the following cost function:

$$J(x) = C + \operatorname{sign}(x)\log_{10}(x) \tag{8}$$

with C a given constant, representing the lowest order of magnitude to be considered for x, and $\operatorname{sign}(x)$ the sign function; $\operatorname{sign}(x) = 1$ if $x > 0$; $\operatorname{sign}(x) = -1$ otherwise.

We choose this specific cost function for its consistency to exponential variations and linear behavior near zero, provided that the constant C is correctly defined. In the following, we use $C = 10^{-8}\,\mathrm{s}^{-2}$ for N^2, $C = 10^{-15}\,\mathrm{m}^2.\mathrm{s}^{-3}$ for B, $C = 10^{-12}\,\mathrm{m}^2.\mathrm{s}^{-2}$ for TKE, and $C = 10^{-8}\,\mathrm{s}^{-1}$ for the vertical shear of horizontal currents Sh. These values are set to have a minimal impact when applying the function to a set of positive values.

To validate the hypothesis formulated above, we first compute the meridional average of $f(\Delta|B|)$, where $\Delta|B|$ is the variation of absolute buoyancy flux with respect to a previous state 3 hours earlier. We consider that a 3-hour time gap is sufficiently small to follow the variations of vertical shear and stratification and sufficiently long to minimize the diagnostic sensitivity to short-scale and transient variations. Thus, for each of the meridional profiles considered, the average $f(\Delta|B|)$ indicates whether $|B|$ consistently increases or decreases. In the following, in order to isolate the mechanism driving meridionally consistent variations of $|B|$, we only consider the cells responsible for these variations. For each meridional profile, we average the image of $|B|$ and TKE variation by the cost function over these cells. Over the analyzed period, the resulting fields are highly correlated (Pearson correlation coefficients between 0.94 and 0.96) over the ocean interior, illustrating a strong relationship between $|B|$ and TKE tendencies. We do not consider the top fifty meters and the cells directly above the seafloor in this analysis because boundary conditions influence the intensity of ΔB in these areas, which may disturb the correlation scores. However, note that the influence of boundary conditions is not an issue in the following as vertical shear variations indirectly reflect it. Thus, we conclude that the buoyancy flux variations are, at least to the first order, resulting from TKE variation.

In light of these results, we consider it reasonable to interpret the variation of $|B|$ using simple logical relations based on the effects of stratification and vertical shear on the TKE tendency. Theses logical relations, summarized in table D.2, are applied to the meridional averages of $f(\Delta|B|)$ (panels (c) of the Figures 3.9, 3.10), $f(\Delta|N^2|)$ and $f(\Delta|\mathrm{Sh}|)$ (panels (a) and (b) of the Figures C.1 and C.2) over the cells responsible for the meridionally consistent variations of $|B|$. When both stratification and vertical shear drive $|B|$, we identify the dominant mechanism by comparing the respective influence of their variation on the Richardson number $Ri = N^2/\mathrm{Sh}$. Namely, we compare the following terms: $\frac{\Delta N^2}{\mathrm{Sh}}$ and $\frac{\Delta \mathrm{Sh} N^2}{\mathrm{Sh}(\mathrm{Sh}+\Delta \mathrm{Sh})}$. Finally, note that the cases marked as N.A. in Table D.2 should never occur if the variations of $|B|$ are fully defined by the TKE tendency. In practice, these cases are encountered at a few locations, shaded in black in Figures 3.9 and 3.10, where the formulated hypothesis fails. However, the few occurrences of these exceptions gives confidence in the consistency of the diagnostics.

F Derivation of the stratification tendency

In this appendix, we formulate the tendency equation for the vertical density stratification. As in Hoskins (1982), we start from the Lagrangian trend of density which we then derive vertically:

$$\begin{aligned} \frac{d\rho}{dt} &= \frac{\partial \rho}{\partial t} + \mathbf{U}\cdot\nabla\rho \\ \Rightarrow \frac{\partial}{\partial z}\left(\frac{d\rho}{dt}\right) &= \frac{\partial^2 \rho}{\partial z\,\partial t} + \frac{\partial \mathbf{U}}{\partial z}\cdot\nabla\rho + \mathbf{U}\cdot\nabla\frac{\partial\rho}{\partial z} \\ \Rightarrow \frac{\partial}{\partial z}\left(\frac{d\rho}{dt}\right) &= \frac{d}{dt}\left(\frac{\partial\rho}{\partial z}\right) + \frac{\partial \mathbf{U}}{\partial z}\cdot\nabla\rho \end{aligned} \tag{9}$$

(a) $\Delta|B| > 0$

	$\Delta\text{Sh} > 0$	$\Delta\text{Sh} < 0$
$\Delta N^2 > 0$	Sh	N.A
$\Delta N^2 < 0$	both	N^2

(b) $\Delta|B| < 0$

	$\Delta\text{Sh} > 0$	$\Delta\text{Sh} < 0$
$\Delta N^2 > 0$	N^2	both
$\Delta N^2 < 0$	N.A	Sh

Table D.2: These tables summarize, for a given variation of the absolute buoyancy flux $|B|$, the possible variations of vertical shear of horizontal currents (Sh) and stratification (N^2) and the driving mechanism that may be deduced from these combinations. In a nutshell, the buoyancy flux is supposed, as for the TKE, to increase when vertical shear intensifies and stratification weakens. The driving mechanism is diagnosed as the one of consistent variations with respect to the buoyancy flux. The acronym N.A. (Not Attributed) indicates combinations not allowed by the theoretical framework. We indicate the cases where both stratification and vertical shear drive the buoyancy flux tendency with the term "both".

With $\mathbf{U} = (u, v, w)$ the velocity vector and ∇ the nabla operator.

Assuming that the Lagrangian tendency of potential density is dominated by turbulent mixing, i.e. $\frac{d\rho}{dt} \simeq -\frac{\partial}{\partial z}\left(K_t \frac{\partial\rho}{\partial z}\right)$, we can write :

$$\begin{aligned} \frac{d}{dt}\left(\frac{\partial\rho}{\partial z}\right) &\simeq -\frac{\partial^2}{\partial z^2}\left(K_t\frac{\partial\rho}{\partial z}\right) - \frac{\partial\mathbf{U}}{\partial z}\cdot\nabla\rho \\ \Rightarrow \frac{\partial}{\partial t}\left(\frac{\partial\rho}{\partial z}\right) &\simeq -\frac{\partial^2}{\partial z^2}\left(K_t\frac{\partial\rho}{\partial z}\right) - \frac{\partial\mathbf{U}}{\partial z}\cdot\nabla\rho - \mathbf{U}\cdot\nabla\frac{\partial\rho}{\partial z} \end{aligned} \tag{10}$$

From the definition of the Brunt-Väisälä frequency : $N^2 = -\frac{g}{\rho_0}\frac{\partial\rho}{\partial z}$ we can thus estimate the vertical stratification Eulerian tendency as follows:

$$\frac{\partial N^2}{\partial t} \simeq \underbrace{-\frac{\partial^2 B}{\partial z^2}}_{D^{N^2}} + \underbrace{\frac{g}{\rho_0}\frac{\partial\mathbf{U}}{\partial z}\cdot\nabla\rho}_{F_u^{N^2}+F_v^{N^2}+F_w^{N^2}} - \underbrace{\mathbf{U}\cdot\nabla N^2}_{T_u^{N^2}+T_v^{N^2}+T_w^{N^2}} \tag{11}$$

with $B = K_t N^2$ the vertical buoyancy flux. This tendency is composed of 7 terms, which can be associated with three mechanisms:

- The turbulent diffusion of vertical stratification D^{N^2}
- The frontogenesis terms, which represent the deformation of density gradients by convergent/divergent velocities: $F_u^{N^2}$,$F_v^{N^2}$, and $F_w^{N^2}$.
- The transport of vertical stratification: zonal $T_u^{N^2}$, meridional $T_v^{N^2}$ and vertical $T_w^{N^2}$. It simply advects the N^2 field.

To validate the estimated density tendency, for each hour illustrated in Figures 3.9 and 3.10, we have compared the sum of the tendency terms computed from 2 hourly averaged fields with a first-order finite-difference 3-hourly spaced upwind scheme estimate of the total tendency. The error in the total density tendency decimal logarithm is lower than 10% over at least 97% of the domain and low in areas of strong tendency.

Chapter 4

Influence of the SoG on the Mediterranean sea and climate

In the previous chapter we have investigated tidal mixing at the strait of Gibraltar (SoG hereinafter), a key process driving the transformation of exchanged water masses through the SoG. In particular, we have highlighted that this process strongly relies on the interaction of tidal currents with abrupt topographic obstacles within the strait. Overall, these results suggest that both tidal and fine-scale dynamics are essential elements shaping the hydrographic and dynamical structure of the exchange flow through the SoG. In addition, given the large influence of the Atlantic water masses on the Mediterranean Sea surface properties, this suggests that local tidal and fine-scale processes at the SoG may have a substantial large-scale impact on the Mediterranean Sea and possibly on the atmosphere over coastal areas. Those aspects are investigated in this chapter with the numerical framework introduced in Chapter 2.

4.1 Introduction

Previous studies have pointed out that local processes at the SoG influence the dynamics and thermodynamics of the Mediterranean Sea. Tide-induced vertical mixing and recirculation at the SoG is known to have a cooling and salting effect on the surface of the Mediterranean Sea Naranjo et al (2014); Harzallah et al (2014); Sannino et al (2015). Consequently, tides are believed to indirectly enhance deep convection over the Northwest Mediterranean and could thus have an impact on deeper layers. On the other hand, the fine-scale dynamical structure of the exchange flow through the SoG has been shown to influence the stratification, circulation and deep convection of the western Mediterranean Basin (WMB hereinafter Sannino et al, 2009b).

Thus, tidal and fine-scale mechanisms at the SoG are relevant not only to the exchanges through the strait, but also to the Mediterranean Sea hydrographic properties and their variability. However, the respective importance of these mechanisms and their possible interactions remain unclear so far. In addition, although their individual influence on the Western Mediterranean surface is relatively well understood, its extent to deeper layers and the Eastern Mediterranean Basin (EMB hereinafter) is less clear. Finally, given the large heat and water exchanges taking place at the air-sea interface of the Mediterranean, the influence of local processes at the SoG on the overlying and coastal atmosphere remains an open question. Therefore, investigation of the remote impacts of tidal and fine-scale exchanges at the SoG would provide a deeper understanding on the Mediterranean Sea mean state, its variability, and its interactions with the atmosphere. On the technical side, this would provide ocean modelers with valuable information on the capabilities and limitations of current state-of-the-art numerical models, which often omit tidal and fine-scale exchanges at the SoG (Harzallah et al, 2014; Soto-Navarro et al, 2015; Sannino et al, 2015; Harzallah et al, 2018; Llasses et al, 2018; Soto-Navarro et al, 2020; Sannino et al, 2022).

Therefore, the present chapter investigates the local effects of tidal and fine-scale mechanisms at the SoG and their influence on the Mediterranean Sea hydrographic properties, convective activity and interactions with the atmosphere. To do so, we make use of the four coupled NEMOMEDGIB configurations introduced in Chapter 2, differing only by the inclusion or omission of the tidal forcing (T/NT) and the enhanced horizontal resolution at the SoG (HR/LR, see Figure 4.1). In the following, we first introduce the conceptual framework used in this study. Then, after validating the simulated tidal forcing at the SoG and the Mediterranean Sea, we first investigate the local impact of the enhanced representation of the SoG on the exchange flow through it. As a second step, we assess the propagation of these effects over the surface layer of the Mediterranean Sea. Then, we investigate the remote effects of the SoG on the Mediterranean convective activity, and its consequences on surface, intermediate, and deep water masses and their variability. Finally, we investigate impacts on air-sea exchanges and on the overlying atmosphere.

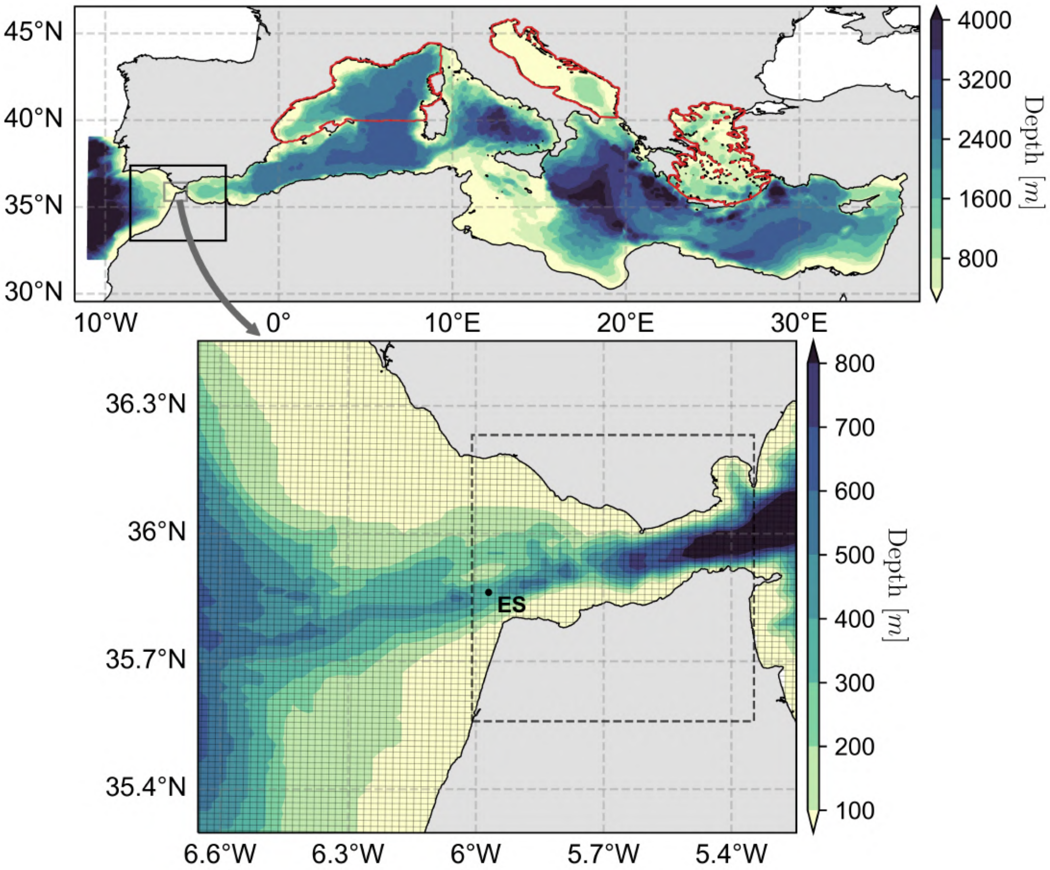

Figure 4.1: NEMOMEDGIB coarse bathymetry (upper panel) and zoom on the refined grid and bathymetry at the Strait of Gibraltar (lower panel, representing the area framed by the grey rectangle). The black rectangle on the upper panel shows the area over which horizontal grid and bathymetry refinements are activated (AGRIF domain). Red contour lines show the masks used for the Northwestern Mediterranean Basin, the Adriatic Sea, and the Aegean Sea. The dashed rectangle on the lower panel displays the area used to investigate average hydrography and dynamics of the Strait of Gibraltar. The black dot at the Espartel Sill (indicated by the acronym "ES") shows the in situ velocity profile measurement site (INGRES project, Sammartino et al, 2015)

4.2 Methods

4.2.1 Decomposing the effects of tidal and fine-scale dynamics at the SoG

As schematized in Figure 4.2, we diagnose the influence of tides at the SoG from the differences (anomalies hereinafter) between the T LR and NT LR simulations (δ_{Tides} = T LR - NT LR), and the influence of fine-scale dynamics from the differences between the NT HR and NT LR simulation (δ_{Res} = NT HR - NT LR). In addition, we diagnose combined effects (δ_{TR}) as the residual anomaly required to explain the total difference between the T HR and NT LR simulation (δ_{TR} = T HR - NT LR - δ_{Tides} - δ_{Res}). Regarding the interpretation of the aforementioned terms, it is essential to specify that although we refer to δ_{Tides} and δ_{Res} as the anomalies induced by ”tides” and “fine-scale” dynamics, these terms more precisely represent the large-scale effects of tides and the non-tidal effects associated to the refined representation of the SoG. In this way, the effect of tides in the context of high-resolution simulation is given by the sum of δ_{Tides} and δ_{TR}. Similarly, the effect of a refined representation of the SoG in the context of tidal simulations is given by the sum of δ_{Tides} and δ_{TR}. In addition, it is noteworthy that the “fine-scale dynamics” diagnosed from δ_{Res} also encompass the influence of fine-scale topographic structures introduced in higher-resolution simulations. For the sake of clarity, we will thus refer to δ_{Res} as the influence of Fine-scale Topography and Dynamics (FTD hereinafter).

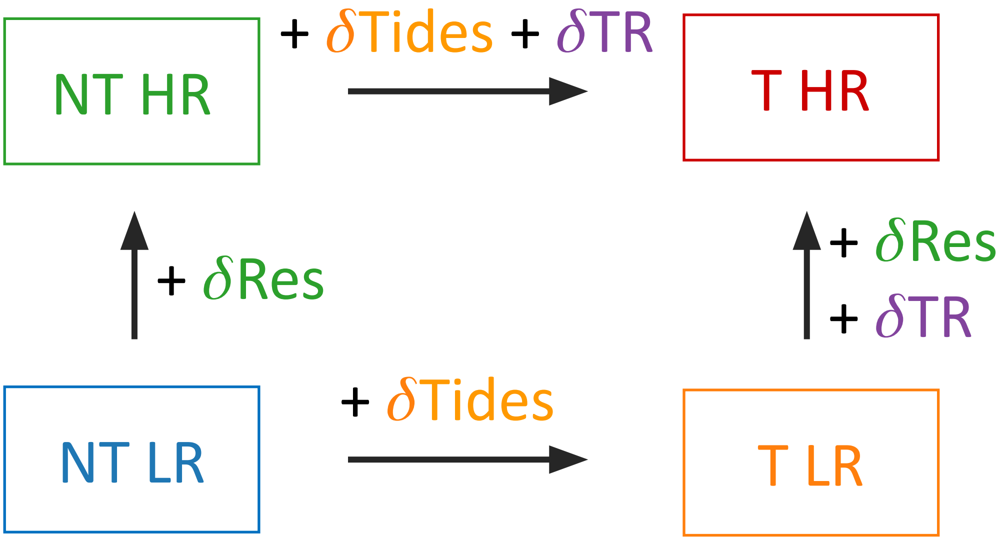

Figure 4.2: Schematic of the investigated simulations and their relations in terms of anomalies induced by tidal (δ_{Tides}), fine-scale (δ_{Res}), and combined (δ_{TR}) mechanisms.

4.2.2 Definition of volume, heat, and salt transports at the SoG

As in the previous chapter, we define the transports through the SoG in the framework of a two-way exchange flow between the Mediterranean Sea and the Atlantic Ocean. We compute the net volume (Q_{net}), heat (QH_{net}), and salt (QS_{net}) transports as specified in the previous chapter, by integrating the currents, heat, and salt fluxes over a section of interest.

Regarding eastward (inflow hereinafter) and westward (outflow hereinafter) transports, their estimation based on a time-varying interface as in Sammartino et al (2015) requires handling a large volume of data. Thus, as in the previous section, we consider two main estimates, capturing different aspects of the temporal variability of the exchanges. For high-frequency transports, we use the Q_{in}^{max} and Q_{out}^{max} estimates introduced in the previous chapter. For low-frequency transports, we rely on estimates computed from average outputs over the simulated period, distinguishing the two flows with the climatological zero-velocity interface. In the following, we refer to these latter estimates as Q_{in}^{A} and Q_{out}^{A}.

As detailed in the following, to validate the simulated volume transports through the strait, we will consider the Q^{A} estimates, which we compare to observation-based estimates corrected from the high-frequency dynamics. More specifically, for the outflow transport, we consider the estimate of Sammartino et al (2015), to which we remove the associated “eddy flux” contribution of 0.04Sv. For the inflowing transport, we consider the former low-frequency outflow transport, to which we add the net transport estimate of 0.04Sv from Jordà et al (2017b, Table 3).

4.3 Model Validation

4.3.1 Tidal validation

In this section, we validate the simulated tides against available observation-based datasets and reference simulations. Tidal amplitudes and phases analyzed in the following are extracted from hourly outputs over 2013 using the “Utide” Python package (version 0.2.5). For the sake of conciseness, we focus on the four most energetic tidal harmonics over the SoG and the Mediterranean region: the principal lunar and solar semidiurnal constituents (M2 and S2, respectively), and the lunisolar and lunar diurnal constituents (K1, O1, respectively).

Strait of Gibraltar

Tidal currents are known to play a key role in the dynamics and thermodynamics of the SoG. In this way, the realism of simulated tides at the SoG is essential to investigate. To start with, we display in Figure 4.3 the amplitude and phase of the simulated tidal elevation patterns in the vicinity of the SoG. As reference datasets, we consider the M2, S2, K1, and O1 observation-based charts of Lafuente et al (1990) (GL90 hereinafter) and the M2 observation-based chart of Candela et al (1990) (CA90 hereinafter), interpreting the differences between the GL90 and CA90 charts as an observational uncertainty (not shown). In addition, we include in Figure 4.3 the tidal amplitudes and phases from the global tidal atlas FES2014 (produced by Noveltis, Legos, and CLS and distributed by Aviso+, with support from CNES: https://www.aviso.altimetry.fr/) as a reference numerical tidal model. Note that the FES2014 model is barotropic and, thus, does not represent the influence of baroclinic processes on the tidal elevation patterns. However, given the large barotropic character of tides at the SoG, it can be considered as a consistent reference.

With respect to the aforementioned references, the T HR and T LR simulations display realistic tidal elevations within the SoG. Specifically, the M2 and S2 tidal amplitudes abruptly decrease from the western entrance of the strait ($\sim 90\, cm$ for M2, $\sim 30 cm$ for S2) to its eastern exit ($\sim 25 cm$ for M2, $\sim 10 cm$ for S2), whereas the associated phases decrease from south to north (Lafuente et al, 1990; Candela et al, 1990). For the K1 and O1 harmonics, both the T HR and T LR simulations capture the north-eastward decrease of tidal amplitudes and zonal variation of tidal phases from the GL90 charts, whereas these patterns are less clear in FES2014. In terms of biases, for both T HR and T LR, the simulated M2 tidal amplitudes fall within the range of the uncertainty interval provided by GL90 and CA90. The associated tidal phases are also consistent with GL90 and CA90, displaying typical biases of a few degrees, with better overall consistency than FES2014. Similar differences from GL90 arise for the S2 harmonic, with a more accurate representation of zonal phase variations at the center of the strait in the T HR simulation. For the K1 and O1 harmonics, the simulated elevation patterns display moderate differences with respect to GL90, typically less than one centimeter, with an overall better consistency than FES2014. The associated tidal phases are subject to larger biases due to their significant variability. However, they remain largely consistent with GL90. In particular, the T HR accurately reproduces the O1 amphidromic point at the southern tip of Spain.

In addition to tidal elevation patterns, we will now validate the baroclinic structure of the simulated tidal currents, which has a notable influence on the structure of the exchange flow at hourly high-frequency (Lafuente et al, 2000). To do so, we display in Figure 4.4 vertical profiles of tidal ellipses at the ES, extracted from the observation-based INGRES dataset (more details in Sánchez-Román et al, 2008, 2009; Sammartino et al, 2015) and the simulated velocity fields at the closest point to the measurement station. In a nutshell, the displayed tidal ellipses synthesize the evolution of horizontal tidal currents throughout the tidal cycle.

Over the upper 100m depth, the simulated tidal currents are in good agreement with INGRES observations. In particular, the intensity and phases of the considered harmonics are well reproduced, although both T LR and T HR moderately overestimate the M2 and S2 amplitudes, and T LR underestimates the K1 and O1 amplitudes. The simulated tidal phases are also consistent with observations, with more significant biases for the K1 and O1 harmonics and a notable improvement in the T HR simulation. Below 100m depth, the T HR simulation remains almost equally realistic and captures well the vertical variations of tidal amplitudes, ex-

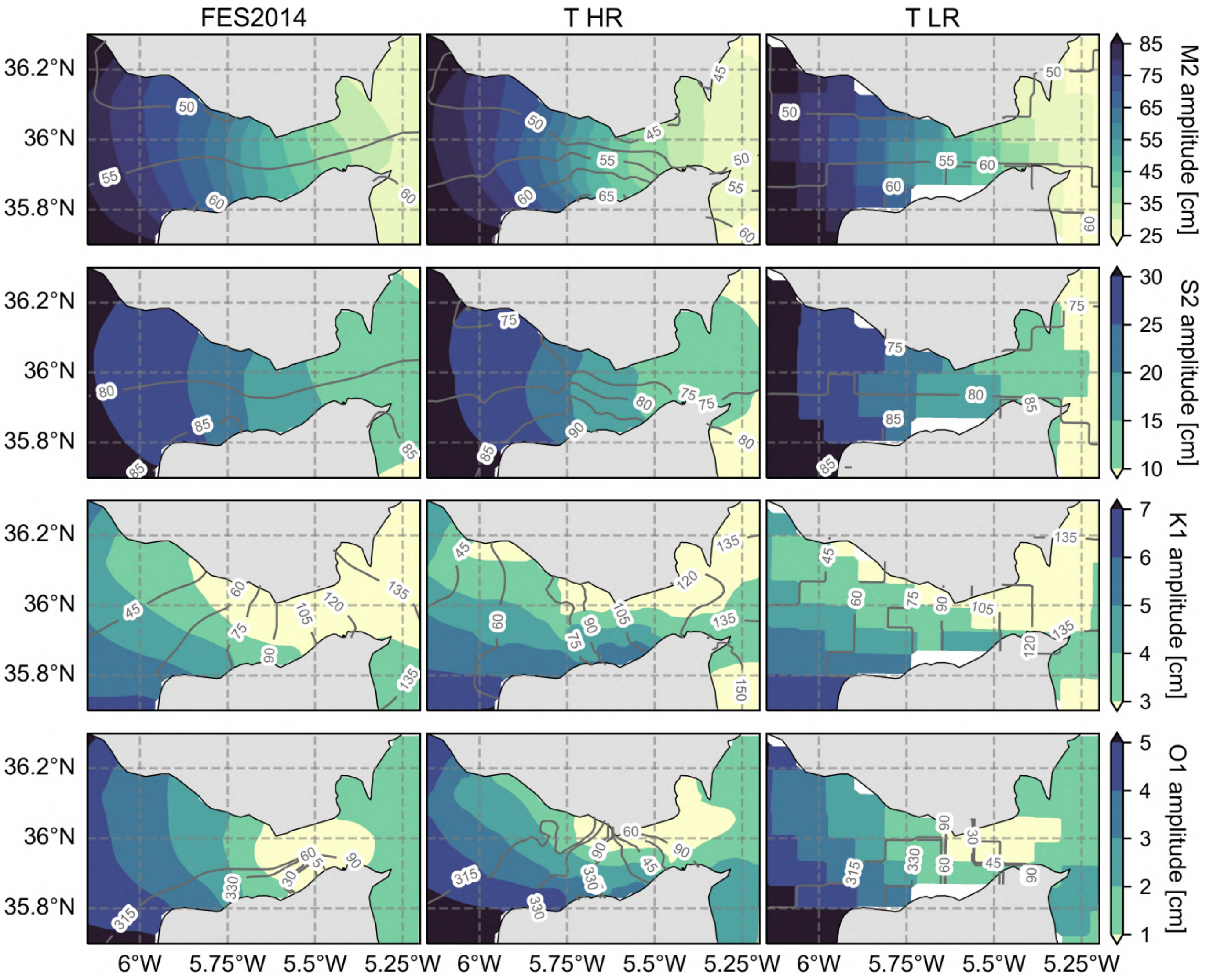

Figure 4.3: In shades from top to bottom, M2, S2, K1 and O1 tidal harmonics elevation amplitudes. We display in contours the associated phases. From left to right, we represent the global tidal atlas FES2014, the high-resolution and low-resolution tidal NEMOMEDGIB simulations. For NEMO simulations, tidal amplitudes and phases are estimated from hourly outputs of instantaneous (not averaged) sea level elevation over 2013 using the "Utide" Python package (version 0.2.5). FES2014 fields are interpolated on the high-resolution model grid through bilinear interpolation, following Xu (2018).

cept for a local overestimation of the M2 amplitude at 199m depth. On the other hand, the T LR configuration largely underestimates the zonal tidal component. Specifically, these discrepancies are attributable to the shallow seafloor in the T LR configuration, which influences tidal currents through bottom friction.

Finally, it is noteworthy that the rotation of tidal ellipses (indicated by "x" and "+" symbols in Figure 4.4) is rarely inverted with respect to observations. The affected ellipses are generally characterized by low meridional currents and consistent phases with respect to observations. Thus, the rotating direction has a minor effect on the associated tidal currents.

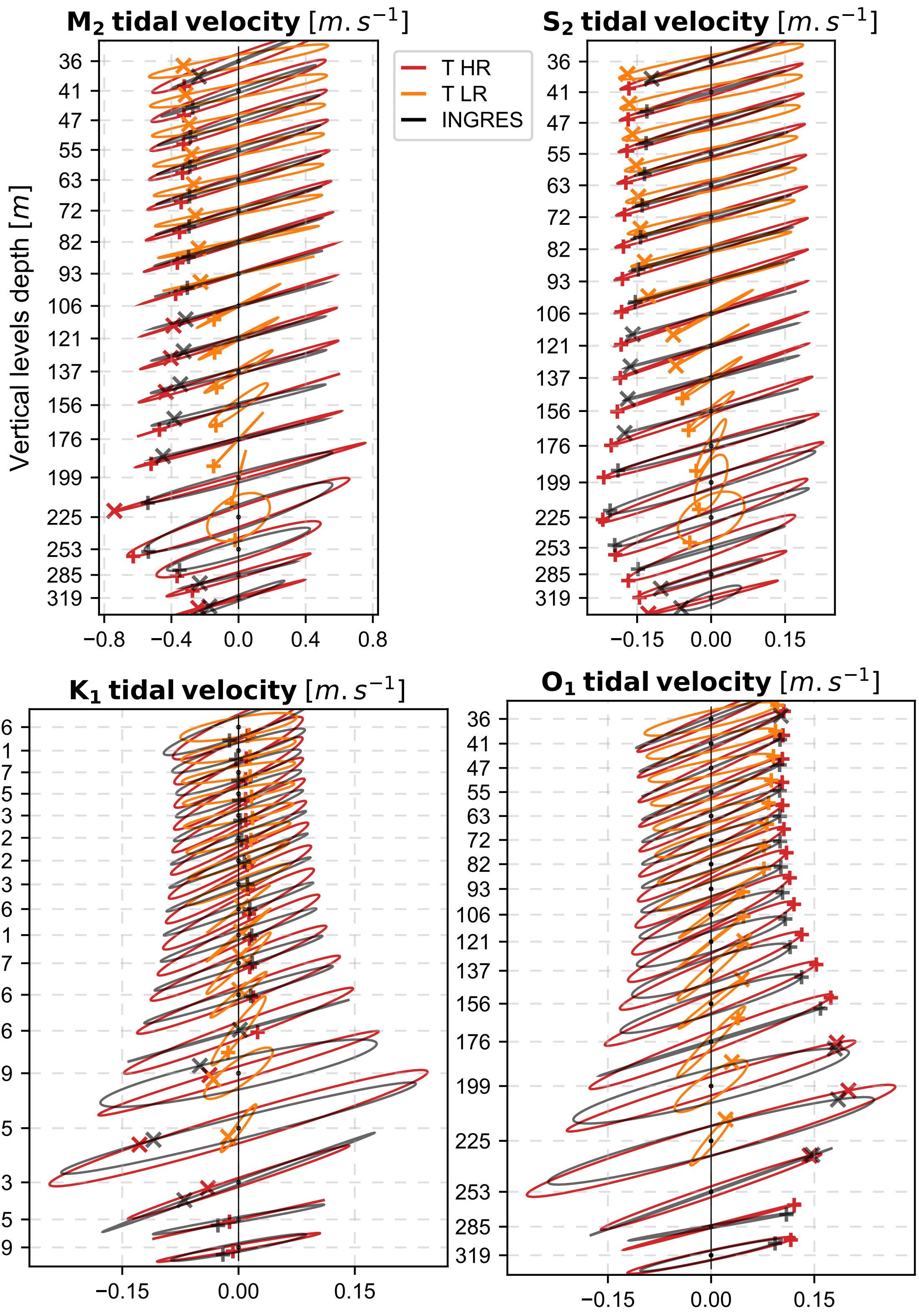

Figure 4.4: Vertical profile of tidal ellipses associated with the M2, S2, K1, and O1 horizontal tidal currents at the Espartel Sill (INGRES location, $\simeq 35.86°N,\ 5.97°W$; black dot in the lower panel of Figure 4.1) over year 2013. In red and orange, we display the NEMOMEDGIB simulation with (T HR) and without (T LR) grid refinement at the SoG, respectively. In black, we display in situ Doppler current profiler measurements from the INGRES project. Meridional currents (along the y-axis) are stretched by a factor of three for the sake of readability. The location of the current vector at the zero Greenwich phase is indicated by the symbols “+” (counterclockwise) and “x” (clockwise). Tidal ellipse parameters are computed using the “Utide” Python package (version 0.2.5) from instantaneous outputs of horizontal currents for NEMOMEDGIB simulations, and instantaneous 30-minute measurements for the INGRES dataset. NEMOMEDGIB horizontal velocities are obtained by projecting the model outputs onto the zonal and meridional directions. Measurements are linearly interpolated onto the model vertical grid.

To conclude on the tidal validation at the SoG, the former analyses indicate an overall consistency with available references, with a notable improvement of the baroclinic tide at high resolution. In light of these results, we consider that the simulations are relevant to study the influence of tides on the exchanged water masses through the SoG and the subsequent impact on the Mediterranean Sea.

Mediterranean Sea

In order to validate the simulated tides over the Mediterranean Sea, we consider two sets of observations. For deep water areas, we refer to tidal harmonics derived from altimetry data (DOI: 10.6096/CTOH_X-TRACK_Tidal_2018_01) developed, validated by the CTOH/LEGOS, France, and distributed by Aviso+ (referred to as XTRACK hereinafter). For coastal areas, we refer to tidal gauge measurements retrieved from the Copernicus in situ TAC network (Copernicus Marine In Situ Tac Data Management Team (2017); Copernicus in situ TAC - CMEMS regions definition. SEANOE. https://doi.org/10.17882/44395). In the following, we quantify the performance of the simulations from the differences between the observed and simulated signals in the sinusoidal basis (Foreman et al, 1993), which will be referred to as tidal misfit errors.

To start with, we display in Figure 4.5 the amplitude and phase of the simulated M2 and S2 tidal elevations over the Mediterranean Sea and overlay the tidal misfit error with respect to the TAC tidal gauge network. As previously done for the SoG, we include the tidal amplitudes and phases from the global tidal atlas FES2014 as a reference numerical tidal model. Overall, The T HR and T LR simulations display highly similar elevation and phase patterns over the Mediterranean Sea and are in good agreement with FES2014. The M2 harmonic reaches typical amplitudes of a few centimeters over most of the Mediterranean and locally exceeds 10cm over the Tyrrhenian Sea, 20cm over the north of the Adriatic Sea, and more than 40cm (not shown) over the Gulf of Gabès. The S2 harmonic displays similar patterns and mainly differs by its lower amplitude, reaching typical values of a few centimeters and locally exceeding 10cm over the gulf of Gabès and the north Adriatic. More specifically, both the T HR and T LR simulations reproduce the main M2 and S2 amphidromic points (Tsimplis et al, 1995) located south of the Balearic islands, within the Sicily channel, in the northern Adriatic Sea, and between the north coast of Africa and the South coast of Crete. We summarize the overall performance of the simulations in Table 4.1, which displays average tidal misfit error with respect to the TAC tidal gauge network and XTRACK. Over coastal areas, the simulations display reasonable tidal misfit errors with respect to the TAC tidal gauge network, higher than those of FES2014 but comparable to errors obtained with similar models (Palma et al, 2020). Maximal discrepancies arise in the Adriatic Sea, where the simulations overestimate the tidal amplitude (colored points in Figure 4.5). Over deep water areas, tidal misfit errors with respect to XTRACK are also reasonable, although higher than FES2014 errors. Maximal discrepancies are found in the Adriatic sea, where the simulations overestimate the tidal amplitude, and in the vicinity of the Gulf of Gabès and the Levantine basin, where they underestimate it (not shown).

As for the M2 and S2 harmonics, we display in Figure 4.6 the amplitude and

Simulation	M2		S2		K1		O1	
	TG	Sat	TG	Sat	TG	Sat	TG	Sat
FES2014	1.12	0.92	0.34	0.85	0.45	1.66	0.24	0.53
T HR	1.54	1.77	0.67	1.26	0.70	1.70	0.24	0.54
T LR	1.66	1.77	0.68	1.24	0.71	1.73	0.4	0.58

Table 4.1: Tidal misfit error (in cm) with respect to the Copernicus tidal gauge dataset (TG) and X-TRACK Tidal Constants (Sat, combinaison of TP+J1+J2 and TPN+J1N datasets) for the global tidal atlas FES2014 and the NEMOMEDGIB simulations with (HR) and without (LR) grid refinement at the SoG. The tidal harmonics of X-TRACK are based on satellite observations covering the 1993/02/28-2015/07/24 (TP+J1+J2) and 2002/09/21-2012/02/02 (TPN+J1N) periods. The associated tidal harmonics are interpolated on the NEMOMEDGIB grid. For the Copernicus dataset, tidal harmonics are estimated from the observed sea surface elevation using the "Utide" Python package (version 0.2.5). The temporal coverage of the considered tidal gauge station varies within the 1992-2022 period. However, most of the data has been obtained between 2005-2022. The obtained harmonics are compared to the NEMOMEDGIB and FES2014 (in its original grid) harmonics at the closest grid point to the measurement station. For NEMOMEDGIB simulations tidal harmonics are also extracted with the "Utide" Python package, using hourly outputs of instantaneous sea surface elevation over 2013.

phase of the NEMOMEDGIB simulations and FES2014 for the K1 and O1 tidal elevations over the Mediterranean Sea and overlay the tidal misfit error with respect to the TAC tidal gauge stations. Once again, The T HR and T LR simulations display highly similar elevation and phase patterns and are in good agreement with FES2014. The K1 and S2 harmonics reach typical amplitudes of a few centimeters and display maximal values over the north of the Adriatic Sea, where K1 exceeds 10cm, and O1 exceeds 5cm. Both T HR and T LR reproduce the K1 amphidromic point in the Sicily channel and the O1 amphidromic point on the northern coast of Libya. Over coastal areas, tidal misfit errors with respect to the TAC tidal gauge network are higher then that of FES2014. However, they remain comparable to errors obtained with similar models (Palma et al, 2020) (Table 4.5). Over deep water areas, the simulations display a similar tidal misfit error with respect to XTRACK than FES2014 (Table 4.5). As for the M2 and S2 harmonics, maximal errors are found over the Adriatic Sea, where the simulations overestimate the tidal amplitude, and in the vicinity of the Gulf of Gabès and the Levantine basin, where they underestimate it.

In light of the former results, we consider that the simulations satisfactorily represent the tidal elevation patterns within the Mediterranean Sea.

4.3.2 Currents at the SoG

As a final step to validate the simulated dynamics at the SoG, we investigate the consistency of the baroclinic zonal velocities with respect to available observations. We display on the left panel of Figure 4.7 the 2005 – 2015 average zonal velocity

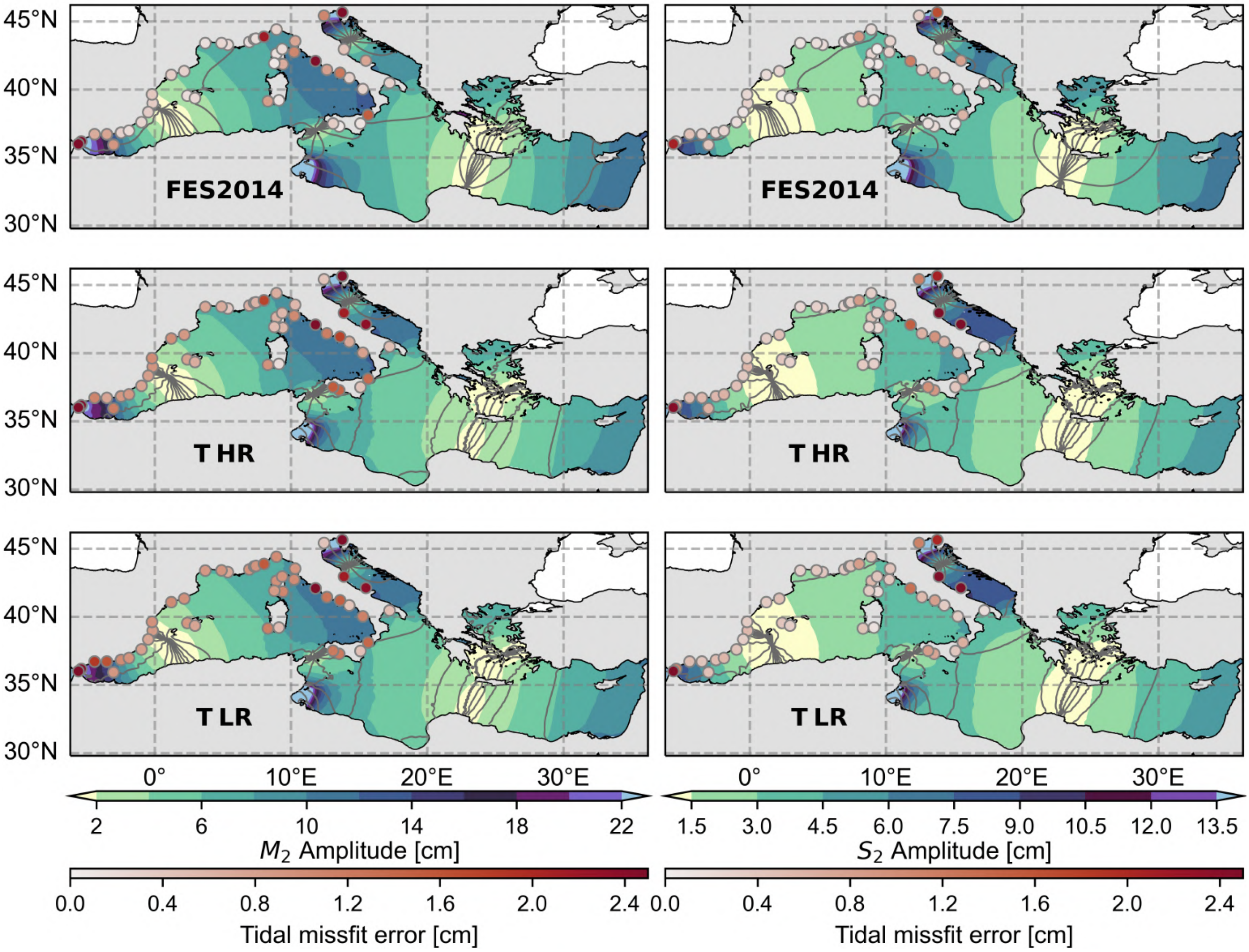

Figure 4.5: In shades, tidal elevation amplitude for the M2 and S2 tidal harmonics (left and right panels, respectively). We display in contours the associated phases, ranging from 0° to 340° with a constant increment of 20°. From top to bottom, we represent the global tidal atlas FES2014 followed by NEMOMEDGIB with (HR) and without (LR) grid refinement at the SoG, respectively. For NEMOMEDGIB simulations, tidal amplitudes and phases are estimated from hourly outputs of instantaneous sea level elevation over 2013 using the "Utide" Python package (version 0.2.5). FES2014 fields are displayed in their original grid.

profile of the T HR, T LR, NT HR, and NT LR simulations and of the INGRES situ Doppler current profiler measurements. To investigate the associated temporal variably, we display on the right panel the 2013 hourly standard deviation (std hereinafter) of zonal velocity. Note that we only consider the 2013 period due to the large volume of data associated with hourly outputs. However, we consider that this provides satisfactory temporal coverage to assess the main simulation biases.

Overall, the simulations all reproduce the two-layer structure of the average exchange flow through the SoG. With respect to INGRES measurements, the NT LR,

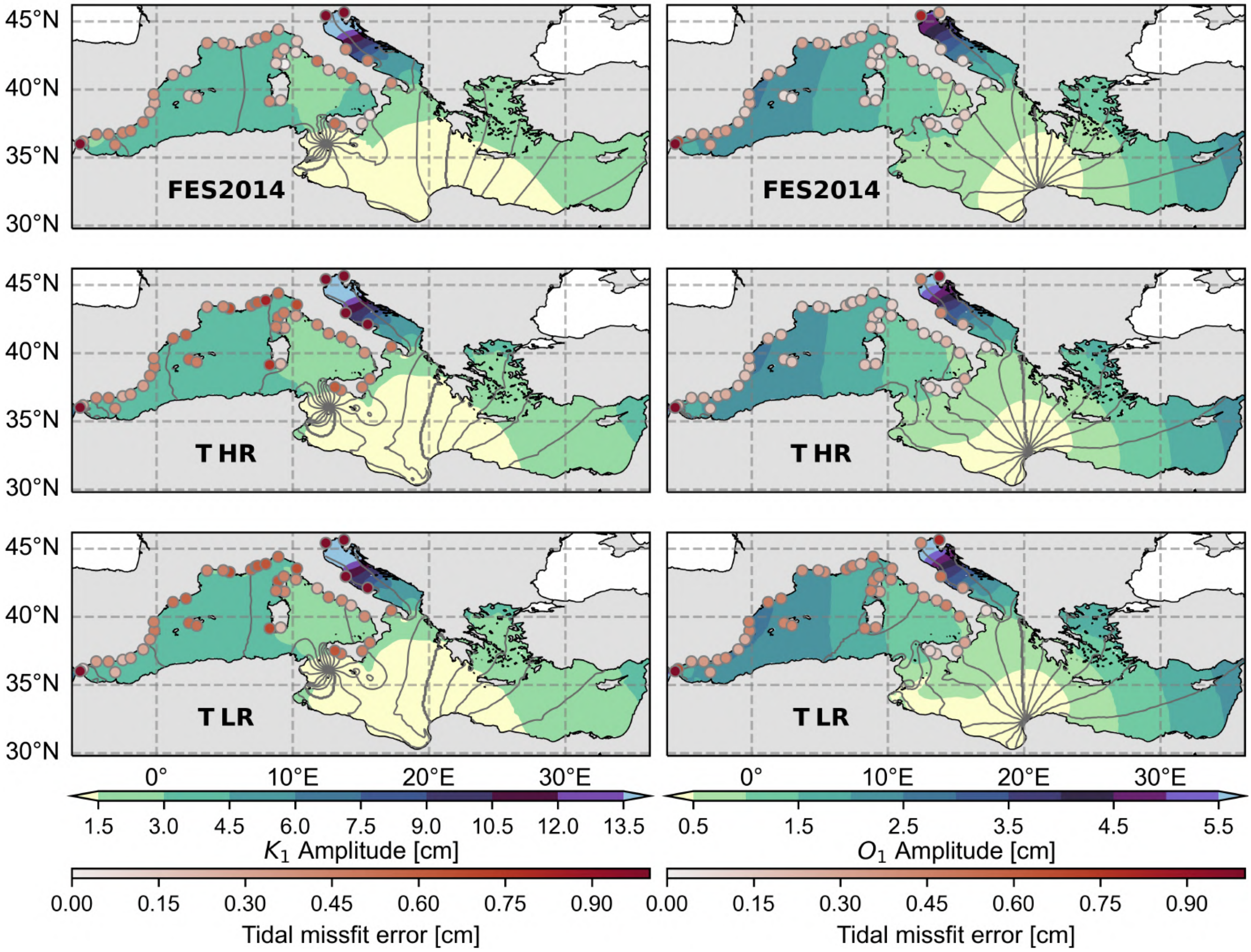

Figure 4.6: Same as Figure 4.5 for the K1 and O1 tidal harmonics.

T LR, NT HR, and T HR simulations exhibit high vertical correlation coefficients of 0.98, 0.96, 0.98, and 1.0 and relatively modest root-mean-square errors (RMSE hereinafter) of 0.15, 0.15, 0.14, and 0.09 m.s^{-1}, respectively, with notable improvements in T HR (red line). More specifically, low-resolution configurations (blue and orange lines) mainly underestimate zonal velocities, whereas simulations with refined resolution (green and red lines) underestimate the zonal velocities between $\sim$ 50 - 180m depth and overestimate them underneath. Regarding the climatological zero-velocity interface, T HR and T LR are in good agreement with INGRES measurements. On the other hand, NT LR underestimates the interface depth by $\sim$ 20m, and NT HR overestimates it by $\sim$ 30m. A comparison of the simulations provides some insight into these discrepancies. It shows that inclusion of tidal forcing results in a rising of the interface (orange versus blue lines and red versus green lines), attributable to tidal recirculation at the ES (Sanchez-Roman et al, 2018) and the presence of a thick interface layer, mainly advected toward the Atlantic Ocean (Bray et al, 1995). Conversely, inclusion of enhanced resolution results in a deepening of the zero-velocity interface, consistent with the deepening of the seafloor. Thus, tides and FTD have opposite effects on the zero-velocity interface, both essential to represent, as suggested by the discrepancies in T LR and NT HR. In NT LR, these discrepancies largely cancel out, explaining the better consistency with INGRES near the interface.

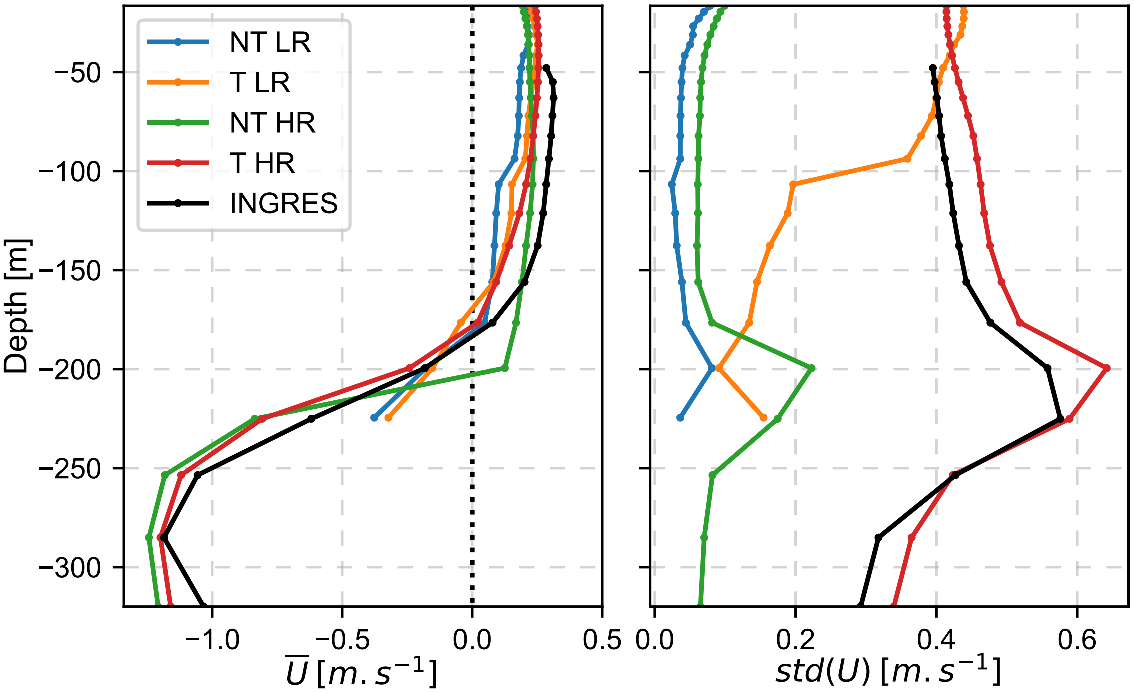

Figure 4.7: Mean (left) and hourly standard deviation (right) of the zonal velocity profile at the Espartel Sill (INGRES location, $\simeq 35.86°N,\ 5.97°W$; black dot in the lower panel of Figure 4.1). In black, in situ Doppler current profiler measurements from the INGRES project, with a sampling interval of 30 minutes (Sammartino et al, 2015). In blue, orange, green, and red, NEMOMEDGIB simulated zonal velocity profiles, taken at the closest point to the measurement site ($\simeq 35.86°N,\ 5.97°W$). The displayed NEMOMEDGIB configurations differ only through the inclusion or omission of tidal forcing (T/NT) and refined horizontal resolution at the SoG (HR/LR). For both the observation and simulated datasets, temporal averages are computed over 2005 – 2015 and hourly standard deviations over 2013. NEMOMEDGIB zonal velocities are obtained by projecting the model outputs onto the zonal direction. Measurements are linearly interpolated onto the model vertical grid.

Regarding the temporal variability of zonal currents, the investigated simulations display substantial differences with respect to each other. More specifically, the 2013 hourly std of zonal velocities is largely underestimated in non-tidal simulations (blue and green lines), with a modest improvement in NT HR (RMSE of 0.34m.s^{-1}, instead of 0.43m.s^{-1} in NT LR). On the other hand, it is noteworthy that the vertical structure of the hourly std is relatively well reproduced in NT HR, which displays correlation coefficients of 0.77 instead of 0.58 for NT LR. In tidal simulations (red and orange lines), the horizontal resolution also significantly influences the simulated temporal variability. Indeed, although the T LR hourly std is relatively similar to that of INGRES measurements near the surface, it abruptly decreases with depth, resulting in a significant low-intensity bias below 100m depth, which drives an overall large RMSE of 0.3m.s^{-1}. This unrealistic decrease in the hourly std is consistent with the weakening of tidal currents above the seafloor (see the tidal validation), mainly attributable to the shallow seafloor in the T LR configuration. Finally, the T HR simulation is by far the most realistic. Despite a general overestimation of the zonal velocity variability, it depicts a satisfactory RMSE of 0.05m.s^{-1} and a correlation coefficient of 0.97 with respect to the INGRES measurements.

To conclude on the model validation, the analyses carried out so far do not reveal any major issue with the simulations, hence their relevance for investigating the impact of local processes at the SoG on the Mediterranean Sea. In addition, the former results highlight the relevance of tidal forcing and kilometric horizontal resolution when representing the exchanges through the SoG. We have focused here on tidal and SoG transport validation. For simplicity, we will complete the model validation in the course of the following analyses.

4.4 Transports at the Strait of Gibraltar

As a first step to assess the influence of the local processes at the SoG on the Mediterranean Sea, it is essential to shed light on their impact in the vicinity of the strait. Therefore, this section aims at reaching a deeper understanding on the mechanisms shaping the dynamics and hydrography of the SoG. To do so, we will build on the results of previous studies regarding the respective influence of tides (Naranjo et al, 2014; Sannino et al, 2015; Harzallah et al, 2014; Sannino et al, 2015; Sanchez-Roman et al, 2018), FTD structures (Sannino et al, 2009b; Alhammoud et al, 2010; Topper and Meijer, 2015; Soto-Navarro et al, 2015) on the exchange flow through the strait and assess of their relative importance and combined effects. In particular, we interpret these effects with regard of the fine-scale tidal recirculation patterns at play within the SoG, described in Gonzalez et al (2023).

4.4.1 Exchange flow through the SoG

To investigate the influence of tidal and fine-scale processes on the exchange flow through the SoG, we display on the upper panel of Figure 4.8, the 1980-2017 average vertical profiles of zonal velocities, salinity, and temperature at the SoG for the T HR and NT LR simulations. In addition, we display on the lower panels the anomalies between the two simulations ($\delta_{tot} = T\,HR - NT\,LR$, red lines) and their decomposition into tidal (δ_{Tides}, orange lines), FTD (δ_{Res}, green lines), and combined effects (δ_{TR}, purple lines). Overall, both the T HR and NT LR simulations depict a typical picture of the two-layer exchange between the Atlantic Ocean and the Mediterranean Sea. The surface layer, composed of relatively warm and fresh Atlantic water masses, is advected toward the Mediterranean, whereas underneath, a colder and saltier layer of Mediterranean water masses is advected toward the Atlantic Ocean. The climatological zero-velocity interface depth is approximately 130m deep in NT LR and 150 m deep in T HR.

Besides the overall structure described above, the simulations display notable dynamic and hydrographic differences. In terms of dynamics, the joint inclusion of tidal forcing and enhanced horizontal resolution at the SoG mainly results in a thickening of the Atlantic layer (red line, positive velocity anomaly between $100 - 250$m depth) and a reorganization of the Mediterranean outflow, which dynamical core deepens and thickens (negative velocity anomaly below 250m depth). Consequently, the vertical shear of zonal velocities at the interface between both layers decreases. To the first order, these modulations are mainly due to the refined representation of the SoG in T HR (green line). More specifically, sensitivity experiments (see appendix A) indicate that the thickening of the Atlantic layer results from the deepening of the seafloor in T HR, which is consistent with results of Sannino et al (2009b); Topper and Meijer (2015). The position of the interface between the Atlantic and Mediterranean layers is also further modulated by the inclusion of abrupt topographic obstacles within the strait. In particular, the refined representation of the Camarinal Sill results in an intensification of the recirculation patterns characterized in (Gonzalez et al, 2023). Those patterns partly compensate for the thickening of the Atlantic layer to its east, where Mediterranean water masses are uplifted, and enhance it to its west, where Atlantic water masses accumulate and are forced to recirculate (not shown). On the other hand, tides have a less intense influence on the vertical structure of averaged zonal currents (orange line). They mainly influence the high-frequency dynamics of the exchange flow and locally modulate its average structure. As described in González et al (2013), mean tidal velocity anomalies result from oscillations of the interface between the Atlantic and Mediterranean layers (García Lafuente et al, 2013) and enhanced water mass recirculation near topographic obstacles (Sanchez-Roman et al, 2018). Both partially cancel out upon averaging due to the slope of the Atlantic-Mediterranean interface and the asymmetry of recirculation cells, respectively. Consequently, tidal modulations of the dynamics are highly dependent on the geometry of the strait, as indicated by the opposite patterns displayed by δ_{Tides} and δ_{TR}, and will not be detailed here.

Regarding hydrographic properties, the T HR simulation displays smoother vertical temperature and salinity profiles than NT LR. The associated anomalies and underlying mechanisms are clearly identifiable from the salinity profile. With respect to NT LR, the T HR simulation displays a significant dipole of salinity anomaly centered at 125m depth. Over the upper 125m, the Atlantic layer is salted (+0.3‰near 100m depth) by the tides, which enhance diapycnal mixing, water masses recirculation, and vertical displacement of the interface between the Atlantic and Mediterranean layers. At greater depths, tides freshen the Mediterranean layer less intensely, such that the total anomaly is driven by the refinement of the spatial representation of the strait (green line). This asymmetry in the tidal anomaly profile can be partly attributed to the lesser recirculation of Atlantic water masses with respect to Mediterranean water masses (Sanchez-Roman et al, 2018; Gonzalez et al, 2023). In addition, the anomaly is also partly canceled by a general salting of the intermediate and deeper layers of the Western Mediterranean in the T LR simulation, which we investigate in the following sections. In this way, the freshening of the water masses below 125m depth (−0.5‰near 170m depth) mainly results from the thickening of the Atlantic layer in higher-resolution configurations (green line). In addition, it is further intensified by a general freshening of the Western Mediterranean deep and intermediate water masses, investigated in the following sections. Finally, the joint inclusion of tidal and FTD has a less intense but notable influence on salinity (purple line). In particular, the associated anomalies indicate an intensification tidal

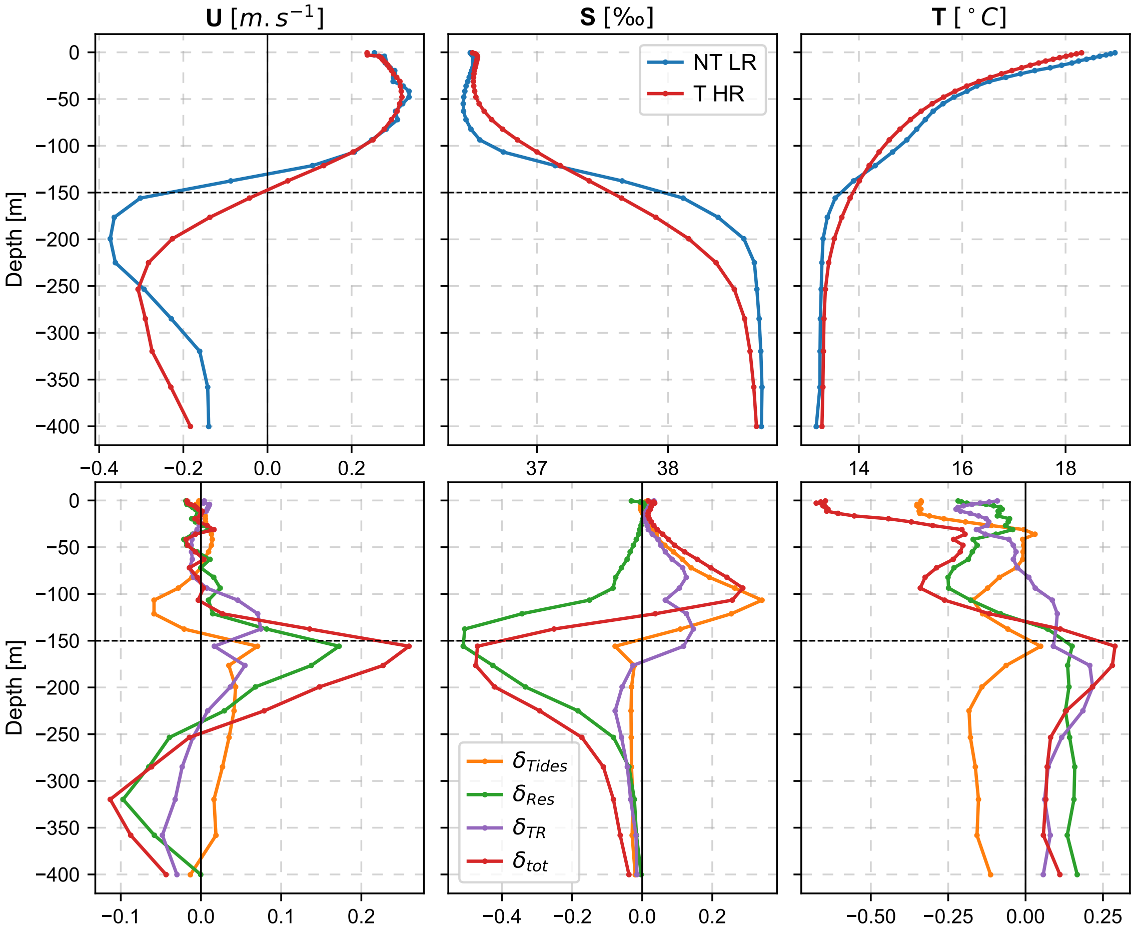

Figure 4.8: Upper panels display the 1980-2017 average vertical profiles of temperature, salinity, and zonal velocity around the Strait of Gibraltar (averaged over area framed by the dashed rectangle in the lower panel of Figure 4.1) for the NEMOMEDGIB non-tidal coarse resolution simulation (NT LR) and the tidal high-resolution simulation (T HR). Lower panels display the anomalies between both simulations (T HR - NT LR = δ_{tot}) and their decomposition into three components, associated with the respective effects of tides, grid nesting (δ_{Tides} and δ_{Res}) and their combined action (δ_{TR}). The horizontal dashed line represents the depth of the zero velocity interface in the T HR simulation.

recirculation and mixing in the presence of abrupt topographic obstacles, which is consistent with the results of Gonzalez et al (2023).

Temperature anomalies between T HR and NT LR are more complex to interpret and require careful analysis. With respect to the NT LR simulation, T HR displays an overall colder Atlantic layer and a warmer Mediterranean layer. Unlike for salinity and zonal velocity, temperature anomalies over the Atlantic layer vary substantially with depth and display two distinct maxima. The upper 20m depth are characterized by an intense cold anomaly (up to −0.7°C), mainly driven by the inclusion of the tidal forcing, whereas underneath, less intense anomalies (up to −0.3°C) are due to the refined spatial representation of the strait. Below the zero-velocity interface, the Mediterranean layer is less intensely warmed, with a maximal anomaly of 0.25°C at 180m depth. However, these anomalies primarily do not result from local processes but from modifications of the intermediate and deep water masses over the WMB. Regarding the Atlantic layer, the cold anomaly resulting from the refined spatial representation of the strait can be simply related to the modification of surface circulation in the Alboran sea. To be more specific, in higher-resolution simulations, the Gulf of Cadiz slope current (Peliz et al, 2007) is intensified, resulting in the advection of fresher and colder water masses from the north of the Iberic Peninsula. On the other hand, investigation of the surface tidal anomaly requires an assessment of the seasonal cycle at the SoG.

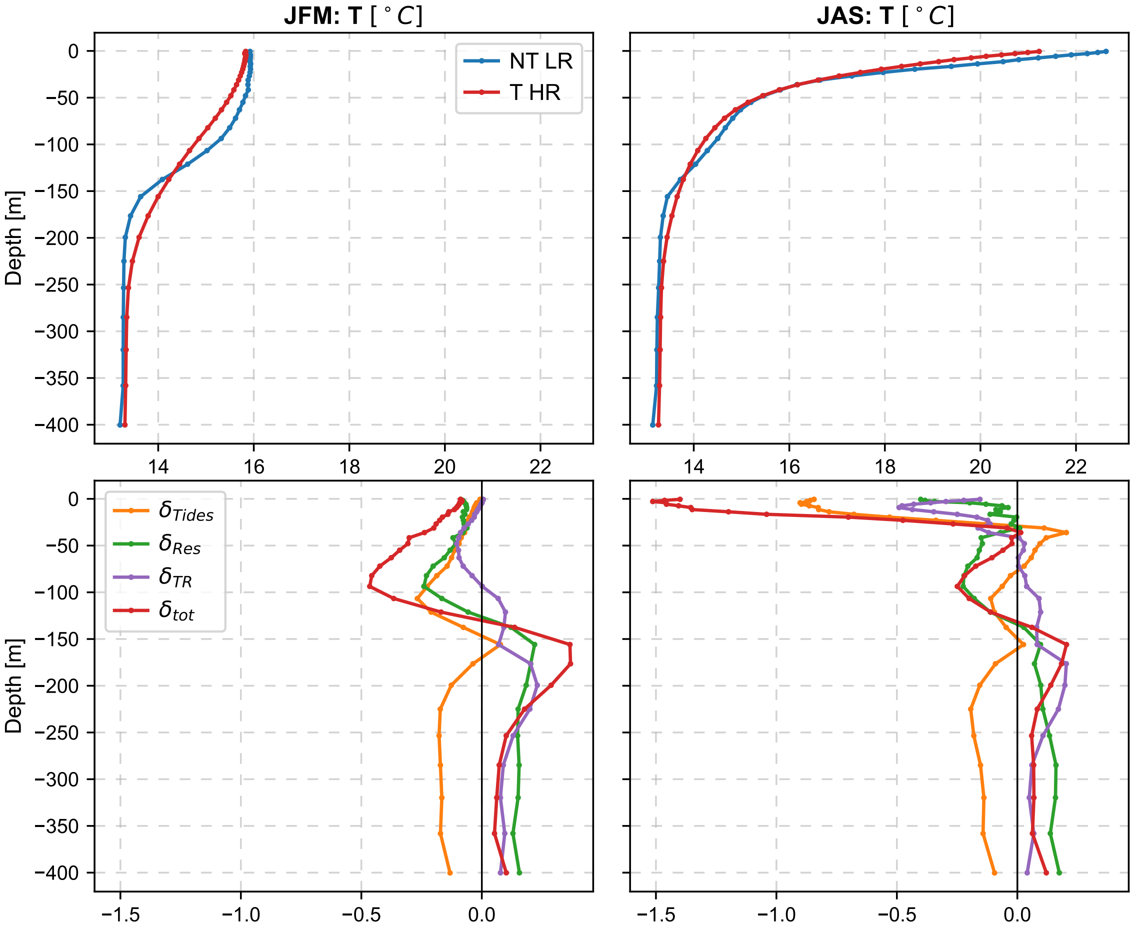

Figure 4.9: Same as Figure 4.8 for the winter (left, January-February-March) and summer (right, July-August-September) 1980-2017 average vertical profiles of temperature

We display in Figure 4.9 climatological winter and summer temperature anomalies at the SoG. Above 150m depth, the temperature is subject to substantial seasonal variations, characterized by a relatively smooth profile in winter and an intense vertical gradient in summer. A comparison of the T LR and T HR simulations indicates that the enhanced representation of the SoG in T HR, particularly the inclusion of tidal forcing, has a notable impact on these patterns. More specifically, local processes within the strait drive the temperature anomalies above 150m depth, whereas remote modifications of the intermediate and deep Western Mediterranean Mediterranean water masses drive the anomalies below, often canceling the overlying anomaly patterns. In winter, tides induce a dipole temperature anomaly centered on 150m depth, which is consistent with enhanced vertical mixing and advection between the Atlantic and Mediterranean layers. On the other hand, during summer, tides induce an additional dipole anomaly centered on 25m depth. This specific pattern denotes tidal ventilation of the surface layer that fluxes heat to depth, driving an intense cooling of the surface (up to $-1.5°$ with respect to NT LR) and partly canceling the cold anomaly at the bottom of the Atlantic layer. In addition, this surface anomaly is substantially intensified in simulations with enhanced horizontal resolution at the SoG (sum of orange and purple lines). In light of the former analyses, this intensification can be related to tidal mixing and recirculation enhancement in the presence of fine-scale topographic obstacles, in agreement with (Gonzalez et al, 2023). Besides tidal anomalies, δ_{Res} also displays notable seasonal variations, with an intensified warm anomaly near 150m depth in winter, although its cause is unclear. Note that it would be tempting to assess the possible enhancement of the deep water suction by tidal forcing discussed in Naranjo et al (2014). However, such analysis is complex to achieve due to the notable long-term difference in the hydrographic properties of intermediate and deep western Mediterranean water masses.

To conclude on the properties of the exchange flow, we highlight that both tides and FTD at the SoG have substantial and complementary effects on the dynamics and hydrographics at the strait. On the one hand, average dynamics are mainly influenced by the geometry of the SoG, which determines the position of the interface between the Atlantic and Mediterranean layers. On the other hand, hydrographic properties are more evenly influenced by tides and FTD. In particular, tides notably modulate the seasonal cycle of surface temperature within the strait, whereas FTD have a more steady effect over time. Finally, the steep topographic obstacles in higher-resolution simulations significantly enhance tidal anomalies.

4.4.2 Integral transports at the SoG

In light of the notable influence of tides and fine-scale structures on the hydrography and dynamics of the SoG, we now investigate the resulting impacts on the exchanges between the Atlantic Ocean and the Mediterranean Sea. We display in Figure 4.10 the inflow (eastward) and net volume, heat, and salt transports through the SoG. In addition, we specify the anomalies between the T HR and NT HR simulation and their decomposition into three components associated with the effects of tides, the refined representation of the SoG, and their combination. As previously discussed, we consider two estimates of the inflow transports: an upper estimate (Q^{max}), accounting for high-frequency tidal and eddy transports, and a lower estimate (Q^{A}), based on time-averaged outputs over 1980-2017. Note that outflow transports are not specified as they can be deduced by subtracting the net flow from Q^{max} or Q^{A}.

Overall, the simulations display reasonable values for Q^{A} and the associated heat and salt transports. More specifically, the volume outflow transports simulated in NT LR and NT HR (-0.78Sv and -0.84Sv, respectively) are consistent with the non-eddy-flux estimate of -0.81Sv from Sammartino et al (2015) considering the associated interannual variability (± 0.03Sv) as an uncertainty range. The T HR simulation moderately overestimates the outflow transport (-0.86 Sv), and the T LR simulation underestimates it (-0.75 Sv). However, both remain reasonably consistent with Sammartino et al (2015). The former conclusions extend to the inflow transports, considering as a reference the inflow transport deduced from the non-eddy-flux outflow estimate of Sammartino et al (2015) and the net volume transport estimate of Jordà et al (2017b) (0.04 Sv).

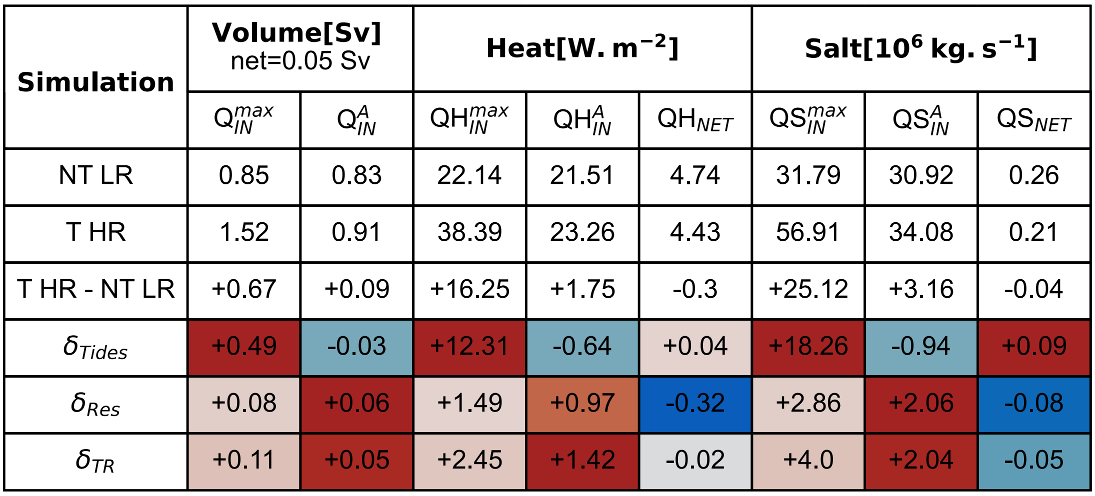

Simulation	Volume[Sv] net=0.05 Sv		Heat[W. m^{-2}]			Salt[10^6 kg. s^{-1}]		
	Q_{IN}^{max}	Q_{IN}^{A}	QH_{IN}^{max}	QH_{IN}^{A}	QH_{NET}	QS_{IN}^{max}	QS_{IN}^{A}	QS_{NET}
NT LR	0.85	0.83	22.14	21.51	4.74	31.79	30.92	0.26
T HR	1.52	0.91	38.39	23.26	4.43	56.91	34.08	0.21
T HR - NT LR	+0.67	+0.09	+16.25	+1.75	-0.3	+25.12	+3.16	-0.04
δ_{Tides}	+0.49	-0.03	+12.31	-0.64	+0.04	+18.26	-0.94	+0.09
δ_{Res}	+0.08	+0.06	+1.49	+0.97	-0.32	+2.86	+2.06	-0.08
δ_{TR}	+0.11	+0.05	+2.45	+1.42	-0.02	+4.0	+2.04	-0.05

Figure 4.10: Average transports of volume, heat, and salt through the SoG. Positive values are oriented toward the Mediterranean Sea. Anomalies between NEMOMEDGIB T HR and T LR simulations are decomposed into three components; associated with the effects of tides, grid nesting (δ_{Tides} and δRes), and their combination (δ_{TR}). Inflowing transports are computed from averages of the eastward velocity components, applying a heaviside function. As traditionally done for comparison purposes with surface fluxes, we convert the heat transport into an equivalent surface flux over the whole Mediterranean Sea, in W.m^{-2}, with a Mediterranean area of $2.5 \cdot 10^{12}$m^2, following Sanchez-Roman et al (2018).

Besides their overall agreement with references, the transports represented by the NEMOMEDGIB simulations display notable differences, indicating that both tidal forcing and FTD at the SoG influence the exchanges through the strait. With respect to the NT LR simulation, the advection intensifies in T HR, as indicated by Q_{IN}^{max}, Q_{IN}^{A} and the associated inflowing heat and salt transports. However, the reasons for this enhancement vary. Concerning Q^{max}, tidal forcing appears as the main driver of the enhanced volume transports, explaining most of the differences between T HR and NT LR. These enhanced high-frequency transports are consistent with results from (Gonzalez et al, 2023) highlighting the periodic reversal of the SoG circulation in response to the barotropic tide. However, their physical interpretation is not straightforward and would require a dedicated study. On the other hand, Q_{IN}^{A} indicates a less intense and more balanced influence of tides, FTD, and their combined effects. Specifically, intensification of the volume transport is mainly attributable to the refined representation of the SoG, which is consistent with the representation of more intense dynamic structures, the reduced influence of lateral friction, and the reduced numerical viscosity. Regarding tidal forcing, as already noted for the average dynamics, its influence on the volume transports significantly varies with the adopted representation of the SoG (δ_{Tides} versus $\delta_{Tides} + \delta_{TR}$). It is noteworthy that the decrease of the volume transports in the T LR simulation can be attributed to tide-induced vertical displacement of the interface between inflowing and outflowing water masses, which results in a canceling of the average currents near the interface. Finally, the inflowing heat and salt transport anomalies are driven by volume transport anomalies.

Regarding the net transports, the simulated net volume, heat, and salt transports all fall within the uncertainty range of 0.04 ± 0.02Sv, 4.5 ± 4.1W.m^2, and $0.1 \pm 0.3\ 10^6$kg.s^{-1} from Jordà et al (2017b, Tables 10, 11, 12), respectively. Comparing the simulations with each other, both the inclusion of tides and FTD at the SoG appear to have a notable impact on the net heat and salt transports, which is consistent with previous studies (Sannino et al, 2009b; Harzallah et al, 2014; Naranjo et al, 2014; Sannino et al, 2015; Sanchez-Roman et al, 2018). With respect to NT LR, the net heat transport displayed by the other simulations varies by up to +6% (δ_{tot}, δ_{Res}) and the salt transport by up to ±35% (δ_{Tides} and δ_{Res}). These anomalies result from local hydrographic and dynamic modulations as well as remote transformations of the Mediterranean water masses. More specifically, in tidal simulations (δ_{Tides}, $\delta_{Tides} + \delta_{TR}$), the well-documented tidal decrease of the net heat transport through the SoG (Harzallah et al, 2014; Sanchez-Roman et al, 2018; Gonzalez et al, 2023) is compensated by a general cooling of Western Mediterranean intermediate and deep water masses (see the following sections). Conversely, the decrease of the net heat transport in higher-resolution simulations (δ_{Res}, $\delta_{Res}+\delta_{TR}$), which is consistent with the cooling of the Atlantic layer due to the modified circulation in the Gulf of Cadiz, is enhanced by a general warming of Western Mediterranean intermediate and deep water masses. The net salt transport is less influenced by the remote saline anomalies, which are relatively moderate (see the following sections). In this way, δ_{Tides} is directly attributable to tidal mixing and recirculation, which increases the net salt transport by fluxing salt to the surface. For δ_{Res}, the decreased salt transport is consistent with an intensification of the volume transports, which intensifies the salt outflow more than the inflow due to the greater salinity of Mediterranean water masses with respect to Atlantic water masses.

Overall, the former results highlight that tides and FTD at the SoG both notably influence the net heat and salt transports through the SoG. On the one hand, tides decrease the net heat transport (not shown) and increase the net salt transport by driving diapycnal mixing and recirculation between the exchanged flows. On the other hand, the inclusion of FTD decreases the net heat and salt transports due to circulation modulations over the Gulf of Cadiz and volume transports intensification through the SoG. These effects are of similar intensity for the salt transport, but this is less clear for the heat transport. In fact, we highlight that tides and FTD also have an indirect influence on the net heat transport related to hydrographic transformations over the Mediterranean Sea, which combines with their local influence.

4.5 Mediterranean Sea adjustments

4.5.1 Atlantic Water properties

In the previous section, we have highlighted that tidal forcing and fine-scale dynamics at the SoG have a notable influence on the hydrographic and dynamical properties of the Atlantic water mass crossing the SoG. In addition, several studies (Sannino et al, 2009b; Naranjo et al, 2014; Harzallah et al, 2014; Sannino et al, 2015; Soto-Navarro et al, 2015) have shown that changes in the dynamic structure and the hydrographic properties of the Atlantic inflow at the SoG propagate to the western Mediterranean. Thus, this section investigates the remote impact of the local processes at the SoG on the Atlantic Waters (AW) of the Mediterranean sea.

Western Mediterranean

To start with, we display on the upper panels of Figure 4.11 the NT LR 1980-2017 meridional average temperature and salinity over the upper 300m depth of the WMB. Lower panels indicate the anomalies between the T HR and NT LR simulations ($\delta_{tot} = THR - NTLR$) and their decomposition into a tidal (δ_{Tides}) and FTD components (δ_{Res}). Several key areas of the WMB can be identified from the temperature and salinity fields. From 5°W to 0°E above $\sim$ 100m depth, the warm and fresh surface layer of AWs delineates the contours of the Alboran Sea. Note also that just east of 5°W, the large vertical extent of the AWs denotes the presence of the Western Alboran gyre. Further east between 0°E – 10°E, the sudden drop in temperature indicates the North WMB. Finally, east of 10°E, the increase in both temperature and salinity at mid-depth and the local temperature minimum near 100m depth reflects the strong signature of Levantine intermediate water masses, indicating the location of the Tyrrhenian Sea.

Over the upper 200 m depth, the T HR simulation displays statistically significant hydrographic anomalies with respect to NT LR (δ_{tot}). Specifically, δ_{Tides} and δ_{Res} indicate that both tides and FTD at the SoG drive these anomalies. In terms of temperature, the enhanced representation of the SoG in T HR results in an overall cooling of the upper 200 m depth (typically reaching -0.1°C). Consistently with previous studies (Harzallah et al, 2014; Naranjo et al, 2014; Sannino et al, 2015) this cold anomaly is mainly attributable to the inclusion of tidal forcing at the SoG (δ_{Tides}). In addition, it is further enhanced by the modification of the Gulf of Cadiz circulation, which results in a cooling of inflowing Atlantic water masses (δ_{res}), and the interaction of tides with topographic obstacles at the SoG (δ_{TR}, not shown). Given the substantial seasonal variation of tidal temperature anomalies at the SoG, the contribution of tides to the cold anomaly at the sea surface requires investigating its seasonal cycle. To do so, we display in Figure 4.12 the seasonal cycle of the temperature anomalies at 11m depth with respect to NT LR for the T HR and T LR simulations. Consistently with tidal anomalies at the SoG, both δ_{tot} and δ_{Tides} display a marked seasonal cycle characterized by an intense surface cooling in summer. More specifically, the anomaly is significantly enhanced in the vicinity of the SoG, where it locally exceeds -1°C, and progressively loses intensity from west to east, typically reaching -0.25°C over the rest of the WMB. East of 15°E the anomaly is locally enhanced by tidal upwelling at the Strait of Messina. However,

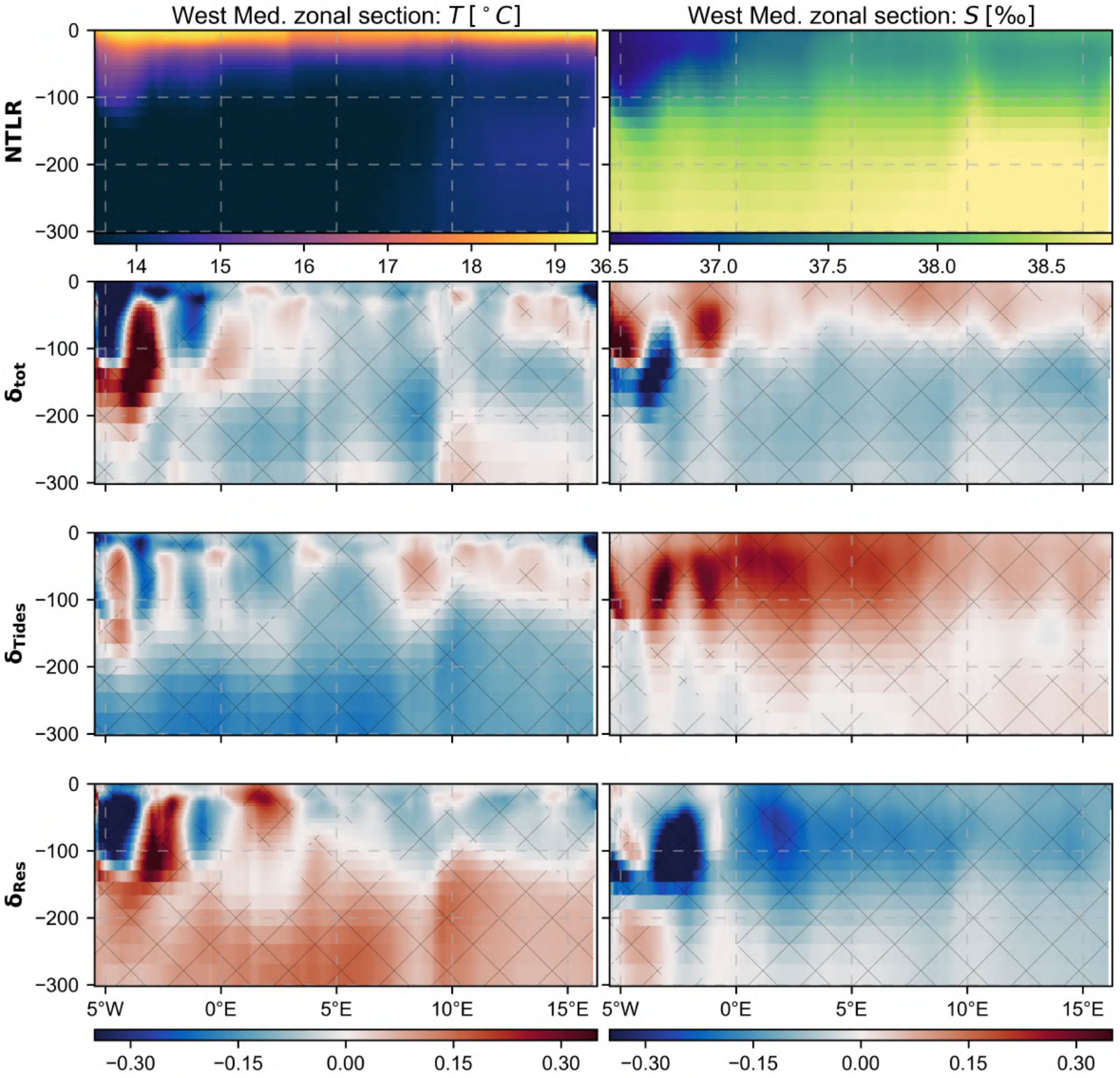

Figure 4.11: Upper panels display the 1980-2017 pseudo-meridional (along the model grid) average temperature and salinity over the Western Mediterranean Basin for the NEMOMEDGIB non-tidal coarse resolution simulation (NT LR). Lower panels display the anomalies induced by the joint inclusion of tidal forcing and enhanced horizontal resolution at the SoG (δ_{tot} = T HR - NT LR) and the sole inclusion of tidal forcing (δ_{Tides} = T LR - NT LR) or enhanced resolution at the SoG (δ_{Res} = NT HR - NT LR). Hatches indicate statistically significant anomalies with respect to the interannual variability (based on a two-tailed student t-test with $p = 0.05$)

the latter effect is relatively local (BOHM et al, 1987; Bignami and Salusti, 1990; Azzaro et al, 2007). In this way, for the first time to our knowledge, the former analysis highlights that tidal processes at the SoG have a notable influence on the seasonal cycle of temperature over the whole WMB.

Going back to average hydrographic properties (Figure 4.11), with respect to the NT LR simulation, T HR displays saltier water masses above 100m depth and fresher ones below. The resulting dipole anomaly, which is statistically significant with respect to the interannual variability, is noticeably similar to that identified at the SoG in the previous section. More specifically, this anomaly can be attributed

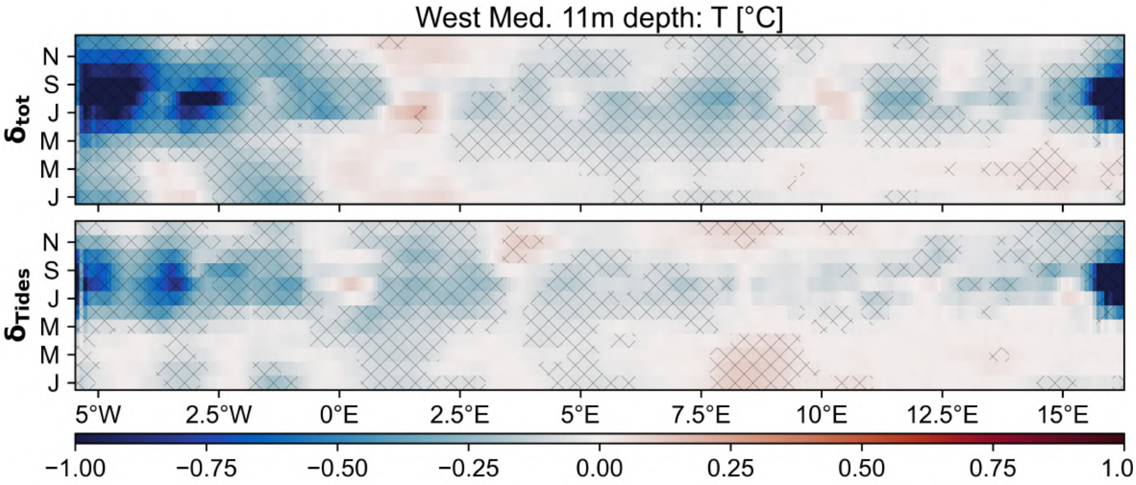

Figure 4.12: Hovmöller diagram (time-space diagram) of the Seasonal 1980-2017 Western Mediterranean pseudo-meridional average temperature anomaly induced by the joint inclusion of tidal forcing and enhanced horizontal resolution at the SoG (upper panel, δ_{tot} = T HR - NT LR) and the sole inclusion of tidal forcing (lower panel, δ_{Tides} = T LR - NT LR). Hatches indicate statistically significant anomalies with respect to the interannual variability (based a two-tailed student t-test with $p = 0.05$)

to the joint influence of tides and FTD at the SoG. On the one hand, the saltening of the surface primarily results from the inclusion of tidal forcing at the SoG (δ_{Tides}), which is consistent with the literature (Harzallah et al, 2014; Naranjo et al, 2014; Sannino et al, 2015). On the other hand, the fresh anomaly below 100m depth is attributable to the refined spatial representation of the SoG in T HR, resulting in a thickening and intensification of the Atlantic inflow through the strait. In particular, this effect is consistent with Sannino et al (2009b), which highlighted that the modification of the Atlantic layer thickness at the SoG propagates to the WMB. Other than reinforcing the results of the aforementioned studies, the dipole salinity anomaly just described indicates that both tidal and FTD at the SoG have an equally important influence on the Mediterranean surface, and thus, both should be considered when modeling the Mediterranean Sea. The latter point is particularly well illustrated by δ_{Tides} and δ_{res}, which indicate that with respect to the T HR and NT LR simulations, T LR and NT HR provide two extreme representations of Atlantic water properties in response to SoG exchanges.

Besides basin-scale hydrographic properties, the simulations display less intense and localized differences over the upper 200m, indicating modulations in the simulated surface circulation. More specifically, the warm anomaly near 1°E in δ_{tot} and δ_{Res} results from the weakening of the Northern current (Pinardi and Masetti, 2000; Pinardi et al, 2015) in the T HR and NT HR simulations (not shown). This circulation modification can be associated with the intensification of the Atlantic inflow through the SoG in both simulations, allowing Atlantic water masses to enter the Liguro-Provençal Basin through a similar pathway to the Western Mid-Mediterranean Current described in Pinardi et al (2015). Conversely, in the NT LR simulation, the Liguro-Provençal-Catalan Current is enhanced, resulting in a cold anomaly near 1°E. The warm anomaly further east near 10°E is more complex to interpret, as it likely results from a combination of circulation modifications with the advection of remote anomalies from the straits of Sicily and Sardinia. More generally, as highlighted in Sannino et al (2015), our results suggest that local processes at the SoG influence the Western Mediterranean circulation and hydrography. However, interpretation of these differences is a complex matter that requires dedicated analyses and is out of the scope of the present study. In the following, we will, thus, mainly focus on basin-scale hydrographic properties.

Bellow 200m depth, the T HR simulation displays colder and fresher water masses than NT LR. Although these anomalies are consistent with those at the bottom of the SoG inflow, they do not directly result from the Atlantic water masses modification at the SoG. This is well depicted by the warm temperature anomaly displayed by δ_{Res}, which is inconsistent with the cold anomaly from the SoG. Rather than tidal mixing and the fine-scale structure of the exchange flow through the strait, these water masses are mainly influenced by the convective activity over the Western Mediterranean (see next section). As suggested from previous studies (Sannino et al, 2009b; Naranjo et al, 2014; Sannino et al, 2015), these anomalies indicate that local processes at the SoG modulate deep convection in the northwestern Mediterranean Sea, which ultimately impacts the basin-scale stratification.

Eastern Mediterranean

To investigate the influence of tidal and fine-scale processes at the SoG on the EMB, we display in Figure 4.13 the NT LR 1980-2017 meridional average temperature and salinity over the upper 300m depth of the EMB, as well as the differences with the T HR configuration (δ_{tot}) and its decomposition into a tidal (δ_{Tides}) and FTD component (δ_{Res}). Note that we exclude the Adriatic and Aegean Seas from the meridional average, as they are subject to localized hydrographic modulations related to convection and will be investigated in the following section. As for the WMB, notable temperature and salinity patterns arise upon meridional averaging. In particular, the tongue of fresh water masses advected from the WMB west of 15°E is readily identifiable from the salinity field. In addition, the general warming and saltening from west to east indicates the formation and subsequent export of LIW from the source region of the Levantine basin.

With respect to the WMB δ_{tot}, δ_{Tides}, and δ_{Res} display less intense hydrographic anomalies (nearly twice as low). Regarding temperature, a notable fraction of the displayed anomalies is insignificant with respect to the interannual variability. Thus, they must be interpreted cautiously. With respect to NT LR, the T HR simulation represents an overall warmer surface. Given the cold anomaly pattern displayed by δ_{tot} over the WMB, this indicates that local processes drive the Eastern Mediterranean temperature anomalies. This conclusion is further reinforced by the notable differences between δ_{tot}, δ_{Tides}, and δ_{Res} east of 15°E, indicating that temperature anomalies rely on mechanisms associated to their joint representation (δ_{TR}, not shown). In this way, given the low intensity of the temperature anomalies, we only emphasize here that the tidal and fine-scale mechanisms at the SoG have a moderate, non-linear, and indirect influence on the surface temperature of the EMB. Although they remain unclear, these effects likely result from modulations in the circulation, convection, and transports through the Sicily, Otranto, and Cretans straits.

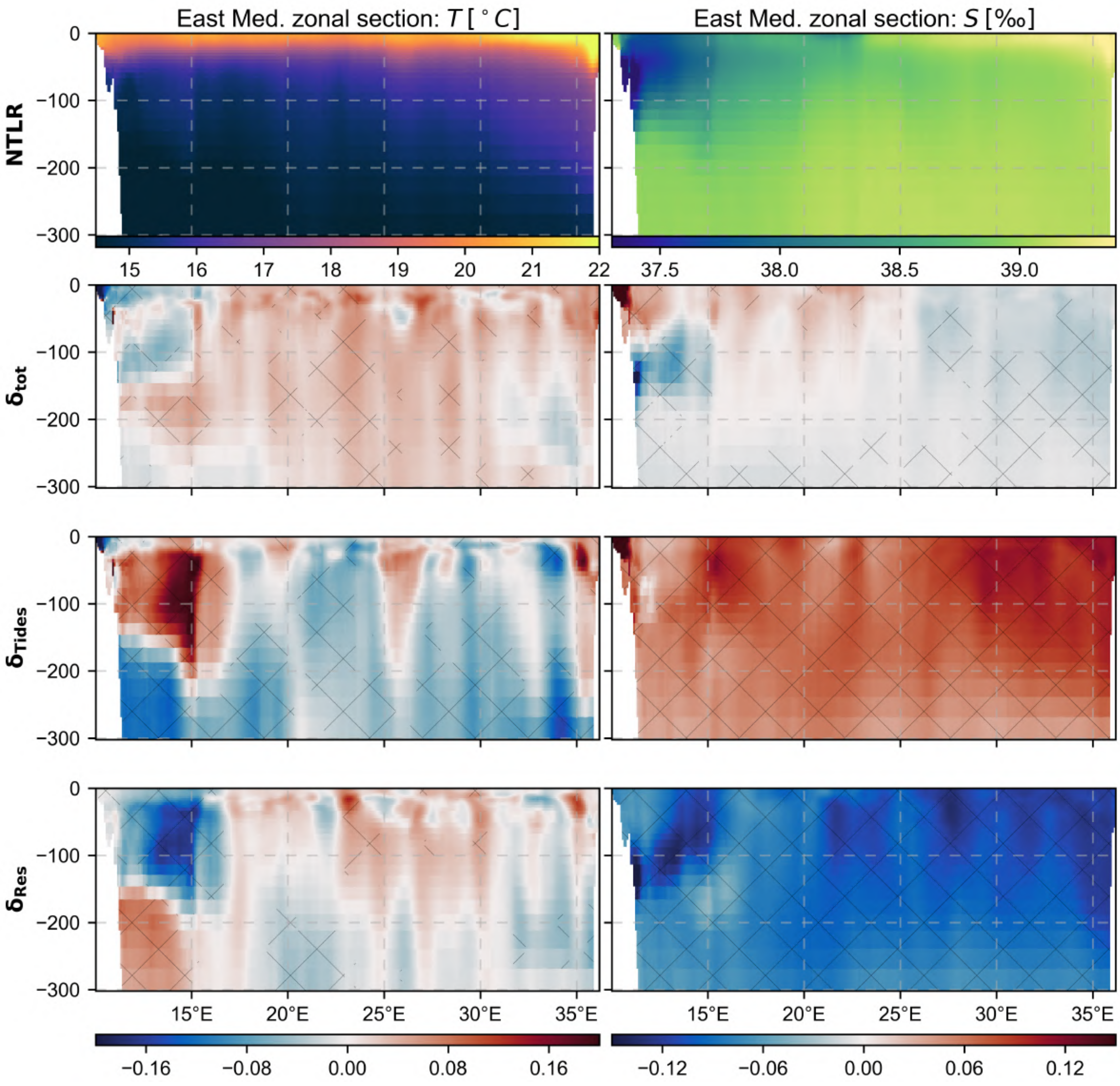

Figure 4.13: Same as Figure 4.11 for the Eastern Mediterranean Basin, excluding the Adriatic and Aegean Seas (namely, restricting to the Ionian and Levantine basins).

On the other hand, salinity anomalies are clearly consistent with the propagation of surface anomalies from the WMB. West of 15°E, δ_{tot} displays a salinity dipole centered on 100m depth consistent with the propagation of the Western Mediterranean saline anomaly. Further east, the dipole abruptly disappears, suggesting that only the surface signal is advected further east to the EMB. On the other hand, δ_{Tides} and δ_{Res} highlight that, when considered separately, tides and FTD at the SoG have an opposite influence on the Eastern Mediterranean Surface. Specifically, the surface is relatively homogeneously saltened in the T LR simulation (δ_{Tides}) and accordingly freshened in the NT HR simulation (δ_{Res}). In addition, although δ_{Tides} and δ_{Res} display homogeneous patterns over the upper 300m depth, investigation of the simulation spin-up (not-shown) indicates that these anomalies first develop over the upper 150m depth of the water column and progressively propagate to depth through dense water formation.

To conclude on AW anomalies, both tides and FTD at the SoG have a notable influence on the surface of the Mediterranean Sea. These processes are relevant to the mean temperature and seasonal cycle of the upper layers of the WMB and their salinity stratification. Over the EMB, the influence of these processes is less intense and mainly relates to the salinity of the upper 300m depth. In addition, we show that, east of the Sicily strait, the effects induced by the inclusion of tidal forcing and FTD at the SoG strongly compensate.

4.5.2 Dense water formation

As an evaporative basin connected to the open ocean by a two-layer flow, the Mediterranean Sea is home to significant vertical exchanges of mass, heat, and salt, in which deep convection takes on a key role (Waldman et al, 2018). This uncommon process over the Wold Ocean is particularly active in the Mediterranean sea due to strong wintertime surface buoyancy losses and relatively dense surface water masses (MEDOC GROUP, 1970). Thus, local processes shaping the hydrographic properties of the AW at the SoG are relevant to the Mediterranean deep convection. In fact, previous studies have already suggested that both tidal mixing (Naranjo et al, 2014; Sannino et al, 2015) and the fine-scale dynamics at the SoG (Sannino et al, 2009b) influence deep convection over the Gulf of Lions. In this section, we build on the results of these studies to reach a deeper and broader understanding of the influence of local processes at the SoG on the Mediterranean deep convection.

To do so, we display in Figure 4.14 the spatio-temporal annual maximum of the mixed layer depth (MLD hereinafter) over the Northwestern Mediterranean Sea (upper panels), the Aegean Sea (middle panels), and the Adriatic Sea (upper panels) for the NT LR (light gray lines all panels), T HR (left panels), T LR (middle panels), and NT HR (right panels) simulations. Following Herrmann et al (2008); Sannino et al (2015), we compute the MLD based on a turbocline criterion. Specifically, we define the MLD as the depth above which the vertical diffusion coefficient continuously exceeds $0.5\text{cm}^2.\text{s}^{-1}$. In addition, to shed light on the modulated convective activity, we overlay to the MLDs the monthly temperature anomalies with respect to the NT LR simulation and plot on lower panels the annual stratification index (SI hereinafter) anomalies with respect to the NT LR. More specifically, we compute the SI (in $\text{m}^2.\text{s}^{-2}$) at the maximal depths reached by the MLD over 1980-2017 (d) following:

$$SI = \int_d^0 \overline{N^2}(z)\, z\, dz \tag{4.1}$$

where $\overline{N^2}$ is the time-average squared Brunt–Väisälä frequency. The SI quantifies the depth-integral vertical stratification that must be overcome to trigger deep convection.

Northwestern Mediterranean Sea

Over the Northwestern Mediterranean Sea (Figure 4.14, left panels), the NEMO-MEDGIB simulations capture relatively well the decadal variability of convection. In particular, all the simulations reproduce the weakening of the convective activity during the 90s (Somot et al, 2018) and the intense convective winters of 1981, 2005–2006, and 2009–2013. With that in mind, comparison of the simulations indicates that tidal and FTD processes at the SoG significantly impact on the convective

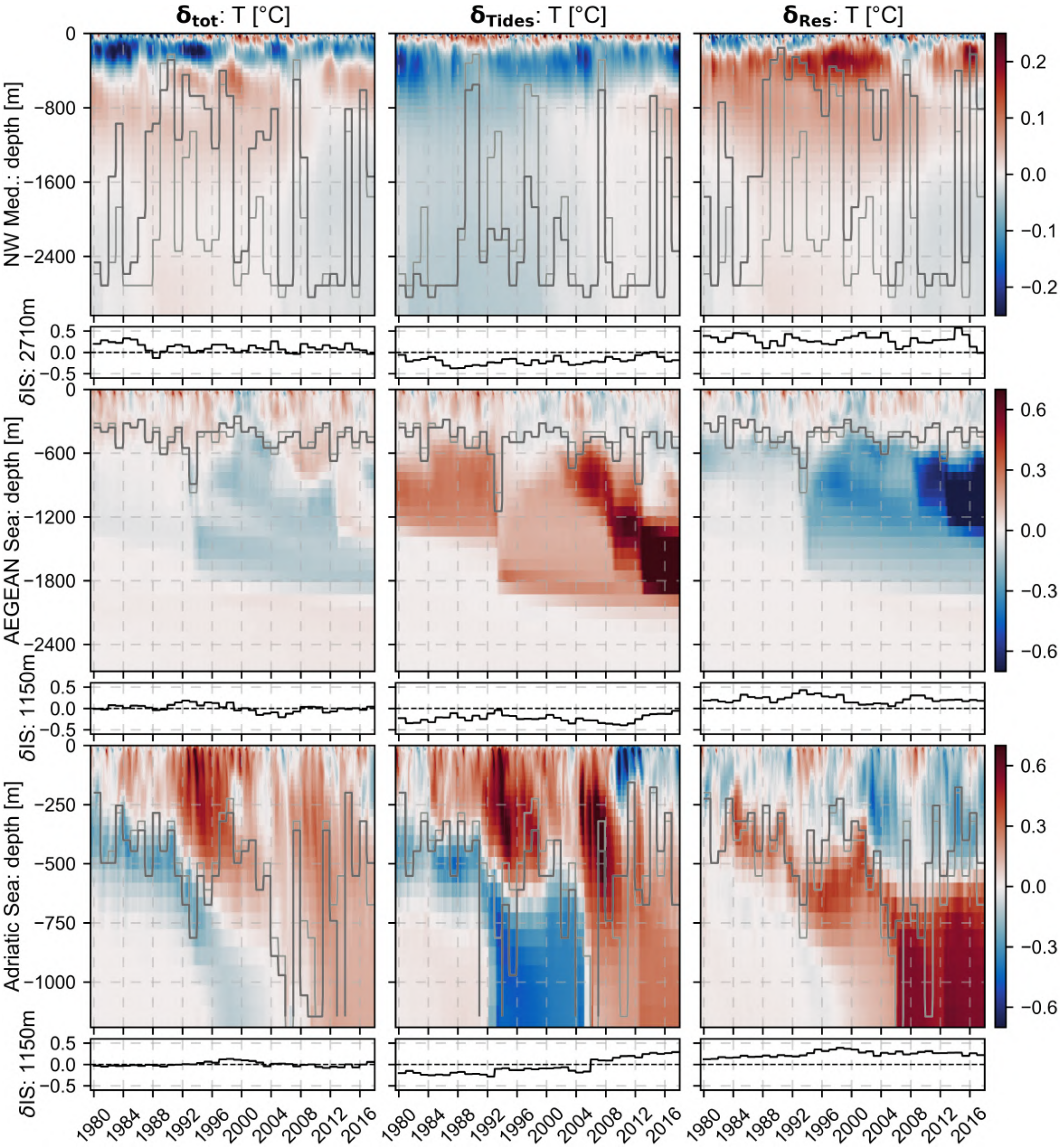

Figure 4.14: In shades, Hovmöller diagram (time-space diagram) of monthly average temperature anomaly induced by the joint inclusion of tidal forcing and enhanced horizontal resolution at the SoG (left panels, δ_{tot} = T HR - NT LR), the sole inclusion of tidal forcing (middle panels, δ_{Tides} = T LR - NT LR), and the sole inclusion of enhanced resolution at the SoG (right panels, δ_{Res} = NT HR - NT LR). Horizontal averages are performed on the Northwest Mediterranean for the upper panels, the Aegean Sea for the middle panels, and the Adriatic Sea for the lower panels (see the areas delineated by red contours in Figure 4.1). Dark grey lines display the spatio-temporal annual maximum mixed layer depth over the same areas, the light grey line showing the control NT LR simulation. Line plots represent the stratification index anomalies averaged over the same areas.

activity. Specifically, the T HR and NT HR simulations (left and right panels, respectively) represent shallower convection with respect to NT LR, whereas, consistently with the literature (Naranjo et al, 2014; Sannino et al, 2015), the T LR simulation (middle panel) displays deeper convection ($\delta Tides$). As expected, these modulations directly relate to the water column stratification. Indeed, T HR and NT HR display a more stratified water column than NT LR (positive SI anomaly), whereas T LR displays a weaker stratification (negative SI anomaly). More specifically, a decomposition of the SI into thermal and haline components (not shown) indicates these differences mainly result from salinity anomalies over the upper 200m depth. In this way, the enhanced convection in T LR is attributable to the surface salting induced by tidal mixing and recirculation at the SoG. Conversely, the weakening of convection in the NT HR simulation results from the surface freshening due to the thicker and more intense AW inflow at the SoG. Finally, for T HR, the water masses freshening below 100m dominates over the surface salting and weakens the convection.

In addition to the MLDs, temperature anomalies between the simulations provide valuable information on convection. Indeed, the anomalies displayed by δ_{tot}, δ_{Tides}, and δ_{Res} (Figure 4.14) are inconsistent with the effect of tides and FTD at the SoG and, thus, can be entirely associated with the modified convective activity. Specifically, δ_{Tides} indicates that the enhanced convection in T LR produces a warmer top 100m layer and colder deeper layers. Conversely, δ_{Res} indicates that the weakened convection in NT HR results in a colder surface and warmer intermediate layers. For δ_{tot} however, the picture is more complex. Although the warm anomaly below 400m depth is consistent with the weakening of convection in T HR, the cold anomaly over the upper 400m depth suggest that convection intensifies.In fact, the cooling of the upper layers in T HR can be explained by the SI at shallower depths (not shown), which indicates that the tidal saltening of AW at the SoG weakens the stratification above 100m depth. This allows the atmosphere to cool the ocean upper layers more efficiently during winter. In addition, the enhanced stratification below 400m depth isolates the colder surface water masses to the warmer layers of LIWs, resulting in a general cooling of the upper 400m depth.

Thus, these results confirm that tides and FTD at the SoG both have a notable influence on the deep convection over the northwestern Mediterranean. In particular, their combined effects modulate the vertical extent and the intensity of convection. Finally, concluding on the realism of the simulations is not straightforward. The simulated MLDs in the T HR and NT HR configuration are in better agreement with the observation-based estimates presented in Somot et al (2018) than NT LR, as they indicate shallow convection for the years 1985, 1988, 1996, and 2004, in addition to those previously mentioned. However, as specified by Somot et al (2018), sampling errors probably lead to an underestimation of the maximum MLD. On the other hand, both the T HR and NT HR simulations underestimate the convective events of 1991 and 1992. Regarding the T LR configuration, it is likely to overestimate the convective activity, particularly during the 1990s, when the simulated MLDs are consistently deeper than 1500m. Regarding the temperature field, a comparison with respect to reference datasets will be conducted in the following section.

Aegean Sea

The NEMOMEGIB simulations reproduce a realistic convective variability over the Aegean Sea (Figure 4.14, middle panels). In particular, all the simulations represent the deep convection of 1993, associated with the Eastern Mediterranean

Transient (EMT hereinafter) (Roether et al, 1996), and the following so-called "stagnation period" of mid-depth convection (1994-2003) (Zervakis et al, 2004; Mamoutos et al, 2021). Other more minor convective events are represented, such as the convection of 1987 (Zodiatis, 1991) and 1989 (Lascaratos et al, 1999; Nittis et al, 2003; Gertman et al, 2006), the deep water formation events of 2003 and 2008 suggested by Georgiou et al (2015), and that of 2012 suggested by Mamoutos et al (2021). On the other hand, the 2016 event (Velaoras et al, 2017) is not represented, and that of 2004 is overestimated. In addition, the overall convection intensity is likely underestimated due to an overestimation of the river runoffs around the Aegean Sea, which tends to isolate the deeper layers from the atmosphere (Zervakis et al, 2000; Nittis et al, 2003).

Overall the NEMOMEDGIB simulations display relatively similar MLDs, which mainly differ during intense convective events. In particular, the T HR and NT LR simulations are very similar, which is consistent with their moderate hydrographic differences over the EMB (Figure 4.14). More specifically, δ_{tot} (Figure 4.14, middle panel) indicates that main modulations between the two simulations arise from the convective events of 1993 and 1996, which are less intense in T HR and result in cold anomalies below 600m, and the convection of 2012, that is more intense in T HR and partly cancels the former temperate anomalies. Given the moderate intensity and temporal variability of these differences, we argue that chaotic circulation anomalies likely drive the observed convection modulation and, thus, that the convective activity is mostly unchanged in T HR and NT LR. On the other hand, the T LR and NT HR simulations display greater differences. Specifically, the simulated convection is systematically deeper in T LR and shallower in NT HR. As for the Northwestern Mediterranean, these modulations are directly related to the salinity of surface layer, which affects the overall water column stratification (Figure 4.14, middle line plots). In this way, the convection deepens in T LR due to the Eastern Mediterranean surface salting induced by tidal mixing and recirculation at the SoG, whereas the convection shoals in NT HR due to the freshening induced by the refined spatial representation of the SoG. The temperature anomalies below 600 depth evidence these modulations of the convective activity. For T LR, the deeper convection of 1993, 2003, 2009, and 2012 results in an overall warming of the deep layers (δ_{Tides}). Conversely, the accordingly shallower convection represented in NT HR (δ_{Res}) results in an overall cooling of the deep layers.

These results highlight that tides and FTD at the SoG are both relevant to dense water formation in the Aegean Sea through their influence on the AW salinity and the consequences on the vertical stratification. However, they have opposite effects, resulting in minor modulations of the convective activity in T HR. Regarding the realism of the simulations, T LR is likely to provide a more accurate picture of the past convection in the Aegean Sea. However, since this improvement results from the compensation of fresh surface biases due to an overestimation of river runoffs, no conclusion can be drawn from the added value of tidal and fine-scale mechanisms at the SoG.

Adriatic Sea

As a third major deep water formation area, we consider the Adriatic Sea. In particular, we mainly focus on the south Adriatic pit, where most of the Adriatic deep water is produced (Gačić et al, 2002; Vilibic and Orli, 2002). Over this area, deep convection is subject to significant interannual variability, (Gačić et al, 2002; Mantziafou and Lascaratos, 2004; Oddo et al, 2005; Mantziafou and Lascaratos, 2008). However, years of intense convection, such as 1986 (Gačić et al, 2001), 1992 (Gačić et al, 2002), 2002 (Manca et al, 2006), or 2006 (Vilibić and Šantić, 2008), and shallow convection, as 1997 (Gačić et al, 2002) and 2015 (Lučić et al, 2017) can be used as references. With respect to the Northwest Mediterranean and the Aegean Sea, the simulations capture less accurately the Adriatic convective variability (Figure 4.14, lower panels). Indeed, the simulated convection is likely underestimated over 1980 – 2004 and overestimated after 2004 for the T HR and NT LR simulations. These discrepancies can be explained by a large fresh bias at the surface, which is due to an overestimation of river runoffs. More specifically, this fresh bias prevents the occurrence of deep convection during the simulations spin-up, allowing LIW to sink to the bottom of the Adriatic Sea, further inhibiting convection. Note that a very similar problem is described in Dunić et al (2019, MED12F3 simulation). With that in mind, we consider that these discrepancies do not obstruct the following analysis. Indeed, as the inclusion of tidal and FTD at the SoG mainly influence convection through surface salinity anomalies, the following results should remain qualitatively similar in bias-free simulations.

Similarly to previous convection areas, a comparison of the simulated MLDs indicates that both tidal and FTD at the SoG have a notable influence on the simulated convection. Specifically, before 2005, the T HR and T LR simulations represent deeper convection than NT LR, whereas NT HR displays shallower convection. Once again, these modulations can be related to the salinity of surface water masses, which is substantially higher in T LR, lower in NT HR, and moderately higher in T HR, as depicted by the SI anomalies (Figure 4.14, lower line plots). For the T HR simulation, the increase of surface salinity with respect to NT LR is likely attributable to tide-induced enhanced volume exchanged at the strait of Otranto, as both simulations display moderate salinity differences over the EMB. In this way, we argue that as for the Aegean Sea, the modulated convection in T HR does not result from the modified representation of the SoG. In addition, this indicates that the salting of the Adriatic surface by tidal forcing at the SoG is likely enhanced by the local effect of tides at the Strait of Otranto. With that in mind, the T LR and NT HR simulations clearly highlight that Adriatic deep convection is indirectly affected by tidal and fine-scale processes at the SoG. On the other hand, after 2005, the picture is more complex for the T LR simulation, which suddenly displays shallower convection than NT LR. Specifically, this modification is directly related to the intense convection simulated in 2006, which homogenizes the water column in the T HR and NT LR configuration, consuming the deep layer LIW at the bottom of the water column. In the T LR simulation, this homogenization is less intense because the layer of LIW was consumed during the winters of 1991-1993, as indicated by the intense temperature dipole anomaly in δ_{Tides}.

These results indicate that convection over the Adriatic Sea is sensitive to the tidal and fine-scale processes at the SoG. In addition, the resulting modulation of the convective activity can substantially modify the local vertical stratification. However, the magnitude of effects highlighted here should be taken with caution as they are likely affected by the misrepresentation of the Adriatic water masses.

4.5.3 Interior water mass properties

In the previous section, we have highlighted that tidal and fine-scale dynamics at the SoG have a notable influence on the Mediterranean convective activity. Given the key role played by deep convection in the Mediterranean overturning circulation (Waldman et al, 2018), these results suggest that local processes at the SoG may indirectly impact the mean properties and variability of the Mediterranean surface, intermediate, and deep water masses. In this section, we investigate this by comparing the properties of the simulated water masses over different layers and their variability over time. We also assess the realism of the studied simulation, considering the MEDHYMAP climatology (Jordà et al, 2017b) as a reference observation-based dataset and the 1987-2017 Mediterranean reanalysis of Escudier et al (2020) (referred to as the CMEMS reanalysis hereinafter; data available on the Copernicus CMEMS database: http://marine.copernicus.eu) as a state-of-the-art reference ocean reanalysis.

Western Mediterranean

We display in Figure 4.15 the simulated and reference annual temperature and salinity averaged over the upper ($0-150$m depth), intermediate ($150-600$m depth), and deep layers (below 600m depth) of the WMB. All simulations capture the warming and salting of the surface and intermediate layers, with similar trends to MEDHYMAP. Over the upper 150m depth, the temperature and salinity RMSEs with respect to MEDHYMAP are similar to those of the CMEMS reanalysis. Over intermediate layers, the simulations display larger discrepancies, but the associated RMSEs remain consistent with the values obtained by other state-of-the-art models (Sannino et al, 2022). Over deeper layers, the interannual variability of deep water masses is less accurately reproduced, but the associated RMSEs are reasonable. It is noteworthy that the RMSEs with respect to MEDHYMAP are mainly bias-dominated. In particular, regarding temperature, the simulations display a cold bias over the upper layer and a warm bias over the intermediate layer, with an overall improved consistency in the T HR simulation. Regarding salinity, the NT LR, NT HR, and T HR simulations underestimate the salinity of the upper layer, which is better represented by T LR, likely due to bias compensations. The NT LR and T LR simulations overestimate the salinity of the intermediate layers, which is improved in NT HR and T HR. Over deeper layers, the RMSEs are mainly explained by the misrepresentation of the temperature and salinity trends.

The NEMOMEDGIB simulations display notable differences over the simulated period, with varying intensity depending on the layer considered. Over the upper 150m depth, the interannual temperature variability is highly similar in all simulations, such that its modulation by local processes at the SoG is hardly interpretable. On the other hand, it is noteworthy that the T HR (red line) and T LR (orange line)

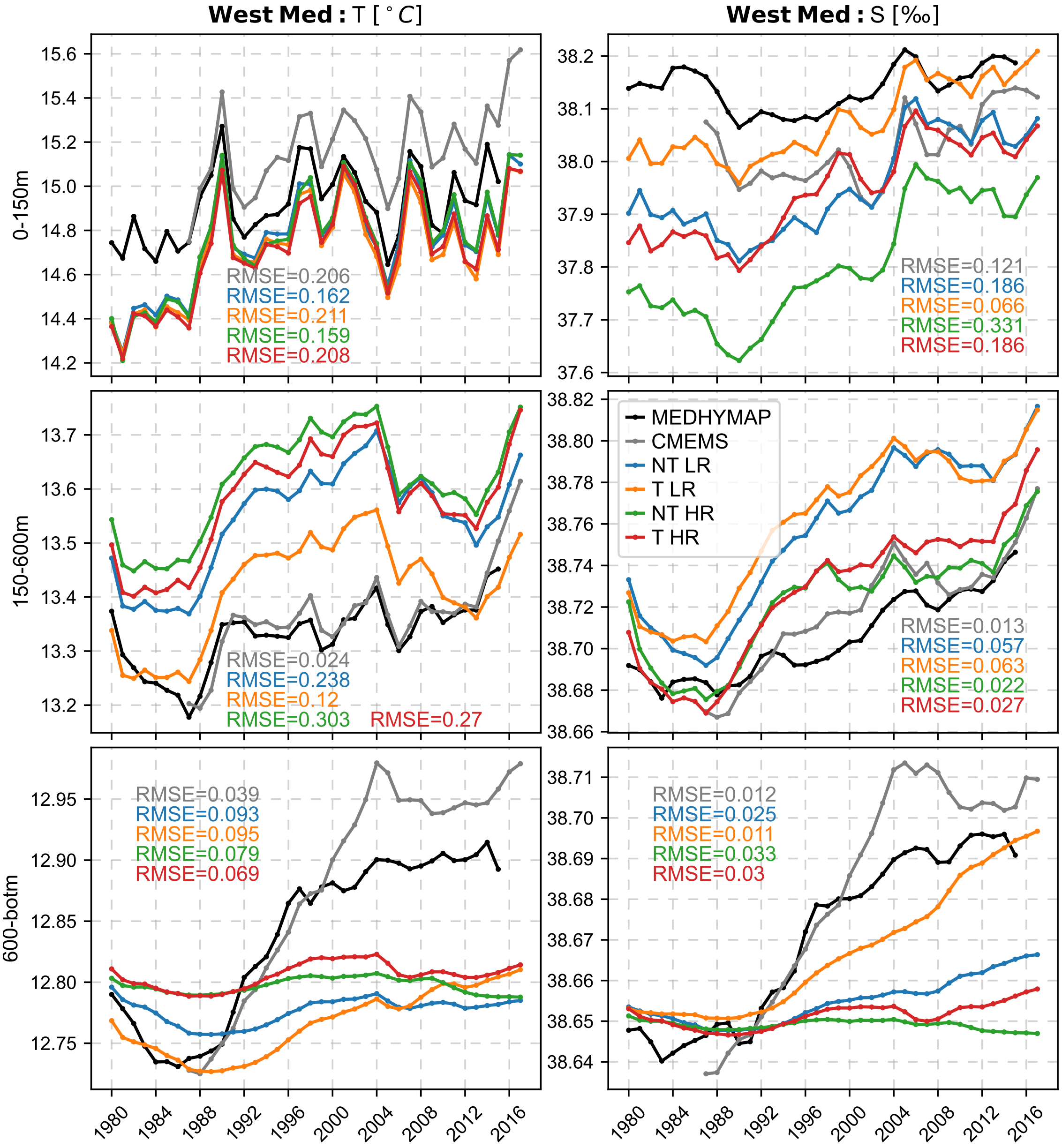

Figure 4.15: Annual average temperature (left) and salinity (right) over the upper (0 – 150m depth), intermediate (150 – 600m depth), and deep (below 600m depth) layers of the Western Mediterranean basin. The considered simulations only differ by the inclusion or omission of tidal forcing (T/NT) and enhanced horizontal resolution at the SoG (HR/LR). In addition, we display in black the average of the MEDHYMAP dataset and in grey that of the 1987-2017 Mediterranean reanalysis of Escudier et al (2020) (referred to as CMEMS). Root Mean Squared Errors (RMSE) are computed from the annual series with respect to the MEDHYMAP dataset considering the 1987-2015 period, which is common to all the datasets.

simulations consistently display a colder surface than NT LR, indicating that the influence of tidal mixing and recirculation at the SoG on the western Mediterranean surface temperature is relatively steady over time. Regarding salinity, the simulations display more marked differences. As expected, the T LR simulation displays a significantly saltier surface, and the NT HR simulation a fresher one, which is consistent with the modified properties of the Atlantic inflow in both simulations.

In the T HR simulation, the compensation of these anomalies results in a salinity similar to NT LR. On the other hand, the salinity anomalies appear relatively steady over time, confirming that the influence of local processes at the SoG does not significantly impact the interannual variability of the water masses above 150m depth.

Over the intermediate layer (150 – 600m depth), the simulations display greater temperature differences than over the upper layer. With respect to the NT LR simulation, NT HR and T HR display warmer water masses, whereas T LR display colder water masses. These differences are consistent with the modified convective activity over the northwest Mediterranean. Indeed, considering that convection erodes the warm layer of LIW present in the Western Mediterranean, the warmer intermediate layer of T HR and NT HR is consistent with shallower convection, and the colder intermediate layer of T LR is consistent with deeper convection. On the other hand, salinity differences are harder to interpret, as they result from a combination of local convection-related anomalies and remote anomalies associated with the LIW advected from the EMB (see the following section). In this way, the moderate salinity differences between the T LR and NT LR simulation likely results from the compensation of these effects and are complex to interpret. For the T HR and NT HR simulation, the relatively intense fresh anomaly with respect to NT LR suggests that fewer compensations are at play. In particular, this fresh anomaly is consistent with the vertical propagation of the fresh surface anomaly present in both simulations and shallower convection, which does not allow surface and intermediate water masses to mix with the saltier deep water masses. However, specific analyses would be needed to confirm these hypotheses. Overall, we mainly emphasize that salinity differences between simulations are significant but relatively steady with respect to the large interannual variability.

Finally, below 600m depth, the simulated hydrographic properties are more clearly marked by intense convective events. Overall the simulations largely underestimate the warming and saltening trends over 1988-2004, with a notable improvement in the T LR simulation, suggesting inaccurate properties of the dense waters formed. More specifically, temperature and salinity variations are clearly attributable to the modulation of deep convection by local processes at the SoG, with increasingly strong warming and salting trends in the NT HR, T HR, NT LR, and T LR configurations. These tendencies are also likely intensified by the advection of the EMT-driven LIW water masses, which is diagnosed to occur a the beginning of the 21th century in the simulations of Pinardi et al (2015).

Eastern Mediterranean

We display in Figure 4.16 the simulated and reference annual temperature and salinity averaged over the upper ($0-150$m depth), intermediate ($150-600$m depth), and deep layers (below 600m depth) of the EMB (including also the Adriatic and Aegean Seas). As for the WMB, the simulations reproduce relatively well the interannual and average hydrographic properties of the Mediterranean water masses over the upper and intermediate layers, as well as the associated warming and salting trends. In particular, the simulations capture the abrupt cooling of the intermediate layer associated with extreme winters, such as 1992, 1993, and 2004-2007. On the other hand, the simulations do not represent the freshening of the intermediate layers in 1993 and 1994 due to the uplifting of old deep water masses following the EMT (Lascaratos et al, 1999), likely due to an underestimation of the EMT intensity. More generally, the RMSEs with respect to MEDHYMAP are bias-dominated and mostly larger than those of the CMEMS reanalysis. However, they remain consistent with those obtained by other state-of-the-art models (Sannino et al, 2022). Over the upper layers, the RMSEs are driven by cold and fresh biases, with a notable decrease in the salinity bias in NT LR. Over the intermediate layer, the temperature RMSE mainly arises from a warm bias during the 1990s, whereas for salinity, it results from a saline bias in T LR and a fresh bias in NT HR, which are mostly corrected in T HR and NT LR. Below 600m depth, the simulations display an overall warm and saline bias, and the interannual variability and average properties of deep water masses are less accurately reproduced. However, the associated RMSEs are reasonable.

As expected from the previous analyses, tides and FTD at the SoG have a lesser but notable influence on the hydrographic properties of the EMB. Over the upper 150m depth, the simulations display a very similar interannual variability. Temperature anomalies are moderate and variable, indicating that they likely result from the compensation of local anomaly patterns and are complex to interpret. On the other hand, salinity anomalies are greater and relatively steady. With respect to the NT LR simulation, T LR displays a saltier surface and NT HR a fresher surface, which is consistent with the anomalies advected from the SoG. On the other hand, these effects cancel out in the T HR simulation, displaying a similar salinity to NT LR. As already noted for the WMB, the salinity differences are relatively steady, indicating that the influence of local processes at the SoG on the surface of the EMB is also steady.

Over the intermediate layer (150 – 600m depth), the interannual temperature variability remains highly similar in the simulations, although moderate differences arise. As for the upper layer, the low intensity and the temporal variability of these anomalies suggest that they result from a combination of different mechanisms and are complex to interpret. Regarding salinity, the simulations also display a similar interannual variability, with a few notable changes, which can be attributed to the deep convection events of 1993 and 2003 over the Aegean Sea. In this way, the salinity anomalies between the simulations are mainly consistent with the vertical propagation of surface saline anomalies in the Levantine Basin. Thus, this indicates that although local processes at the SoG have a notable influence on the Adriatic and Aegean deep convection, the effects on the salinity of intermediate water masses are moderate.

Below 600m depth, the interannual variability of the deep water masses is more sensitive to the modulation of convection by local processes at the SoG. In particular, the deep convections in 1993, 2003, 2008, and 2012 notably impact the temperature and salinity tendencies below 600m depth. In the T LR simulation, they result in a notable salting and warming of the deep layers, whereas these tendencies are less marked in the other simulations, with a clear consistency between the intensity of the trend and the simulated convection.

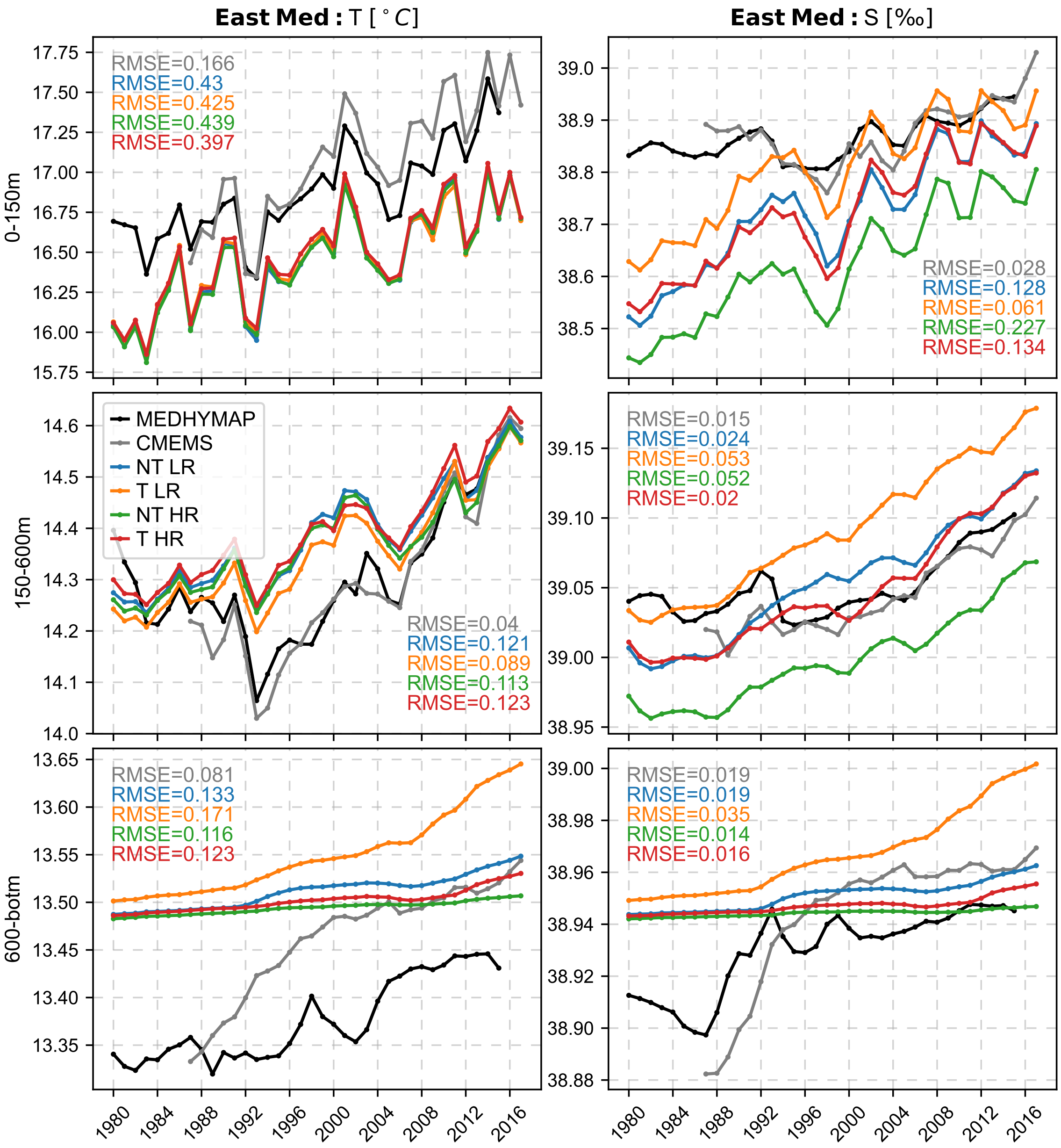

Figure 4.16: Same as Figure 4.15 for the Eastern Mediterranean Basin.

To conclude on this section, the former results suggest that tidal and FTD processes at the SoG have a notable impact on Mediterranean water masses, with different implications depending on the layer considered. Upper and intermediate water masses are mainly influenced by the Atlantic water masses inflowing from the SoG and the long-term intensity of convection. Consequently, their hydrographic interannual variability is mostly unaffected by the processes investigated at the SoG. On the other hand, deep water masses are influenced through the modulation of intense convective events, which substantially influence the long-term temperature and salinity trends.

4.6 Air-sea interactions and atmospheric adjustment

Over the previous sections, we have shown that local processes at SoG notably influence the upper layers of the WMB. In particular, summer tidal mixing and recirculation within the strait leads to an overall cooling of the Western Mediterranean Surface. Given the intense summer heat and water fluxes between the Mediterranean Sea and the atmosphere, this modulation of the sea surface temperature (SST hereinafter) suggests that the exchanges through the SoG may influence the lower troposphere during summer. In this section, we investigate this hypothesis by comparing the ocean-atmosphere interface in those coupled numerical simulations. More specifically, since we have shown in the previous chapter and the former sections that these processes strongly rely on the interaction of tides with fine-scale topographic obstacles within the SoG, we consider the T HR and NT LR simulations for this analysis. In the following, we focus on 1980-2017 summer averages, considering the months of June, July and August, which are the warmer months of the year in the atmosphere.

4.6.1 Air-sea fluxes

To start with, we investigate the impact of the SST differences between T HR and NT LR on the ocean-atmosphere heat fluxes. In particular, we decompose the net ocean-atmosphere heat flux into the following components:

- The latent heat flux (LHF hereinafter), which represents the turbulent heat flux resulting from water vapor exchanges at the ocean-atmosphere interface. The latent heat flux is mainly driven by the near-surface relative wind and the specific humidity contrast at the air-sea interface. In NEMOMEDGIB simulations, the sea surface water vapor content is considered at the saturating humidity (the maximum quantity of water vapor that air can contain, which mainly depends on temperature). Thus, the latent heat flux is a function of the surface wind velocity, the atmosphere surface humidity, and the SST.

- The sensible heat flux (SHF hereinafter), which represents the turbulent heat flux due to the temperature gradient at the ocean-atmosphere interface. As for the latent heat flux, the sensible heat flux is also proportional to the wind velocity at 10m.

- The net longwave radiation (LW hereinafter), which represents the sum of the upward and downward infra-red radiative fluxes at the air-sea interface. Both fluxes depend on the temperature of the body emitting the radiation.

- The shortwave radiation (SW hereinafter), controlled by the incoming solar radiation. Specifically, solar radiation depends on the zenith angle, the albedo of the surface receiving the radiation (assumed constant at 0.06), and the proportion of radiation transmitted through the atmosphere, which mainly depends on cloudiness.

With that in mind, we display over the upper panels of Figure 4.17 the average SST, LHF, sum of SHF and LW, and SW in the NT LR simulation. On the lower panels, we display the anomalies induced by the inclusion of tides and the refined spatial representation of the SoG (T HR - NT LR). Note that we consider the sum of SHF and LW as they display very similar patterns, dominated by the SHF and driven by SST changes. In the NT LR simulation, the SST displays a classical summer pattern, with increasing temperatures from northwest to southeast and a local temperature minimum in the northwestern Mediterranean. Surface heat fluxes also display a typical picture of the ocean-atmosphere exchanges in summer. The ocean surface, loses heat to it through the LHF and LW radiation. Conversely, the ocean is mainly heated through the SW, which largely intensifies in summer, and marginally through SHF, the near-surface atmosphere being warmer than the sea surface. The net heat flux (not shown) is positive and intensified over the ocean, indicating a heating mainly driven by shortwave radiation.

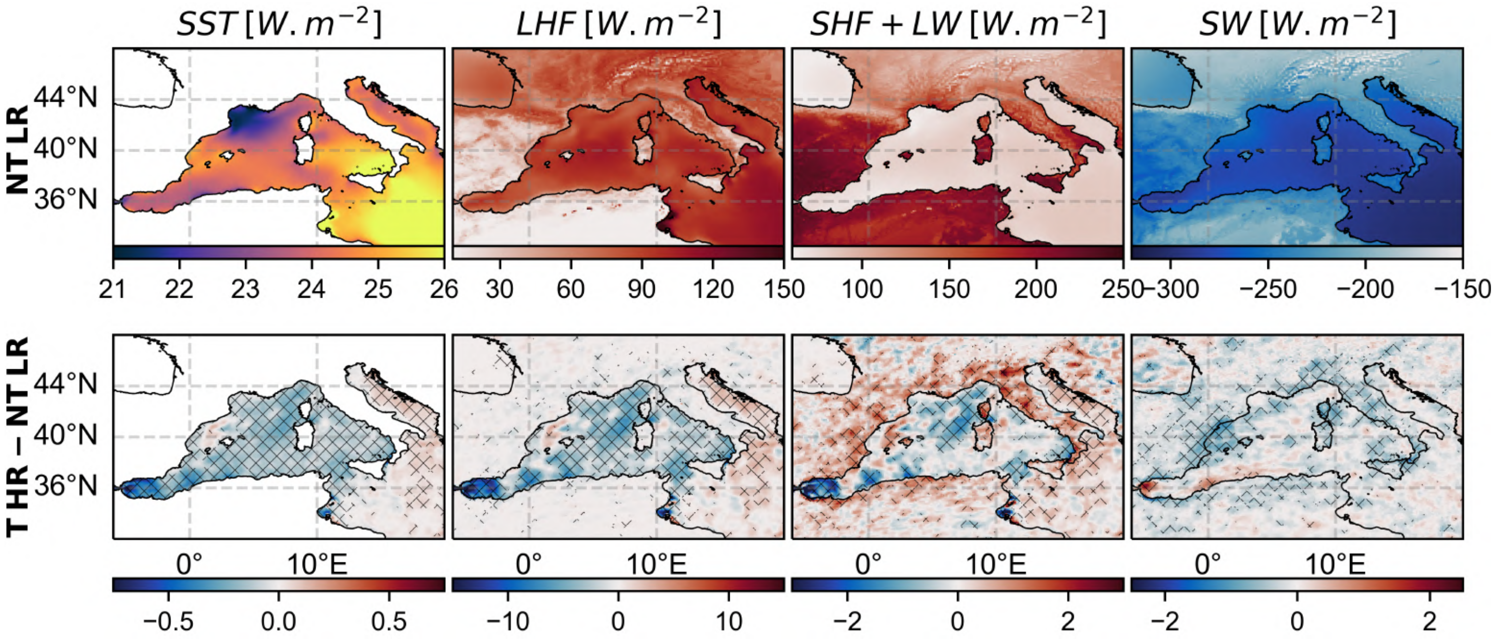

Figure 4.17: Upper panels display 1980-2017 summer averages (June-July-August) sea surface temperature (SST), latent heat flux (LHF), sum of the sensible heat flux and the longwave radiation (SHF + LW), and the shortwave radiation (SW). Lower panels display the anomalies induced by the inclusion of tides and refined spatial representation of the SoG (T HR - NT LR). Hatches indicate statistically significant anomalies with respect to the interannual variability (based on a two-tailed student test with $p = 0.05$)

The NT LR and T HR simulations display notable differences in SST and heat fluxes. In T HR, the sea surface is colder over most of the WMB, except over the Balearic Sea, due to a greater inflow of Atlantic water masses than in NT LR. The tidal anomaly is maximal in the vicinity of the SoG, where it locally exceeds −1°C and takes weaker values over the rest of the WMB, ranging from −0.25°C to −0.1°C. Note that a moderate warming pattern develops over the Adriatic Sea, likely due to enhanced exchanges with the Ionian Sea. However, it will not be discussed in further detail because of its weak influence on the atmospheric surface conditions.

Regarding heat fluxes, the modified representation of the SoG in T HR results in a decreased net heat flux over the ocean (not shown). This is primarily driven by the reduced latent heat loss. It is characterized by a notable decrease in the Alboran Sea and a less intense decrease over the rest of the Western Mediterranean. In this way, cooling of the sea surface by tides at the SoG results in decreased oceanic heat and water vapor supply to the atmosphere. Besides the LHF, the net heat flux further decreased through the SHF and LW, which display negative anomalies over areas of intense surface cooling or significant atmospheric circulation, such as the Alboran and Ligurian Seas. In particular, the decrease of the LW (displaying a similar pattern to the sum of SHF and LW) is driven by the upward component associated with the SST. Over the land, although the net heat flux is close to zero, the sum of SHF and LW display an increase in the upward heat flux, indicating a warming of the continental surface. In fact, this warming pattern is consistent with the decrease in the downward shortwave radiation, which indicates an intensification of the downward solar heat flux and, thus, suggests that the modified ocean-atmosphere fluxes impact on the atmospheric water vapor content.

4.6.2 Atmospheric adjustment

To assess the impact of the modified ocean-atmosphere fluxes on the atmosphere, we first investigate the near-surface atmosphere temperature and vapor content. To do so, we display in the upper panels of Figure 4.18 the near-surface (2m height) atmospheric temperature (T2m), near-surface specific humidity (SH) and near-surface relative humidity (RH). The latter quantifies the fraction between the specific humidity and the saturating humidity. In addition, we display on the lower panels the anomalies induced by tidal and fine-scale dynamics at the SoG (T HR - NT LR). Overall, the atmospheric surface temperature is mainly characterized by increasing temperatures from north to south, orographic patterns and a more homogeneous temperature over the Mediterranean Sea. The SH is mainly intensified over the sea and near coastal areas. The RH displays a similar pattern except over the north-eastern part of the domain. In fact, over these areas, in particular over orography, the saturating humidity decreases with the temperature, increasing the RH.

With respect to NT LR, the T HR simulation displays a colder near-surface temperature over the WMB, which is consistent with the reduced ocean heat loss to the atmosphere. The cooling pattern is mainly contained over the sea and is largely similar to that previously described for the SST. Specifically, the cold anomaly reaches maximal values in the vicinity of the SoG, locally exceeding -0.8°C and loose in intensity over the WMB, where it typically ranges from -0.15°C to -0.1°C. In terms of water vapor content, the specific humidity mainly decreases over the WMB, indicating a drying of the atmosphere, which is consistent with the reduced evaporative flux. As for temperature, the intensity of the anomaly reaches its maximum near the SoG and progressively loses in intensity from west to east. On the other hand, unlike for temperature, the dry anomaly noticeably propagates up to a few hundred kilometers over the surrounding land. Due to the opposite effect of the atmosphere cooling and drying on relative humidity, the latter displays dipole anomalies centered on the coastline. Specifically, the relative humidity mainly increases over the ocean, where the cooling of the near-surface atmosphere drives an intense decrease in the saturating humidity, compensating for the atmosphere drying. On the other

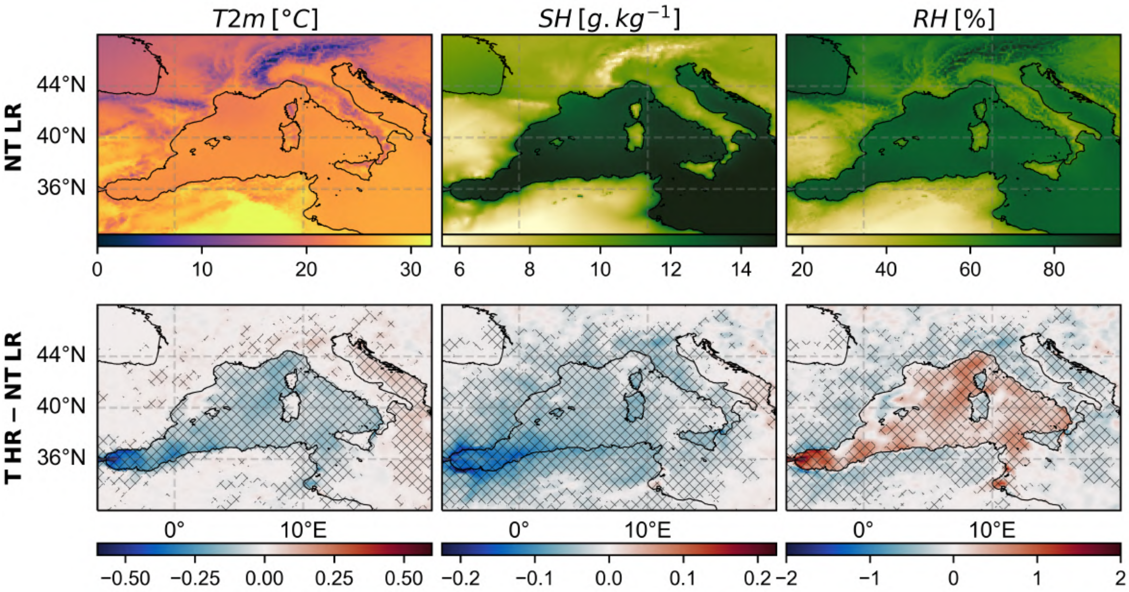

Figure 4.18: Upper panels display 1980-2017 summer averages (June-July-August) of the near-surface (2m height) atmospheric temperature (T2m), specific humidity (SH) and relative humidity (RH). Lower panels display the anomalies induced by the inclusion of tides and refined spatial representation of the SoG (T HR - NT LR). Hatches indicate statistically significant anomalies with respect to the interannual variability (based on a two-tailed student t-test with $p = 0.05$)

hand, over land, the atmosphere drying is not compensated by cooling, resulting in a general decrease in relative humidity.

Thus, the seasonal cooling of the WMB surface induced by tidal mixing and recirculation at the SoG influences the temperature and water vapor content of the near-surface atmosphere, suggesting a possible impact on its upper layers. To address this hypothesis, we display in Figure 4.19 the average precipitations and cloud fraction in the NT LR simulation and the anomalies induced by the inclusion of tides and the refined representation of the SoG in T HR (T HR - NT LR). Summer average precipitations display similar patterns to those described for the relative humidity, with the exception of the Mediterranean Sea where they are almost absent. Specifically, precipitations increase from south to north, reaching greater values over highland areas. The cloud fraction also displays a notable meridional gradient, with values increasing from south to north.

With respect to NT LR, the modified surface fluxes in the T HR simulation moderately impact precipitations. Specifically, precipitation anomalies organize in small-scale dipoles, mainly concentrated north of 40°N and are mostly insignificant with respect to the interannual summer variability. However, when considering the average anomaly, we find a statistically significant precipitation decrease of $\sim 0.01 mm/day$ over the whole domain shown in Fig.4.19, which is consistent with the drying of the atmosphere resulting from the decreased latent heat flux. Regarding the cloud fraction, anomalies between the NT LR and T HR simulations are significant. The cloud fraction mainly decreases above the western Mediterranean and within 500km of the coastline, which is consistent with the local drying of the

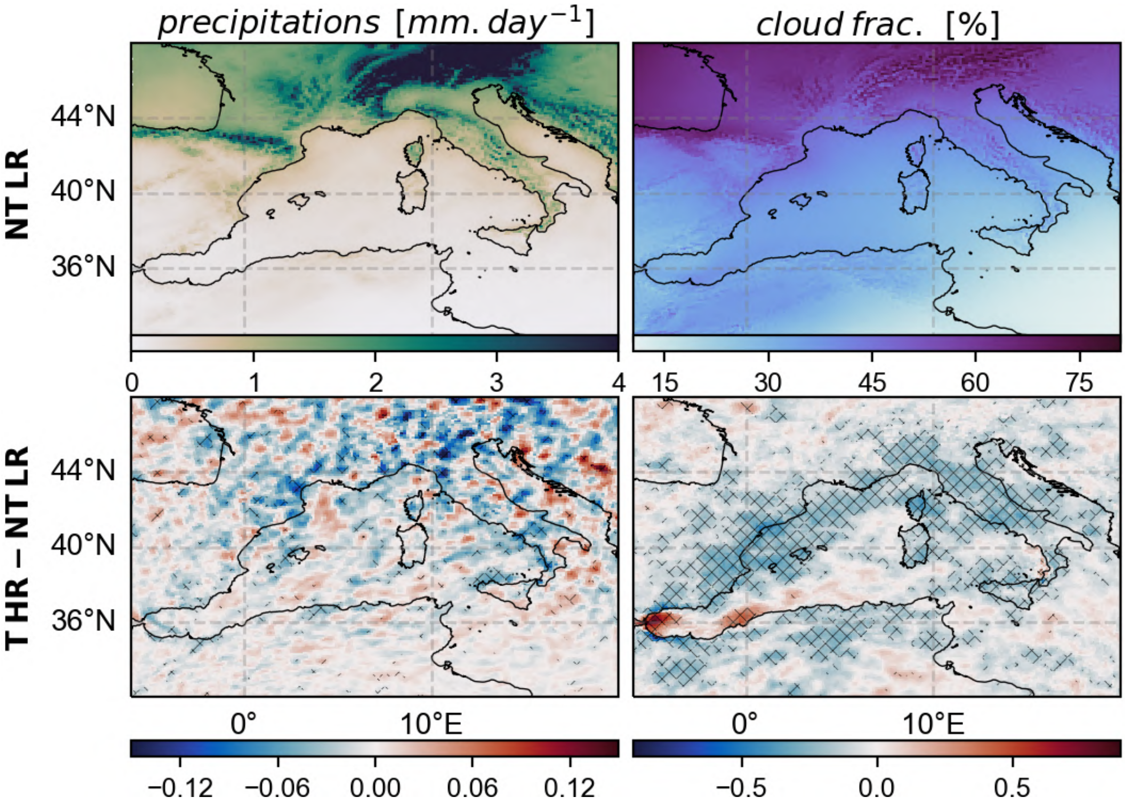

Figure 4.19: Upper panels display 1980-2017 summer averages (June-July-August) of precipitation and cloud fraction. Lower panels display the anomalies induced by the inclusion of tides and refined spatial representation of the SoG (T HR - NT LR). Hatches indicate statistically significant anomalies with respect to the interannual variability (based on a two-tailed student t-test with $p = 0.05$)

atmosphere. In particular, this coastal reduction of the cloud fraction is consistent with the intensification of the shortwave flux previously mentioned. Conversely, in the vicinity of the SoG, the cloud fraction increases due to the local intensification of the RH, mainly driven by the intense cooling of the sea surface.

Thus, the former analysis indicates that tidal cooling of the Western Mediterranean Sea surface in summer has a moderate but notable impact on the lower troposphere of the Mediterranean region. Specifically, it results in a reduction of the sensible heat and water vapor loss to the atmosphere. Consequently, this participates in the seasonal drying of the atmospheric boundary layer and reduces the summer warming of the near-surface atmosphere over the ocean. The surface drying results in a moderate decrease of precipitations over the western Mediterranean region and a more general decrease in cloudiness within 500km of the the WMB. Conversely, in the vicinity of the SoG, the intense tidal cooling of the sea surface results in a notable increase in cloudiness.

4.7 Conclusions

This chapter investigates the influence of local processes at the SoG on the Mediterranean region in a coupled regional climate model. In particular, we focus here on the tidal and fine-scale processes at play within the strait, which were shown to influence the hydrographic properties of the incoming Atlantic Waters and deep convection over the Northwestern Mediterranean (Sannino et al, 2009b; Harzallah et al, 2014; Naranjo et al, 2014; Sannino et al, 2015; Soto-Navarro et al, 2015). To do so, we compare four fully-coupled hindcast simulations, differing only by the inclusion or omission of tidal forcing and enhanced horizontal resolution at the SoG. Our results reinforce the conclusions of previous studies and provide new insights into the influence of tidal and fine-scale processes at the SoG and their relevance to the climatological properties of Mediterranean water masses, their interannual variability, and the Mediterranean deep convection. In addition, for the first time to our knowledge, we shed light on the influence of the SoG on ocean-atmosphere exchanges and the resulting impacts on the atmosphere.

The simulations display satisfactory performances with respect to reference observational datasets and provide a realistic picture of the main processes at stake at the SoG and in the Mediterranean Sea. Specifically, The simulated tides are in good agreement with available observation-based references, both at the SoG and over the Mediterranean Sea. In the same way, the dynamics of the SoG and the associated transports are consistent with the latest estimates and observational datasets available. Deep convection and its interannual variability are well reproduced over the northwestern Mediterranean and the Aegean Sea. On the other hand, it is less consistent with observations over the Adriatic Sea due to an overestimation of river runoff that results in a misrepresentation of the vertical structure of temperature and salinity. Regarding hydrographic properties, the simulations display reasonable biases with respect to the MEDHYMAP dataset, with greater discrepancies over the Adriatic Sea. Finally, the past interannual variability of the Mediterranean water masses is well captured over the upper and intermediate layers and less accurately over deeper layers.

At the SoG, a comparison of the simulations indicates that both tides and Fine-scale Topography and Dynamics (FTD) have a notable impact on the hydrographic properties and the dynamic structure of the exchange flow. We emphasize that FTD primarily shapes the average dynamic structure of the exchange flow and that tidal currents further refine it. Regarding hydrographic properties, we show that fine-scale representation of the strait and its vicinity impacts the Atlantic water masses entering the strait, whereas the well-known tidal mixing and recirculation (Harzallah et al, 2014; Naranjo et al, 2014; Sannino et al, 2015; Sanchez-Roman et al, 2018) mainly drives the water masses transformation within the strait. In addition, we highlight that tides substantially modulate the seasonal cycle of temperature at the surface of the Atlantic layer by ventilating the upper 50m depth of the water column in summer. We then show that these hydrographic and dynamic modulations and their remote impact on intermediate and deep Mediterranean water masses noticeably modulate the net heat and salt transport through the strait. In addition, we find that the refined representation of the strait results in an intensification of the volume transports, mainly attributable to the enhanced spatial resolution. Further work is needed to assess the influence of tides on the inflowing and outflowing transports, but we emphasize that it denotes intense water mass recirculation on both sides of the strait, consistently with Gonzalez et al (2023).

Over the Mediterranean Sea, a first investigation of the simulations focusing on the upper 300m depth of the water column suggests that both tides and FTD at the SoG are relevant to the climatological hydrography of the Mediterranean Sea. On the one hand, the refined spatial representation of the SoG results in a general freshening of the Mediterranean surface due to the thickening and intensification of the Atlantic inflow across the SoG. On the other hand, as expected from previous studies (Sannino et al, 2009b; Harzallah et al, 2014; Naranjo et al, 2014; Sannino et al, 2015), tidal forcing and recirculation at the SoG significantly saltens and cools the Western Mediterranean surface. In addition, we show that the summer tidal cooling of the sea surface at the SoG propagates to the Western Mediterranean Basin (WMB) and modulates the basin-scale seasonal cycle of SST. When both considered, the effects of tides and FTD at the SoG combine over the Western Mediterranean and mainly cancel out over the Eastern Mediterranean.

Then, investigation of the simulated deep convection highlights that both tides and FTD at the SoG influence the Mediterranean convective activity through the modulation of the Atlantic Water (AW) salinity. As suggested by Naranjo et al (2014); Sannino et al (2015), we find that tides enhance the deep convection over the northwestern Mediterranean, and we extend this conclusion to the Adriatic Sea and the Aegean Sea. Conversely, the refined spatial representation of the SoG in the high-resolution simulations accordingly weakens the Mediterranean convective activity. When both included, the combined influence of tides and FTD induces varying effects depending on the area considered, suggesting that both are essential to the accurate representation of Mediterranean convection.

To assess the impact of the modulated convection and hydrography on deeper layers, we investigate the interannual variability of salinity and temperature over the entire water column. Above 600m depth, we highlight that the hydrographic anomalies induced by tides and FTD are relatively steady. Tides primarily increase the climatological basin-scale salinity above 150m depth. Consequently, over the WMB, the deep convection sustainably intensifies, modulating the average stratification between 150-600m depth. Over the EMB, the surface saline anomaly propagates to intermediate depths. Conversely, the inclusion of FTD at the SoG has opposite effects, triggered by the decrease of the climatological basin-scale salinity above 150m depth. Below 600m depth, tides and FTD at the SoG have a notable influence on the long-term tendencies of temperature and salinity, which are substantially impacted by the modulation of intense convective events.

Finally, in light of the notable modification of the Western Mediterranean surface temperature in summer, we investigate the possible impact on the atmosphere. We show that the tidal cooling over the Western Mediterranean surface in summer mainly results in decreased ocean heat and water fluxes to the atmosphere. Consequently, the seasonal drying of the near-surface atmosphere locally intensifies, whereas its warming moderately weakens. This results in a modulation of cloudiness, which mainly decreases within 500km of the coastline due to the drier atmosphere and increases in the Alboran Sea due to the temperature-driven increased relative humidity. Finally, precipitation is weakly affected, but we note a statistically significant decrease over the whole western Mediterranean region.

To conclude, this study highlights that tidal and fine-scale processes at the SoG are relevant to the Mediterranean Sea hydrographic properties, convective activity, and summer air-sea fluxes. Furthermore, we emphasize that the inclusion of these processes in numerical models is particularly relevant when investigating the exchanges through the SoG, the Mediterranean Sea surface, and physical mechanisms related to the upper Mediterranean vertical stratification, such as convection. When explicit tides and sine-scale resolution at the SoG are not affordable, our results suggest that, at least, the effects of tides and fine-scale mechanisms should be parameterized. Such parameterization will be investigated in the next chapter. In the future, this study would gain from investigations of the large-scale impact of non-hydrostatic processes at the SoG, which are not included in the simulations investigated. In addition, further work is needed to clarify the influence of fine-scale processes at play within the strait on the Mediterranean circulation. Finally, this study points to several relevant large-scale impacts. In particular, their notable influence on the Mediterranean convective activity suggests that local processes within the strait are relevant when investigating the future evolution of this phenomenon (Parras-Berrocal et al, 2022).

Appendices

A Enhanced resolution at the SoG: decomposition into dynamical and bathymetric effects

In this section, we investigate the respective influence of fine-scale topography and dynamics on the exchange flow through the SoG. To do so, we compare three forced 19-year non-tidal ocean simulations differing only through their representation of the SoG. At the SoG, the simulations use either coarse resolution (1/12° NT LR), enhanced resolution (1/60° NT HR), or an enhanced resolution with coarse horizontal geometry and smoothed topography (NT HRs). More specifically, we create the topography of the T HRs simulation from the bi-linear interpolation of the NT LR topography. We diagnose the effect of fine-scale horizontal dynamics as the difference between the NT HRs and NT LR simulations ($\delta R_h = NTHRs - NTLR$) and the effect of the fine-scale topography as the difference between the NT HR and NT HRs simulations ($\delta R_b = NTHR - NTHRs$).

We display on the upper panels of Figure A.1 the average vertical profiles of zonal velocity, salinity, and temperature at the SoG for the NT LR (blue line) and NT HR (green line) simulations. On lower panels, we display the anomaly induced by the inclusion of refined spatial representation of the SoG (δR, green line) and its decomposition into two components related to the horizontal grid refinement (δR_h, light green line) and the inclusion of fine-scale topography (δR_b, dark green line). Overall, both NT LR and NT HR display a typical picture of the two-layer exchange flow between the Atlantic Ocean and the Mediterranean Sea. Differences between the simulations are highly similar to that observed for the hindcast simulations (Figure 4.8 in the main body of this chapter). To be more specific, with respect to NT LR, the NT HR configuration simulates a thicker Atlantic layer and a deeper Mediterranean layer, separated by a more homogeneous interface, both in terms of velocity and hydrographic properties.

Comparing the NT HR and NT LR simulations, δR indicates that the inclusion of FTD results in substantial modulations of the strait dynamics. More specifically, the anomaly patterns displayed by δR_b and δR_h suggest that these modulations relatively equally result from the inclusion of refined horizontal resolution and fine-scale topography. Below 100m, δR_b and δR_h display similar dipole patterns mainly shifted over the depth. These dipole patterns indicate a progressive thickening of the Atlantic layer (positive anomaly near 150m depth) and a deepening of the Mediterranean outflow core (negative anomaly near 300m depth) as the geometric representation of the strait is refined. In particular, this reorganization of the exchanged flow is attributable to the progressive inclusion of fine-scale topographic cavities above the seafloor, through which Mediterranean water masses are advected. Above 100m depth, δR_h and δR_b display opposite patterns, providing further indications on the modified dynamics. For δR_h, the negative velocity anomaly is consistent with a thickening of the Atlantic layer, which results in a decrease of surface zonal velocities due to the relatively similar volume inflow in NT LR and NT HRs. On the other hand, for δR_b, the positive anomaly pattern results from enhanced water recirculation due to the inclusion of abrupt topographic obstacles in T HR. Similarly to what is described in Gonzalez et al (2023), east of the CS, upwelled Mediterranean water masses at the CS force the Atlantic layer to thin and accelerate, resulting in a positive velocity anomaly above 100m depth. Conversely, west of the CS, downwelled Atlantic water masses forces the Mediterranean layer to deepen and accelerate, further intensifying the anomaly below 100m depth due to its natural deepening with the refined representation of the seafloor.

Regarding hydrographic properties, anomalies induced by the refined representation of the SoG are mainly consistent with the dynamic modifications just described. Specifically, the substantial decrease of salinity near 150m depth primarily results from the overall thickening of the Atlantic layer due to the horizontal grid refinement (δR_h). The vertical profile of salinity is also modulated to a lesser extent by the inclusion of fine-scale topography (δR_b), which results in a dipole anomaly centered on 150m, consistent with water masses recirculation. A similar reasoning applies to temperature anomalies below 100m depth. However, the average anomaly above 150m depth is mainly driven by modification in the Gulf of Cadiz circulation, and that below 150m by modulations of the Mediterranean intermediate and deep water masses temperature.

To conclude, in terms of dynamics, the inclusion of fine-scale dynamics mainly allows representing bottom currents that develop in small topographic cavities, resulting in a deepening of the Mediterranean outflow and a thickening of the Atlantic layer. This effect is further enhanced when including fine-scale topography, which also enhances water mass recirculation, modulating the thickness of the exchanged layers on each side of the CS. In this way, the overall thickening of the Atlantic inflow in NT HR with respect to NT LR can be mainly attributed to the deepening of the seafloor, whereas zonal modulations of the interface depth are attributable

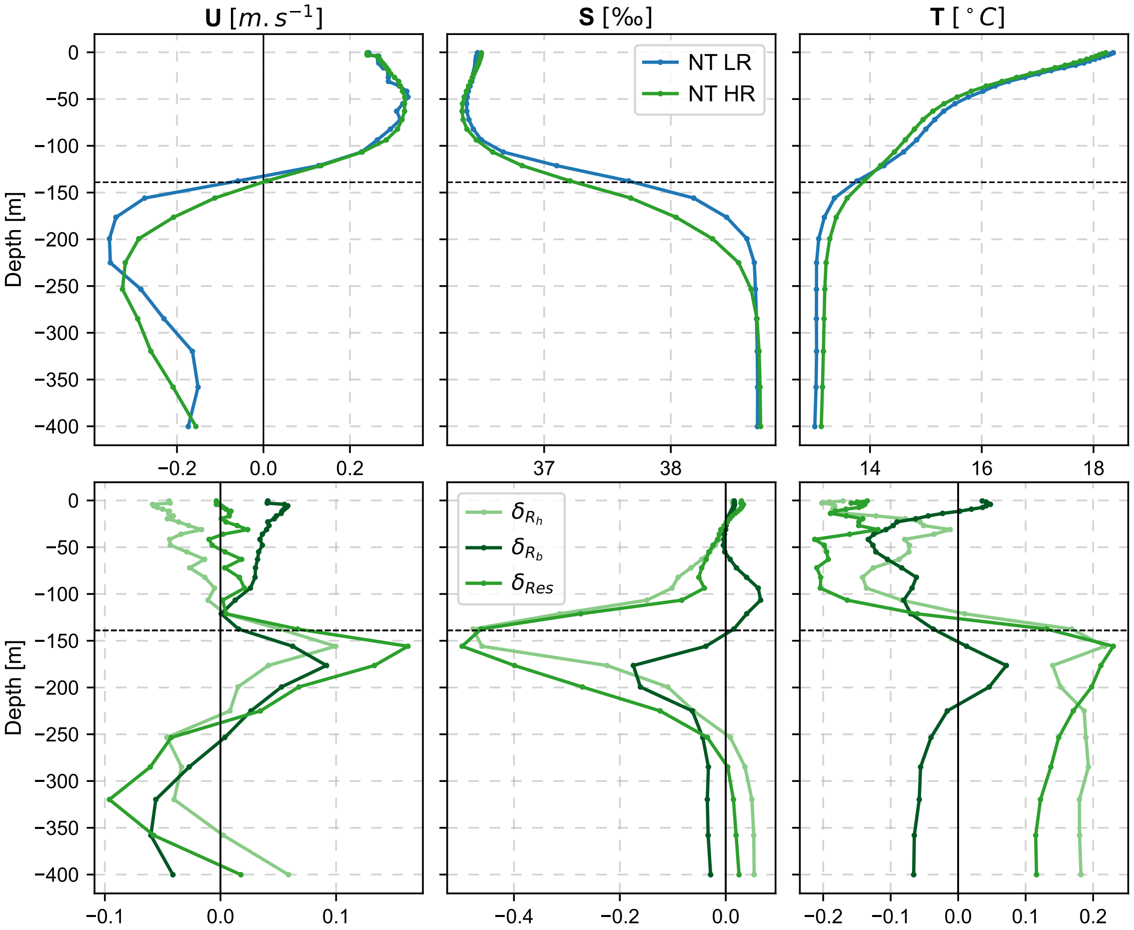

Figure A.1: Upper panels display 19-year average vertical profiles of temperature, salinity, and zonal velocity around the Strait of Gibraltar (averaged over area framed by the dashed rectangle in the lower panel of Figure 4.1) for the forced NEMOMEDGIB non-tidal coarse resolution simulation (NT LR) and the non-tidal high-resolution simulation (NT HR). Lower panels display the anomalies between both simulations (NT HR - NT LR = δ_{Res}) and their decomposition into two components, associated with the inclusion of fine-scale horizontal dynamics (δ_{Rh}) and fine-scale topography (δ_{R_b}). The horizontal dashed line represents the depth of the zero velocity interface in the NT HR simulation.

to fine-scale topographic obstacles. Salinity anomalies are driven by the reorganization of the exchanged flow, whereas temperature anomalies result from remote modulation of circulation or water masses properties.

Chapter 5

Parameterizing tidal mixing at the Strait of Gibraltar

Over the previous chapters, we have shown that fine-scale dynamics and tides at the SoG have a notable influence on the Mediterranean Sea hydrography, deep convection, and air-sea fluxes. All these results highlight the relevance of high-resolution and tidal forcing in numerical models of the Mediterranean Sea. However, their inclusion is technically challenging and leads to significant increases in the numerical cost of simulations. In addition, global ocean climate models still lack the necessary refinement to explicitly resolve baroclinic tides. In this chapter, we take a first step to lift these technical barriers by investigating a parameterization of tidal mixing to be used in non-tidal numerical models with coarse resolution at the SoG. This work has been done in collaboration and with the technical support from Jérôme Chanut (MERCATOR ocean) and Ariane Koch-Larrouy (LEGOS).

5.1 Introduction

The Mediterranean Sea is an area of strong scientific interest for oceanographers. In fact, as a semi-enclosed sea with an active overturning circulation (Waldman et al, 2018), the Mediterranean Sea can be considered a "miniature ocean" (Bethoux et al, 1999), making it an ideal test bed for the study of various oceanic phenomena. However, understanding the details of the processes driving the Mediterranean Sea mean state and its variability is still a scientific challenge today. In particular, the role played by fine-scale and non-linear mechanisms is often complex to assess, as observing and modeling their long-term remote impact is challenging. Among these mechanisms, the tide-induced water mass transformation through the SoG, so-called tidal mixing, has been subject of particular interest over the last decade (Bruno et al, 2002; Macias et al, 2006; Macías et al, 2007; García-Lafuente et al, 2011; Sanchez-Garrido et al, 2011; Bruno et al, 2013; García Lafuente et al, 2013; Harzallah et al, 2014; Naranjo et al, 2014; Sannino et al, 2015; Sanchez-Roman et al, 2018; Hilt et al, 2020; Gonzalez et al, 2023). In particular, several studies have highlighted its relevance to the modeling of the Mediterranean Sea hydrography, circulation and overturning circulation (Harzallah et al, 2014; Naranjo et al, 2014; Sannino et al, 2015). However, interaction of tidal currents with fine-scale topography and stratification upon which tidal mixing relies (Gonzalez et al, 2023) represents a technical barrier for its representation in numerical models.

An alternative to the explicit representation of tidal mixing at the SoG is to impose the tide-induced turbulence as a forcing based on estimates of the baroclinic tidal dissipation. This approach, so-called tidal mixing parameterization, has been recently developed in de Lavergne et al (2016, 2019, 2020) and provides a promising solution to the representation of tidal mixing at the SoG in coarse resolution numerical models.

This present chapter investigates the relevance of parameterizing tidal mixing to represent the unresolved tide-induced water mass transformation across the SoG. Specifically, we aim to implement a tidal mixing parameterization for use in non-tidal models of the Mediterranean Sea. In the following, we first produce and evaluate a climatology of baroclinic tidal dissipation in the Mediterranean Sea. Then, we assess the impact of the parameterized tidal mixing on the physical state of the Mediterranean Sea and compare it to the explicit approach presented in the previous chapter.

5.2 Model and Methods

5.2.1 Numerical simulations

We focus on a set of forced NEMOMEDGIB simulations, providing an increasingly realistic representation of the SoG. We consider three simulations with coarser resolution at the SoG, differing only by the omission (NT LR), parameterization (pT LR), or explicit representation (T LR) of tides. These simulations allow us to assess the effect of the parameterized mixing (δ_{pTides} =pT LR - NT LR) and compare it to that of explicit tides (δ_{Tides} =pT LR - NT LR). In addition, we consider two simulations with refined horizontal resolution at the SoG (see Figure 5.1), differing only by the omission (NT HR) or inclusion (T HR) of explicit tides. These simulations provide a more realistic picture of the effect of tidal mixing at the SoG ($\delta_{T\,HR}$ =T HR - NT HR) accounting for the interaction of tidal currents with fine-scale topography.

The simulations are initialized in August 1979 from the outputs of a preliminary decadal NEMOMEDGIB simulation with no explicit tides and use identical forcings (to within a Newtonian SST restoring inherent to the flux forcing), which do not follow the historical climatic chronology. Specifically, the forcings consist of 19-year annual datasets of the ALDERA regional reanalysis (Herrmann et al (2011), see chapter 2 for more details) starting in August and taken randomly over 1979/08/01 - 1986/07/31. The aim is to simulate a relatively steady climate free of transient climatic trends.

5.2.2 Tidal mixing parameterization

This section introduces the tidal mixing parameterization used in this study, which is based on de Lavergne et al (2020). Simply put, the parameterization provides the NEMOMEDGIB model with a tidal mixing coefficient K_{Tides} (in m^2.s^{-1}) to be added to the vertical eddy viscosity and diffusivity coefficients. More specifically, K_{Tides} is computed from an estimate of the baroclinic tidal dissipation ϵ_{Tides} (in $m^2.s^{-1}$), which drives diapycnal mixing through tidal buoyancy flux BF_{Tides} (in W.kg^{-1}), as expressed below:

$$BF_{Tides} = K_{Tides}\, N^2 = R_f\, \epsilon_{Tides} \tag{5.1}$$

where N^2 is the squared Brunt–Väisälä frequency and R_f the flux Richardson number or mixing efficiency. R_f separates the fraction of dissipation energy available for mixing from that converted into heat by friction. In this study, we consider $R_f = 1/6$ as generally assumed for oceanic stratified conditions (Gregg et al, 2018).

Thus, the former parameterization requires three-dimensional estimates of baroclinic tidal dissipation. More specifically, the version used in this study considers that baroclinic tide dissipation results from three distinct dissipative processes, for each of which a climatology of depth-integrated dissipation energy must be provided. The vertical distribution of the tidal dissipation energy is then determined from a

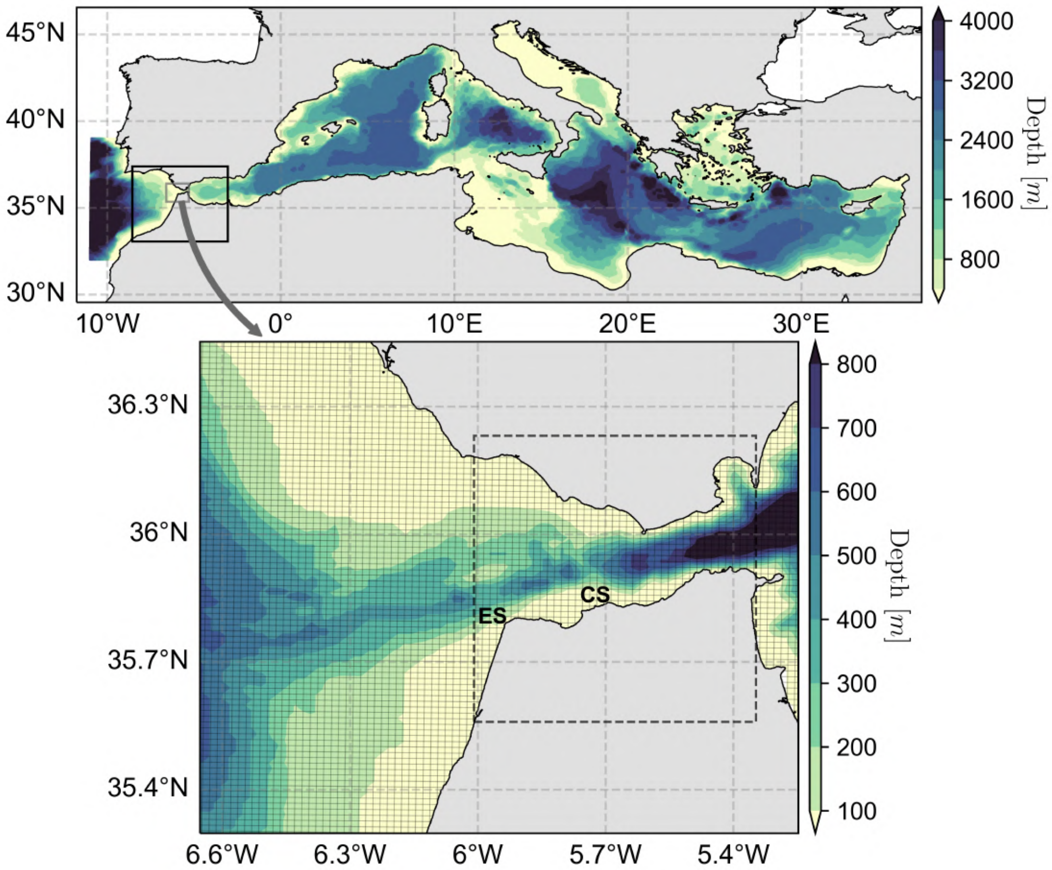

Figure 5.1: NEMOMEDGIB coarse bathymetry (upper panel) and zoom on the refined grid and bathymetry at the Strait of Gibraltar (lower panel, representing the area framed by the grey rectangle). The black rectangle on the upper panel shows the area over which horizontal grid and bathymetry refinement are available (AGRIF domain). The dashed rectangle on the lower panel displays the area used to investigate average hydrography and dynamics of the Strait of Gibraltar. The acronyms "ES" and "CS" refer to the Espartel and Camarinal Sills, respectively

simplified representation of the associated dissipative processes and the simulated hydrography. We detail below the considered dissipative processes and their representation. Note that although it is introduced in de Lavergne et al (2020), we do not include baroclinic tidal dissipation by shoaling. However, given the low intensity of the associated dissipation rate over the Mediterranean Sea (de Lavergne et al, 2019), its omission should have a moderate effect.

Wave-wave interactions

Wave-wave interactions account for the energy provided by the breaking of low mode (1-10) baroclinic tides from interaction with other waves (ϵ_{wwi}, in W.kg^{-1}). Following de Lavergne et al (2020), ϵ_{wwi} is supposed to scale with the square of the buoyancy frequency as follows:

$$\epsilon_{wwi}(t,z) = \frac{D_{wwi}}{\rho_0} \frac{N^2(t,z)}{\int N^2(t,z')\,dz'} \tag{5.2}$$

where D_{wwi} is the depth-integrated climatological dissipation energy attributed to wave-wave interactions (in W.m^{-2}) and $\rho_0 = 1025\,\mathrm{kg.m^{-3}}$ is a reference density.

Interaction with critical slopes

Interaction with critical slopes accounts for the energy provided by the breaking of low-mode baroclinic tides on abrupt topography ($\epsilon_{cri}(z)$ in W.kg^{-1}), which mainly occurs near continental slopes. Following de Lavergne et al (2020), $\epsilon_{cri}(z)$ is expressed as an exponential decay from the seafloor with an e-folding scale H_{cri} function of the local topographic slope:

$$\epsilon_{cri}(z) = \frac{D_{cri}}{\rho_0} \frac{e^{-z/H_{cri}}}{H_{cri}(1 - e^{-z/H_{cri}})} \tag{5.3}$$

where D_{cri} is the depth-integrated climatological dissipation energy attributed to the interactions with critical slopes (in W.m^{-2}) and H the depth of the seafloor.

Interactions with abyssal hills

Interactions with abyssal hills account for the energy provided by the scattering of low-mode baroclinic tides and the generation of high-mode baroclinic tides on abyssal hills which ultimately dissipate locally (ϵ_{hil}, in W.kg^{-1}). Following Lefauve et al (2015), we supposed ϵ_{hil} to depend on a stratification-weighted height above the bottom (the so-called Wentzel-Kramers-Brillouin stretching) given by:

$$h_{WKB}(t, z) = H \frac{\int_{-H}^{z} N^2(t, z')\, dz'}{\int_{-H}^{0} N^2(t, z')\, dz'} \tag{5.4}$$

More specifically, ϵ_{hil} follows:

$$\epsilon_{hil}(t, z) = \frac{D_{hil}}{\rho_0} \frac{N^2(t, z)\, e^{-h_{WKB}(t,z)/H_L}}{\int N^2(t, z')\, e^{-h_{WKB}(t,z')/H_L}\, dz'} \tag{5.5}$$

Where D_{hil} is the depth-integrated climatological dissipation energy attributed interactions with abyssal hills (in W.m^{-2}) and H_L is a space-variable height scale depending on local bottom conditions.

As specified in de Lavergne et al (2020), alternative versions of this parameterization can provide more accurate results. However, the present version performs well above the first upper 3000m depth of the water column, which is sufficient for the Mediterranean Sea.

5.3 A climatology of baroclinic tidal dissipation for the Mediterranean Sea

This section aims to construct the three-dimensional climatologies of baroclinic tidal dissipation to be provided to the tidal mixing parameterization of de Lavergne et al (2019). Specifically, we first aim a producing a general depth-integrated climatology of baroclinic tidal dissipation energy for the Mediterranean Sea and then attribute a fraction of this energy to each dissipative process considered in the parameterization. This allows us to project tidal dissipation vertically throughout the water column. As shown below, observations are too scarce to produce large-scale estimates of baroclinic tidal dissipation. Henceforth, we will rely on reference numerical datasets. Note that we will also consider estimates of baroclinic tidal generation, which are better constrained from barotropic tidal models and may be relevant in areas where baroclinic tides dissipate in the vicinity of their generation site.

5.3.1 Tidal models

We consider four reference numerical models which provide estimates of either or both baroclinic tidal generation and dissipation rates.

- de Lavergne et al (2019) (DL19 hereinafter): 1° Baroclinic (three-dimensional) tidal energy model, which provides the default tidal dissipation climatology available in the NEMO model. Computation of the climatology relies on a global observational climatology of stratification and maps of baroclinic tidal generation for the M_2, S_2, and K_1 tidal harmonics. More specifically, baroclinic tide dissipation rates are computed from the generation energy, propagated with a Lagrangian tracking of low-mode energy beams, and dissipated based on simplified representations of wave-wave interactions and interaction with critical slopes and abyssal hills. Thus, this model provides the respective contributions of wave-wave interactions and interaction with critical slopes and abyssal hills to the total dissipation energy.

- FES2014 (Finite Element Solution): 1/16° Global barotropic (two-dimensional) tidal model based on the resolution of the shallow water hydrodynamic equations in a spectral configuration (Lyard et al, 2021). It resolves the main semidiurnal M_2, S_2, N_2, K_2, N_2 and diurnal K_1, O_1, Q_1, P_1 tidal harmonics. The tidal baroclinic generation energy is computed from the barotropic energy through an internal wave drag parameterization. Because of the high resolution of the model (with respect to the other ones considered) and the good knowledge of barotropic tides dynamics, this estimate will be used as a reference for the basin integral baroclinic tidal generation rate (Lyard et al, 2006). In addition, a regional configuration with higher resolution (1/100°) at the Strait of Gibraltar and the Alboran sea is also available and used as a refinement in those areas.

- HYCOM (HYbrid Coordinate Ocean Model): Hybrid isopycnal-sigma-pressure (generalized) coordinates global ocean model with a 1/12° horizontal resolution (Buijsman et al, 2016). The model uses explicit tidal forcing with a parameterized internal wave drag on semidiurnal tides (M_2, S_2, N_2, K_2). Baroclinic tidal generation is inferred from band-passed sea surface height and mean baroclinic dissipation. Baroclinic tidal dissipation is computed from the band-passed tidal velocities with a linear separation technique (Kang and Fringer, 2012).

- NEMO (Nucleus for European Modelling of the Ocean): Global baroclinic ocean model with a curvilinear horizontal grid of 1/12° and 75 levels of z-coordinates. The model includes explicit tidal forcing for the M_2, S_2, K_1, N_2, P_1, and S_1 tidal harmonics. Baroclinic tide dissipation and generation energies are estimated from the model's governing equations following Carter et al (2008); Zilberman et al (2009).

For each of the former estimates, we interpolate the associated baroclinic tide generation and dissipation energies onto the NEMOMEDGIB grid using an energy-conservative scheme. Specifically, the interpolation consists in distributing the energy contained in each point of the original grids to the closest one in the NEMOMEDGIB grid. The points that do not contain any energy at the end of the process take a fraction of their neighbours.

Note that the numerical method used for the NEMO and HYCOM estimates produces negative energies, which are meaningful only upon averaging. At the end of the interpolation process, relatively large areas of negative energies remain, such that their suppression through spatial averaging would significantly deteriorate the spatial pattern of the estimates. As an alternative solution, we replace these negative values with their nearest positive neighbour. It is noteworthy that this scheme is not energy-conservative, but we address this issue in the following section.

5.3.2 Tidal dissipation estimates

As a first step to assess the realism of the considered estimates, we investigate the consistency of their integral energetic content with respect to the FES2014 estimate of baroclinic tidal generation. To do so, we display in Figure 5.2 the integral energy of the considered estimates over the Mediterranean Sea. In addition, we specify the share of energy contained over the interior Mediterranean Sea, where tides are weak, and over the Alboran Sea and the SoG, where the propagation of the Atlantic tide locally intensifies them. For the NEMO and HYCOM estimates, we indicate their total energetic content before (H_G^{org},H_D^{org},NM_G^{org},NM_D^{org}) and after (H_G,H_D,NM_G,NM_D) the interpolation of negative value.

Overall, the considered estimates display substantial differences, both in terms of integral energy and spatial distribution. On the other hand, baroclinic tidal dissipation and generation are highly similar when estimated by the same model (H_G^{org} and H_D^{org}; NM_G^{org} and NM_D^{org}). This indicates that baroclinic tidal generation can be used as a reference for the basin-integrated tidal dissipation. With that in mind, the FES2014 model displays a total baroclinic tidal generation of $\sim$ 1.8GW over the Mediterranean Sea, two thirds of which are generated over the Alboran Sea and the SoG. This uneven distribution is consistent with the large differences in intensity of tides in the vicinity of the SoG and over the rest of the Mediterranean Sea.

With respect to FES2014, the other model estimates all display significantly weaker baroclinic tides. The HYCOM estimates (H_G^{org} and H_D^{org}) are the most consistent with FES2014, both in terms of integral energy and spatial distribution. Specifically, it displays a similar energy distribution to FES2014 but underestimates

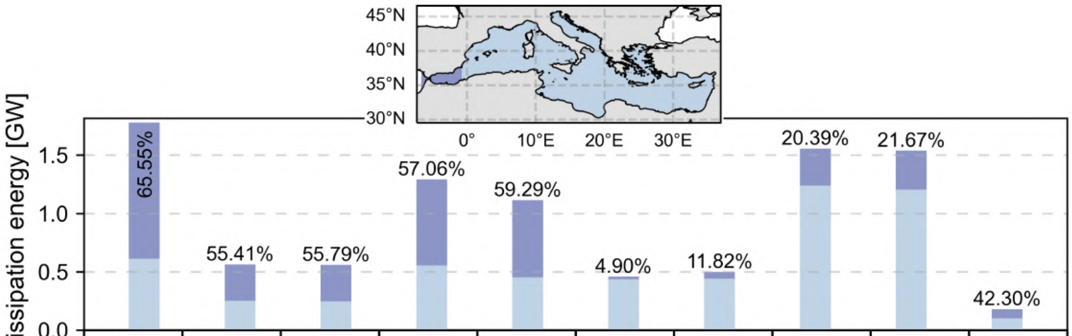

	FES_G	H_D^{org}	H_G^{org}	H_D^{PT}	H_G^{PT}	NM_D^{org}	NM_G^{org}	NM_D^{PT}	NM_G^{PT}	DL19
int. Med	0.613	0.251	0.247	0.555	0.453	0.436	0.442	1.238	1.205	0.104
SoG & AS	1.166	0.313	0.312	0.737	0.660	0.022	0.059	0.317	0.333	0.076
Whole Med	1.779	0.564	0.560	1.292	1.113	0.459	0.501	1.556	1.538	0.180

Figure 5.2: Energy content of the considered estimates of baroclinic tidal dissipation and generation. We specify the share of the integral energy located west of $6°W$. Subscript ”_PT” refers to post-treated NEMO and HYCOM fields with interpolated negative values

the integral energy content. On the other hand, the NEMO estimates (NM_G^{org} and NM_D^{org}) display similar baroclinic tide energy to FES2014 over the interior Mediterranean but underestimate it over the Alboran Sea and the SoG. As expected, the post-treated HYCOM and NEMO estimates (H_G^{PT},H_D^{PT},NM_G^{PT},NM_D^{PT}) display significantly higher integral energy than the original estimates. More specifically, the interpolation of negative values results in an uneven intensification, making the total energy level closer to that of FES2014, but changing its distribution. In particular, the original balance of the NEMO estimates leads to a highly energetic content in the Mediterranean basin compared to FES2014. Finally, the DL19 estimate substantially underestimates the energetic content of both the Mediterranean interior, the Alboran Sea, and the SoG.

In light of the former analysis, the NEMO, HYCOM, and DL19 models all likely underestimate the baroclinic tidal energy over the Mediterranean Sea. In addition, for the NEMO and HYCOM estimates, the interpolation of negative values results in a substantial increase in their integral energy, making them unreliable. Therefore, in the following, we will normalize the integral energy content of the post-treated NEMO and HYCOM estimates and the DL19 estimate with that of FES2014, which is more reliable. We now aim to validate the spatial distribution of the energy displayed by the estimates.

The resulting fields are shown in Figure 5.3 and 5.4. Except for the DL19 estimate, both baroclinic tidal dissipation and generation display substantial variations over the Mediterranean Sea. In particular, the Alboran basin, the SoG, and the straits of Sicily and Otranto stand out as areas of intense baroclinic tidal generation and dissipation. The main differences between tidal generation and dissipation arise over deep water areas, where the generation energy abruptly decreases, whereas the dissipation rate takes on larger values. Overall, the FES2014, HYCOM and NEMO models produce very similar spatial patterns of tidal energy. The HYCOM baroclinic tidal dissipation is exeptionnaly intensified along 26°E, but this is likely spurious as there is no ridge or steep bottom at this location. Finally, note that the FES2014 generation energy is null over shallow shelves.

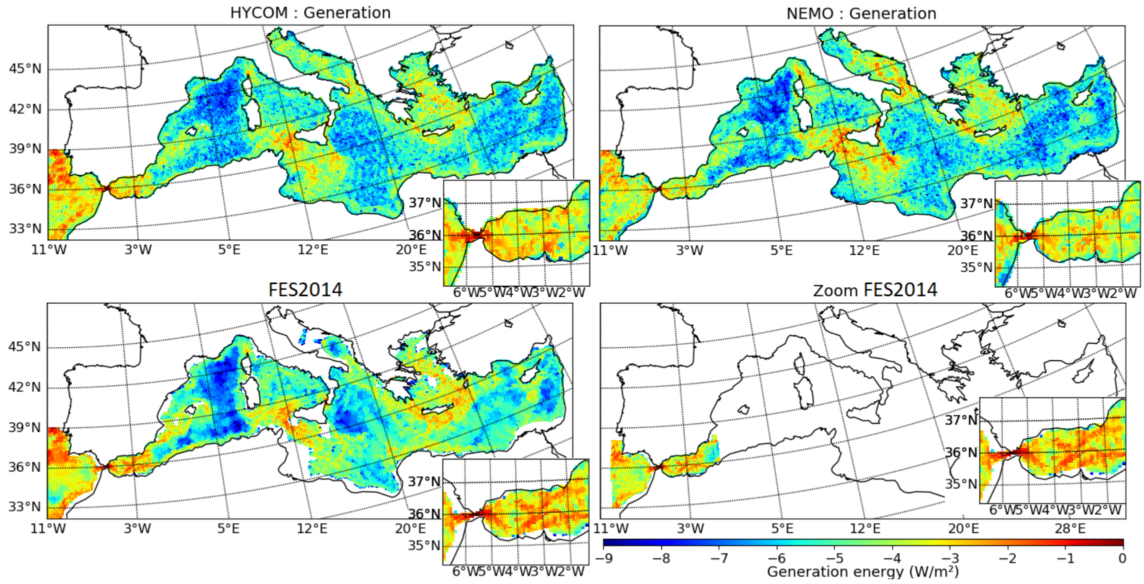

Figure 5.3: Decimal logarithm of baroclinic tidal generation estimates from the HYCOM, NEMO, and FES2014 numerical models. The estimates are interpolated onto the NEMOMEDGIB grid and post-treated as detailed in the body of this chapter

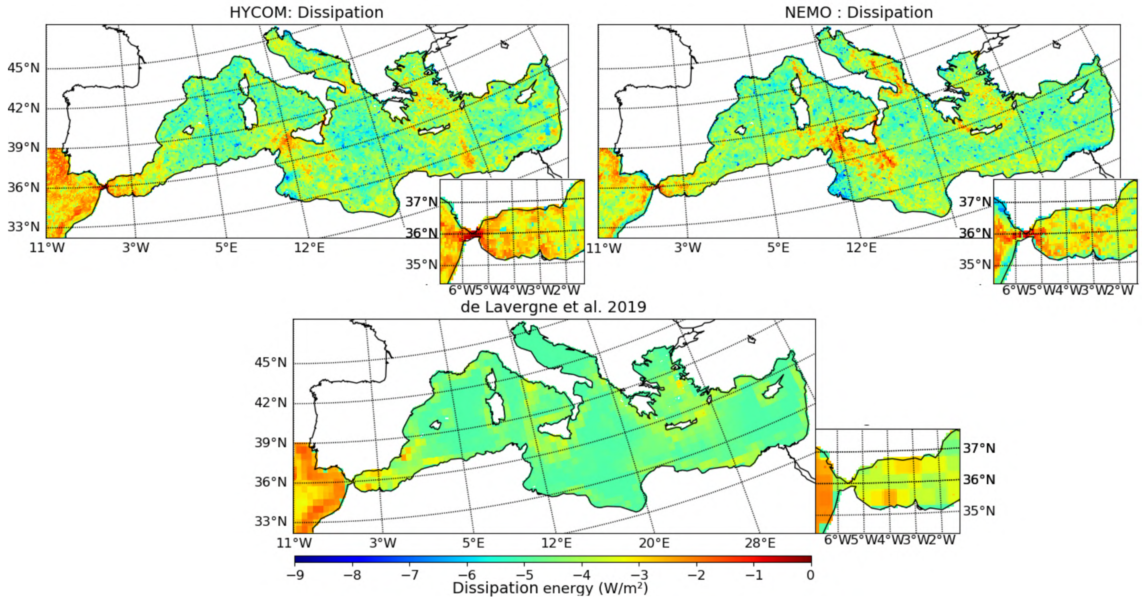

Figure 5.4: Decimal logarithm of baroclinic tidal dissipation estimates from the HYCOM, NEMO, and DL19 numerical models. The estimates are interpolated on the NEMOMEDGIB grid and post-treated as detailed in the body of this chapter

5.3.3 Comparison with in situ measurements

In this section, we compare the baroclinic tide dissipation and generation energy estimates to available observations. Specifically, we rely on Vertical Microstructure turbulence Profiler (VMP hereinafter) measurements, which quantify the turbulent dissipation rate along the water column. It is noteworthy that these measurements are not specific to baroclinic tides. Thus, we assume that the spatial variations of turbulence are representative of that of baroclinic tidal dissipation. In addition, we consider that the measurements performed over areas of low tidal energy provide an upper bound of baroclinic tide dissipation energy. For energetic areas, where tides drive intense turbulence, we consider that the measurements provide the order of magnitude of the baroclinic tidal dissipation rate.

In the following, we compare the model estimates of baroclinic tide dissipation and generation energies with the depth-integral dissipation energy from the measurements. It follows :

$$D_{obs} = \int \epsilon_{obs}(z)\ \rho_0\ dz \tag{5.6}$$

With ϵ_{obs} the measured dissipation rate in W.kg^{-1}.

Strait of Gibraltar

In the absence of digitalized VMP measurements at the SoG, we rely on printed VMP datasets from Wesson and Gregg (1994), sampled during the Gibraltar experiment in 1985-1986. Specifically, we compute the depth-integral dissipation energy from Tables 2a, 2b, and 2c of Wesson and Gregg (1994), which display average turbulent dissipation rates over three different layers (defined by density thresholds). Given the large intensity of tides at the SoG, we consider the entirety of the vertical profiles, assuming that tides drive turbulence over most of the water column.

We display in Figure 5.5 a boxplot of the modeled baroclinic tide energetics and observed dissipation rates over the area investigated in Wesson and Gregg (1994), that is, in the vicinity of the Camarinal Sill. Considering that high values make up most of the integral baroclinic tide energy within the SoG, we mainly aim for the simulations to capture the higher part of the data spread. With that in mind, except for DL19, the model estimates all reproduce relatively consistent dissipation energies, with medians above or close to $10^{-1} W.m^{-2}$. More specifically, the FES2014 estimates (FES_G and $FES_z\ G$) stand out as the most accurate. This consistency suggests that most of the baroclinic tides generated within the strait dissipate locally. This is confirmed by the large similarity between the dissipation and generation estimates considered in the HYCOM and NEMO models. In particular, the high-resolution FES2014 simulation ($FES_{z\,G}$) displays an improved consistency with the observations over the higher values. The NEMO and HYCOM estimates are also in good agreement with observations, particularly for tidal generation, which is more energetic. However, those estimates generally underestimate the total energy compared to measurements. Finally, the DL19 estimate largely underestimates the dissipation, a likely consequence of the model's limited horizontal resolution.

Western Mediterranean Basin

Over the Mediterranean Sea, we only have at our disposal the VMP measurements dataset of Ferron et al (2017), which cover the Western Mediterranean Basin

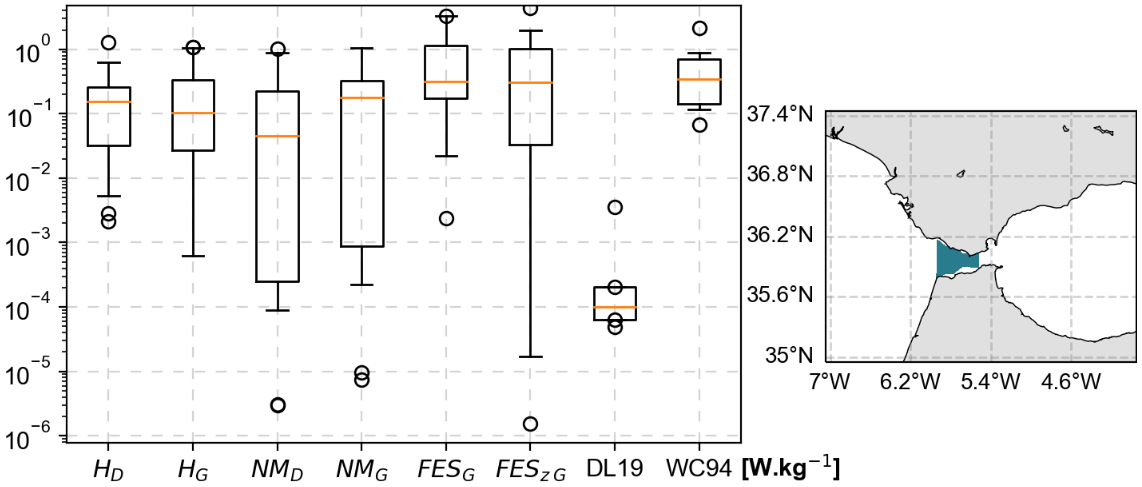

Figure 5.5: Boxplot of vertically integrated measurements computed from the Tables 2a, 2b, and 2c of Wesson and Gregg (1994) (WC90) and estimated from tidal numerical simulations. We display the domain considered for averaging on the right panel. The acronyms ”H”, ”NM”, ”FES”, and ”DL19” stand for the HYCOM, NEMO, FES2014, and de Lavergne et al (2019) numerical models. The subscript ”G” indicates estimates of baroclinic tide generation energy, and the subscript ”D” indicates estimates of baroclinic tide dissipation energy. The box extends from the 25th and 75th percentiles, with a line at the median, and whiskers show the 5th and 95th percentiles. Flier points are those past the end of the whiskers.

(WMB hereinafter), east of 5°E. However, we consider that this region is relevant to assess the realism of the modeled estimates over the Mediterranean Sea as it covers both areas of weak (interior of the WMB) and locally intensified (Strait of Sicily, Corsica channel) baroclinic tide generation. In this dataset, vertical profiles mostly range from 5m depth to the seafloor. However, due to the relatively low intensity of tides over the WMB, we hypothesize that non-tidal processes (such as wind-driven inertial wave breaking) drive the turbulence over the upper 50m of the water column. Thus, we discard this depth range in the vertical integration of turbulence dissipation (Equation 5.6).

We display on the upper and middle panels of Figure 5.6 the modelled estimates of tidal dissipation and generation and overlay the depth-integrated observations of Ferron et al (2017). In addition, we display on the underlying panels a boxplot of the depth-integrated observations and the model estimates at the nearest point to the measurement stations. Aside from DL19, the model estimates all display relatively similar patterns of the baroclinic tide energetics. In particular, both dissipation and generation estimates indicate intense baroclinic tides in the vicinity of the Strait of Sicily and the Corsica channel, which is consistent with the Ferron et al (2017) measurements. As expected, differences between tidal generation and dissipation mainly arise over deep water areas, where tidal generation reaches very low values ($\approx 10^{-9}$ W.m^{-2}), whereas dissipation remains more intense ($\approx 10^{-6}$ W.m^{-2}).

With respect to the measurements from Ferron et al (2017), the model estimates appear relatively realistic. Except from DL19, all the estimates capture the local intensification of turbulence in the Strait of Sicily and the Corsica channel.

Regarding baroclinic tide generation energy estimates (upper panels), the main discrepancies arise over deep water areas, where they display values several orders of magnitude below the measurements. Conversely, the dissipation estimates (lower panels) remain consistent with the observations in these areas. Thus, this highlights the irrelevance of baroclinic tide generation energies as a proxy of the baroclinic tide dissipation in low-generation sites.

The boxplots displayed in Figure 5.6 provide additional details on the consistency and limitations of the model estimates. In particular, the NEMO dissipation estimate stands out as the most realistic with respect to the observed values. HYCOM and FES2014 estimates are also in good agreement with the in situ data. However, they lack energy compared to the NEMO estimates, particularly in the Corsica channel and Ligurian Sea. The DL19 estimate is again set aside because of its low spatial variability that fails to capture the high-energy areas.

In light of these results, we take the NEMO dissipation map as a reference for the spatial distribution of tidal dissipation within the Mediterranean Sea. More specifically, this choice is motivated by the good consistency of the NEMO estimates with respect to the observation, the underestimated energy from generation maps in weakly energetic areas, the low energetic content of HYCOM dissipation estimate within the Corsica channel, and its unexpected intensification along the 26°E meridian.

5.3.4 Reference baroclinic tidal dissipation climatology

In light of the aforementioned results, none of the considered estimates is uniformly more realistic. Thus, we choose to construct our reference baroclinic tidal dissipation climatology from a combination of estimates, taking advantage of their respective strengths. Specifically, we consider one estimate for the vicinity of the SoG and the Alboran Sea, where tidal dissipation is very intense, and a second estimate for the rest of the Mediterranean Sea and the Atlantic Ocean, separating these domains with a bathymetry threshold of 2000m depth. Over the Strait of Gibraltar and the Alboran Sea, we consider the spatial distribution and integral energy of the high-resolution FES2014 simulation, which is the most consistent with the measurements of Wesson and Gregg (1994). Over the rest of the Atlantic Ocean and the Mediterranean Sea, we consider the spatial distribution of the NEMO tidal dissipation estimate, which is the most consistent with the measurements of Ferron et al (2017), and the integral energy of the FES2014 estimate, which is better constrained. Finally, for numerical stability reasons, we apply to the estimate a background energy of $10^{-6} W.m^2$. We display the reference field obtained in Figure 5.7.

As a final step, we need to split the climatology of baroclinic tidal dissipation energy between the processes of wave-wave interactions, interactions with critical slopes, and interactions with abyssal hills. To do so, we use the share of energy attributed to each phenomenon from the maps of DL19. Concretely, at each point of the domain, the energy associated with the phenomenon ”i” is defined as follows

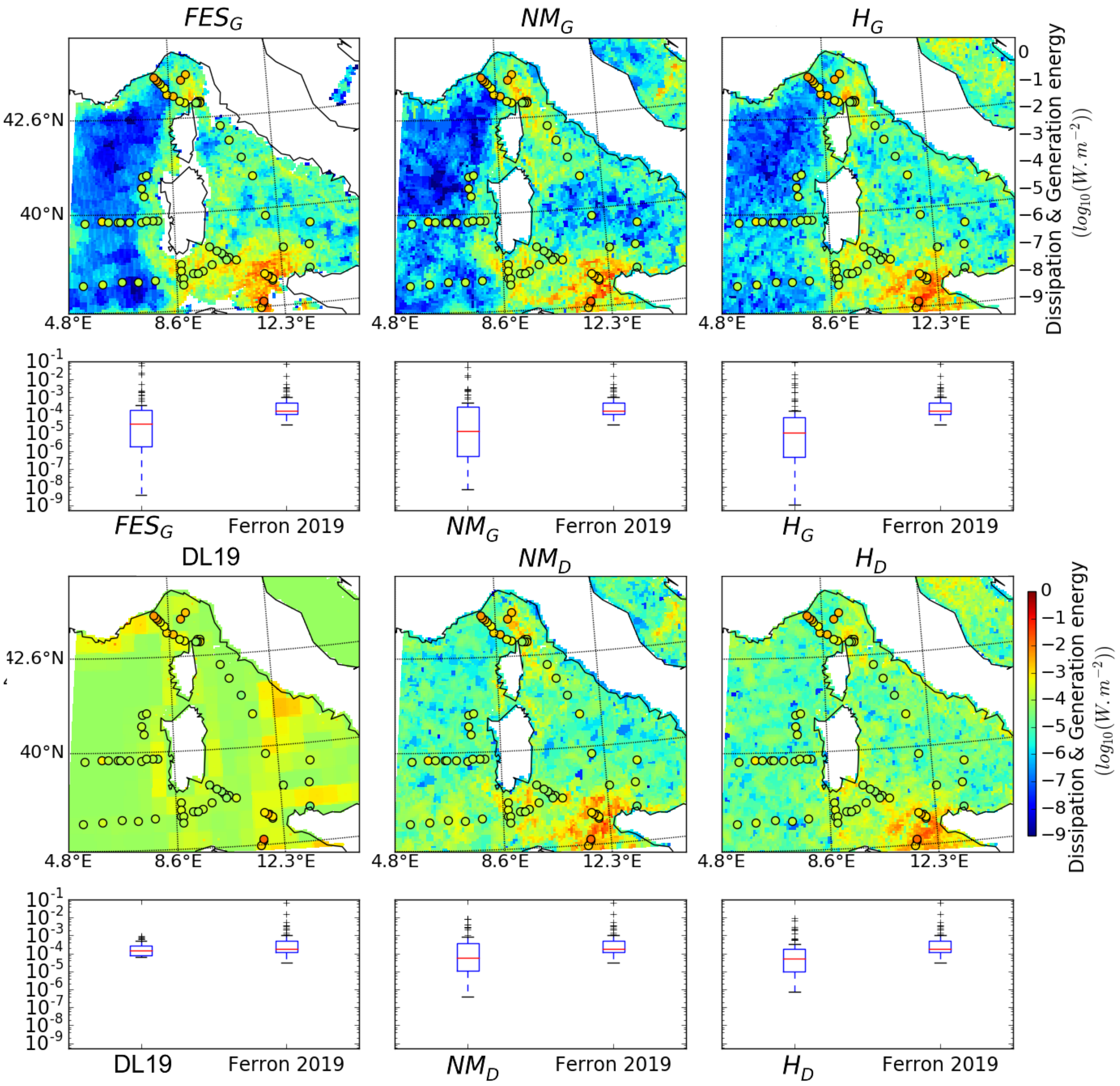

Figure 5.6: Baroclinic tide generation (upper panels) and dissipation (lower panels) energy estimates from the FES2014 (FES), NEMO (NM), HYCOM (H), and de Lavergne et al (2019) (DL19) models. The colored scatter points represent depth-integrated measurements from Ferron et al (2017). The boxplot are computed from the depth-integrated measurements of Ferron et al (2017) and the co-located model estimates.

:

$$D_i = D\,\frac{D_{DL19\,i}}{D_{DL19\,pic} + D_{DL19\,ww} + D_{DL19\,bot}}$$

With $D_{DL19\,i}$ the energy produced by the phenomenon i in DL19 and D the energy contained in tide dissipation climatology just created.

5.4 Effect of parameterized tidal mixing at the SoG

In this section, we aim at assessing the relevance of the tidal mixing parameterization to represent water mass transformations at the SoG. To do so, we compare

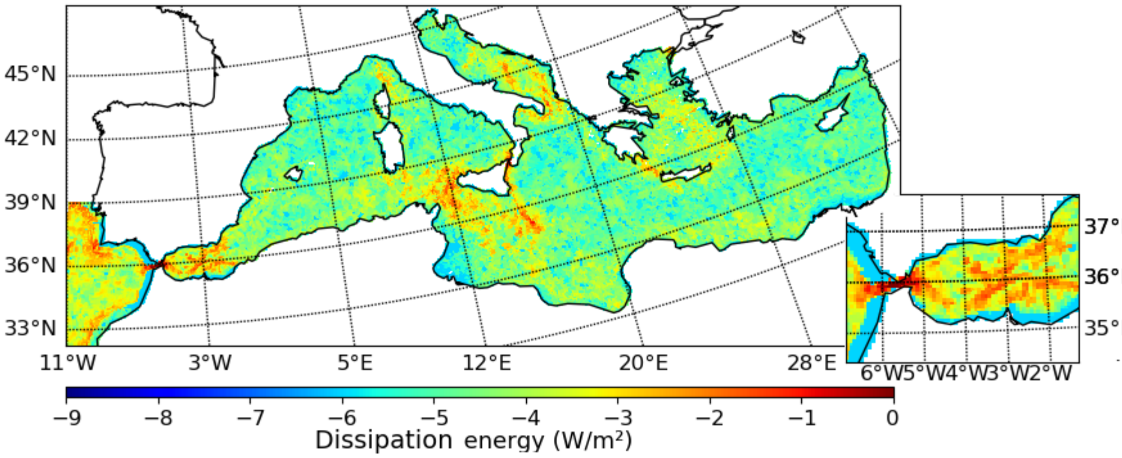

Figure 5.7: Decimal logarithm of the reference depth-integrated tidal dissipation climatology for the Mediterranean Sea. It merges the FES2014 zoomed estimate within the SoG and Alborán Sea and the NEMO 1/12° dissipation estimate within the Mediterranean Sea, re-normalized by the global tidal generation from the FES2014 dataset.

the effect of parameterized mixing on the exchanged water masses within the SoG to that produced by explicit tides in simulations with increasing resolution at the SoG.

5.4.1 Exchange flow through the SoG

To start with, we display on the upper panel of Figure 5.8 the 19-year mean zonal velocities, salinity, and temperature in the NT LR simulation, averaged meridionally in the domain illustrated in Figure 5.1 (lower panel, dashed rectangle). On the lower panels, we display the anomalies induced by the inclusion of parameterized tidal mixing (δ_{pTides} = pT LR - NT LR), explicit tides (δ_{Tides} = T LR - NT LR), and explicit tides in the context of simulations with higher resolution at the SoG ($\delta_{T\,HR}$ = T HR - NT HR).

Overall, the simulations all depict a realistic picture of the two-layer exchange flow through the SoG (not shown for T HR). Specifically, the average velocities display intense zonal currents (typically 0.5 m.s^{-1}) transporting a surface layer of relatively warm and fresh water masses ($\sim$ 15°C – 17.5°C, 36 ‰– 37 ‰) towards the Mediterranean Sea a deeper layer of colder and saltier water masses ($\sim$ 13°C – 14°C, 37.5 ‰– 38.5 ‰) towards the Atlantic Ocean. The climatological zero-velocity interface (black line) separating these layers is smoothly slanted downward towards the Atlantic, at approximately 150 – 170m depth. Across this interface, salinity and temperature display a sharp vertical gradient, varying by typically 2 ‰and 2°C within 100m depth.

A comparison of the hydrographic and dynamical anomalies induced by parameterized (δ_{pTides}) and explicit (δ_{Tides}, $\delta_{T\,HR}$) tides highlights that they drive qualitatively similar water mass transformations, but have more different effects on the dynamics. With respect to the NT LR simulation, pT LR displays notable differences in hydrographic and dynamical properties (δ_{pTides}). Regarding the dynamics, the parameterized mixing mainly intensifies the vertical eddy viscosity coefficient at the

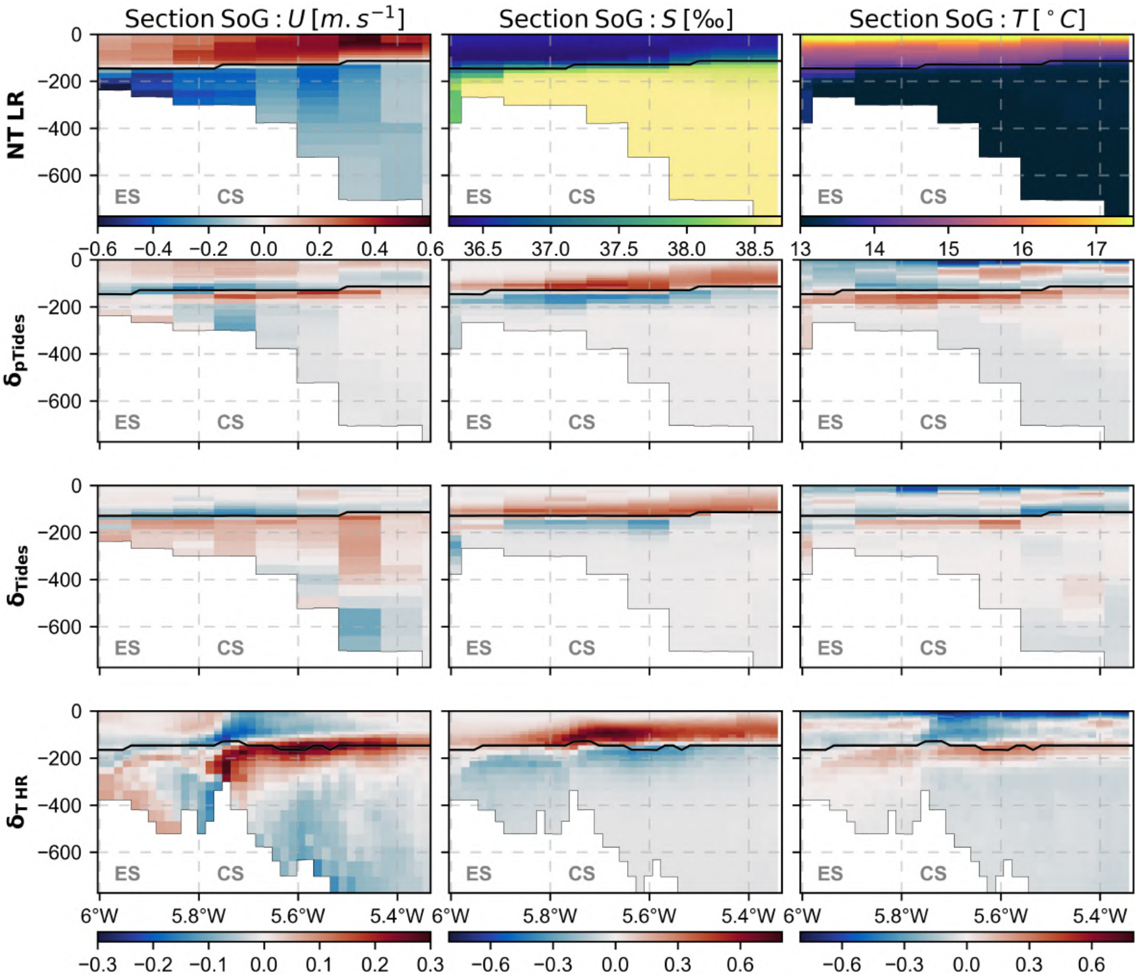

Figure 5.8: Upper panels display the 19-year mean zonal velocities, salinity, and temperature in the NT LR simulation, averaged along the model pseudo-meridional direction for the domain illustrated in Figure 5.1 (lower panel, dashed rectangle). Lower panels display the anomalies induced by the inclusion of parameterized tidal mixing (δ_{pTides} = pT LR - NT LR), explicit tides (δ_{Tides} = T LR - NT LR), and explicit tides in the context of simulations with higher-resolution at the SoG ($\delta_{T\,HR}$ = T HR - NT HR). The black line shows the depth of the climatological zero-velocity interface in the NT LR, pT LR, T LR, and T HR simulations

interface between the Atlantic and Mediterranean layers (not shown). Consequently, the vertical shear of zonal currents decreases near the climatological zero-velocity interface, particularly in the vicinity of the Camarinal Sill (CS hereinafter). Due to the conservation of the volume transports through the strait, the water masses away from the interface accelerate, resulting in a dipole anomaly pattern within each layer. Explicit tides induce similar dipole anomaly patterns to that of parameterization near the zero-velocity interface (δ_{Tides}, $\delta_{T\,HR}$), but with a significantly larger vertical extent. These discrepancies highlight that parameterized and explicit tides modulate the dynamics of the exchange flow through different processes. Indeed, rather than enhancing vertical eddy viscosity, explicit tidal currents directly interact with the exchange flow, modulating its dynamical structure at high-frequency. In particular, tides drive vertical oscillation of the interface depth between Atlantic and Mediterranean layers and periodically reverse the exchange flow (Gonzalez et al, 2023). This results in a decrease of the average zonal currents within $\sim$ 100m of the zero-velocity interface. In the presence of fine-scale topographic obstacles, these effects are further enhanced, and the upwelling and entrainment of Mediterranean water masses east of the SoG result in a thickening of the Atlantic layer ($\delta_{T\,HR}$). On the other hand, the parameterized tidal mixing does not account for the advective effect of tides and only represents their local impact on mixing. With that in mind, it is worth noting that the parameterization captures well the local intensification of tidal anomalies in the vicinity of the CS, which is evident in $\delta_{T\,HR}$, but not in δ_{Tides}. This indicates that the parameterization reproduces the interactions of tidal currents with fine-scale topography, which are not represented in the coarse-resolution tidal simulation.

As expected, the parameterized tidal mixing provides more realistic effects on the hydrographic properties of the exchanged water masses through the SoG. Specifically, with respect to the NT LR simulation, pT LR displays a weaker salinity stratification at the interface between the Atlantic and Mediterranean layers. This homogenization of the vertical profile of salinity, indicated by a dipole anomaly centered on the zero-velocity interface in δ_{pTides}, can be directly related to an intensification of diapycnal mixing in pT LR. In addition, a comparison of δ_{pTides} with δ_{Tides} and $\delta_{T\,HR}$ indicates that the parameterized mixing provides a realistic picture of the tide-induced mixing. More specifically, considering $\delta_{T\,HR}$ as a reference, pT LR better captures the intensification of tidal water masses transformation above the CS than T LR. On the other hand, the parameterized mixing does not reproduce the asymmetry of the tidal salinity dipoles, which directly results from the asymmetry of recirculation cells at the SoG (Gonzalez et al, 2023). This highlights the limitations of the tidal mixing parameterization, which does not represent the advective influence of tides.

Regarding temperature, inclusion of parameterized tidal mixing induces two vertical temperature dipoles (δ_{pTides}). The first one, centered on the zero-velocity interface, is consistent with enhanced vertical mixing between the Atlantic and Mediterranean layers. The second one, centered on $\sim$ 25m depth, relates to the seasonal thermocline and requires an analysis of the temporal variation of the temperature anomalies within the strait. To do so, we display in Figure 5.9 climatological winter and summer temperature anomalies averaged along the model pseudo-meridional direction for the domain illustrated in Figure 5.1 (lower panel, dashed rectangle). The summer and winter averages from NT LR indicate that above 150m depth, temperature is subject to substantial seasonal variations, characterized by a relatively smooth profile in winter and an intense vertical gradient in summer.

Overall, the parameterized and explicit tides drive qualitatively similar seasonal temperature anomalies within the SoG. During wintertime, they mainly enhance the heat fluxes between the Atlantic and Mediterranean layers, producing a dipole temperature anomaly centered on the zero-velocity interface. As previously noted for the dynamics and salinity, the parameterization better captures the intensity of the high-resolution tidal anomalies ($\delta_{T\,HR}$) than the tidal simulation with a coarse resolution at the SoG (δ_{Tides}). However, it does not reproduce the asymmetry of the tide-induced temperature anomalies. In summer, the parameterization also reproduces the tidal cooling of the Atlantic surface but with more discrepancies compared to the winter anomalies. Indeed, the parameterized mixing mainly homogenizes the upper Atlantic layer, producing an intense dipole anomaly near ~ 25m depth. On the other hand, explicit tides drive a more homogeneous cooling of the Atlantic layer, with moderate warming of the underlying water masses. This, once again, highlights the effect of tidal advection. Indeed, unlike the parameterized tidal mixing, which only enhances diapycnal mixing within the Atlantic layer, explicit tides additionally advect cold Mediterranean water masses into the Atlantic layer, which as a result, is more homogeneously cooled. This process is evident in the T HR simulation, in which tidal anomalies abruptly intensify over the CS, where an intense upwelling of Mediterranean water masses takes place (Gonzalez et al, 2023).

Thus, the former results highlight that the parameterized tidal mixing at the SoG reproduces the tidal water mass transformations throughout the SoG relatively well. In addition, it consistently accounts for the interactions between tidal currents and fine-scale topographic obstacles, which are not represented in tidal simulations with coarse resolution at the SoG. On the other hand, the omission of the advective effect of tides results in discrepancies regarding the dynamics of the exchange flow, the seasonal cycle of temperature over the Atlantic layer, and the vertical structure of tidal hydrographic anomalies.

5.4.2 Integral transports through the SoG

To investigate the impact of the parameterized tidal mixing at the SoG on the exchanges between the Atlantic Ocean and the Mediterranean Sea, we display in Figure 5.10 the 19-year average inflow (eastward) and net volume, heat, and salt transports through the SoG in the NT LR simulation. In addition, we specify the anomalies induced by the inclusion of parameterized tidal mixing (δ_{pTides}) and explicit tides (δ_{Tides}) as well as the transports represented by a non-tidal simulation with enhanced resolution at the SoG (NT HR) and their modulation by explicit tides ($\delta_{T\,HR}$). As in the previous chapter, we consider two estimates of the inflow transports: an upper estimate (Q^{max}), accounting for high-frequency tidal and eddy transports, and a lower estimate (Q^{A}), based on the 19-year average outputs. Note that outflow transports are not specified as they can be deduced by subtracting the net flow from Q^{max} or Q^{A}.

Overall, the simulations display reasonable values for Q^{A} and the associated heat and salt transports. More specifically, the volume outflow transports simulated in NT LR and pT LR (-0.78Sv and -0.79Sv, respectively) are consistent with the non-eddy-flux estimate of -0.81Sv from Sammartino et al (2015) considering the associated interannual variability (±0.03Sv) as an uncertainty range. The T LR simulation underestimates the outflow transport (-0.73 Sv), and the NT HR and T HR simulations overestimate it (-0.86 Sv). However, both remain reasonably consistent with Sammartino et al (2015). The former conclusions extend to the inflow transports, considering as a reference the inflow transport deduced from the non-eddy-flux outflow estimate of Sammartino et al (2015) and the net volume transport estimate of Jordà et al (2017b) (0.04 Sv).

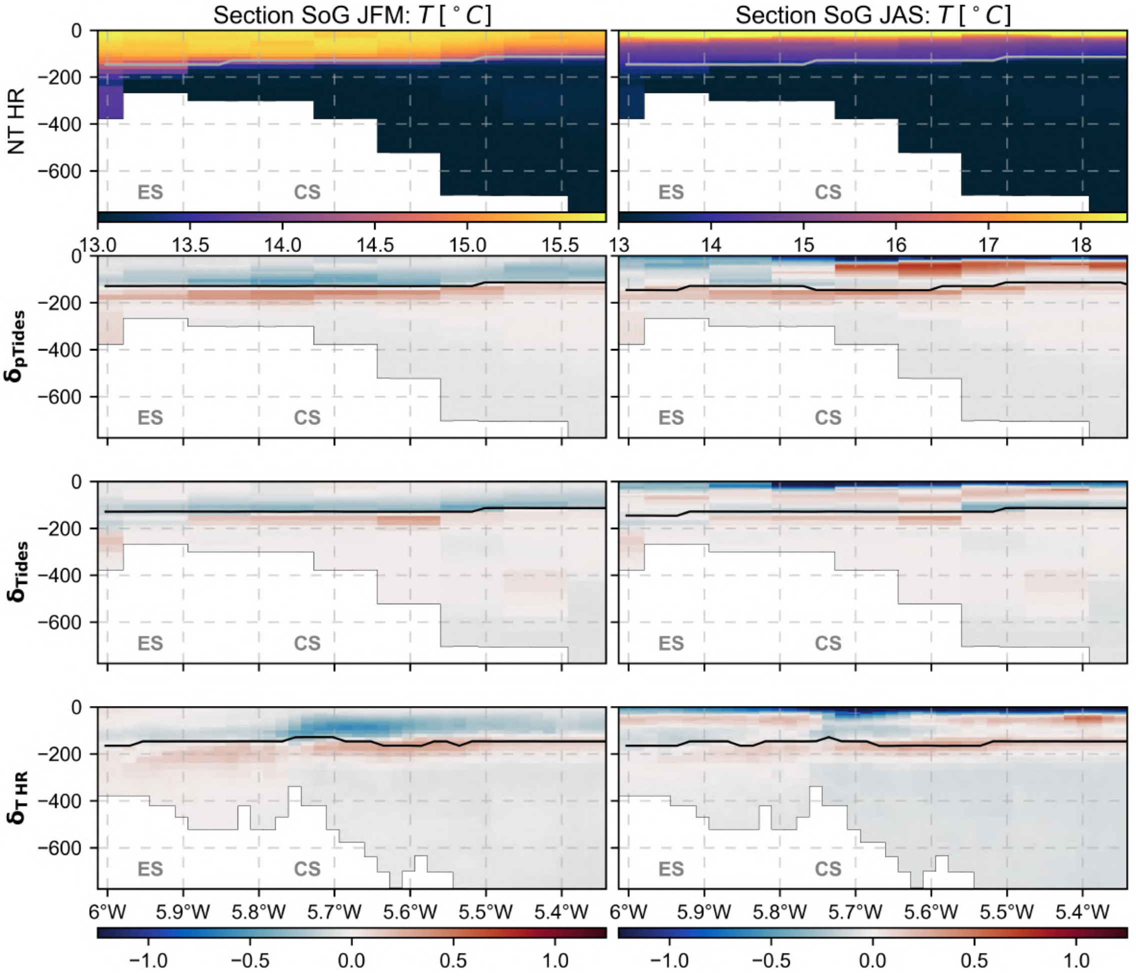

Figure 5.9: Same as Figure 5.8 for the winter (left, January-February-March) and summer (right, July-August-September) averages of temperature

With respect to the NT LR simulation, the transports displayed by pT LR (δ_{pTides}) indicate that the parameterized tidal mixing has a modest effect on the volume exchanges through the SoG. Conversely, explicit tides drive a substantial high-frequency intensification of the advection through the strait, as indicated by the intensification of Q_{IN}^{max} (δ_{Tides} and $\delta_{T\,HR}$). A similar reasoning applies to high-frequency heat and salt transports, which are primarily driven by volume transports. As expected, this highlights that the parameterized mixing at the SoG does not represent the advective effects of tides and, thus, has a modest influence on the high-frequency inflowing and outflowing transports through the strait. On the other hand, it has a more relevant effect on the net heat and salt transports, which strongly depend on the hydrographic properties of the exchanged water masses.

Regarding the net transports, the parameterized tidal mixing drives a moderate but notable decrease in the net heat transport towards the Mediterranean Sea (δ_{pTides}). More specifically, this decrease of the net heat transport is consistent with the cooling of the Atlantic layer and the warming of the Mediterranean layer due to the enhanced diapycnal mixing within the strait. As depicted by δ_{Tides} and $\delta_{T\,HR}$, explicit tides drive a similar decrease in the net heat transport. In terms of intensity, the pT LR and T HR simulations display a noticeably less intense decrease of

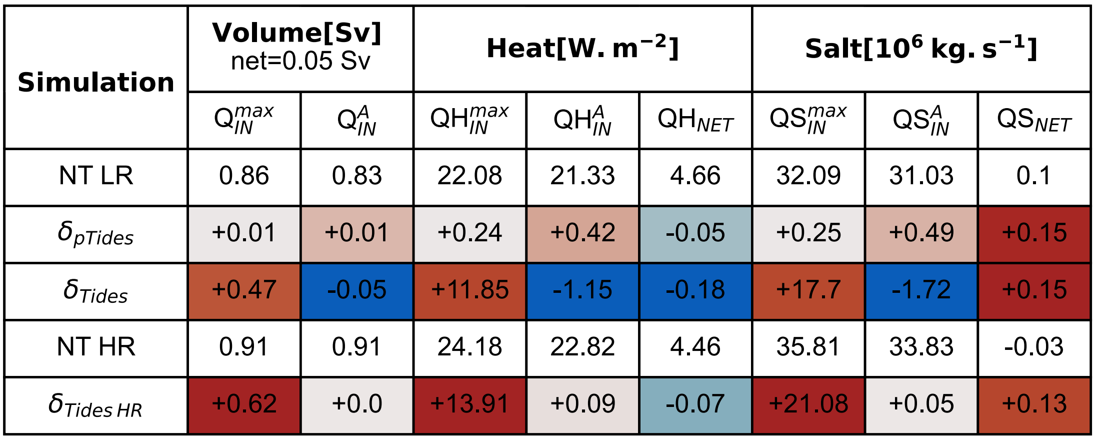

Simulation	**Volume[Sv]** net=0.05 Sv		**Heat[W. m^{-2}]**			**Salt[10^6 kg. s^{-1}]**		
	Q_{IN}^{max}	Q_{IN}^{A}	QH_{IN}^{max}	QH_{IN}^{A}	QH_{NET}	QS_{IN}^{max}	QS_{IN}^{A}	QS_{NET}
NT LR	0.86	0.83	22.08	21.33	4.66	32.09	31.03	0.1
δ_{pTides}	+0.01	+0.01	+0.24	+0.42	-0.05	+0.25	+0.49	+0.15
δ_{Tides}	+0.47	-0.05	+11.85	-1.15	-0.18	+17.7	-1.72	+0.15
NT HR	0.91	0.91	24.18	22.82	4.46	35.81	33.83	-0.03
$\delta_{Tides\,HR}$	+0.62	+0.0	+13.91	+0.09	-0.07	+21.08	+0.05	+0.13

Figure 5.10: NT LR and NT HR average transports of volume, heat, and salt through the SoG. Positive values are oriented toward the Mediterranean Sea. We specify the anomalies induced by the inclusion of parameterized tidal mixing (δ_{pTides}) and explicit tides (δ_{Tides}, $\delta_{T\,HR}$). Inflowing transports are computed from averages of the eastward velocity components, applying a Heaviside function. As traditionally done for comparison purposes with surface fluxes, we convert the heat transport into an equivalent surface flux over the whole Mediterranean Sea, in W.m^{-2}, with a Mediterranean area of $2.5 \cdot 10^{12}$m^2, following Sanchez-Roman et al (2018).

the net heat transport than the NT LR simulation. However, the reason for these differences varies in both simulations. In the case of pT LR, although the average net heat transport decreases with respect to NT LR, it temporally increases in summertime. Indeed, at that time, the parameterized diapycnal mixing at the surface of the Atlantic layer allows for a greater ocean heat uptake, which results in a warming of the Atlantic layer. On the other hand, in T HR, the cooling of the Atlantic layer due to tidal mixing and recirculation is partly canceled by the tidal thickening of the Atlantic layer at the SoG.

Finally, inclusion of parameterized tidal mixing results in a substantial intensification of the net salt transport (δ_{pTides}), which is consistent with the saltening of the Atlantic inflow and the freshening of the Mediterranean outflow at the SoG. In addition, a comparison with δ_{Tides} and $\delta_{T\,HR}$ indicates that this intensification of the net salt transport is highly similar to that induced by explicit tides. However, the saltening of the Atlantic layer at the SoG in the pT LR and T HR simulations is likely to have a greater effect on the Mediterranean Sea than that of the T LR simulation. Indeed, the increased net salt transport in pT LR is partly compensated by a relatively intense freshening of the Mediterranean outflow. Similarly, for T HR, the increased net salt transport is partly compensated by the thickening of the Atlantic layer at the SoG.

To conclude, the former results highlight that the tidal mixing parameterization has a limited effect on the inflowing and outflowing transport through the strait, mainly driven by the volume transports. On the other hand, it is more relevant to the net heat and salt transports through the strait. Specifically, the parameterized tidal mixing decreases the net heat transport and increases the net salt transport by cooling and saltening the Atlantic inflow and warming and freshening the Mediterranean outflow. A comparison with tidal simulations indicates that these effects are similar to that of explicit tides but with notable differences for the net heat flow. Specifically, the parameterized tidal mixing induces a temporary increase in heat transport in summer due to a greater ocean heat uptake, which is inconsistent with the effect of explicit tides.

5.5 Impact on the Mediterranean Sea

In the previous section, we have highlighted that the parameterized tidal mixing at the SoG drives significant water mass transformations across the strait, with a similar overall effect to explicit tides. Furthermore, as highlighted in the previous chapter, such modifications of the AW can influence Mediterranean upper layers and ultimately modulate the Mediterranean convective activity and the properties of intermediate and deep water masses. In this section, we assess the overall effect of the parameterized tidal mixing at the SoG on the top 300m of the Mediterranean Sea and compare it to that induced by explicit tides.

5.5.1 Western Mediterranean

To start with, we display on the upper panels of Figure 5.11 the NT LR 19-year meridional average temperature and salinity over the upper 300m depth of the Western Mediterranean Basin (WMB hereinafter). Lower panels indicate the anomalies induced by the inclusion of parameterized tidal mixing (δ_{pTides} = pT LR - NT LR) and the inclusion of tides in simulations with coarse (δ_{Tides} = T LR - NT LR) and enhanced resolution ($\delta_{T\,HR}$ = NT HR - T HR) at the SoG. The meridional average temperature and salinity fields display characteristic features of the WMB. In particular, the warm and fresh tongue of AW entering the Mediterranean between 5°W – 0°E indicates the position of the Alboran Sea. Further east, the Northwestern Mediterranean Basin is evidenced by a sudden drop in temperature and salinity between 0°E – 10°E. Conversely, the Tyrrhenian Sea can be distinguished by a local increase in temperature and salinity at mid-depth east of 10°E.

Overall, comparison of the δ_{pTides}, δ_{Tides}, and $\delta_{T\,HR}$ indicates that the parameterized tidal mixing at the SoG has a similar overall effect to explicit tides on the top 300m depth. Temperature anomalies are relatively modest but provide insight into the differences between the explicit and parameterized tidal mixing at the SoG. Over the upper 100m depth, the displayed anomalies are mostly statistically significant west of 5°W, where they are consistent with the propagation of tide-induced anomalies from the SoG. In particular, inclusion of parameterized tidal mixing in pT LR produces a dipole temperature anomaly centered on $\sim$ 25m depth, resulting from the enhanced diapycnal mixing over the Atlantic layer in the summertime. On the other hand, simulations with explicit tides mainly display a cold anomaly, which is consistent with the more homogeneous cooling of the Atlantic layer by explicit tides. The impact of these differences in the processes driving explicit and parameterized tidal mixing at the SoG is particularly well evidenced east of 5°E, where the parameterized mixing drives a notable warming of the surface, attributable to the

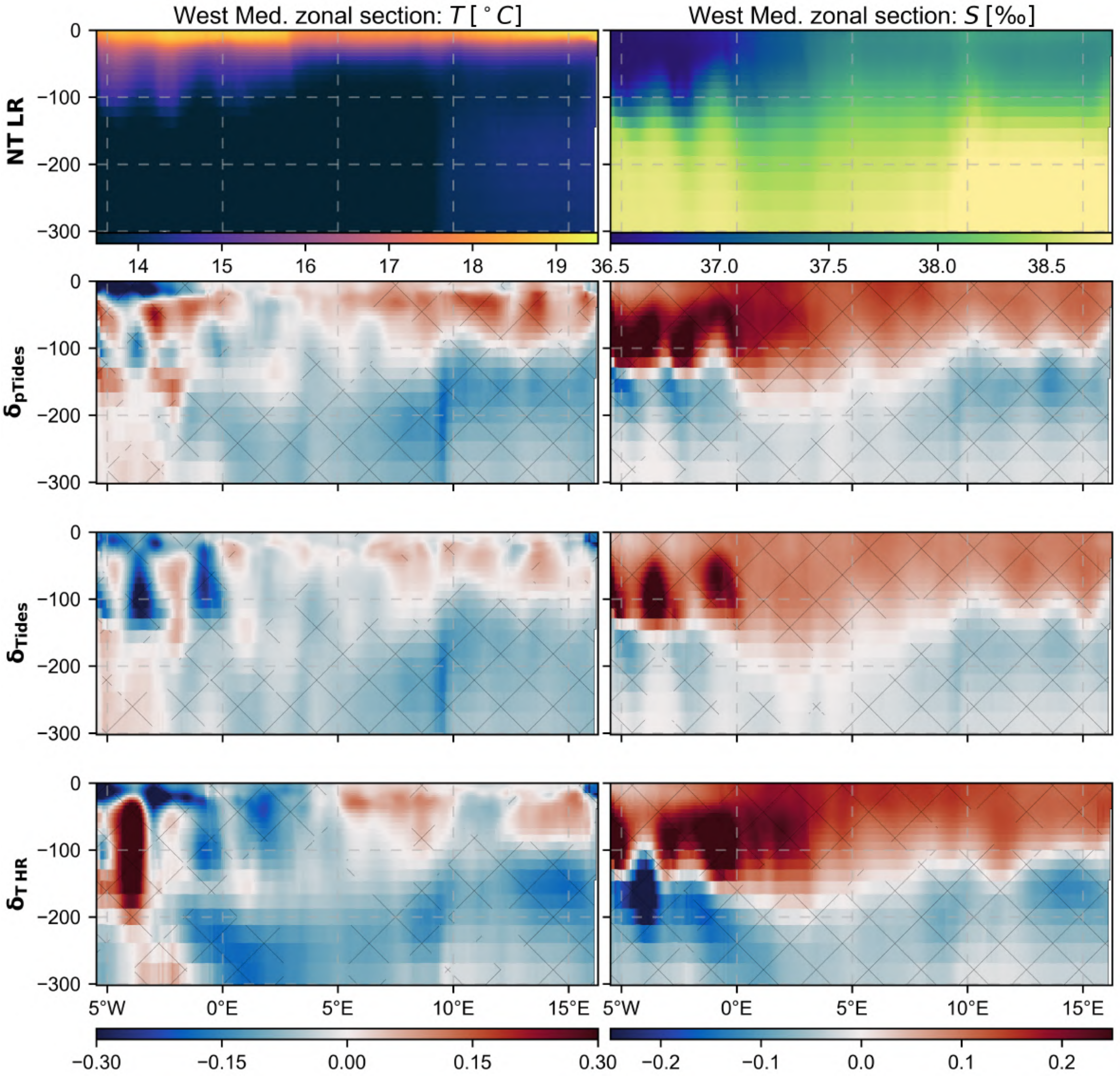

Figure 5.11: Upper panels display the 19-year pseudo-meridional (along the model grid) average temperature and salinity over the Western Mediterranean Basin for the forced NEMOMEDGIB non-tidal coarse resolution simulation (NT LR). Lower panels display the anomalies induced by the inclusion of parameterized tidal mixing (δ_{pTides}), explicit tides (δ_{Tides}), and explicit tides with a refined spatial representation of the strait ($\delta_{T\,HR}$). Hatches indicate statistically significant anomalies with respect to the interannual variability (based on a student t-test with a p-value of 0.05)

increased net heat transport towards the Mediterranean Sea in summer. Conversely, explicit tidal anomalies (δ_{Tides}, $\delta_{T\,HR}$) are mostly insignificant with respect to the interannual variability and are mainly attributable to modulations of the circulation. Below 100m depth, parameterized and explicit tides have more similar effects. Specifically, they induce a general cooling of the water column, which can be related to an intensification of the convective activity over the northwestern Mediterranean Sea. As shown in the previous chapter, this modulation of the convective activity can be explained by the impact of tidal mixing at the SoG on the Mediterranean surface salinity.

Regarding salinity, inclusion of parameterized tidal mixing results in a general saltening of the Mediterranean Sea over the upper 100m depth. In light of the previous analyses, this saltening can be directly related to the enhanced diapycnal mixing between Atlantic and Mediterranean water masses at the SoG. In addition, the anomalies displayed by δ_{Tides} and $\delta_{T\,HR}$ indicate that the parameterized mixing realistically reproduces the effect of explicit tides at the SoG. More specifically, the intensity of the surface saltening simulated in pT LR is more consistent with that simulated T HR than T LR. This indicates that the parameterized tidal mixing captures the intensity of diapycnal mixing at the SoG better than the T LR simulation. Indeed, the simplified topography of the SoG in the T LR simulation does not allow for a representation of the interaction of tidal currents with the abrupt topographic obstacles within the strait (Gonzalez et al, 2023). Consistently with the results of the previous chapter, the tidal saltening of the Mediterranean surface intensifies the deep convection over the northwestern Mediterranean Sea (not shown). Below 100m depth, this enhanced convection induces a freshening of the water column. In terms of magnitude, the pT LR and T HR simulations display a more intense freshening, which is consistent with the higher salinity of the surface water masses.

5.5.2 Eastern Mediterranean

To assess the effect of the parameterized tidal mixing on the Eastern Mediterranean Basin (EMB hereinafter), we display in Figure 5.12 the 19-year meridional average temperature and salinity over the upper 300m depth of the EMB for the NT LR simulation. Lower panels indicate the anomalies induced by the inclusion of parameterized tidal mixing (δ_{pTides} = pT LR - NT LR) and the inclusion of tides in simulations with coarse (δ_{Tides} = T LR - NT LR) and enhanced resolution ($\delta_{T\,HR}$ = NT HR - T HR) at the SoG. As for the WMB, several characteristics of the WMB arise from the temperature and salinity fields. The local salinity minimum west of 15°E indicates the tongue of AW propagating from the WMB, whereas that near 25°E highlights the position of the Black Sea tongue in the Aegean Sea. Further east, the general warming and saltening of the water masses indicates the position of the Levantine Basin.

Regarding temperature, inclusion of parameterized (δ_{pTides}) and explicit (δ_{Tides}, and $\delta_{T\,HR}$) tidal mixing at the SoG induces very similar anomalies of weak amplitude over the EMB. Note that the large differences with respect to the anomalies highlighted over the WMB indicate that these temperature anomalies mainly result from local processes. Specifically, west of 15°E, the freshening of the sea surface and the warming of the underlying water masses in pT LR can be attributed to enhanced diapycnal mixing, which fluxes heat downwards, particularly during summertime. A comparison with δ_{Tides} and $\delta_{T\,HR}$ indicates that explicit tides have a similar but less intense effect, suggesting that the baroclinic tide dissipation energy at the Strait of Sicily is overestimated in pT LR. Further east, inclusion of parameterized or explicit tides induces a cold anomaly between 18°E – 25°E and a warm anomaly further east. This large-scale temperature dipole anomaly can be related to reduced exchanges between the Ionian and Levantine Seas and a weakening of the cyclonic circulation in the Ionian Sea (not shown). Note that similar anomalies develop in the T LR and T HR simulations, although they are less intense in the latter. Thus this suggests

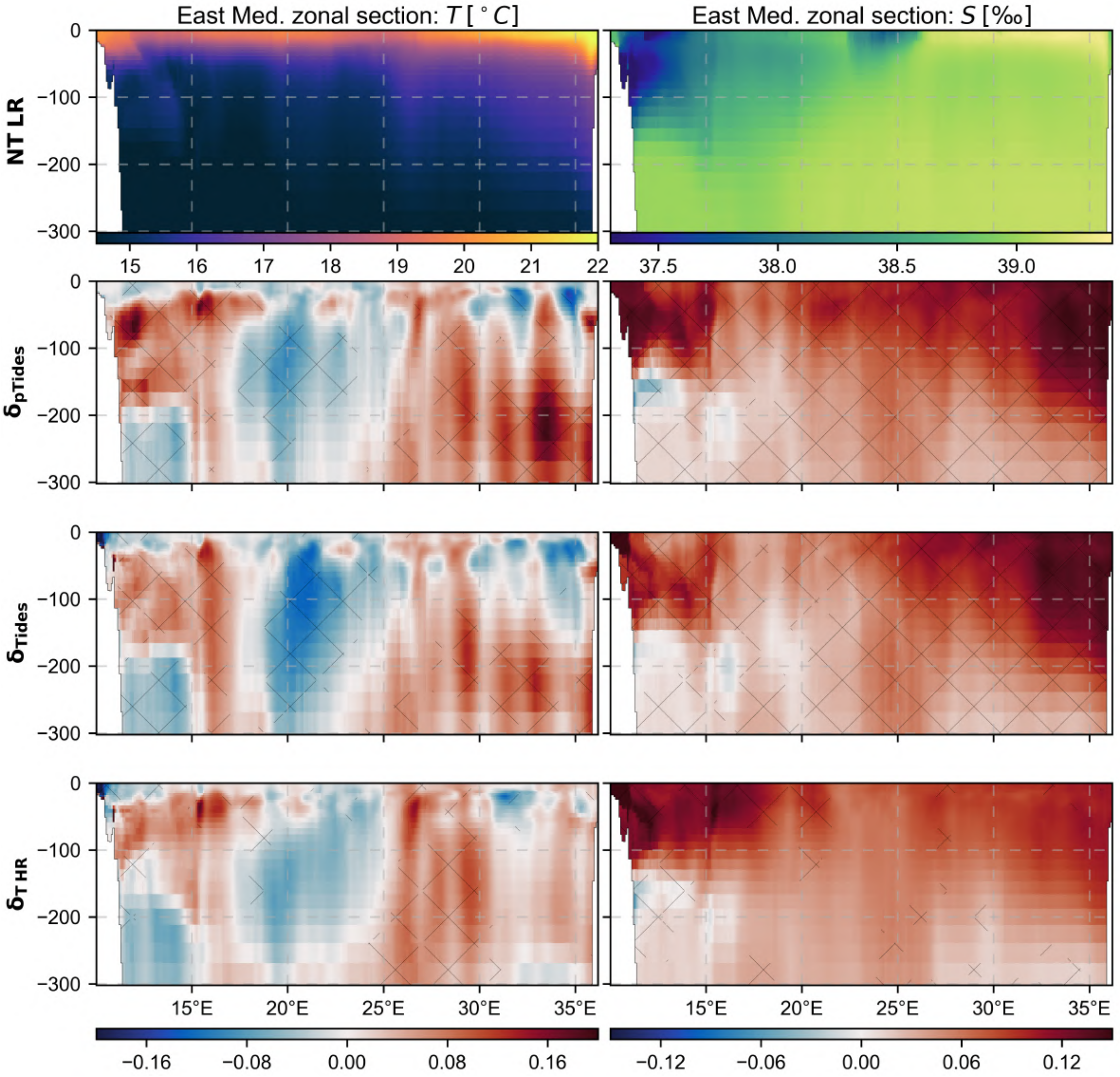

Figure 5.12: Same as Figure 5.11 for the Eastern Mediterranean Basin.

a connection between the circulation of the EMB and the tidal mixing at the SoG or other straits of the EMB. However, further work is needed to shed light on this mechanism.

Regarding salinity, inclusion of parameterized mixing (δ_{pTides}) also produces similar effects to that of explicit tides (δ_{Tides}, $\delta_{T\,HR}$). Specifically, it results in a general saltening of the EMB surface, attributable to the propagation of the AW saltened by tidal mixing at the SoG. In terms of magnitude, west of 15°E, both the parameterized tides in pT LR and the explicit tides in T HR induce a more intense saltening than the explicit tides in T LR, which is consistent with the improved representation of interactions between tides and topography at the SoG in pT LR and T LR. On the other hand, east of 15°E, the saline anomalies are more intense in pT LR and T LR. These zonal variations of the saline anomalies are mainly attributable to the modified circulation of AW in the Ionian and Levantine Basins (not shown).

Thus, the former results highlight that the tidal mixing parameterization realistically reproduces the influence of explicit tidal mixing at the SoG on the Mediterranean surface. In particular, it better captures the saltening effect of tidal mixing on the Mediterranean surface than the simulation with explicit tidal forcing and coarse resolution at the SoG. Although not investigated here, this suggests that the parameterized tidal mixing at the SoG should be able to reproduce the influence of tides at the SoG on the Mediterranean convective activity and the intermediate and deep water masses. On the other hand, the parameterization misrepresents the influence of tides at the SoG on the temperature over the upper 100m depth of the WMB. Specifically, these discrepancies are mainly due to misrepresenting the seasonal cycle of surface temperature within the SoG.

5.6 Conclusions

This chapter details the implementation and investigation of a baroclinic tidal mixing parameterization for non-tidal ocean models of the Mediterranean Sea. In particular, it focuses on assessing the relevance of such parameterization to represent tidal mixing at the SoG, which is challenging to represent in models with coarse resolution at the SoG. To do so, we consider the tidal mixing parameterization of de Lavergne et al (2020), which acts as a forcing of vertical mixing based on climatologies of the baroclinic tidal dissipation energy. In addition, we assess the consistency of the parameterized mixing based on 19-year-long forced ocean simulations with either parameterized or explicit tides in the Mediterranean Sea.

We first focus on the implementation of the tidal mixing parameterization, which requires creating a climatology of baroclinic tide dissipation energy for the Mediterranean Sea. To do so, we rely on baroclinic tide dissipation energy estimates from tidal ocean models, which we compare to available in-measurements of turbulent dissipation at the Strait of Gibraltar (Wesson and Gregg, 1994) and over the western Mediterranean (Ferron et al, 2017). In the end, we select two model estimates to create the climatology. At the SoG, we consider the baroclinic tide generation energy from the FES2014 model, and over the rest of the Mediterranean, we consider the baroclinic tide dissipation energy diagnosed in global NEMO simulations.

To assess the relevance of the tidal mixing parameterization at the SoG, we start by investigating its effect on the exchange flow through the SoG. We find that the parameterized mixing reproduces the main characteristics of the tide-induced water mass transformations within the SoG, that is, the cooling and saltening of the Atlantic water masses and the warming and freshening of Mediterranean water masses. In addition, we show that the parameterization better captures the local intensification of tidal mixing in the vicinity of the SoG than the tidal simulation with coarse resolution at the SoG, which does not represent the interaction of tidal currents with the fine-scale topographic obstacles. On the other hand, the omission of the advective effects of tides results in discrepancies regarding the dynamics of the exchange flow, the seasonal cycle of temperature over the Atlantic layer, and the vertical structure of tidal hydrographic anomalies.

Regarding the volume, heat, and salt transport through the SoG, we find that the parameterized tidal mixing mainly influences the net heat and salt transport. Consistently with explicit tides, it moderately decreases the net heat transport towards the Mediterranean and significantly intensifies the net salt transport. More specifically, the intensified net salt transport is particularly consistent with that of tidal simulations. However, the net heat transport shows some discrepancies related to the misrepresentation of the seasonal cycle of temperature over the surface Atlantic layer.

Finally, we investigate the impact of the water mass transformations induced by the parameterized mixing at the SoG on the top 300m hydrography within the Mediterranean. We find that the parameterization realistically reproduces the tidal saltening of the Atlantic Waters and the subsurface hydrographic modulations over the upper 300m depth, related to the enhancement of the Mediterranean convective activity. In addition, we show that the simulation with parameterized tidal mixing better captures the intensity of these modulations than the tidal simulation with coarse resolution at the SoG. The main discrepancies with respect to simulations with explicit tides arise for the temperature of the WMB upper 100m depth, which is affected by the misrepresentation of the seasonal cycle of sea surface temperature within the SoG.

Overall, this study represents a first step towards the development of valid alternatives to explicit tidal forcing and fine-scale resolution at the SoG. Our results indicate that parameterization of tidal mixing are a good candidate for this purpose. However, further development is needed to address the highlighted discrepancies. Although it is challenging, inclusion of the advective effects of tides would represent a notable improvement of the parameterization. In the meantime, the refinement of the vertical distribution of the baroclinic tidal dissipation could be relatively simple to perform by considering the additional dissipation processes, such as the shoaling of baroclinic tides, introduced in de Lavergne et al (2019), and by refining the horizontal resolution of the energy fraction attributed to each dissipative processes. In addition, investigations of the parameterized mixing sensitivity to alternative vertical distributions of the dissipation energy or to variable mixing efficiency (de Lavergne et al, 2016), and comparison with in-situ measurements of turbulence at the SoG would also be valuable.

Chapter 6

Conclusions and Prospects

This final chapter summarises the work accomplished during this PhD and the main results. I first come back to the numerical developments and the main conclusions that can be drawn from them. Then, I summarise the main scientific conclusions on the functioning and remote impacts of the exchange flow at the Strait of Gibraltar. Finally, I provide prospects on future research that could build on results from this PhD.

6.1 Representing the SoG in numerical ocean models

6.1.1 Key elements shaping the exchange flow through the SoG

This PhD aimed to provide insights into the key elements required to represent the SoG in numerical models. In particular, I have assessed the respective importance of tides and fine-scale resolution. To do so, I have developed a new regional configuration of the NEMO model for the Mediterranean region. This configuration, called NEMOMEDGIB, builds on the NEMOMED12 regional configuration and allows easy access to explicit tidal forcing and refined spatial resolution at the SoG. Specifically, the NEMOMEDGIB configuration includes open boundary conditions, time splitting of the barotropic dynamics, explicit tidal forcing, and an adaptive horizontal mesh refinement at the SoG based on the AGRIF Fortran package.

Using this NEMOMEDGIB configuration, I have produced a hierarchy of fully-coupled hindcast numerical simulations allowing me to isolate the respective and combined effects of tides and fine-scale horizontal resolution at the SoG on the Mediterranean region. More specifically, I have focused on four configurations, differing only by the inclusion or omission of tidal forcing and refined resolution at the SoG. Comparison of these simulations has revealed that both tides and fine-scale resolution are essential to simulate the SoG. On the one hand, tides are necessary to represent the water mass transformations across the strait, and the zonal slope of the interface between the exchanged Atlantic and Mediterranean flows. On the other hand, fine-scale horizontal resolution, particularly the fine-scale geometry of the strait, is essential to accurately represent the Atlantic layer thickness and the magnitude of its inflow.

I conclude that omission of either or both tides and fine-scale resolution will likely lead to discrepancies in the simulated hydrographic and dynamic properties of the exchange flow through the strait. Over the Mediterranean Sea, these discrepancies result in misrepresentations of the hydrographic properties of the surface Atlantic Waters, particularly over the western Mediterranean. More specifically, the absence of tidal forcing leads to a basin-scale fresh and warm bias over the Western Mediterranean Basin (WMB hereinafter). On the other hand, the use of coarse resolution produces opposite biases, although this highly depends on the geometry of the strait at coarse resolution.

6.1.2 Can we represent the SoG at a reduced numerical cost?

This PhD highlights the relevance of explicit tides and fine-scale resolution to represent the SoG. However, their inclusion in coarse-resolution models remains a challenge. To address this issue, I have investigated a low-cost alternative to explicit tides and fine-scale resolution at the SoG. I have implemented in the NEMO-MEDGIB configuration a tidal mixing parameterization based on de Lavergne et al (2020). This parameterization acts as a forcing of vertical mixing to represent tide-induced water mass transformations at the SoG. More specifically, the parameterization relies on two-dimensional climatologies of baroclinic tidal dissipation, which I have constructed from a combination of model estimates selected based on a validation against turbulence microstructure measurements over the SoG and the WMB.

I have addressed the relevance of the parameterization by comparing forced ocean simulations of the Mediterranean sea with varying resolutions at the SoG, differing only by the omission, parameterization, or explicit representation of tides. I show that the parameterization reproduces the essential aspects of tidal mixing across the SoG and its impacts on the Mediterranean Sea. In addition, when using a baroclinic tidal dissipation estimate from a high-resolution model, the parameterization realistically represents the local intensification of tidal mixing above the main topographic obstacle of the strait. On the other hand, the parameterization misrepresents some aspects of the SoG thermodynamics and dynamics. In particular, omission of the tidal advection leads to discrepancies in the average dynamical structure of the exchange flow and the seasonal cycle of temperature over the Atlantic layer. Ultimately, these discrepancies have a modest impact on the net heat transport through the SoG that propagates to the WMB.

Overall, these results represent a first step towards lifting the technical barrier of explicit tidal forcing and fine-scale resolution in coarse-resolution numerical models of the SoG. The investigated tidal mixing parameterization represents a promising start toward fully parameterizing exchanges at the SoG and provides insights into the current capabilities and limitations of the state-of-the-art tidal mixing parameterizations, paving the way for future improvements.

6.2 Mechanisms and impacts of the exchange flow at the Strait of Gibraltar

6.2.1 What drives tidal mixing at the SoG ?

The first task carried out during this PhD was to investigate tidal mixing at the SoG, a mechanism driving the water mass transformations across the strait. To do so, I have compared twin tidal and non-tidal yearly MITgcm simulations over the Mediterranean Sea with kilometric resolution at the SoG. More specifically, I have investigated tidal mixing through the model's turbulence closure scheme, based on a turbulent kinetic energy budget.

The results provide insight into the location, intensity, and mechanisms of tidal mixing at the SoG. I show that tidal mixing strongly relies on the interaction of tides with the abrupt topography of the strait and that the underlying mechanisms vary over depth. Near the seafloor, diapycnal mixing periodically intensifies with the vertical shear induced by westward tidal currents. At mid-depth, diapycnal mixing develops in the vicinity of topographic obstacles, where tidal currents locally reduce or reverse the vertical stratification, triggering turbulent mixing. In particular, vertical stratification is controlled by vertical recirculation cells on each side of the main topographic obstacles of the strait, which I relate to tide-induced convergence and divergence patterns. Finally, I show that diapycnal mixing also develops within the Atlantic layer, where upwelled Mediterranean water masses are incorporated by the eastward internal wave released at the Camarinal Sill, which intensifies the vertical shear and reduces or reverses the stratification.

Overall, these results provide valuable insights into interpreting water mass transformations across the SoG. The evidenced processes allow for a better understanding of the dynamic and thermodynamics simulated by numerical models at the SoG and the limitation of coarse-resolution or non-tidal models. In addition, these results provide valuable indications for observational campaigns investigating the location, intensity, and processes involved in turbulent mixing at the SoG. Finally, the highlighted mechanisms may be relevant to other straits of the world and can be useful to the development of tidal mixing parameterizations, such as that investigated in this PhD.

6.2.2 Influence of the SoG on the Mediterranean mean state

This PhD aimed at investigating the role of the SoG on the Mediterranean climate. In this regard, I have first addressed the influence of local processes at the SoG on the hydrographic properties of the Mediterranean Sea. In particular, I have focused on tidal and fine-scale processes. I have diagnosed the effects of these processes based on a hierarchy of fully-coupled hindcast numerical simulations of the Mediterranean Sea, differing only by the inclusion or omission of tides and horizontal grid refinement at the SoG.

I highlight that local processes at the SoG notably influence the Mediterranean Sea hydrography as they modify the net heat and salt transports through the SoG. In particular, tide-induced diapycnal mixing and recirculation across the strait significantly saltens the Atlantic Waters (above 200m depth) and cool the upper WMB. In addition, I show for the first time to my knowledge that tidal mixing at the SoG influences the seasonal cycle of surface temperature over the WMB. On the other hand, the fine-scale structure of the exchange flow through the SoG shapes the thickness of the inflowing Atlantic layer over the Mediterranean Sea. Finally, I show that local processes at the SoG indirectly influence the average properties of intermediate and deep water masses. This influence results from the modification of the upper Mediterranean stratification, and the hydrographic properties of the surface water masses, which both affect the vertical fluxes of heat and salt.

These results highlight that local processes at the SoG have a large-scale influence on the Mediterranean Sea and are relevant to consider when investigating its mean state.

6.2.3 Do local processes at the SoG influence the Mediterranean convective activity?

This PhD also aimed to clarify the influence of the SoG on Mediterranean deep convection. With respect to previous studies, it benefits from a hierarchy of simulations of long temporal coverage, allowing us to isolate the long-term influence of local processes at the SoG.

I show that the local processes at the SoG notably influence the Mediterranean deep convection. In particular, our results confirm that the saltening of Atlantic water masses by tidal mixing at the SoG enhances deep convection over the northwestern Mediterranean Sea, where it appears essential to the regular occurrence of bottom convection. In addition, I show that it also enhances the Adriatic and Aegean deep convection. Conversely, I find that the fine-scale dynamical structure of the exchange flow through the SoG inhibits deep convection through its influence on the thickening of the fresh and buoyant Atlantic Waters. More generally, the influence of the investigated processes is particularly intense over the northwestern Mediterranean Sea and less intense over the Adriatic and Aegean Seas, where they mainly modulate the intensity of bottom convective events, such as the Eastern Mediterranean transient.

Overall, these results show that local processes at the SoG are relevant to the Mediterranean thermohaline circulation. In particular, the tidal saltening of Atlantic water masses at the SoG and the shaping of the Atlantic layer thickness can be considered as preconditioners for the Mediterranean deep convection sites.

6.2.4 Do the local processes at the SoG influence the Mediterranean sea variability?

I have finally investigated the Mediterranea Sea interannual variability. I show that tidal and fine-scale processes at the SoG moderately influence the interannual variability of Mediterranean water masses above 600m depth. On the other hand, they notably influence temperature and salinity trends below 600m depth through their impact on dense water formation events.

These results highlight that water mass transformations across the SoG are relatively steady over time. Thus, the variability of the upper and intermediate Mediterranean water masses is mainly forced by the atmosphere. On the other hand, long-term temperature and salinity trends over deep layers rely on isolated extreme climatic events and on the Mediterranean mean state, which altogether control the occurrence of intense convection events.

6.2.5 Influence of the SoG on the atmosphere

Finally, for the first time to my knowledge, this PhD has investigated the influence of the SoG on the atmosphere. To do so, I have compared the summer air-sea fluxes and atmospheric properties of two fully coupled hindcast simulations, differing only by the representation of tides and enhanced resolution at the SoG.

I find that local processes at the SoG have a moderate but notable influence on the atmosphere. Specifically, during summertime, the Mediterranean surface cooling by tidal mixing at the SoG decreases the ocean heat and water loss to the atmosphere. Consequently, tidal mixing at the SoG moderately reduces the seasonal warming of the atmosphere over the sea and participates to its seasonal drying over the sea and coastal areas. Ultimately, the tide-induced drying of the atmosphere generally reduces the cloudiness over the sea and coastal areas and moderately reduces precipitation over the western Mediterranean region.

Overall, these results evidence a new coupled mechanism over the Mediterranean Sea whereby ocean physics impact on the seasonal cycle of the atmospheric heat and water contents. With that in mind, the effects on the atmosphere are moderate and mainly concentrated over the sea. Further investigations are needed to extend this conclusion to the future climate.

6.3 Prospects

6.3.1 Short and medium term

Understanding and modeling tidal mixing at the SoG

This PhD has proposed several mechanisms to explain tidal mixing at the SoG. However, some of the non-linear processes at play within the strait could not be investigated. In particular, non-hydrostatic processes were not included in the analyzed simulations. In the future, the influence of these processes on water mass transformations across the strait should be addressed in a dedicated study. In particular, the train of solitary waves that develops along the trail of the internal bore released at the Camarinal Sill is likely to drive intense diapycnal mixing remotely. Besides numerical simulations, these processes could be investigated during observational campaigns at the SoG based on microstructure turbulence, hydrographic, and velocity measurements. In addition, the resulting in-situ observations could be used to assess the realism of the mechanisms highlighted in this PhD and provide insight into the performance of the current numerical models at the SoG.

Investigation of non-linear processes at the SoG would also provide valuable insights to develop valid alternatives to explicit tides and high-resolution for numerical models representing the SoG. Indeed, we have shown that the tidal mixing parameterizations of de Lavergne et al (2020) can produce relatively realistic water mass transformations across the SoG. However, further work is needed to overcome the simplifications and assumptions upon which the parameterization relies. In particular, the high sensitivity of the parameterization to the vertical distribution of tidal dissipation asks for validation of the simulated tidal dissipation. Including tidal advection in the parameterized processes would also result in notable improvements regarding the vertical structure of the simulated water mass transformations, their seasonal variation, and the dynamics of the exchange flow. In this regard, the simple parameterization proposed by Sanchez-Roman et al (2018) would provide a sensible starting point. Finally, inclusion of tidal dissipation directly into the turbulence closure scheme of the model would provide better consistency of simulated turbulence. In particular, this would unify the treatment of turbulence sources and the mixing efficiency in the model.

Understanding the Mediterranean mean and future state

This PhD highlights several mechanisms whereby local processes at the SoG influence the Mediterranean mean state and its past variability. However, further work is needed to provide a complete picture of the role played by the SoG on the Mediterranean climate.

In particular, the large-scale impact of local processes at the SoG on basin-scale circulation remains unclear and asks for a dedicated study. More specifically, the influence of fine-scale dynamics of the SoG on the Alboran Sea circulation would be relevant to investigate, building on the results of Sánchez-Garrido et al (2013); Romero-Cózar et al (2021) regarding the effects of tides on the gyre circulation. Similarly, the influence of the SoG on the exchanges between the Eastern and Western Mediterranean Basins and on the propagation of Levantine Intermediate water is relevant to investigate (Sannino et al, 2015).

Further investigations are also needed regarding the influence of the SoG on the atmosphere of the Mediterranean region. Although the highlighted large-scale impacts of local processes at the SoG are moderate, their local influence on coastal areas remains to be investigated. In particular, the Alboran Sea, where tidal mixing substantially influences the sea surface temperature, should be investigated in priority. In addition, variation in the influence of local processes at the SoG depending on specific weather regimes and extremes would also be relevant to investigate.

Finally, several studies have suggested that the Mediterranean sea will undergo significant changes related to global warming in the future. Results from this PhD indicate that explicit tides and fine-scale resolution at the SoG are relevant to investigate these changes. In particular, the saltening and cooling of Atlantic water masses induced by tidal mixing at the SoG is likely to inhibit the future increase of surface stratification. Thus, local processes at the SoG may participate in maintaining future deep convection. Similarly, given the influence of these processes on the heat and salt transport through the strait, whether they modulate the warming signal over the Mediterranean Sea remains an open question.

I will investigate the former questions in the upcoming months based on fully coupled numerical simulations using the NEMOMEDGIB configuration developed in this PhD.

6.3.2 Long term

On the influence of local processes at the SoG on the Mediterranean sea biogeochemistry

This PhD evidences intense vertical velocities at the SoG. Given the relevance of vertical transports to biogeochemistry, our results suggest that local processes at the SoG may control the basin-scale biogeochemical balances and their temporal variability.

In particular, in the context of global warming, a detailed understanding of the role played by local processes at the SoG in the Mediterranean biogeochemical cycles is essential to assess the key elements needed to represent their future evolution. Indeed, the influence of non-linear processes at the SoG may have greater importance in the future, as marine biomass production (primary productivity) is projected to decline due to increased vertical stratification and the weakening of deep convection.

A numerical study investigating this question could rely on similar simulations to those investigated in this PhD, with the addition of an online marine biogeochemistry module.

On the formation and export of Mediterranean Outflow Waters toward the Atlantic ocean

This PhD highlights that local processes at the SoG notably influence Mediterranean outflow water masses (MOW hereinafter) exiting the SoG. In particular, tidal mixing and recirculation at the SoG freshen the Mediterranean outflow by typically 0.1‰ and warm it by approximately 0.1°C. These transformations, and their impact on the net heat and salt exchanges between the Atlantic Ocean and the Mediterranean Sea, suggest that local processes at the SoG are also relevant to the Atlantic hydrography. In particular, given that the MOWs were shown to influence deep convection over Nordic Seas (Reid, 1979; McCartney and Mauritzen, 2001), their local transformation at the SoG may have an indirect impact on the Atlantic Meridional Overturning Circulation.

Thus, the role played by local processes at the SoG in the Atlantic Ocean mean state and variability is also relevant to investigate. To do so, a similar numerical framework to that presented in this PhD could be used as the respective and combined effects of tidal and fine-scale mechanisms should all be relevant to investigate. In addition, this study could provide valuable information on how to represent the SoG in models of the Atlantic and global oceans. In this regard, special attention should be paid to the representation of the Mediterranean overflow. In particular, sensitivity of the simulated dynamics and thermodynamics to the vertical coordinates system should be investigated.

Toward a better understanding of straits in the global ocean

This PhD emphasizes that local processes at the SoG modulate the hydrographic and volume exchanges between the Atlantic Ocean and the Mediterranean Sea. Given the similarity of the SoG with other straits of the global ocean, the processes highlighted here may be relevant to other regions of the world. In particular, the mechanisms driving tidal mixing may be relevant to straits located over areas of intense tidal currents and steep topography, such as Indonesian straits. Similarly, the processes related to fine-scale dynamics and topography are likely relevant to other straits characterized by small scale layered exchange flows (for example, the Baltic, Luzon, Bussol straits). In the future, investigating the role played by these local processes in the global ocean would be interesting. In particular, this may allow us to deepen our understanding of the global thermohaline circulation as well as ocean diapycnal mixing, which is believed to partly rely on the exchanges and turbulent mechanisms at play within straits (Bryden and Nurser, 2003).

Investigation of the former question could rely on a similar numerical framework to that used in this PhD, allowing the authors to isolate the effects of local processes at play within straits. In this way, numerical development would be needed to overcome the challenges in representing these processes in global ocean models. Doing so may require developing a parameterization of the processes driving water-mass transformation and fine-scale dynamics within straits or focusing on a set of straits, where grid refinement methods could be applied.

Bibliography

Adcroft A, Campin JM (2004) Rescaled height coordinates for accurate representation of free-surface flows in ocean circulation models. Ocean Modelling 7(3-4):269–284, DOI 10.1016/j.ocemod.2003.09.003, URL `https://linkinghub.elsevier.com/retrieve/pii/S1463500303000544`

Adcroft A, Hill C, Marshall J (1997) Representation of topography by shaved cells in a height coordinate ocean model. Monthly Weather Review 125(9):2293–2315, DOI 10.1175/1520-0493(1997)125⟨2293:ROTBSC⟩2.0.CO;2, URL `http://journals.ametsoc.org/doi/10.1175/1520-0493(1997)125%3C2293:ROTBSC%3E2.0.CO;2`

Adloff F, Somot S, Sevault F, Jordà G, Aznar R, Déqué M, Herrmann M, Marcos M, Dubois C, Padorno E, Alvarez-Fanjul E, Gomis D (2015) Mediterranean Sea response to climate change in an ensemble of twenty first century scenarios. Climate Dynamics 45(9-10):2775–2802, DOI 10.1007/s00382-015-2507-3, URL `http://dx.doi.org/10.1007/s00382-015-2507-3`

Adloff F, Jordà G, Somot S, Sevault F, Arsouze T, Meyssignac B, Li L, Planton S (2018) Improving sea level simulation in Mediterranean regional climate models. Climate Dynamics 51(3):1167–1178, DOI 10.1007/s00382-017-3842-3

Aiki H, Yamagata T (2004) A numerical study on the successive formation of Meddy-like lenses. Journal of Geophysical Research: Oceans 109(6):1–25, DOI 10.1029/2003JC001952

Alhammoud B, Meijer PT, Dijkstra HA (2010) Sensitivity of Mediterranean thermohaline circulation to gateway depth: A model investigation. Paleoceanography 25(2):1–20, DOI 10.1029/2009PA001823

Alpers W, Brandt P, Rubino A (2008) Internal waves generated in the Straits of Gibraltar and Messina: Observations from space. Remote Sensing of the European Seas pp 319–330, DOI 10.1007/978-1-4020-6772-3{_}24

Álvarez O, González CJ, Mañanes R, López L, Bruno M, Izquierdo A, Gómez-Enri J, Forero M (2011) Analysis of short-period internal waves using wave-induced surface displacement: A three-dimensional model approach in Algeciras Bay and the Strait of Gibraltar. Journal of Geophysical Research: Oceans 116(12):C12,033, DOI 10.1029/2011JC007393, URL `http://doi.wiley.com/10.1029/2011JC007393`

Álvarez O, Izquierdo A, González CJ, Bruno M, Mañanes R (2019) Some considerations about non-hydrostatic vs. hydrostatic simulation of short-period internal waves. A case study: The Strait of Gibraltar. Continental Shelf Research 181(November 2018):174–186, DOI 10.1016/j.csr.2019.05.016, URL `https://doi.org/10.1016/j.csr.2019.05.016https://linkinghub.elsevier.com/retrieve/pii/S0278434318303236`

von Appen WJ, Koszalka IM, Pickart RS, Haine TW, Mastropole D, Magaldi MG, Valdimarsson H, Girton J, Jochumsen K, Krahmann G (2014) The East Greenland Spill Jet as an important component of the Atlantic Meridional Overturning Circulation. Deep-Sea Research Part I: Oceanographic Research Papers 92:75–84, DOI 10.1016/j.dsr.2014.06.002, URL `http://dx.doi.org/10.1016/j.dsr.2014.06.002`

Arhan M, De Verdiere AC, Memery L (1994) The eastern boundary of the subtropical North Atlantic. Journal of Physical Oceanography 24(6):1295–1316, DOI 10.1175/1520-0485(1994)024⟨1295:TEBOTS⟩2.0.CO;2, URL `http://journals.ametsoc.org/doi/10.1175/1520-0485(1994)024%3C1295:TEBOTS%3E2.0.CO;2`

Artale V, Levi D (1987) Nonlinear internal waves in a one-dimensional channel. Il Nuovo Cimento C 10(1):61–76, DOI 10.1007/BF02508697, URL `http://link.springer.com/10.1007/BF02508697`

Azzaro F, Decembrini F, Raffa F, Crisafi E (2007) Seasonal variability of phytoplankton fluorescence in relation to the Straits of Messina (Sicily) tidal upwelling. Ocean Science 3(4):451–460, DOI 10.5194/os-3-451-2007

Baird ME, Ridgway KR (2012) The southward transport of sub-mesoscale lenses of Bass Strait Water in the centre of anti-cyclonic mesoscale eddies. Geophysical Research Letters 39(2):2–7, DOI 10.1029/2011GL050643

Balmaseda MA, Mogensen K, Weaver AT (2013) Evaluation of the ECMWF ocean reanalysis system ORAS4. Quarterly Journal of the Royal Meteorological Society 139(674):1132–1161, DOI 10.1002/qj.2063

Baringer MO, Price JF (1999) A review of the physical oceanography of the Mediterranean outflow. Marine Geology 155(1-2):63–82, DOI 10.1016/S0025-3227(98)00141-8, URL `https://linkinghub.elsevier.com/retrieve/pii/S0025322798001418`

Barnier B, Madec G, Penduff T, Molines JM, Treguier AM, Le Sommer J, Beckmann A, Biastoch A, Böning C, Dengg J, Derval C, Durand E, Gulev S, Remy E, Talandier C, Theetten S, Maltrud M, McClean J, De Cuevas B (2006) Impact of partial steps and momentum advection schemes in a global ocean circulation model at eddy-permitting resolution. Ocean Dynamics 56(5-6):543–567, DOI 10.1007/s10236-006-0082-1

Baschek B, Send U, Lafuente JG, Candela J (2001) Transport estimates in the Strait of Gibraltar with a tidal inverse model. Journal of Geophysical Research: Oceans 106(C12):31,033–31,044, DOI 10.1029/2000jc000458

Bashmachnikov I, Neves F, Calheiros T, Carton X (2015) Properties and pathways of Mediterranean water eddies in the Atlantic. Progress in Oceanography 137(June):149–172, DOI 10.1016/j.pocean.2015.06.001, URL `http://dx.doi.org/10.1016/j.pocean.2015.06.001`

Béranger K, Mortier L, Gasparini GP, Gervasio L, Astraldi M, Crépon M (2004) The dynamics of the Sicily Strait: a comprehensive study from observations and models. Deep Sea Research Part II: Topical Studies in Oceanography 51(4-5):411–440, DOI 10.1016/j.dsr2.2003.08.004, URL `https://linkinghub.elsevier.com/retrieve/pii/S096706450400027X`

Béranger K, Mortier L, Crépon M (2005) Seasonal variability of water transport through the Straits of Gibraltar, Sicily and Corsica, derived from a high-resolution model of the Mediterranean circulation. Progress in Oceanography 66(2-4):341–364, DOI 10.1016/j.pocean.2004.07.013, URL `https://linkinghub.elsevier.com/retrieve/pii/S0079661105000777`

Berné S, Carré D, Loubrieu B, Mazé JP, Morvan L, Normand A (2004) Le golfe du Lion–Carte morpho-bathymétrique. Ifremer, Brest, France

Berrisford P, Dee DP, Fielding M, Fuentes M, K\r allberg PW, Kobayashi S, Uppala S (2009) The ERA-Interim archive. URL `https://www.ecmwf.int/node/8173`

Bethoux J, Gentili B, Morin P, Nicolas E, Pierre C, Ruiz-Pino D (1999) The Mediterranean Sea: a miniature ocean for climatic and environmental studies and a key for the climatic functioning of the North Atlantic. Progress in Oceanography 44(1-3):131–146, DOI 10.1016/S0079-6611(99)00023-3, URL `https://linkinghub.elsevier.com/retrieve/pii/S0079661199000233`

Beuvier J, Sevault F, Herrmann M, Kontoyiannis H, Ludwig W, Rixen M, Stanev E, Branger K, Somot S (2010a) Modeling the Mediterranean Sea interannual variability during 1961-2000: Focus on the Eastern Mediterranean Transient. Journal of Geophysical Research: Oceans 115(8), DOI 10.1029/2009JC005950

Beuvier J, Sevault F, Herrmann M, Kontoyiannis H, Ludwig W, Rixen M, Stanev E, Branger K, Somot S (2010b) Modeling the Mediterranean Sea interannual variability during 1961-2000: Focus on the Eastern Mediterranean Transient. Journal of Geophysical Research: Oceans 115(8), DOI 10.1029/2009JC005950

Beuvier J, Béranger K, Lebeaupin Brossier C, Somot S, Sevault F, Drillet Y, Bourdallé-Badie R, Ferry N, Lyard F (2012) Spreading of the Western Mediterranean Deep Water after winter 2005: Time scales and deep cyclone transport. Journal of Geophysical Research: Oceans 117(C7):n/a–n/a, DOI 10.1029/2011JC007679, URL `http://doi.wiley.com/10.1029/2011JC007679`

Biastoch A, Böning CW, Lutjeharms JR (2008) Agulhas leakage dynamics affects decadal variability in Atlantic overturning circulation. Nature 456(7221):489–492, DOI 10.1038/nature07426

Bignami F, Salusti E (1990) Tidal Currents and Transient Phenomena in the Strait of Messina: a Review. In: The Physical Oceanography of Sea Straits, Springer

Netherlands, Dordrecht, pp 95–124, DOI 10.1007/978-94-009-0677-8{_}4, URL http://link.springer.com/10.1007/978-94-009-0677-8_4

Bignami F, Marullo S, Santoleri R, Schiano ME (1995) Longwave radiation budget in the Mediterranean Sea. Journal of Geophysical Research 100(C2):2501–2514, DOI 10.1029/94JC02496

de Boer AM, Hutchinson DK, Roquet F, Sime LC, Burls NJ, Heuzé C (2022) The Impact of Southern Ocean Topographic Barriers on the Ocean Circulation and the Overlying Atmosphere. Journal of Climate 35(18):5805–5821, DOI 10.1175/jcli-d-21-0896.1, URL https://journals.ametsoc.org/view/journals/clim/35/18/JCLI-D-21-0896.1.xml

BOHM E, MAGAZZU G, WALD L, ZOCCOLOTTI M (1987) Coastal currents on the Sicilian shelf south of Messina. Oceanologica acta 10(2):137–142, URL https://archimer.ifremer.fr/doc/00108/21914/

Bouffard D, Boegman L (2013) A diapycnal diffusivity model for stratified environmental flows. Dynamics of Atmospheres and Oceans 61-62:14–34, DOI 10.1016/j.dynatmoce.2013.02.002, URL http://dx.doi.org/10.1016/j.dynatmoce.2013.02.002

Bougeault P, Andre JC (1986) On the stability of the third-order turbulence closure for the modeling of the stratocumulus-topped boundary layer. Journal of the Atmospheric Sciences 43(15):1574–1581, DOI 10.1175/1520-0469(1986)043⟨1574:OTSOTT⟩2.0.CO;2

Bougeault P, Lacarrere P (1989) Parameterization of orography-induced turbulence in a mesobeta-scale model. DOI 10.1175/1520-0493(1989)117⟨1872:POOITI⟩2.0.CO;2

Boutov D, Peliz A, Miranda PM, Soares PM, Cardoso RM, Prieto L, Ruiz J, García-Lafuente J (2014) Inter-annual variability and long term predictability of exchanges through the Strait of Gibraltar. Global and Planetary Change 114:23–37, DOI 10.1016/j.gloplacha.2013.12.009, URL http://dx.doi.org/10.1016/j.gloplacha.2013.12.009

Bower AS, Serra N, Ambar I (2002) Structure of the Mediterranean Undercurrent and Mediterranean Water spreading around the southwestern Iberian Peninsula. Journal of Geophysical Research: Oceans 107(10):1–19, DOI 10.1029/2001jc001007

Brandt P, Alpers W, Backhaus JO (1996) Study of the generation and propagation of internal waves in the Strait of Gibraltar using a numerical model and synthetic aperture radar images of the European ERS 1 satellite. Journal of Geophysical Research: Oceans 101(C6):14,237–14,252, DOI 10.1029/96JC00540, URL http://doi.wiley.com/10.1029/96JC00540

Bray NA, Ochoa J, Kinder TH (1995) The role of the interface in exchange through the Strait of Gibraltar. Journal of Geophysical Research 100(C6), DOI 10.1029/95jc00381

Bruno M, Juan Alonso J, Cózar A, Vidal J, Ruiz-Cañavate A, Echevarria F, Ruiz J (2002) The boiling-water phenomena at Camarinal Sill, the strait of Gibraltar. Deep Sea Research Part II: Topical Studies in Oceanography 49(19):4097–4113, DOI 10.1016/S0967-0645(02)00144-3, URL `https://linkinghub.elsevier.com/retrieve/pii/S0967064502001443`

Bruno M, Chioua J, Romero J, Vázquez A, Macías D, Dastis C, Ramírez-Romero E, Echevarria F, Reyes J, García C (2013) The importance of sub-mesoscale processes for the exchange of properties through the Strait of Gibraltar. Progress in Oceanography 116:66–79, DOI 10.1016/j.pocean.2013.06.006, URL `https://linkinghub.elsevier.com/retrieve/pii/S0079661113000943`

Bryan F (1987) Parameter sensitivity of primitive equation ocean general circulation models. J Phys Oceanogr 17(7 , Jul. 1987):970–985, DOI 10.1175/1520-0485(1987) 017⟨0970:psopeo⟩2.0.co;2, URL `http://journals.ametsoc.org/doi/10.1175/1520-0485(1987)017%3C0970:PSOPEO%3E2.0.CO;2`

Bryden H, Stommel H (1984) Limiting processes that determine basic features of the circulation in the Mediterranean Sea. Oceanologica acta 7(3):289–296

Bryden HL, Kinder TH (1986) Gibraltar experiment : a plan for dynamic and kinematic investigations of strait mixing, exchange and turbulence. Woods Hole Oceanographic Institution, Woods Hole, MA, DOI 10.1575/1912/7955, URL `https://hdl.handle.net/1912/7955`

Bryden HL, Kinder TH (1991) Recent Progress in Strait Dynamics. Reviews of Geophysics 29(S2):617–631, DOI 10.1002/rog.1991.29.s2.617, URL `https://onlinelibrary.wiley.com/doi/10.1002/rog.1991.29.s2.617`

Bryden HL, Nurser AJ (2003) Effects of strait mixing on ocean stratification. Journal of Physical Oceanography 33(8):1870–1872, DOI 10.1175/1520-0485(2003) 033⟨1870:EOSMOO⟩2.0.CO;2, URL `http://journals.ametsoc.org/doi/10.1175/1520-0485(2003)033%3C1870:EOSMOO%3E2.0.CO;2`

Bryden HL, Candela J, Kinder TH (1994) Exchange through the Strait of Gibraltar. Progress in Oceanography 33(3):201–248, DOI 10.1016/0079-6611(94)90028-0

Buijsman MC, McWilliams JC, Jackson CR (2010) East-west asymmetry in nonlinear internal waves from Luzon Strait. Journal of Geophysical Research: Oceans 115(10):2009JC006,004, DOI 10.1029/2009JC006004, URL `https://onlinelibrary.wiley.com/doi/10.1029/2009JC006004`

Buijsman MC, Ansong JK, Arbic BK, Richman JG, Shriver JF, Timko PG, Wallcraft AJ, Whalen CB, Zhao Z (2016) Impact of parameterized internal wave drag on the semidiurnal energy balance in a global ocean circulation model. Journal of Physical Oceanography 46(5):1399–1419, DOI 10.1175/JPO-D-15-0074.1

Campin JM, Adcroft A, Hill C, Marshall J (2004) Conservation of properties in a free-surface model. Ocean Modelling 6(3-4):221–244, DOI 10.1016/S1463-5003(03)00009-X, URL `https://linkinghub.elsevier.com/retrieve/pii/S146350030300009X`

Candela J (1991) The Gibraltar Strait and its role in the dynamics of the Mediterranean Sea. Dynamics of Atmospheres and Oceans 15(3-5):267–299, DOI 10.1016/0377-0265(91)90023-9

Candela J, Winant CD, Bryden HL (1989) Meteorologically forced subinertial flows through the Strait of Gibraltar. Journal of Geophysical Research: Oceans 94(C9):12,667–12,679, DOI 10.1029/JC094iC09p12667, URL `http://dx.doi.org/10.1029/JC094iC09p12667;doi:10.1029/JC094iC09p12667`

Candela J, Winant C, Ruiz A (1990) Tides in the strait of gibraltar. Journal of Geophysical Research 95(C5):7313–7335, DOI 10.1029/JC095iC05p07313

Carracedo LI, Gilcoto M, Mercier H, Pérez FF (2014) Seasonal dynamics in the Azores-Gibraltar Strait region: A climatologically-based study. Progress in Oceanography 122:116–130, DOI 10.1016/j.pocean.2013.12.005, URL `http://dx.doi.org/10.1016/j.pocean.2013.12.005`

Carter GS, Merrifield MA, Becker JM, Katsumata K, Gregg MC, Luther DS, Levine MD, Boyd TJ, Firing YL (2008) Energetics of M2 barotropic-to-baroclinic tidal conversion at the Hawaiian Islands. Journal of Physical Oceanography 38(10):2205–2223, DOI 10.1175/2008JPO3860.1

Chan WL, Motoi T (2003) Effects of stopping the Mediterranean Outflow on the southern polar region. Polar meteorology and glaciology 17:25–35, DOI 10.15094/00002958, URL `http://ci.nii.ac.jp/naid/110000034872/en/`

Chanut J, Barńier B, Large W, Debreu L, Penduff T, Molines JM, Mathiot P (2008) Mesoscale eddies in the Labrador Sea and their contribution to convection and restratification. Journal of Physical Oceanography 38(8):1617–1643, DOI 10.1175/2008JPO3485.1

Chérubin L, Serpette A, Carton X, Paillet J, Connan O, Morin P, Rousselet R, Le Cann B, Le Corre P, Labasque T, Corman D, Poete N (1997) Descriptive analysis of the hydrology and currents on the Iberian shelf from Gibraltar to Cape Finisterre: Preliminary results from the Semane and Interafos experiments. Annales Hydrographiques 21(768):5–16

Chérubin L, Carton X, Dritschel DG (2007) Vortex dipole formation by baroclinic instability of boundary currents. Journal of Physical Oceanography 37(6):1661–1677, DOI 10.1175/JPO3079.1

Colin J, DéQué M, Radu R, Somot S (2010) Sensitivity study of heavy precipitation in Limited Area Model climate simulations: Influence of the size of the domain and the use of the spectral nudging technique. Tellus, Series A: Dynamic Meteorology and Oceanography 62(5):591–604, DOI 10.1111/j.1600-0870.2010.00467.x

Craig A, Valcke S, Coquart L (2017) Development and performance of a new version of the OASIS coupler, OASIS3-MCT-3.0. Geoscientific Model Development 10(9):3297–3308, DOI 10.5194/gmd-10-3297-2017

Daniault N, Mazé JP, Arhan M (1994) Circulation and mixing of Mediterranean water west of the Iberian Peninsula. Deep-Sea Research Part I 41(11-12):1685–1714, DOI 10.1016/0967-0637(94)90068-X

Daniel M, Lemonsu A, Déqué M, Somot S, Alias A, Masson V (2019) Benefits of explicit urban parameterization in regional climate modeling to study climate and city interactions. Climate Dynamics 52(5-6):2745–2764, DOI 10.1007/s00382-018-4289-x, URL `http://dx.doi.org/10.1007/s00382-018-4289-x`

Darmaraki S, Somot S, Sevault F, Nabat P (2019) Past Variability of Mediterranean Sea Marine Heatwaves. Geophysical Research Letters 46(16):9813–9823, DOI 10.1029/2019GL082933

D'Asaro EA (1988) Generation of submesoscale vortices: A new mechanism. Journal of Geophysical Research 93(C6):6685, DOI 10.1029/jc093ic06p06685, URL `http://doi.wiley.com/10.1029/JC093iC06p06685`

Davies HC (1976) A laterul boundary formulation for multi-level prediction models. Quarterly Journal of the Royal Meteorological Society 102(432):405–418, DOI 10.1002/qj.49710243210

De Pascual-Collar A, Sotillo MG, Levier B, Aznar R, Lorente P, Amo-Baladrón A, Álvarez-Fanjul E (2019) Regional circulation patterns of Mediterranean Outflow Water near the Iberian and African continental slopes. Ocean Science 15(3):565–582, DOI 10.5194/os-15-565-2019, URL `https://os.copernicus.org/articles/15/565/2019/`

Debreu L, Vouland C, Blayo E (2008) AGRIF: Adaptive grid refinement in Fortran. Computers and Geosciences 34(1):8–13, DOI 10.1016/j.cageo.2007.01.009, URL `https://linkinghub.elsevier.com/retrieve/pii/S009830040700115X`

Debreu L, Marchesiello P, Penven P, Cambon G (2012) Two-way nesting in split-explicit ocean models: Algorithms, implementation and validation. Ocean Modelling 49-50:1–21, DOI 10.1016/j.ocemod.2012.03.003, URL `http://dx.doi.org/10.1016/j.ocemod.2012.03.003`

Decharme B, Delire C, Minvielle M, Colin J, Vergnes JP, Alias A, Saint-Martin D, Séférian R, Sénési S, Voldoire A (2019) Recent Changes in the ISBA-CTRIP Land Surface System for Use in the CNRM-CM6 Climate Model and in Global Off-Line Hydrological Applications. Journal of Advances in Modeling Earth Systems 11(5):1207–1252, DOI 10.1029/2018MS001545

Demirov E, Pinardi N (2002) Simulation of the Mediterranean Sea circulation from 1979 to 1993: Part I. The interannual variability. Journal of Marine Systems 33-34:23–50, DOI 10.1016/S0924-7963(02)00051-9, URL `https://linkinghub.elsevier.com/retrieve/pii/S0924796302000519`

Dickson R, Brown J (1994) The production of North Atlantic Deep Water : Sources , rates , and pathways la . Worthington ' s scheme conversion paths North Circled numbers are transport estimates in Sverdrups , where lb . The recasting of Worthington ' s scheme by McCartney and. Journal of Geophysical Research 99(C6):12,319–12,341, URL `https://agupubs.onlinelibrary.wiley.com/doi/abs/10.1029/94JC00530`

Djath B, Melet A, Verron J, Molines JM, Barnier B, Gourdeau L, Debreu L (2014) A 1/36° model of the Solomon Sea embedded into a global ocean model: On the setting up of an interactive open boundary nested model system. Journal of Operational Oceanography 7(1):34–46, DOI 10.1080/1755876X.2014.11020151, URL `http://www.tandfonline.com/doi/full/10.1080/1755876X.2014.11020151`

Dunić N, Vilibić I, Šepić J, Mihanović H, Sevault F, Somot S, Waldman R, Nabat P, Arsouze T, Pennel R, Jordà G, Precali R (2019) Performance of multi-decadal ocean simulations in the Adriatic Sea. Ocean Modelling 134(5247):84–109, DOI 10.1016/j.ocemod.2019.01.006, URL `https://doi.org/10.1016/j.ocemod.2019.01.006https://linkinghub.elsevier.com/retrieve/pii/S1463500318301951`

Egbert GD, Erofeeva SY (2002) Efficient inverse modeling of barotropic ocean tides. Journal of Atmospheric and Oceanic Technology 19(2):183–204, DOI 10.1175/1520-0426(2002)019⟨0183:EIMOBO⟩2.0.CO;2

ENGEDAHL H (1995) Use of the flow relaxation scheme in a three-dimensional baroclinic ocean model with realistic topography. Tellus A 47(3):365–382, DOI 10.1034/j.1600-0870.1995.t01-2-00006.x, URL `http://tellusa.net/index.php/tellusa/article/view/11523`

Escudier R, Clementi E, Omar M, Cipollone A, Pistoia J, Aydogdu A, Drudi M, Grandi A, Lyubartsev V, Lecci R (2020) Mediterranean Sea Physical Reanalysis (CMEMS MED-Currents)(Version 1)[Data set]. Copernicus Monitoring Environment Marine Service (CMEMS) DOI 10.25423/CMCC/MEDSEA{_}MULTIYEAR{_}PHY{_}006{_}004{_}E3R1

Estournel C, Marsaleix P, Ulses C (2021) A new assessment of the circulation of Atlantic and Intermediate Waters in the Eastern Mediterranean. Progress in Oceanography 198:102,673, DOI 10.1016/j.pocean.2021.102673, URL `https://doi.org/10.1016/j.pocean.2021.102673`

Farmer DM, Armi L (1985) The internal hydraulics of the Strait of Gibraltar and associated sills and narrows. Oceanologica acta 8(1):37–46, URL `https://archimer.ifremer.fr/doc/00112/22325/`

Farmer DM, Armi L (1986) Maximal two-layer exchange over a sill and through the combination of a sill and contraction with barotropic flow. Journal of Fluid Mechanics 164(10):53–76, DOI 10.1017/S002211208600246X

Farmer DM, Armi L, Armi L, Farmer DM (1988) The flow of Atlantic water through the Strait of Gibraltar. Progress in Oceanography 21(1):1, DOI 10.1016/0079-6611(88)90055-9, URL `https://doi.org/10.1016/0079-6611(88)90055-9`

Farmer DM, Alford MH, Lien RC, Yang YJ, Chang MH, Li Q (2011) From Luzon Strait to Dongsha Plateau: Stages in the life of an internal wave. Oceanography 24(4):65–77, DOI 10.5670/oceanog.2011.95, URL `http://dx.doi.org/10.5670/oceanog.2011.95.https://tos.org/oceanography/article/from-luzon-strait-to-dongsha-plateau-stages-in-the-life-of-an-internal-wave`

Fenoglio-Marc L, Mariotti A, Sannino G, Meyssignac B, Carillo A, Struglia MV, Rixen M (2013) Decadal variability of net water flux at the Mediterranean Sea Gibraltar Strait. Global and Planetary Change 100:1–10, DOI 10.1016/j.gloplacha.2012.08.007, URL `http://dx.doi.org/10.1016/j.gloplacha.2012.08.007`

Fernando HJ (1991) Turbulent mixing in stratified fluids. Annual Review of Fluid Mechanics 23(1):455–493, DOI 10.1146/annurev.fl.23.010191.002323

Ferrarin C, Bellafiore D, Sannino G, Bajo M, Umgiesser G (2018) Tidal dynamics in the inter-connected Mediterranean, Marmara, Black and Azov seas. Progress in Oceanography 161(November 2017):102–115, DOI 10.1016/j.pocean.2018.02.006

Ferron B, Bouruet Aubertot P, Cuypers Y, Schroeder K, Borghini M (2017) How important are diapycnal mixing and geothermal heating for the deep circulation of the Western Mediterranean? Geophysical Research Letters 44(15):7845–7854, DOI 10.1002/2017GL074169

Flather RA (1994) A storm surge prediction model for the northern Bay of Bengal with application to the cyclone disaster in April 1991. Journal of Physical Oceanography 24(1):172–190, DOI 10.1175/1520-0485(1994)024⟨0172:ASSPMF⟩2.0.CO;2, URL `http://journals.ametsoc.org/doi/10.1175/1520-0485(1994)024%3C0172:ASSPMF%3E2.0.CO;2`

Foreman MG (1977) Manual for Tidal Heights And Prediction. Pac Mar Sci Rep 77–10

Foreman MGG, Henry RF, Walters RA, Ballantyne VA (1993) A finite element model for tides and resonance along the north coast of British Columbia. Journal of Geophysical Research: Oceans 98(C2):2509–2531, DOI 10.1029/92JC02470, URL `https://onlinelibrary.wiley.com/doi/10.1029/92JC02470http://doi.wiley.com/10.1029/92JC02470`

Gačić M, Lascaratos A, Manca BB, Mantziafou A (2001) Adriatic Deep Water and Interaction with the Eastern Mediterranean Sea. In: Physical Oceanography of the Adriatic Sea, Springer Netherlands, Dordrecht, pp 111–142, DOI 10.1007/978-94-015-9819-4{_}4, URL `http://link.springer.com/10.1007/978-94-015-9819-4_4`

Gačić M, Civitarese G, Miserocchi S, Cardin V, Crise A, Mauri E (2002) The open-ocean convection in the Southern Adriatic: A controlling mechanism of the spring phytoplankton bloom. Continental Shelf Research 22(14):1897–1908, DOI 10.1016/S0278-4343(02)00050-X

García Lafuente J, Álvarez Fanjul E, Vargas JM, Ratsimandresy AW (2002) Subinertial variability in the flow through the Strait of Gibraltar. Journal of Geophysical Research: Oceans 107(10):3168, DOI 10.1029/2001jc001104, URL `http://doi.wiley.com/10.1029/2001JC001104`

García Lafuente J, Sánchez Román A, Díaz del Río G, Sannino G, Sánchez Garrido JC (2007) Recent observations of seasonal variability of the Mediterranean outflow in the Strait of Gibraltar. Journal of Geophysical Research: Oceans 112(10):1–11, DOI 10.1029/2006JC003992

García-Lafuente J, Delgado J, Sánchez Román A, Soto J, Carracedo L, Díaz del Río G (2009) Interannual variability of the Mediterranean outflow observed in Espartel sill, western Strait of Gibraltar. Journal of Geophysical Research 114(C10):C10,018, DOI 10.1029/2009JC005496, URL `http://doi.wiley.com/10.1029/2009JC005496`

García-Lafuente J, Sánchez-Román A, Naranjo C, Snchez-Garrido JC (2011) The very first transformation of the Mediterranean outflow in the Strait of Gibraltar. Journal of Geophysical Research: Oceans 116(7):1–7, DOI 10.1029/2011JC006967

García Lafuente J, Bruque Pozas E, Sánchez Garrido JC, Sannino G, Sammartino S (2013) The interface mixing layer and the tidal dynamics at the eastern part of the Strait of Gibraltar. Journal of Marine Systems 117-118:31–42, DOI 10.1016/j.jmarsys.2013.02.014, URL `http://dx.doi.org/10.1016/j.jmarsys.2013.02.014`

García-Lafuente J, Sammartino S, Sánchez-Garrido JC, Naranjo C (2018) Asymmetric Baroclinic Response to Tidal Forcing Along the Main Sill of the Strait of Gibraltar Inferred from Mooring Observations. Springer International Publishing, pp 193–210, DOI 10.1007/978-3-319-71934-4{_}14, URL `http://dx.doi.org/10.1007/978-3-319-71934-4_14http://link.springer.com/10.1007/978-3-319-71934-4_14`

García-Lafuente J, Sammartino S, Huertas IE, Flecha S, Sánchez-Leal RF, Naranjo C, Nadal I, Bellanco MJ (2021) Hotter and Weaker Mediterranean Outflow as a Response to Basin-Wide Alterations. Frontiers in Marine Science 8(March):1–16, DOI 10.3389/fmars.2021.613444, URL `https://www.frontiersin.org/articles/10.3389/fmars.2021.613444/full`

Gaspar P, Grégoris Y, Lefevre JM (1990) A simple eddy kinetic energy model for simulations of the oceanic vertical mixing: Tests at station Papa and long-term upper ocean study site. Journal of Geophysical Research 95(C9):16,179, DOI 10.1029/jc095ic09p16179

GEBCO Bathymetric Compilation Group (2022) The GEBCO_2022 Grid - a continuous terrain model of the global oceans and land. DOI 10.5285/e0f0bb80-ab44-2739-e053-6c86abc0289c

Georgiou S, Mantziafou A, Sofianos S, Gertman I, Özsoy E, Somot S, Vervatis V (2015) Climate variability and deep water mass characteristics in the Aegean Sea. Atmospheric Research 152:146–158, DOI 10.1016/j.atmosres.2014.07.023

Gertman I, Pinardi N, Popov Y, Hecht A (2006) Aegean sea water masses during the early stages of the Eastern Mediterranean Climatic Transient (1988-90). Journal of Physical Oceanography 36(9):1841–1859, DOI 10.1175/JPO2940.1

Giorgi F, Jones C, Asrar G (2009) Addressing climate information needs at the regional level: the CORDEX framework. ... Organization (WMO) Bulletin 58(July):175–183, URL `http://www.euro-cordex.net/uploads/media/Download_01.pdf`

Girton JB, Sanford TB (2003) Descent and modification of the overflow plume in the Denmark strait. Journal of Physical Oceanography 33(7):1351–1364, DOI 10.1175/1520-0485(2003)033⟨1351:DAMOTO⟩2.0.CO;2

Gökaşan E, Tur H, Ecevitoğlu B, Görüm T, Türker A, Tok B, Çağlak F, Birkan H, Şimşek M (2005) Evidence and implications of massive erosion along the Strait of Istanbul (Bosphorus). Geo-Marine Letters 25(5):324–342, DOI 10.1007/s00367-005-0216-3

Gökaşan E, Ergin M, Özyalvaç M, Sur HI, Tur H, Görüm T, Ustaömer T, Batuk FG, Alp H, Birkan H, Türker A, Gezgin E, Özturan M (2007) Factors controlling the morphological evolution of the Çanakkale Strait (Dardanelles, Turkey). Geo-Marine Letters 28(2):107–129, DOI 10.1007/s00367-007-0094-y

González CJ, Álvarez O, Mañanes R, Izquierdo A, Bruno M, Gomiz JJ, Chioua J, López L (2013) Baroclinic M 2 tidal circulation in Algeciras Bay and its implications for the water exchange with the Strait of Gibraltar: Observational and 3-D model results. Journal of Geophysical Research: Oceans 118(10):5398–5411, DOI 10.1002/jgrc.20404, URL `http://doi.wiley.com/10.1002/jgrc.20404`

Gonzalez N, Waldman R, Sannino G, Giordani H, Somot S (2023) Understanding tidal mixing at the Strait of Gibraltar: A high-resolution model approach. Progress in Oceanography 212:102,980, DOI 10.1016/j.pocean.2023.102980, URL `https://linkinghub.elsevier.com/retrieve/pii/S007966112300023X`

Gregg M, Nodland W, Aagaard E, Hirt D (1982) Use of a fiber-optic cable with a free-fall microstructure profiler. In: OCEANS 82, IEEE, vol 260, pp 260–265, DOI 10.1109/OCEANS.1982.1151839, URL `http://ieeexplore.ieee.org/document/1151839/`

Gregg MC, D'Asaro EA, Riley JJ, Kunze E (2018) Mixing efficiency in the ocean. Annual Review of Marine Science 10:443–473, DOI 10.1146/annurev-marine-121916-063643

Group M (2005) Morpho-bathymetry of the Mediterranean Sea. Ifremer

Hamon M, Beuvier J, Somot S, Lellouche JM, Greiner E, Jordà G, Bouin MN, Arsouze T, Béranger K, Sevault F, Dubois C, Drevillon M, Drillet Y (2016) Design and validation of MEDRYS, a Mediterranean Sea reanalysis over the period 1992-2013. Ocean Science 12(2):577–599, DOI 10.5194/os-12-577-2016, URL `https://os.copernicus.org/articles/12/577/2016/`

Harzallah A, Alioua M, Li L (2014) Mass exchange at the Strait of Gibraltar in response to tidal and lower frequency forcing as simulated by a Mediterranean Sea model. Tellus A: Dynamic Meteorology and Oceanography 66(1):23,871, DOI 10.3402/tellusa.v66.23871, URL `https://doi.org/10.3402/tellusa.v66.23871`

Harzallah A, Jordà G, Dubois C, Sannino G, Carillo A, Li L, Arsouze T, Cavicchia L, Beuvier J, Akhtar N (2018) Long term evolution of heat budget in the Mediterranean Sea from Med-CORDEX forced and coupled simulations. Climate Dynamics 51(3):1145–1165, DOI 10.1007/s00382-016-3363-5

Herrmann M, Somot S, Sevault F, Estournel C, Déqué M (2008) Modeling the deep convection in the northwestern Mediterranean sea using an eddy-permitting and an eddy-resolving model: Case study of winter 1986-1987. Journal of Geophysical Research: Oceans 113(4):1–25, DOI 10.1029/2006JC003991

Herrmann M, Sevault F, Beuvier J, Somot S (2010) What induced the exceptional 2005 convection event in the northwestern Mediterranean basin? Answers from a modeling study. Journal of Geophysical Research: Oceans 115(12), DOI 10.1029/2010JC006162

Herrmann M, Somot S, Calmanti S, Dubois C, Sevault F (2011) Representation of spatial and temporal variability of daily wind speed and of intense wind events over the Mediterranean Sea using dynamical downscaling: Impact of the regional climate model configuration. Natural Hazards and Earth System Science 11(7):1983–2001, DOI 10.5194/nhess-11-1983-2011

Hill AE, Mitchelson-Jacob EG (1993) Observations of a poleward-flowing saline core on the continental slope west of Scotland. Deep-Sea Research Part I 40(7):1521–1527, DOI 10.1016/0967-0637(93)90127-O

Hilt M, Auclair F, Benshila R, Bordois L, Capet X, Debreu L, Dumas F, Jullien S, Lemarié F, Marchesiello P, Nguyen C, Roblou L (2020) Numerical modelling of hydraulic control, solitary waves and primary instabilities in the Strait of Gibraltar. Ocean Modelling 151(May):101,642, DOI 10.1016/j.ocemod.2020.101642, URL `https://linkinghub.elsevier.com/retrieve/pii/S146350032030144X`

Hoskins JB (1982) The mathematical theory of frontogenesis. in: Annual Review of Fluid Mechanics 14 , M. Va(3611):131–151, DOI 10.1146/annurev.fl.14.010182.001023, URL `https://doi.org/10.1146/annurev.fl.14.010182.001023`

Hu A, Meehl GA, Han W, Otto-Bliestner B, Abe-Ouchi A, Rosenbloom N (2015) Effects of the Bering Strait closure on AMOC and global climate under different background climates. Progress in Oceanography 132:174–196, DOI 10.1016/j.pocean.2014.02.004, URL `http://dx.doi.org/10.1016/j.pocean.2014.02.004https://linkinghub.elsevier.com/retrieve/pii/S0079661114000172`

Huertas IE, Ríos AF, García-Lafuente J, Navarro G, Makaoui A, Sánchez-Román A, Rodriguez-Galvez S, Orbi A, Ruíz J, Pérez FF (2012a) Atlantic forcing of the Mediterranean oligotrophy. Global Biogeochemical Cycles 26(2):n/a–n/a, DOI 10.1029/2011GB004167, URL `http://doi.wiley.com/10.1029/2011GB004167`

Huertas IE, Ríos AF, García-Lafuente J, Navarro G, Makaoui A, Snchez-Romn A, Rodriguez-Galvez S, Orbi A, Ruíz J, Pérez FF (2012b) Atlantic forcing of the Mediterranean oligotrophy. Global Biogeochemical Cycles 26(2):1–9, DOI 10.1029/2011GB004167

Ienna F, Bashmachnikov I, Dias J (2022) Meddies and their Sea Surface Expressions: Observations and Theory. Journal of Physical Oceanography pp 2643–2656, DOI 10.1175/jpo-d-22-0081.1

Iorga MC, Lozier MS (1999a) Signatures of the Mediterranean outflow from a North Atlantic climatology 1. Salinity and density fields. Journal of Geophysical Research: Oceans 104(C11):25,985–26,009, DOI 10.1029/1999jc900115

Iorga MC, Lozier MS (1999b) Signatures of the Mediterranean outflow from a North Atlantic climatology: 2. Diagnostic velocity fields. Journal of Geophysical Research: Oceans 104(C11):26,011–26,029, DOI 10.1029/1999JC900204, URL `http://doi.wiley.com/10.1029/1999JC900204`

Itoh S, Yasuda I, Yagi M, Osafune S, Kaneko H, Nishioka J, Nakatsuka T, Volkov YN (2011) Strong vertical mixing in the Urup Strait. Geophysical Research Letters 38(16):n/a–n/a, DOI 10.1029/2011GL048507, URL `http://doi.wiley.com/10.1029/2011GL048507`

Ivanovic RF, Valdes PJ, Gregoire L, Flecker R, Gutjahr M (2014) Sensitivity of modern climate to the presence, strength and salinity of Mediterranean-Atlantic exchange in a global general circulation model. Climate Dynamics 42(3-4):859–877, DOI 10.1007/s00382-013-1680-5

Izquierdo A, Mikolajewicz U (2019) The role of tides in the spreading of Mediterranean Outflow waters along the southwestern Iberian margin. Ocean Modelling 133(August 2018):27–43, DOI 10.1016/j.ocemod.2018.08.003, URL `https://doi.org/10.1016/j.ocemod.2018.08.003`

Izquierdo A, Tejedor L, Sein DV, Backhaus JO, Brandt P, Rubino A, Kagan BA (2001) Control variability and internal bore evolution in the Strait of Gibraltar: A 2-D two-layer model study. Estuarine, Coastal and Shelf Science 53(5):637–651, DOI 10.1006/ecss.2000.0706

Jackett DR, Mcdougall TJ (1995) Minimal Adjustment of Hydrographic Profiles to Achieve Static Stability. Journal of Atmospheric and Oceanic Technology 12(2):381–389, DOI 10.1175/1520-0426(1995)012⟨0381:maohpt⟩2.0.co;2

Jackson PR, Rehmann CR (2014) Experiments on differential scalar mixing in turbulence in a sheared, stratified flow. Journal of Physical Oceanography 44(10):2661–2680, DOI 10.1175/JPO-D-14-0027.1

Jacobsen JP, Thomsen H (1934) Periodical variations in temperature and salinity in the Strait of Gibraltar. James Johnstone Memorial Volume pp 275–293

Jordà G, Sánchez-Román A, Gomis D (2017a) Reconstruction of transports through the Strait of Gibraltar from limited observations. Climate Dynamics 48(3-4):851–865, DOI 10.1007/s00382-016-3113-8, URL `http://link.springer.com/10.1007/s00382-016-3113-8`

Jordà G, Von Schuckmann K, Josey SA, Caniaux G, García-Lafuente J, Sammartino S, Özsoy E, Polcher J, Notarstefano G, Poulain PM, Adloff F, Salat J, Naranjo C, Schroeder K, Chiggiato J, Sannino G, Macías D (2017b) The Mediterranean Sea heat and mass budgets: Estimates, uncertainties and perspectives. Progress in Oceanography 156:174–208, DOI 10.1016/j.pocean.2017.07.001

Jouanno J, Sheinbaum J, Barnier B, Molines JM, Candela J (2012) Seasonal and interannual modulation of the eddy kinetic energy in the Caribbean sea. Journal of Physical Oceanography 42(11):2041–2055, DOI 10.1175/JPO-D-12-048.1

Kang D, Fringer O (2012) Energetics of barotropic and baroclinic tides in the Monterey Bay area. Journal of Physical Oceanography 42(2):272–290, DOI 10.1175/JPO-D-11-039.1

Kawasaki T, Hasumi H (2010) Role of localized mixing around the Kuril Straits in the Pacific thermohaline circulation. Journal of Geophysical Research 115(C11):C11,002, DOI 10.1029/2010JC006130, URL `http://doi.wiley.com/10.1029/2010JC006130`

Kida S, Price JF, Yang J (2008) The Upper-Oceanic Response to Overflows: A Mechanism for the Azores Current. Journal of Physical Oceanography 38(4):880–895, DOI 10.1175/2007JPO3750.1, URL `http://journals.ametsoc.org/doi/10.1175/2007JPO3750.1`

Kinder T, Parilla G (1987) Yes, some of the Mediterranean outflow does come from great depth. Journal of Geophysical Research: Oceans 92(C3):2901–2906, DOI 10.1029/JC092iC03p02901

Kinder TH, Bryden HL (1990) Aspiration of Deep Waters through Straits. In: Pratt LJ (ed) The Physical Oceanography of Sea Straits, Springer Netherlands, Dordrecht, pp 295–319, DOI 10.1007/978-94-009-0677-8{_}14, URL `https://doi.org/10.1007/978-94-009-0677-8_14`

Koch-Larrouy A, Lengaigne M, Terray P, Madec G, Masson S (2010) Tidal mixing in the Indonesian Seas and its effect on the tropical climate system. Climate Dynamics 34(6):891–904, DOI 10.1007/s00382-009-0642-4, URL `http://link.springer.com/10.1007/s00382-009-0642-4`

Kolmogorov AN (1942) Equations of turbulent motion in an incompressible fluid. Dokl Akad Nauk SSSR pp 56–58

Kurkin A, Kurkina O, Rybin A, Talipova T (2020) Comparative analysis of the first baroclinic Rossby radius in the Baltic, Black, Okhotsk, and Mediterranean seas. Russian Journal of Earth Sciences 20(4):1–10, DOI 10.2205/2020ES000737

La Violette PE, Lacombe H (1988) Tidal-induced pulses in the flow through the Strait of Gibraltar. Oceanologica Acta d(Special Issue):13–27

Lacombe H, Richez C (1982) The regime of the strait of gibraltar. Elsevier Oceanography Series 34(C):13–73, DOI 10.1016/S0422-9894(08)71237-6

Lafuente JG, Almazan JL, Castillejo F, Khribeche A, Hakimi A (1990) Sea level in the Strait of Gibraltar: tides. Int Hydrographic Rev 67(1 , Jan., 1990):111–125

Lafuente JG, Vargas JM, Plaza F, Sarhan T, Candela J, Bascheck B (2000) Tide at the eastern section of the Strait of Gibraltar. Journal of Geophysical Research: Oceans 105(C6):14,197–14,213, DOI 10.1029/2000jc900007

Lafuente JG, Delgado J, Vargas JM, Vargas M, Plaza F, Sarhan T (2002) Low-frequency variability of the exchanged flows through the Strait of Gibraltar during CANIGO. Deep Sea Research Part II: Topical Studies in Oceanography 49(19):4051–4067, DOI 10.1016/S0967-0645(02)00142-X, URL `https://linkinghub.elsevier.com/retrieve/pii/S096706450200142X`

Lahaye N, Gula J, Roullet G (2020) Internal Tide Cycle and Topographic Scattering Over the North Mid-Atlantic Ridge. Journal of Geophysical Research: Oceans 125(12):1–21, DOI 10.1029/2020JC016376, URL `https://onlinelibrary.wiley.com/doi/10.1029/2020JC016376`

Large WG, Yeager SG (2004) Diurnal to decadal global forcing for ocean and sea-ice models: The data sets and flux climatologies. NCAR Tech Note TN–460+ST(May):105pp, DOI 10.5065/D6KK98Q6

Lascaratos A, Roether W, Nittis K, Klein B (1999) Recent changes in deep water formation and spreading in the Eastern Mediterranean Sea: A review. Progress in Oceanography 44(1-3):5–36, DOI 10.1016/S0079-6611(99)00019-1

de Lavergne C, Madec G, Le Sommer J, Nurser AJG, Naveira Garabato AC (2016) The Impact of a Variable Mixing Efficiency on the Abyssal Overturning. Journal of Physical Oceanography 46(2):663–681, DOI 10.1175/JPO-D-14-0259.1, URL `https://journals.ametsoc.org/view/journals/phoc/46/2/jpo-d-14-0259.1.xml`

de Lavergne C, Falahat S, Madec G, Roquet F, Nycander J, Vic C (2019) Toward global maps of internal tide energy sinks. Ocean Modelling 137(April):52–75, DOI 10.1016/j.ocemod.2019.03.010, URL `https://doi.org/10.1016/j.ocemod.2019.03.010`

de Lavergne C, Vic C, Madec G, Roquet F, Waterhouse AF, Whalen CB, Cuypers Y, Bouruet-Aubertot P, Ferron B, Hibiya T (2020) A Parameterization of Local and Remote Tidal Mixing. Journal of Advances in Modeling Earth Systems 12(5), DOI 10.1029/2020MS002065, URL `https://doi.org/10.1029/2020MS002065`

Le Moigne P, Colin J, Colin J, Decharme B (2016) Impact of lake surface temperatures simulated by the FLake scheme in the CNRM-CM5 climate model. Tellus A: Dynamic Meteorology and Oceanography 68(1):31,274, DOI 10.3402/tellusa.v68.31274, URL `https://a.tellusjournals.se/article/10.3402/tellusa.v68.31274/`

Le Sommer J, Penduff T, Theetten S, Madec G, Barnier B (2009) How momentum advection schemes influence current-topography interactions at eddy permitting resolution. Ocean Modelling 29(1):1–14, DOI 10.1016/j.ocemod.2008.11.007, URL `http://dx.doi.org/10.1016/j.ocemod.2008.11.007`

Lee T, Fukumori I, Menemenlis D, Xing Z, Fu LL (2002) Effects of the Indonesian Throughflow on the Pacific and Indian Oceans. Journal of Physical Oceanography 32(5):1404–1429, DOI 10.1175/1520-0485(2002)032⟨1404:EOTITO⟩2.0.CO;2, URL `http://journals.ametsoc.org/doi/10.1175/1520-0485(2002)032%3C1404:EOTITO%3E2.0.CO;2`

Lefauve A, Muller C, Melet A (2015) A three-dimensional map of tidal dissipation over abyssal hills. Journal of Geophysical Research: Oceans 120(7):4760–4777, DOI 10.1002/2014JC010598, URL `http://doi.wiley.com/10.1002/2014JC010598`

Legg S, Jackson L, Hallberg RW (2008) Eddy-resolving modeling of overflows. In: Ocean Modeling in an Eddying Regime, pp 63–81, DOI 10.1029/177GM06, URL `https://onlinelibrary.wiley.com/doi/10.1029/177GM06`

Legg S, Briegleb B, Chang Y, Chassignet EP, Danabasoglu G, Ezer T, Gordon AL, Griffies S, Hallberg R, Jackson L, Large W, Özgökmen TM, Peters H, Price J, Riemenschneider U, Wu W, Xu X, Yang J (2009) Improving Oceanic Overflow Representation in Climate Models: The Gravity Current Entrainment Climate Process Team. Bulletin of the American Meteorological Society 90(5):657–670, DOI 10.1175/2008BAMS2667.1, URL `https://journals.ametsoc.org/doi/10.1175/2008BAMS2667.1`

Llasses J, Jordà G, Gomis D, Adloff F, Macías D, Harzallah A, Arsouze T, Akthar N, Li L, Elizalde A, Sannino G (2018) Heat and salt redistribution within the Mediterranean Sea in the Med-CORDEX model ensemble. Climate Dynamics 51(3):1119–1143, DOI 10.1007/s00382-016-3242-0

Lozier MS, Stewart NM (2008) On the temporally varying northward penetration of mediterranean overflow water and eastward penetration of Labrador sea water. Journal of Physical Oceanography 38(9):2097–2103, DOI 10.1175/2008JPO3908.1

Lozier MS, Li F, Bacon S, Bahr F, Bower AS, Cunningham SA, De Jong MF, De Steur L, DeYoung B, Fischer J, Gary SF, Greenan BJ, Holliday NP, Houk A, Houpert L, Inall ME, Johns WE, Johnson HL, Johnson C, Karstensen J, Koman G, Le Bras IA, Lin X, Mackay N, Marshall DP, Mercier H, Oltmanns M, Pickart RS, Ramsey AL, Rayner D, Straneo F, Thierry V, Torres DJ, Williams RG, Wilson C, Yang J, Yashayaev I, Zhao J (2019) A sea change in our view of overturning in the subpolar North Atlantic. Science 363(6426):516–521, DOI 10.1126/science.aau6592

Lučić D, Ljubešić Z, Babić I, Bosak S, Cetinić I, Vilibić I, Mihanović H, Hure M, Njire J, Lučić P, Kružić P (2017) Unusual winter zooplankton bloom in the open southern Adriatic sea. Turkish Journal of Zoology 41(6):1024–1035, DOI 10.3906/zoo-1702-17

Ludwig W, Dumont E, Meybeck M, Heussner S (2009) River discharges of water and nutrients to the Mediterranean and Black Sea: Major drivers for ecosystem changes during past and future decades? Progress in Oceanography 80(3-4):199–217, DOI 10.1016/j.pocean.2009.02.001, URL `http://dx.doi.org/10.1016/j.pocean.2009.02.001`

Lyard F, Lefevre F, Letellier T, Francis O (2006) Modelling the global ocean tides: Modern insights from FES2004. Ocean Dynamics 56(5-6):394–415, DOI 10.1007/s10236-006-0086-x

Lyard FH, Allain DJ, Cancet M, Carrère L, Picot N (2021) FES2014 global ocean tide atlas: design and performance. Ocean Science 17(3):615–649, DOI 10.5194/os-17-615-2021, URL `https://os.copernicus.org/articles/17/615/2021/`

Macias D, García CM, Echevarría Navas F, Vázquez-López-Escobar A, Bruno Mejías M (2006) Tidal induced variability of mixing processes on Camarinal Sill (Strait of Gibraltar): A pulsating event. Journal of Marine Systems 60(1-2):177–192, DOI 10.1016/j.jmarsys.2005.12.003, URL `https://linkinghub.elsevier.com/retrieve/pii/S0924796305002095`

Macías D, Martin A, García-Lafuente J, García C, Yool A, Bruno M, Vázquez-Escobar A, Izquierdo A, Sein D, Echevarría F (2007) Analysis of mixing and biogeochemical effects induced by tides on the Atlantic–Mediterranean flow in the Strait of Gibraltar through a physical–biological coupled model. Progress in Oceanography 74(2-3):252–272, DOI 10.1016/j.pocean.2007.04.006, URL `https://linkinghub.elsevier.com/retrieve/pii/S0079661107000699`

Madec G (2016) NEMO ocean engine, version 3.6 stable. Note du Pole de modelisation de l'Institut Pierre-Simon Laplace 27

Durrieu de Madron X, Guieu C, Sempéré R, Conan P, Cossa D, D'Ortenzio F, Estournel C, Gazeau F, Rabouille C, Stemmann L, Bonnet S, Diaz F, Koubbi P, Radakovitch O, Babin M, Baklouti M, Bancon-Montigny C, Belviso S, Bensoussan N, Bonsang B, Bouloubassi I, Brunet C, Cadiou JF, Carlotti F, Chami M, Charmasson S, Charrière B, Dachs J, Doxaran D, Dutay JC, Elbaz-Poulichet F, Eléaume M, Eyrolles F, Fernandez C, Fowler S, Francour P, Gaertner J, Galzin R, Gasparini S, Ghiglione JF, Gonzalez JL, Goyet C, Guidi L, Guizien K, Heimbürger LE, Jacquet S, Jeffrey W, Joux F, Le Hir P, Leblanc K, Lefèvre D, Lejeusne C, Lemé R, Loÿe-Pilot MD, Mallet M, Méjanelle L, Mélin F, Mellon C, Mérigot B, Merle PL, Migon C, Miller W, Mortier L, Mostajir B, Mousseau L, Moutin T, Para J, Pérez T, Petrenko A, Poggiale JC, Prieur L, Pujo-Pay M, Pulido-Villena, Raimbault P, Rees A, Ridame C, Rontani JF, Ruiz Pino D, Sicre M, Taillandier V, Tamburini C, Tanaka T, Taupier-Letage I, Tedetti M, Testor P, Thébault H, Thouvenin B, Touratier F, Tronczynski J, Ulses C, Van Wambeke F, Vantrepotte V, Vaz S, Verney R (2011) Marine ecosystems' responses to climatic and anthropogenic forcings in the Mediterranean. Progress in Oceanography 91(2):97–166, DOI 10.1016/j.pocean.2011.02.003, URL `http://dx.doi.org/10.1016/j.pocean.2011.02.003https://linkinghub.elsevier.com/retrieve/pii/S0079661111000188`

Mamoutos IG, Potiris E, Tragou E, Zervakis V, Petalas S (2021) A high-resolution numerical model of the north aegean sea aimed at climatological studies. Journal of Marine Science and Engineering 9(12), DOI 10.3390/jmse9121463

Manca B, Ibello V, Pacciaroni M, Scarazzato P, Giorgetti A (2006) Ventilation of deep waters in the Adriatic and Ionian Seas following changes in thermohaline circulation of the Eastern Mediterranean. Climate Research 31(2-3):239–256, DOI 10.3354/cr031239, URL `http://www.int-res.com/abstracts/cr/v31/n2/p239-256/`

Mantziafou A, Lascaratos A (2004) An eddy resolving numerical study of the general circulation and deep-water formation in the Adriatic Sea. Deep-Sea Research Part I: Oceanographic Research Papers 51(7):921–952, DOI 10.1016/j.dsr.2004.03.006

Mantziafou A, Lascaratos A (2008) Deep-water formation in the Adriatic Sea: Interannual simulations for the years 1979–1999. Deep Sea Research Part I: Oceanographic Research Papers 55(11):1403–1427, DOI 10.1016/j.dsr.2008.06.005, URL `https://linkinghub.elsevier.com/retrieve/pii/S0967063708001258`

Marshall J, Adcroft A, Hill C, Perelman L, Heisey C (1997a) A finite-volume, incompressible navier stokes model for, studies of the ocean on parallel computers. Journal of Geophysical Research C: Oceans 102(C3):5753–5766, DOI 10.1029/96JC02775

Marshall J, Hill C, Perelman L, Adcroft A (1997b) Hydrostatic, quasi-hydrostatic, and nonhydrostatic ocean modeling. Journal of Geophysical Research C: Oceans 102(C3):5733–5752, DOI 10.1029/96JC02776

Masson V, Le Moigne P, Martin E, Faroux S, Alias A, Alkama R, Belamari S, Barbu A, Boone A, Bouyssel F, Brousseau P, Brun E, Calvet JC, Carrer D, Decharme B, Delire C, Donier S, Essaouini K, Gibelin AL, Giordani H, Habets F, Jidane M, Kerdraon G, Kourzeneva E, Lafaysse M, Lafont S, Lebeaupin Brossier C, Lemonsu A, Mahfouf JF, Marguinaud P, Mokhtari M, Morin S, Pigeon G, Salgado R, Seity Y, Taillefer F, Tanguy G, Tulet P, Vincendon B, Vionnet V, Voldoire A (2013) The SURFEXv7.2 land and ocean surface platform for coupled or offline simulation of earth surface variables and fluxes. Geoscientific Model Development 6(4):929–960, DOI 10.5194/gmd-6-929-2013

Matte D, Laprise R, Thériault JM, Lucas-Picher P (2017) Spatial spin-up of fine scales in a regional climate model simulation driven by low-resolution boundary conditions. Climate Dynamics 49(1-2):563–574, DOI 10.1007/s00382-016-3358-2, URL `http://link.springer.com/10.1007/s00382-016-3358-2`

McCartney MS, Mauritzen C (2001) On the origin of the warm inflow to the Nordic Seas. Progress in Oceanography 51(1):125–214, DOI 10.1016/S0079-6611(01)00084-2

McDougall TJ (1987) Neutral Surfaces. Journal of Physical Oceanography 17(11):1950–1964, DOI 10.1175/1520-0485(1987)017⟨1950:ns⟩2.0.co;2, URL `http://journals.ametsoc.org/doi/10.1175/1520-0485(1987)017%3C1950:NS%3E2.0.CO;2`

MEDOC GROUP (1970) Observation of Formation of Deep Water in the Mediterranean Sea, 1969. Nature 227(5262):1037–1040, DOI 10.1038/2271037a0, URL `https://doi.org/10.1038/2271037a0https://www.nature.com/articles/2271037a0`

Mesinger F, Arakawa A (1976) Numerical methods used in atmospheric models, volume 1. Global Atmospheric Research Program World Meteorological Organization 1(17):1–65

Middleton JF, Cirano M (2005) Wintertime circulation off southeast Australia: Strong forcing by the East Australian Current. Journal of Geophysical Research: Oceans 110(12):1–12, DOI 10.1029/2004JC002855

Millot C (2007) Interannual salinification of the Mediterranean inflow. Geophysical Research Letters 34(21):L21,609, DOI 10.1029/2007GL031179, URL `http://doi.wiley.com/10.1029/2007GL031179`

Millot C (2009) Another description of the Mediterranean Sea outflow. Progress in Oceanography 82(2):101–124, DOI 10.1016/j.pocean.2009.04.016, URL `http://dx.doi.org/10.1016/j.pocean.2009.04.016https://linkinghub.elsevier.com/retrieve/pii/S0079661109000366`

Millot C, Taupier-Letage I (2005) Circulation in the Mediterranean Sea. In: Life in the Mediterranean Sea: A Look at Habitat Changes, vol 5, pp 29–66, DOI 10.1007/b107143, URL `http://link.springer.com/10.1007/b107143`

Millot C, Candela J, Fuda JL, Tber Y (2006) Large warming and salinification of the Mediterranean outflow due to changes in its composition. Deep-Sea Research Part I: Oceanographic Research Papers 53(4):656–666, DOI 10.1016/j.dsr.2005.12.017

Morozov EG, Trulsen K, Velarde MG, Vlasenko VI (2002) Internal tides in the Strait of Gibraltar. Journal of Physical Oceanography 32(11):3193–3206, DOI 10.1175/1520-0485(2002)032⟨3193:ITITSO⟩2.0.CO;2, URL `http://journals.ametsoc.org/doi/10.1175/1520-0485(2002)032%3C3193:ITITSO%3E2.0.CO;2`

Nabat P, Somot S, Mallet M, Sevault F, Chiacchio M, Wild M (2015) Direct and semi-direct aerosol radiative effect on the Mediterranean climate variability using a coupled regional climate system model. Climate Dynamics 44(3-4):1127–1155, DOI 10.1007/s00382-014-2205-6

Nabat P, Somot S, Cassou C, Mallet M, Michou M, Bouniol D, Decharme B, Drugé T, Roehrig R, Saint-martin D (2020) Modulation of radiative aerosols effects by atmospheric circulation over the Euro-Mediterranean region pp 8315–8349

Nagy H, Di Lorenzo E, El-Gindy A (2019) The impact of climate change on circulation patterns in the Eastern Mediterranean Sea upper layer using Med-ROMS model. Progress in Oceanography 175(April 2018):226–244, DOI 10.1016/j.pocean.2019.04.012, URL `https://linkinghub.elsevier.com/retrieve/pii/S0079661118300958`

Nakamura T, Toyoda T, Ishikawa Y, Awaji T (2004) Tidal Mixing in the Kuril Straits and Its Impact on Ventilation in the North Pacific Ocean. Journal of Oceanography 60(2):411–423, DOI 10.1023/B:JOCE.0000038225.15056.c6, URL `http://link.springer.com/10.1023/B:JOCE.0000038225.15056.c6`

Naranjo C, García Lafuente J, Sánchez Garrido JC, Sánchez Román A, Delgado Cabello J (2012) The Western Alboran Gyre helps ventilate the Western Mediterranean Deep Water through Gibraltar. Deep Sea Research Part I: Oceanographic Research Papers 63:157–163, DOI 10.1016/j.dsr.2011.10.003, URL `https://linkinghub.elsevier.com/retrieve/pii/S0967063711001919`

Naranjo C, Garcia-Lafuente J, Sannino G, Sanchez-Garrido JC (2014) How much do tides affect the circulation of the Mediterranean Sea? From local processes in the Strait of Gibraltar to basin-scale effects. Progress in Oceanography 127:108–116, DOI 10.1016/j.pocean.2014.06.005

Naranjo C, Sammartino S, García-Lafuente J, Bellanco MJ, Taupier-Letage I (2015) Mediterranean waters along and across the Strait of Gibraltar, characterization and zonal modification. Deep-Sea Research Part I: Oceanographic Research Papers 105:41–52, DOI 10.1016/j.dsr.2015.08.003, URL `http://dx.doi.org/10.1016/j.dsr.2015.08.003`

Naranjo C, García-Lafuente J, Sammartino S, Sánchez-Garrido JC, Sánchez-Leal R, Jesús Bellanco M (2017) Recent changes (2004-2016) of temperature and salinity in the Mediterranean outflow. Geophysical Research Letters 44(11):5665–5672, DOI 10.1002/2017GL072615, URL `http://doi.wiley.com/10.1002/2017GL072615`

Nittis K, Lascaratos A, Theocharis A (2003) Dense water formation in the Aegean Sea: Numerical simulations during the Eastern Mediterranean Transient. Journal of Geophysical Research: Oceans 108(9):1–15, DOI 10.1029/2002jc001352

Oddo P, Pinardi N, Zavatarelli M (2005) A numerical study of the interannual variability of the Adriatic Sea (2000-2002). Science of the Total Environment 353(1-3):39–56, DOI 10.1016/j.scitotenv.2005.09.061

Oddo P, Adani M, Pinardi N, Fratianni C, Tonani M, Pettenuzzo D (2009) A nested Atlantic-Mediterranean Sea general circulation model for operational forecasting. Ocean Science 5(4):461–473, DOI 10.5194/os-5-461-2009, URL `https://os.copernicus.org/articles/5/461/2009/`

Ono K, Ohshima KI, Kono T, Itoh M, Katsumata K, Volkov YN, Wakatsuchi M (2007) Water mass exchange and diapycnal mixing at Bussol' Strait revealed by water mass properties. Journal of Oceanography 63(2):281–291, DOI 10.1007/s10872-007-0028-3, URL `https://link.springer.com/10.1007/s10872-007-0028-3`

Osborn TR (1980) Estimates of the Local Rate of Vertical Diffusion from Dissipation Measurements. Journal of Physical Oceanography 10(1):83–89, DOI 10.1175/1520-0485(1980)010⟨0083:eotlro⟩2.0.co;2, URL `https://doi.org/10.1175/1520-0485(1980)010%3C0083:EOTLRO%3E2.0.CO;2`

Palma M, Iacono R, Sannino G, Bargagli A, Carillo A, Fekete BM, Lombardi E, Napolitano E, Pisacane G, Struglia MV (2020) Short-term, linear, and non-linear local effects of the tides on the surface dynamics in a new, high-resolution model of the Mediterranean Sea circulation. Ocean Dynamics 70(7):935–963, DOI 10.1007/s10236-020-01364-6

Parras-Berrocal IM, Vázquez R, Cabos W, Sein DV, Álvarez O, Bruno M, Izquierdo A (2022) Surface and Intermediate Water Changes Triggering the Future Collapse of Deep Water Formation in the North Western Mediterranean. Geophysical Research Letters 49(4):1–10, DOI 10.1029/2021GL095404, URL `https://onlinelibrary.wiley.com/doi/10.1029/2021GL095404`

Pawlowicz R, Beardsley B, Lentz S (2002) Classical tidal harmonic analysis including error estimates in MATLAB using T_TIDE. Computers & Geosciences 28(8):929–937, DOI 10.1016/S0098-3004(02)00013-4, URL `https://linkinghub.elsevier.com/retrieve/pii/S0098300402000134`

Peliz A, Dubert J, Marchesiello P, Teles-Machado A (2007) Surface circulation in the Gulf of Cadiz: Model and mean flow structure. Journal of Geophysical Research 112(C11):C11,015, DOI 10.1029/2007JC004159, URL `http://doi.wiley.com/10.1029/2007JC004159`

Peliz A, Marchesiello P, Santos AMP, Dubert J, Teles-Machado A, Marta-Almeida M, Le Cann B (2009) Surface circulation in the Gulf of Cadiz: 2. Inflow-outflow coupling and the Gulf of Cadiz slope current. Journal of Geophysical Research 114(C3):C03,011, DOI 10.1029/2008JC004771, URL `http://doi.wiley.com/10.1029/2008JC004771`

Peliz A, Boutov D, Cardoso RM, Delgado J, Soares PM (2013) The Gulf of Cadiz–Alboran Sea sub-basin: Model setup, exchange and seasonal variability. Ocean Modelling 61:49–67, DOI 10.1016/j.ocemod.2012.10.007, URL `https://linkinghub.elsevier.com/retrieve/pii/S1463500313001182https://linkinghub.elsevier.com/retrieve/pii/S1463500312001527`

Penduff T, Le Sommer J, Barnier B, Treguier AM, Molines JM, Madec G (2007) Influence of numerical schemes on current-topography interactions in 1/4° global ocean simulations. Ocean Science 3(4):509–524, DOI 10.5194/os-3-509-2007, URL `https://os.copernicus.org/articles/3/509/2007/`

Peters H, Johns WE, Bower AS, Fratantoni DM (2005) Mixing and entrainment in the Red Sea outflow plume. Part I: Plume structure. Journal of Physical Oceanography 35(5):569–583, DOI 10.1175/JPO2679.1, URL `http://journals.ametsoc.org/doi/10.1175/JPO2679.1`

Petrusevich VY, Dmitrenko IA, Kozlov IE, Kirillov SA, Kuzyk ZZA, Komarov AS, Heath JP, Barber DG, Ehn JK (2018) Tidally-generated internal waves in Southeast Hudson Bay. Continental Shelf Research 167(August):65–76, DOI 10.1016/j.csr.2018.08.002, URL `https://doi.org/10.1016/j.csr.2018.08.002https://linkinghub.elsevier.com/retrieve/pii/S0278434317306350`

Pettigrew NR, Hyde RA (1990) The Structure of the Internal Bore in the Strait of Gibraltar and its Influence on the Atlantic Inflow. In: The Physical Oceanography of Sea Straits, Springer Netherlands, Dordrecht, pp 493–508, DOI 10.1007/978-94-009-0677-8{_}24, URL `http://link.springer.com/10.1007/978-94-009-0677-8_24`

Philander SGH, Pacanowski RC (1980) The generation of equatorial currents. Journal of Geophysical Research 85(C2):1123, DOI 10.1029/jc085ic02p01123

Pichevin T, Nof D (1996) The eddy cannon. Deep Sea Research Part I: Oceanographic Research Papers 43(9):1475–1507, DOI 10.1016/S0967-0637(96)00064-7, URL `https://linkinghub.elsevier.com/retrieve/pii/S0967063796000647`

Pinardi N, Masetti E (2000) Variability of the large scale general circulation of the Mediterranean Sea from observations and modelling: A review. Palaeogeography, Palaeoclimatology, Palaeoecology 158(3-4):153–173, DOI 10.1016/S0031-0182(00)00048-1

Pinardi N, Zavatarelli M, Adani M, Coppini G, Fratianni C, Oddo P, Simoncelli S, Tonani M, Lyubartsev V, Dobricic S, Bonaduce A (2015) Mediterranean Sea large-scale low-frequency ocean variability and water mass formation rates from 1987 to 2007: A retrospective analysis. Progress in Oceanography 132:318–332, DOI 10.1016/j.pocean.2013.11.003, URL `http://dx.doi.org/10.1016/j.pocean.2013.11.003https://linkinghub.elsevier.com/retrieve/pii/S007966111300222X`

Potter RA, Lozier MS (2004) On the warming and salinification of the Mediterranean outflow waters in the North Atlantic. Geophysical Research Letters 31(1):1–4, DOI 10.1029/2003GL018161

Prandtl L (1949) Report on investigation of developed turbulence. NACA Report TM-1231 1231:1–8

Purwandana A, Cuypers Y, Bouruet-Aubertot P, Nagai T, Hibiya T, Atmadipoera AS (2020) Spatial structure of turbulent mixing inferred from historical CTD datasets in the Indonesian seas. Progress in Oceanography 184(June 2019):102,312, DOI 10.1016/j.pocean.2020.102312, URL `https://doi.org/10.1016/j.pocean.2020.102312https://linkinghub.elsevier.com/retrieve/pii/S0079661120300513`

Purwandana A, Cuypers Y, Bouruet-Aubertot P (2021) Observation of internal tides, nonlinear internal waves and mixing in the Lombok Strait, Indonesia. Continental Shelf Research 216(December 2020):104,358, DOI 10.1016/j.csr.2021.104358, URL `https://doi.org/10.1016/j.csr.2021.104358https://linkinghub.elsevier.com/retrieve/pii/S0278434321000157`

Ramírez-Romero E, Macías D, García CM, Bruno M (2014) Biogeochemical patterns in the Atlantic Inflow through the Strait of Gibraltar. Deep-Sea Research Part I: Oceanographic Research Papers 85:88–100, DOI 10.1016/j.dsr.2013.12.004, URL `http://dx.doi.org/10.1016/j.dsr.2013.12.004`

Reid JL (1979) On the contribution of the Mediterranean Sea outflow to the Norwegian-Greenland Sea. Deep Sea Research Part A, Oceanographic Research Papers 26(11):1199–1223, DOI 10.1016/0198-0149(79)90064-5, URL `https://linkinghub.elsevier.com/retrieve/pii/0198014979900645`

Renault L, Oguz T, Pascual A, Vizoso G, Tintore J (2012) Surface circulation in the Alborn Sea (western Mediterranean) inferred from remotely sensed data. Journal of Geophysical Research: Oceans 117(8):1–11, DOI 10.1029/2011JC007659

Richardson PL, Bower AS, Zenk W (2000) A census of Meddies tracked by floats. Progress in Oceanography 45(2):209–250, DOI 10.1016/S0079-6611(99)00053-1

Richez C (1994) Airborne synthetic aperture radar tracking of internal waves in the Strait of Gibraltar. Progress in Oceanography 33(2):93–159, DOI 10.1016/0079-6611(94)90023-X, URL `https://linkinghub.elsevier.com/retrieve/pii/007966119490023X`

Richon C, Dutay JC, Bopp L, Le Vu B, Orr JC, Somot S, Dulac F (2019) Biogeochemical response of the Mediterranean Sea to the transient SRES-A2 climate change scenario. Biogeosciences 16(1):135–165, DOI 10.5194/bg-16-135-2019

Roether W, Manca BB, Klein B, Bregant D, Georgopoulos D, Beitzel V, Kovačević V, Luchetta A (1996) Recent changes in eastern Mediterranean deep waters. Science 271(5247):333–335, DOI 10.1126/science.271.5247.333, URL `https://www.science.org/doi/10.1126/science.271.5247.333`

Romero-Cózar J, Chioua J, Bolado-Penagos M, Reyes-Pérez J, Gómiz-Pascual JJ, Vázquez Sirviente S, Bruno M (2021) Tidally-induced submesoscale features in the atlantic jet and Western Alboran Gyre. A study based on HF radar and satellite images. Estuarine, Coastal and Shelf Science 250:107,122, DOI 10.1016/j.ecss.2020.107122, URL `https://doi.org/10.1016/j.ecss.2020.107122`

Rouchy JM, Caruso A (2006) The Messinian salinity crisis in the Mediterranean basin: A reassessment of the data and an integrated scenario. Sedimentary Geology 188-189:35–67, DOI 10.1016/j.sedgeo.2006.02.005, URL `https://linkinghub.elsevier.com/retrieve/pii/S0037073806000467`

Roullet G, Madec G (2000) Salt conservation, free surface, and varying levels: A new formulation for ocean general circulation models. Journal of Geophysical Research: Oceans 105(C10):23,927–23,942, DOI 10.1029/2000jc900089

Ruti PM, Somot S, Giorgi F, Dubois C, Flaounas E, Obermann A, Dell'Aquila A, Pisacane G, Harzallah A, Lombardi E, Ahrens B, Akhtar N, Alias A, Arsouze T, Aznar R, Bastin S, Bartholy J, Béranger K, Beuvier J, Bouffies-Cloché S, Brauch J, Cabos W, Calmanti S, Calvet JC, Carillo A, Conte D, Coppola E, Djurdjevic V, Drobinski P, Elizalde-Arellano A, Gaertner M, Galàn P, Gallardo C, Gualdi S, Goncalves M, Jorba O, Jordà G, L'Heveder B, Lebeaupin-Brossier C, Li L, Liguori G, Lionello P, Maciàs D, Nabat P, Önol B, Raikovic B, Ramage K, Sevault F, Sannino G, Struglia MV, Sanna A, Torma C, Vervatis V (2016) Med-CORDEX initiative for Mediterranean climate studies. Bulletin of the American Meteorological Society 97(7):1187–1208, DOI 10.1175/BAMS-D-14-00176.1, URL `https://journals.ametsoc.org/doi/10.1175/BAMS-D-14-00176.1`

Sammartino S, García Lafuente J, Sánchez Garrido JC, De los Santos FJ, Álvarez Fanjul E, Naranjo C, Bruno M, Calero C (2014) A numerical model analysis of the tidal flows in the Bay of Algeciras, Strait of Gibraltar. Continental Shelf Research 72:34–46, DOI 10.1016/j.csr.2013.11.002, URL `http://dx.doi.org/10.1016/j.csr.2013.11.002`

Sammartino S, García Lafuente J, Naranjo C, Sánchez Garrido JC, Sánchez Leal R, Sánchez Román A (2015) Ten years of marine current measurements in Espartel Sill, Strait of Gibraltar. Journal of Geophysical Research: Oceans 120(9):6309–6328, DOI 10.1002/2014JC010674

Sánchez Garrido JC, García Lafuente J, Criado Aldeanueva F, Baquerizo A, Sannino G (2008) Time-spatial variability observed in velocity of propagation of the internal bore in the Strait of Gibraltar. Journal of Geophysical Research: Oceans 113(7):1–6, DOI 10.1029/2007JC004624

Sanchez-Garrido JC, Sannino G, Liberti L, García Lafuente J, Pratt L (2011) Numerical modeling of three-dimensional stratified tidal flow over Camarinal Sill, Strait of Gibraltar. Journal of Geophysical Research: Oceans 116(12):1–17, DOI 10.1029/2011JC007093

Sánchez-Garrido JC, García Lafuente J, Álvarez Fanjul E, Sotillo MG, de los Santos FJ (2013) What does cause the collapse of the western alboran gyre? results of an operational ocean model. Progress in Oceanography 116:142–153, DOI 10.1016/j.pocean.2013.07.002, URL `http://dx.doi.org/10.1016/j.pocean.2013.07.002`

Sánchez-Román A, Criado-Aldeanueva F, García-Lafuente J, Sánchez J (2008) Vertical structure of tidal currents over Espartel and Camarinal sills, Strait of Gibraltar. Journal of Marine Systems 74(1-2):120–133, DOI 10.1016/j.jmarsys.2007.11.007, URL `http://dx.doi.org/10.1016/j.jmarsys.2007.11.007https://linkinghub.elsevier.com/retrieve/pii/S0924796307002333`

Sánchez-Román A, Sannino G, García-Lafuente J, Carillo A, Criado-Aldeanueva F (2009) Transport estimates at the western section of the Strait of Gibraltar: A combined experimental and numerical modeling study. Journal of Geophysical Research: Oceans 114(6), DOI 10.1029/2008JC005023

Sánchez-Román A, García-Lafuente J, Delgado J, Sánchez-Garrido JC, Naranjo C (2012) Spatial and temporal variability of tidal flow in the Strait of Gibraltar. Journal of Marine Systems 98-99:9–17, DOI 10.1016/j.jmarsys.2012.02.011, URL `http://dx.doi.org/10.1016/j.jmarsys.2012.02.011`

Sanchez-Roman A, Jorda G, Sannino G, Gomis D (2018) Modelling study of transformations of the exchange flows along the Strait of Gibraltar. Ocean Science 14(6):1547–1566, DOI 10.5194/os-14-1547-2018

Sannino G, Bargagli A, Artale V (2002) Numerical modeling of the mean exchange through the Strait of Gibraltar. Journal of Geophysical Research: Oceans 107(8), DOI 10.1029/2001jc000929

Sannino G, Bargagli A, Artale V (2004) Numerical modeling of the semidiurnal tidal exchange through the Strait of Gibraltar. Journal of Geophysical Research C: Oceans 109(5), DOI 10.1029/2003JC002057

Sannino G, Carillo A, Artale V (2007) Three-layer view of transports and hydraulics in the Strait of Gibraltar: A three-dimensional model study. Journal of Geophysical Research: Oceans 112(3), DOI 10.1029/2006JC003717

Sannino G, Carillo A, Pratt L (2009a) Hydraulic criticality of the exchange flow through the strait of Gibraltar. Journal of Physical Oceanography 39(11):2779–2799, DOI 10.1175/2009JPO4075.1

Sannino G, Herrmann M, Carillo A, Rupolo V, Ruggiero V, Artale V, Heimbach P (2009b) An eddy-permitting model of the Mediterranean Sea with a two-way grid refinement at the Strait of Gibraltar. Ocean Modelling 30(1):56–72, DOI 10.1016/j.ocemod.2009.06.002, URL `http://dx.doi.org/10.1016/j.ocemod.2009.06.002`

Sannino G, Garrido JC, Liberti L, Pratt L (2014) Exchange Flow through the Strait of Gibraltar as Simulated by a σ-Coordinate Hydrostatic Model and a z-Coordinate Nonhydrostatic Model. The Mediterranean Sea: Temporal Variability and Spatial Patterns 9781118847:25–50, DOI 10.1002/9781118847572.ch3

Sannino G, Carillo A, Pisacane G, Naranjo C (2015) On the relevance of tidal forcing in modelling the Mediterranean thermohaline circulation. Progress in Oceanography 134:304–329, DOI 10.1016/j.pocean.2015.03.002

Sannino G, Sözer A, Özsoy E (2017) A high-resolution modelling study of the Turkish Straits System, vol 67. Ocean Dynamics, DOI 10.1007/s10236-017-1039-2

Sannino G, Carillo A, Iacono R, Napolitano E, Palma M, Pisacane G, Struglia M (2022) Modelling present and future climate in the Mediterranean Sea: a focus on sea-level change. Climate Dynamics (0123456789), DOI 10.1007/s00382-021-06132-w, URL `https://doi.org/10.1007/s00382-021-06132-whttps://link.springer.com/10.1007/s00382-021-06132-w`

Sanz JL, Acosta Yepes J, Esteras M, Herranz P, Palomo C, Sandoval N (1991) Prospección geofísica del Estrecho de Gibraltar: resultados del programa Hércules (1980-1983). Publicaciones Especiales del Instituto Espanol de Oceanografia pp 7–48

Schmidt J (1922) Oceanography of the Gibraltar region. Nature 109(2724):45–47, DOI 10.1038/109045a0

Schober P, Boer C, Schwarte LA (2018) Correlation Coefficients. Anesthesia & Analgesia 126(5):1763–1768, DOI 10.1213/ANE.0000000000002864, URL `http://journals.lww.com/00000539-201805000-00050`

Send U, Baschek B (2001) Intensive shipboard observations of the flow through the Strait of Gibraltar. Journal of Geophysical Research: Oceans 106(C12):31,017–31,032, DOI 10.1029/2000JC000459, URL `http://doi.wiley.com/10.1029/2000JC000459`

Send U, Lankhorst M, Kanzow T (2011) Observation of decadal change in the Atlantic meridional overturning circulation using 10 years of continuous transport data. Geophysical Research Letters 38(24):1–5, DOI 10.1029/2011GL049801

Serra N, Sadoux S, Ambar I, Renouard D (2002) Observations and laboratory modeling of meddy generation at Cape St. Vincent. Journal of Physical Oceanography 32(1):3–25, DOI 10.1175/1520-0485(2002)032⟨0003:OALMOM⟩2.0.CO;2

Sevault F, Somot S, Beuvier J (2009) A regional version of the NEMO ocean engine on the Mediterranean Sea: NEMOMED8 user's guide. Note de centre pp 1–39, URL `http://scholar.google.com/scholar?hl=en&btnG=Search&q=intitle:A+regional+version+of+the+NEMO+ocean+engine+on+the+Mediterranean+Sea:+NEMOMED8+user's+guide#0`

Sevault F, Somot S, Alias A, Dubois C, Lebeaupin-Brossier C, Nabat P, Adloff F, Déqué M, Decharme B (2014) A fully coupled Mediterranean regional climate system model: design and evaluation of the ocean component for the 1980–2012 period. Tellus A: Dynamic Meteorology and Oceanography 66(1):23,967, DOI 10.3402/tellusa.v66.23967

Shchepetkin AF, McWilliams JC (2005) The regional oceanic modeling system (ROMS): A split-explicit, free-surface, topography-following-coordinate oceanic model. Ocean Modelling 9(4):347–404, DOI 10.1016/j.ocemod.2004.08.002

Somot S, Sevault F, Déqué M (2006) Transient climate change scenario simulation of the Mediterranean Sea for the twenty-first century using a high-resolution ocean circulation model. Climate Dynamics 27(7-8):851–879, DOI 10.1007/s00382-006-0167-z

Somot S, Sevault F, Déqué M, Crépon M (2008) 21st century climate change scenario for the Mediterranean using a coupled atmosphere-ocean regional climate model. Global and Planetary Change 63(2-3):112–126, DOI 10.1016/j.gloplacha.2007.10.003

Somot S, Houpert L, Sevault F, Testor P, Bosse A, Taupier-Letage I, Bouin MN, Waldman R, Cassou C, Sanchez-Gomez E, Durrieu de Madron X, Adloff F, Nabat P, Herrmann M (2018) Characterizing, modelling and understanding the climate variability of the deep water formation in the North-Western Mediterranean Sea. Climate Dynamics 51(3):1179–1210, DOI 10.1007/s00382-016-3295-0

Song Q (2004) Significance of the vertical profile of the Indonesian Throughflow transport to the Indian Ocean. Geophysical Research Letters 31(16):L16,307, DOI 10.1029/2004GL020360, URL `http://doi.wiley.com/10.1029/2004GL020360`

Soto-Navarro J, Somot S, Sevault F, Beuvier J, Criado-Aldeanueva F, García-Lafuente J, Béranger K (2015) Evaluation of regional ocean circulation models for the Mediterranean Sea at the Strait of Gibraltar: volume transport and thermohaline properties of the outflow. Climate Dynamics 44(5-6):1277–1292, DOI 10.1007/s00382-014-2179-4

Soto-Navarro J, Jordá G, Amores A, Cabos W, Somot S, Sevault F, Macías D, Djurdjevic V, Sannino G, Li L, Sein D (2020) Evolution of Mediterranean Sea water properties under climate change scenarios in the Med-CORDEX ensemble. Climate Dynamics 54(3-4):2135–2165, DOI 10.1007/s00382-019-05105-4, URL `http://link.springer.com/10.1007/s00382-019-05105-4`

Soto-Navarro J, Criado-Aldeanueva F, García-Lafuente J, Sánchez-Román A (2010) Estimation of the Atlantic inflow through the Strait of Gibraltar from climatological and in situ data. Journal of Geophysical Research:

Oceans 115(C10):2010JC006,302, DOI 10.1029/2010JC006302, URL https://onlinelibrary.wiley.com/doi/10.1029/2010JC006302

Sparrow M, Boebel O, Zervakis V, Zenk W, Cantos-Figuerola A, Gould WJ (2002) Two circulation regimes of the Mediterranean outflow revealed by Lagrangian measurements. Journal of Physical Oceanography 32(5):1322–1330, DOI 10.1175/1520-0485(2002)032⟨1322:TCROTM⟩2.0.CO;2

Stanev EV, Peneva EL (2001) Regional sea level response to global climatic change: Black Sea examples. Global and Planetary Change 32(1):33–47, DOI 10.1016/S0921-8181(01)00148-5

Stommel) H, Bryden) H, Mangelsdorf) P (1973) Does some of the Mediterranean outflow come from great depth? Pure and Applied Geophysics PAGEOPH 105(1):879–889, DOI 10.1007/BF00875837, URL http://link.springer.com/10.1007/BF00875837

Strandberg G, Bärring L, Hansson U, Jansson C, Jones C, Kjellström E, Michael Kolax G Marco Kupiainen, Nikulin PS, Wang AU, Shiyu (2014) CORDEX scenarios for Europe from the Rossby Centre regional climate model RCA4. Rep Meteorol Climatol 116(116):1–84, URL https://www.smhi.se/polopoly_fs/1.90273!/Menu/general/extGroup/attachmentColHold/mainCol1/file/RMK_116.pdf

Struglia MV, Mariotti A, Filograsso A (2004) River discharge into the Mediterranean sea: Climatology and aspects of the observed variability. Journal of Climate 17(24):4740–4751, DOI 10.1175/JCLI-3225.1

Swingedouw D, Colin C, Eynaud F, Ayache M, Zaragosi S (2019) Impact of freshwater release in the Mediterranean Sea on the North Atlantic climate. Climate Dynamics 53(7-8):3893–3915, DOI 10.1007/s00382-019-04758-5, URL https://doi.org/10.1007/s00382-019-04758-5http://link.springer.com/10.1007/s00382-019-04758-5

Talandier C, Deshayes J, Treguier AM, Capet X, Benshila R, Debreu L, Dussin R, Molines JM, Madec G (2014) Improvements of simulated Western North Atlantic current system and impacts on the AMOC. Ocean Modelling 76:1–19, DOI 10.1016/j.ocemod.2013.12.007, URL http://dx.doi.org/10.1016/j.ocemod.2013.12.007

Tamburini C, Canals M, Durrieu de Madron X, Houpert L, Lefèvre D, Martini S, D'Ortenzio F, Robert A, Testor P, Aguilar JA, Samarai IA, Albert A, André M, Anghinolfi M, Anton G, Anvar S, Ardid M, Jesus ACA, Astraatmadja TL, Aubert JJ, Baret B, Basa S, Bertin V, Biagi S, Bigi A, Bigongiari C, Bogazzi C, Bou-Cabo M, Bouhou B, Bouwhuis MC, Brunner J, Busto J, Camarena F, Capone A, Cârloganu C, Carminati G, Carr J, Cecchini S, Charif Z, Charvis P, Chiarusi T, Circella M, Coniglione R, Costantini H, Coyle P, Curtil C, Decowski P, Dekeyser I, Deschamps A, Donzaud C, Dornic D, Dorosti HQ, Drouhin D, Eberl T, Emanuele U, Ernenwein JP, Escoffier S, Fermani P, Ferri M, Flaminio V, Folger F, Fritsch U, Fuda JL, Galatà S, Gay P, Giacomelli G, Giordano V, Gómez-González JP, Graf K, Guillard G, Halladjian G, Hallewell G, van Haren H, Hartman J, Heijboer AJ, Hello Y, Hernández-Rey JJ, Herold B, Hößl J, Hsu

CC, de Jong M, Kadler M, Kalekin O, Kappes A, Katz U, Kavatsyuk O, Kooijman P, Kopper C, Kouchner A, Kreykenbohm I, Kulikovskiy V, Lahmann R, Lamare P, Larosa G, Lattuada D, Lim G, Presti DL, Loehner H, Loucatos S, Mangano S, Marcelin M, Margiotta A, Martinez-Mora JA, Meli A, Montaruli T, Moscoso L, Motz H, Neff M, Nezri En, Palioselitis D, Păvălaş GE, Payet K, Payre P, Petrovic J, Piattelli P, Picot-Clemente N, Popa V, Pradier T, Presani E, Racca C, Reed C, Riccobene G, Richardt C, Richter R, Rivière C, Roensch K, Rostovtsev A, Ruiz-Rivas J, Rujoiu M, Russo VG, Salesa F, Sánchez-Losa A, Sapienza P, Schöck F, Schuller JP, Schussler F, Shanidze R, Simeone F, Spies A, Spurio M, Steijger JJM, Stolarczyk T, Taiuti MGF, Toscano S, Vallage B, Van Elewyck V, Vannoni G, Vecchi M, Vernin P, Wijnker G, Wilms J, de Wolf E, Yepes H, Zaborov D, De Dios Zornoza J, Zúñiga J (2013) Deep-Sea Bioluminescence Blooms after Dense Water Formation at the Ocean Surface. PLoS ONE 8(7):e67,523, DOI 10.1371/journal.pone.0067523, URL `https://dx.plos.org/10.1371/journal.pone.0067523`

Tejedor L, Izquierdo A, Sein DV, Kagan BA (1998) Tides and tidal energetics of the Strait of Gibraltar: A modelling approach. Tectonophysics 294(3-4):333–347, DOI 10.1016/S0040-1951(98)00110-3, URL `https://linkinghub.elsevier.com/retrieve/pii/S0040195198001103`

Tejedor L, Izquierdo A, Kagan BA, Sein DV (1999) Simulation of the semidiurnal tides in the Strait of Gibraltar. Journal of Geophysical Research: Oceans 104(C6):13,541–13,557, DOI 10.1029/1998JC900102, URL `http://doi.wiley.com/10.1029/1998JC900102`

Tian J, Yang Q, Zhao W (2009) Enhanced Diapycnal Mixing in the South China Sea. Journal of Physical Oceanography 39(12):3191–3203, DOI 10.1175/2009JPO3899.1, URL `http://journals.ametsoc.org/doi/10.1175/2009JPO3899.1`

Timmermans ML, Marshall J (2020) Understanding Arctic Ocean Circulation: A Review of Ocean Dynamics in a Changing Climate. Journal of Geophysical Research: Oceans 125(4):1–35, DOI 10.1029/2018JC014378

Tintoré J, Gomis D, Alonso S, Parrilla G (1991) Mesoscale Dynamics and Vertical Motion in the Alborán Sea. Journal of Physical Oceanography 21(6):811–823, DOI 10.1175/1520-0485(1991)021⟨0811:mdavmi⟩2.0.co;2, URL `http://journals.ametsoc.org/doi/10.1175/1520-0485(1991)021%3C0811:MDAVMI%3E2.0.CO;2`

Tonani M, Pinardi N, Dobricic S, Pujol I, Fratianni C (2008) A high-resolution free-surface model of the Mediterranean Sea. Ocean Science 4(1):1–14, DOI 10.5194/os-4-1-2008

Topper RP, Meijer PT (2015) Changes in Mediterranean circulation and water characteristics due to restriction of the Atlantic connection: A high-resolution ocean model. Climate of the Past 11(2):233–251, DOI 10.5194/cp-11-233-2015, URL `https://cp.copernicus.org/articles/11/233/2015/`

Toumoulin A, Donnadieu Y, Ladant J, Batenburg SJ, Poblete F, Dupont-Nivet G (2020) Quantifying the Effect of the Drake Passage Opening on the Eocene Ocean.

Paleoceanography and Paleoclimatology 35(8):1–22, DOI 10.1029/2020PA003889, URL `https://onlinelibrary.wiley.com/doi/10.1029/2020PA003889`

Tsimplis MN, Bryden HL (2000) Estimation of the transports through the Strait of Gibraltar. Deep-Sea Research Part I: Oceanographic Research Papers 47(12):2219–2242, DOI 10.1016/S0967-0637(00)00024-8

Tsimplis MN, Proctor R, Flather RA (1995) A two-dimensional tidal model for the Mediterranean Sea. Journal of Geophysical Research 100(C8), DOI 10.1029/95jc01671

Umlauf L, Burchard H (2005) Second-order turbulence closure models for geophysical boundary layers. A review of recent work. Continental Shelf Research 25(7-8):795–827, DOI 10.1016/j.csr.2004.08.004, URL `https://linkinghub.elsevier.com/retrieve/pii/S0278434304003152`

University of Wisconsin-Madison (2005) Global River Discharge Database. UNESCO, Paris, international Hydrological Program, Global Hydrological Archive and Analysis Systems HRAF mean 90th perc max corr HL 117(414):17, URL `http://www.sage.wisc.edu/riverdata/`

Vargas JM, García-Lafuente J, Candela J, Sánchez AJ (2006) Fortnightly and monthly variability of the exchange through the Strait of Gibraltar. Progress in Oceanography 70(2-4):466–485, DOI 10.1016/j.pocean.2006.07.001

Vázquez A, Stashchuk N, Vlasenko V, Bruno M, Izquierdo A, Gallacher PC (2006) Evidence of multimodal structure of the baroclinic tide in the Strait of Gibraltar. Geophysical Research Letters 33(17):L17,605, DOI 10.1029/2006GL026806, URL `http://doi.wiley.com/10.1029/2006GL026806`

Vázquez A, Bruno M, Izquierdo A, Macías D, Ruiz-Cañavate A (2008) Meteorologically forced subinertial flows and internal wave generation at the main sill of the Strait of Gibraltar. Deep Sea Research Part I: Oceanographic Research Papers 55(10):1277–1283, DOI 10.1016/j.dsr.2008.05.008, URL `https://linkinghub.elsevier.com/retrieve/pii/S0967063708000939`

Vázquez A, Flecha S, Bruno M, Macías D, Navarro G (2009) Internal waves and short-scale distribution patterns of chlorophyll in the Strait of Gibraltar and Alborán Sea. Geophysical Research Letters 36(23):L23,601, DOI 10.1029/2009GL040959, URL `http://doi.wiley.com/10.1029/2009GL040959`

Velaoras D, Papadopoulos VP, Kontoyiannis H, Papageorgiou DK, Pavlidou A (2017) The Response of the Aegean Sea (Eastern Mediterranean) to the Extreme 2016–2017 Winter. Geophysical Research Letters 44(18):9416–9423, DOI 10.1002/2017GL074761

Viebahn JP, von der Heydt AS, Le Bars D, Dijkstra HA (2016) Effects of Drake Passage on a strongly eddying global ocean. Paleoceanography 31(5):564–581, DOI 10.1002/2015PA002888

Vilibic I, Orli M (2002) Adriatic water masses, their rates of formation and transport through the Otranto Strait. Deep-Sea Research Part I: Oceanographic Research Papers 49(8):1321–1340, DOI 10.1016/S0967-0637(02)00028-6

Vilibić I, Šantić D (2008) Deep water ventilation traced by Synechococcus cyanobacteria. Ocean Dynamics 58(2):119–125, DOI 10.1007/s10236-008-0135-8

Viúdez A, Pinot JM, Haney RL (1998) On the upper layer circulation in the Alboran Sea. Journal of Geophysical Research: Oceans 103(C10):21,653–21,666, DOI 10.1029/98JC01082, URL `http://doi.wiley.com/10.1029/98JC01082`

Viúdez Tintoré J, Haney RL (1996) Circulation in the Alboran Sea as Determined by Quasi-Synoptic Hydrographic Observations. Part I: Three-Dimensional Structure of the Two Anticyclonic Gyres. Journal of Physical Oceanography 26(5):684–705, DOI 10.1175/1520-0485(1996)026⟨0684:CITASA⟩2.0.CO;2, URL `http://journals.ametsoc.org/doi/10.1175/1520-0485(1996)026%3C0684:CITASA%3E2.0.CO;2`

Vlasenko V, Sanchez Garrido JC, Stashchuk N, Lafuente JG, Losada M (2009) Three-dimensional evolution of large-amplitude internal waves in the Strait of Gibraltar. Journal of Physical Oceanography 39(9):2230–2246, DOI 10.1175/2009JPO4007.1

Voelker AH, Lebreiro SM, Schönfeld J, Cacho I, Erlenkeuser H, Abrantes F (2006) Mediterranean outflow strengthening during northern hemisphere coolings: A salt source for the glacial Atlantic? Earth and Planetary Science Letters 245(1-2):39–55, DOI 10.1016/j.epsl.2006.03.014, URL `https://linkinghub.elsevier.com/retrieve/pii/S0012821X06002202`

Voldoire A, Decharme B, Pianezze J, Lebeaupin Brossier C, Sevault F, Seyfried L, Garnier V, Bielli S, Valcke S, Alias A, Accensi M, Ardhuin F, Bouin MN, Ducrocq V, Faroux S, Giordani H, Léger F, Marsaleix P, Rainaud R, Redelsperger JL, Richard E, Riette S (2017) SURFEX v8.0 interface with OASIS3-MCT to couple atmosphere with hydrology, ocean, waves and sea-ice models, from coastal to global scales. Geoscientific Model Development 10(11):4207–4227, DOI 10.5194/gmd-10-4207-2017, URL `https://gmd.copernicus.org/articles/10/4207/2017/`

Wadley MR, Bigg GR (2002) Impact of flow through the Canadian Archipelago and Bering Strait on the North Atlantic and Arctic circulation: An ocean modelling study. Quarterly Journal of the Royal Meteorological Society 128(585):2187–2203, DOI 10.1256/qj.00.35, URL `http://doi.wiley.com/10.1256/qj.00.35`

Waldman R, Herrmann M, Somot S, Arsouze T, Benshila R, Bosse A, Chanut J, Giordani H, Sevault F, Testor P (2017a) Impact of the Mesoscale Dynamics on Ocean Deep Convection: The 2012–2013 Case Study in the Northwestern Mediterranean Sea. Journal of Geophysical Research: Oceans 122(11):8813–8840, DOI 10.1002/2016JC012587

Waldman R, Somot S, Herrmann M, Bosse A, Caniaux G, Estournel C, Houpert L, Prieur L, Sevault F, Testor P (2017b) Modeling the intense 2012–2013 dense water formation event in the northwestern Mediterranean Sea: Evaluation with an ensemble simulation approach. Journal of Geophysical Research: Oceans 122(2):1297–1324, DOI 10.1002/2016JC012437, URL `http://doi.wiley.com/10.1002/2016JC012437`

Waldman R, Brüggemann N, Bosse A, Spall M, Somot S, Sevault F (2018) Overturning the Mediterranean Thermohaline Circulation. Geophysical Research Letters 45(16):8407–8415, DOI 10.1029/2018GL078502

Wang DP (1987) The strait surface outflow. Journal of Geophysical Research: Oceans 92(C10):807–825, DOI 10.1029/JC092iC10p10807, URL `http://doi.wiley.com/10.1029/JC092iC10p10807`

Wang DP (1989) Model of mean and tidal flows in the Strait of Gibraltar. Deep Sea Research Part A Oceanographic Research Papers 36(10):1535–1548, DOI 10.1016/0198-0149(89)90056-3, URL `https://linkinghub.elsevier.com/retrieve/pii/0198014989900563`

Wang DP (1993) The strait of Gibraltar model: internal tide, diurnal inequality and fortnightly modulation. Deep-Sea Research Part I 40(6):1187–1203, DOI 10.1016/0967-0637(93)90133-N, URL `https://linkinghub.elsevier.com/retrieve/pii/096706379390133N`

Watson G, Robinson IS (1990) A study of internal wave propagation in the Strait of Gibraltar using shore-based marine radar images. J Physical Oceanography 20(3 , Mar., 1990):374–395, DOI 10.1175/1520-0485(1990)020⟨0374:asoiwp⟩2.0.co;2, URL `http://journals.ametsoc.org/doi/10.1175/1520-0485(1990)020%3C0374:ASOIWP%3E2.0.CO;2`

Weijer W, De Ruijter WPM, Dijkstra HA (2001) Stability of the Atlantic Overturning Circulation: Competition between Bering Strait Freshwater Flux and Agulhas Heat and Salt Sources. Journal of Physical Oceanography 31(8):2385–2402, DOI 10.1175/1520-0485(2001)031⟨2385:SOTAOC⟩2.0.CO;2, URL `http://journals.ametsoc.org/doi/10.1175/1520-0485(2001)031%3C2385:SOTAOC%3E2.0.CO;2`

Wesson JC, Gregg MC (1988) Turbulent Dissipation in the Strait of Gibraltar and Associated Mixing. In: Elsevier Oceanography Series, vol 46, pp 201–212, DOI 10.1016/S0422-9894(08)70547-6, URL `https://linkinghub.elsevier.com/retrieve/pii/S0422989408705476`

Wesson JC, Gregg MC (1994) Mixing at Camarinal Sill in the Strait of Gibraltar. Journal of Geophysical Research 99(C5):9847–9878, DOI 10.1029/94JC00256

Xu G, Yang J, Dong C, Chen D, Wang J (2015) Statistical study of submesoscale eddies identified from synthetic aperture radar images in the Luzon Strait and adjacent seas. International Journal of Remote Sensing 36(18):4621–4631, DOI 10.1080/01431161.2015.1084431

Xu Z (2018) A note on interpreting tidal harmonic constants. Ocean Dynamics 68(2):211–222, DOI 10.1007/s10236-017-1122-8, URL `http://link.springer.com/10.1007/s10236-017-1122-8`

Yagi M, Yasuda I (2012) Deep intense vertical mixing in the Bussol' Strait. Geophysical Research Letters 39(1):n/a–n/a, DOI 10.1029/2011GL050349, URL `http://doi.wiley.com/10.1029/2011GL050349`

Yang J, Price JF (2007) Potential Vorticity Constraint on the Flow between Two Basins. Journal of Physical Oceanography 37(9):2251–2266, DOI 10.1175/JPO3116.1, URL `http://journals.ametsoc.org/doi/10.1175/JPO3116.1`

Zervakis V, Georgopoulos D, Drakopoulos PG (2000) The role of the North Aegean in triggering the recent Eastern Mediterranean climatic changes. Journal of Geophysical Research: Oceans 105(C11):26,103–26,116, DOI 10.1029/2000jc900131

Zervakis V, Georgopoulos D, Karageorgis AP, Theocharis A (2004) On the response of the Aegean Sea to climatic variability: A review. International Journal of Climatology 24(14):1845–1858, DOI 10.1002/joc.1108

Zhang X, Zhang Z, McWilliams JC, Sun Z, Zhao W, Tian J (2022) Submesoscale Coherent Vortices Observed in the Northeastern South China Sea. Journal of Geophysical Research: Oceans 127(2), DOI 10.1029/2021JC018117

Zhang Z, Zhang Y, Qiu B, Sasaki H, Sun Z, Zhang X, Zhao W, Tian J (2020) Spatiotemporal Characteristics and Generation Mechanisms of Submesoscale Currents in the Northeastern South China Sea Revealed by Numerical Simulations. Journal of Geophysical Research: Oceans 125(2):1–21, DOI 10.1029/2019JC015404

Zhu Y, Sun J, Wang Y, Li S, Xu T, Wei Z, Qu T (2019) Overview of the multi-layer circulation in the South China Sea. Progress in Oceanography 175(April 2018):171–182, DOI 10.1016/j.pocean.2019.04.001, URL `https://doi.org/10.1016/j.pocean.2019.04.001`

Ziegenbein J (1969) Short internal waves in the Strait of Gibraltar. Deep Sea Research and Oceanographic Abstracts 16(5):479–487, DOI 10.1016/0011-7471(69)90036-9, URL `https://linkinghub.elsevier.com/retrieve/pii/0011747169900369`

Ziegenbein J (1970) Spatial observations of short internal waves in the Strait of Gibraltar. Deep-Sea Research and Oceanographic Abstracts 17(5):867–875, DOI 10.1016/0011-7471(70)90004-5, URL `https://linkinghub.elsevier.com/retrieve/pii/0011747170900045`

Zilberman NV, Becker JM, Merrifield MA, Carter GS (2009) Model estimates of M2 internal tide generation over Mid-Atlantic ridge topography. Journal of Physical Oceanography 39(10):2635–2651, DOI 10.1175/2008JPO4136.1

Zodiatis G (1991) Water masses and deep convection in the Cretan Sea during late winter 1987. In: Annales Geophysicae, vol 9, pp 367–376

Zweng Mm Reagan Jr SDBTLMGHMABOWKPCSI (2019) World Ocean Atlas 2018, Volume 2: Salinity. Tech. rep., URL `https://archimer.ifremer.fr/doc/00651/76339/`